MICROFLUIDIC SYSTEMS FOR INTERROGATING HOST-PATHOGEN INTERACTIONS

A Dissertation

by

CAN HUANG

Submitted to the Graduate and Professional School of
Texas A&M University
in partial fulfillment of requirements for the degree of

DOCTOR OF PHILOSOPHY

Chair of Committee,	Arum Han
Committee Members,	Paul de Figueiredo
	Pao-Tai Lin
	Byung-Jun Yoon
Head of Department,	Miroslav Begovic

December 2021

Major Subject: Electrical and Computer Engineering

ABSTRACT

Microorganisms in the environment is extremely diverse, yet those that are identified and their functions known are extremely small. Humans have been increasingly coming in contact with these diverse microorganisms stemming from increases in global transportation and urbanization. The emergence of readily available gene editing tools as well as continuing evolution of these microorganisms as they come in contact with human make the biocomplexity even higher. Together, the potential bacterial pathogens in these environments pose significant risk to the public. Methods and tools that can provide comprehensive, systematic, and rapid analyses of these microorganisms can greatly contribute to our understanding of these extremely complex microbial world, especially for microbial pathogens. The research presented here provides three new strategies: first, a proactive strategy to study and understand the molecular mechanisms by which pathogens emerge and evolve, and second, an effective surveillance system that is capable of detecting and analyzing the emerging pathogens in timely manner, and third, development of microfluidic technologies that can enable high-throughput investigation of biological samples. With these strategies in mind, this dissertation presents the development, testing, and utilization of several novel microfluidics systems that each allow different microbial interrogation approaches to be performed in a high-throughput lab-on-a-chip format for combating the emergence of microbial pathogens.

The first platform developed is a microfluidic system named SEER platform, System for Evaluating the Emergence of Replicating pathogens, which enables the fully automated, multi-round directed evolution of intracellular parasitism in the laboratory. The SEER platform utilizes a porous membrane filter-based selective cell manipulation microfluidic technology, and can direct naïve bacterial populations that are initially incapable of intracellular bacterial parasitism to evolve and generate populations that can display enhanced survival within macrophages, so to determine genetic loci that confer this phenotype. This platform was successfully utilized to study the symbiotic evolutionary process between *E. coli* DH5α strain and RAW264.7 macrophage and have confirmed the contribution of cpxR gene on the enhanced survival phenotype. The second platform is a high-throughput, dielectrophoresis-based microfluidics platform that can achieve selective manipulation of cells from mixed cell communities in a non-destructive, single-cell resolution manner, which allows microorganisms that adhere to mammalian host cells to be selected and sorted for further analysis of their pathogenicity. This platform was successfully utilized to investigate two environmental soil samples and various adherent pathogens that originally presented in the soil with low abundancy were extracted and identified with this high-throughput microfluidic method.

In addition to the successful development of two microfluidic systems for host-pathogen interaction studies, several microfluidic technology advancements have also been achieved based on the utilization of dielectrophoresis phenomena. These include the development of in-droplet cell separation technology, in-droplet solution exchange technology, droplet size-based sorting technology, as well as new microfabrication architectures that can significantly improve the performances of microfluidic systems. All developed technologies have been successfully validated and their utilities demonstrated, and are expected to greatly expand the potential application of microfluidic systems in conducting cell biology assays.

To my wife, my parents
for their endless love and support

ACKNOWLEDGEMENTS

I would like to express my sincerest gratitude to Dr. Arum Han for advising me throughout my academic program. Thanks to his patience and endless support, and countless inspirational guidance. I feel so lucky to be receiving my academic training from NanoBio Systems Lab.

I also would like to acknowledge Dr. Paul de Figueiredo for his valuable input and his encouragement throughout my research. I am very grateful to have this opportunity to learn microbiology throughout my research. I also want to make a special thanks to Dr. Jing Yang, Dr. Fengguang Guo, and Jasmine Olivares from Dr. Paul de Figueiredo' s lab for their efforts on the collaboration projects.

I would like to thank Dr. Pao-Tai Lin and Dr. Byung-Jun Yoon for being my academic committee member and provide unpriced suggestion to my research.

I would thank all our group members in the NanoBio Systems lab for their supports, helps, precious discussions, and friendships! I would like to give special thanks to Song-I Han for her initial lab training and extra guidance over the years.

Lastly, thanks to my family. Thanks to my parents for unconditional support and understanding, without them I would not be able to succeed. Thanks for my wife for her many sacrifices to my academic pursues. And thanks to my pet, Matuan, who brought me endless laugh and smile to face the challenges.

CONTRIBUTORS AND FUNDING SOURCES

Contributors

This dissertation was supervised by committee consisting of Dr. Arum Han, Dr. Paul de Figueiredo, Dr. Pao-Tai Lin, and Dr. Byung-Jun Yoon. Biological sample preparation and analysis was completed with the assistance of Dr. Fengguang Guo and Dr. Jing Yang from Dr. Paul de Figueiredo' s lab.

Funding Sources

The project shown in Chapter 2 was supported by the Bill and Melinda Gates Foundation grant #OPP1058695.

The project shown in Chapters 3, 4, 5, 7 was sponsored by the Defense Advanced Research Projects Agency agreement #W911NF1920013.

The project shown in Chapter 6 was supported by the U.S. Army Combat Capabilities Development Command (DEVCOM) Army Research Laboratory (ARL) Cooperative agreement #W911NF-17-2-0144.

NOMENCLATURE

ε_c^* = complex permittivity of cells

ε_m^* = complex permittivities of suspension media

ε = permittivity of the material

σ = electrical conductivity of the material

t = time

η = apparent viscosity of cell in a suspension media

S = maximum cross-sectional area

l = characteristic length of cells

a = effective radius of the electrode

d = half width and half spacing of a planal interdigitated electrode

F_{DEP} = x-directional pDEP force

$Re[f_{CM}]$ = real part of the Clausius-mossotti factor

V_c = cell volume

v_a = applied voltage

$\vec{A}$ = calculated electric field

x = x-directional cell position ($-d/2 < x < d/2$)

z = levitation height of cell from the electrode array

$\overrightarrow{a_x}$ = x-directional unit vector

$\overrightarrow{a_z}$ = z-directional unit vector

TABLE OF CONTENTS

Page

ABSTRACT ii

DEDICATION iv

ACKNOWLEDGEMENTS v

CONTRIBUTIORS AND FUNDING SOURCES vi

NOMENCLATURE vii

TABLE OF CONTENTS viii

LIST OF FIGURES xii

LIST OF TABLES xvi

1. INTRODUCTION 1

    1.1 Host-pathogen interaction study and current limitations 1
    1.2 Objectives and chapter outlines 3

2. MEMBRANED-BASED MICROFLUIDICS SYSTEM FOR MICROBIAL ENDOSYMBIOSIS EVOLUTION STUDY 6

    2.1 Overview 6
    2.2 Introduction 7
    2.3 Evolutionary assay design 10
    2.4 Device design and fabrication 12
        2.4.1 Membrane-based microfluidic cell trapping and release system 12
        2.4.2 SEER microfluidic system design and validation 15
        2.4.3 Device design details and fabrication 17
        2.4.4 Operations of on-chip evolutionary assay 19
    2.5 Biological material and methods 20
        2.5.1 Cell preparation 20
        2.5.2 Characterization of endosymbiosis phenotype 21
        2.5.3 Stress response assay 22
    2.6 Results 22
        2.6.1 Evolved strain characterization 22
        2.6.2 Gene mutation identification 24
        2.6.3 cpxR mutation promotes *E. coli* survival in J774A.1 macrophage 30
        2.6.4 cpxR mutant resists to other stresses 32
        2.6.5 Other stress-related genes also affect *E. coli* intracellular survival 33
    2.7 Automation of the SEER platform 34
    2.8 Discussion 39

2.9 Conclusion 40

3. MICROFLUIDIC SYSTEM FOR DIGITAL ANALYSIS OF ADHERENT BACTERIA TO IDENTIFIES EMERGENT PATHOGENS 42

3.1 Overview 42
3.2 Introduction 43
3.3 Working principle of the microfluidic device 46
3.4 Microfluidic device design and microfabrication 49
3.5 Biological material and methods 50
  3.5.1 A549 cell culture conditions 50
  3.5.2 A549 suspension cell adaptation 50
  3.5.3 Bacterial cell preparation 51
  3.5.4 Bacterial community preparation 51
  3.5.5 Preparation of low-conductivity medium 53
  3.5.6 Adherence assay on multi-well plate format 54
  3.5.7 Cell viability assay 55
  3.5.8 Sequencing and analysis 55
3.6 Microfluidic device operation 55
3.7 Results 56
  3.7.1 DEP response of host cells and bacterial cells in the microfluidic system 56
  3.7.2 Separating adherent bacterial cells using the microfluidic system 58
  3.7.3 Bacteria mixing community testing using lateral DEP device (Sensitivity and Selectivity) 60
3.8 Current progress on environmental sample tests 63
3.9 Conclusion 64

4. IN-DROPLET CELL SEPARATION BASED ON BIPOLAR DIELECTROPHORETIC RESPONSE TO FACILITATE CELLULAR DROPLET ASSAYS 66

4.1 Overview 66
4.2 Introduction 67
4.3 Working principle 71
4.4 Device design and fabrication 75
  4.4.1 Device design 75
  4.4.2 Microfabrication 75
  4.4.3 In-droplet cell separation operation 76
4.5 Biological material and methods 77
  4.5.1 Preparation of conductivity media 77
  4.5.2 cell preparation 77
  4.5.3 Cell viability assay 78
  4.5.4 Statistical analysis of separation efficiency 79
4.6 Results 79
  4.6.1 Characterization of in-droplet bacterial cell manipulation 79

4.6.2 Characterization of in-droplet mammalian cell manipulation 82
4.6.3 In-droplet cell separation of cell mixture 84
4.7 Simulation analysis and comparison 86
4.7.1 Electric field simulation 86
4.7.2 Calculation of Stokes drag force 88
4.7.3 Calculation of dielectrophoretic (DEP) force 89
4.7.4 DEP force calculation and comparison 90
4.8 Conclusion and Discussion 91

5. CELL WASHING AND SOLUTION EXCHANGE IN DROPLET MICROFLUIDIC SYSTEMS 96

5.1 Overview 96
5.2 Introduction 97
5.3 Microfluidic system design 100
5.3.1 Device design and operating principle 100
5.3.2 Device fabrication 103
5.3.3 Experimental setup for evaluating the droplet cleaving, pairing, and merging functions 104
5.4 Cells and reagent preparation for the two cell biology assays 105
5.5 Experiment setup 106
5.5.1 Application demonstration using nDEP force for microalga *C. reinhardtii* culture solution exchange 106
5.5.2 Application demonstration using pDEP force with GFP-*S. enterica* for in-droplet cell detection with higher sensitivity 107
5.6 Results and discussion 107
5.6.1 Testing and characterization of the droplet microfluidics platform 107
5.6.2 Identifying parameters that affect the degree of cell washing and solution exchange 110
5.6.3 Cellular application 1 – Detecting lipid induction after exchanging microalgae culture media 113
5.6.4 Cellular application 2 – Improved fluorescent detection of cells in droplets 116
5.7 Future works 118
5.8 Conclusion 118

6. ELIMINATING AIR BUBBLE IN MICROFLUIDIC SYSTEMS UTILIZING INTEGRATED IN-LINE SLOPED MICROSTRUCTURES 120

6.1 Overview 120
6.2 Introduction 121
6.3 Device design and working principle 126
6.4 Device Fabrication 127
6.5 Experiment setup 128
6.6 Results 129

6.6.1 Air bubble accumulation and trapping using the sloped microchamber............. 129
6.6.2 Removal of accumulated air bubbles... 131
6.6.3 Long-term cell cultivation in the microfluidic chamber without disruption by air bubbles 132
6.7 Alternative sloped microstructures for air bubble trapping and removal 133
6.8 Discussion.. 134
6.9 Conclusion 138

7. SIZE-BASED BANDPASS FILTER FOR DROPLET MICROFLUIDIC SYSTEM USING INTERDIGITATED ELECTRODE ARRAY 139

7.1 Overview.. 139
7.2 Introduction.. 140
7.3 Theory and simulation 144
7.4 Design and operating principle 146
7.5 Device fabrication... 148
7.6 Experiment setup 150
7.6.1 Droplet preparation 150
7.6.2 Cell preparation and cultivation after collection.. 151
7.6.3 Experimental setup for proof-of-concept experiment... 151
7.6.4 Experimental setup for device characterization using sonication generated droplets 152
7.6.5 In-droplet IVTT workflow.. 153
7.6.6 Data collection and analysis... 154
7.7 Results 155
7.7.1 Proof of concept validation 155
7.7.2 Characterization using sonication generated droplets... 156
7.7.3 Biocompatibility of the IDE system 159
7.7.4 Application 1: exclude the unmerged and over-merged droplets 160
7.7.5 In-droplet IVTT 161
7.8 Discussion 164
7.9 Conclusion 166

8. OVERALL REVIEW AND CONCLUSIONS 167

REFERENCE... 170

APPENDIX A.. 191

APPENDIX B 200

APPENDIX C 203

LIST OF FIGURES

Page

Fig 2.1 Evolutionary assay design and validation 11

Fig 2.2 Side view of shaking culture carrying GFP-*Salmonella* cells flowing through porous polycarbonate membrane 14

Fig 2.3 Functions of porous membrane-based microfluidics trapping unit with macrophages and bacterial cells 14

Fig 2.4 SEER platform configuration and validation 16

Fig 2.5 SEER platform design 17

Fig 2.6 Flow chart of SEER system operation.. 18

Fig 2.7 Cleaning of the standby chambers and comparison of remained residuals................. 20

Fig 2.8 Validating survival capability of evolved strains 24

Fig 2.9 cpxR is critical for *E. coli* survival in J774A.1 macrophage 31

Fig. 2.10 GFP expressed in constructed *E. coli* strains, and Western blot showed cxpR and cpxR (G89A) expressed in engineered *E. coli* strains P_{WT} and P_{G89A} separately introduced with plasmids 32

Fig 2.11 Stress related genes, cpxA, SoxR, and CyoD play important role in *E. coli* intracellular survival.. 33

Fig 2.12 Block diagram of automated SEER platform 34

Fig 2.13 Illustration diagram showing connections between each functional block 35

Fig 2.14 LabView controller interface, indicating the elapsed time as well as open/close status of each pneumatic controlled valve unit 37

Fig 3.1 Calculated real part of Clausius-Mossotti Factor of mammalian cells and bacterial cells 47

Fig 3.2 Proposed lateral dielectrophoretic screening microfluidic system 48

Fig 3.3 LDEP Device illustration.. 49

Fig 3.4 Example of the adherence assay on multi-well plate format...................................... 54

Fig 3.5 Trajectory comparison of bacterial cells and host cells when DEP turned on/off 57

Fig 3.6 Zoomed in picture shows that bacterial cells that attached on host cell surface were also successfully collected along with host cells during this process........................... 59

Fig 3.7 Comparison of mixture before/after the DEP filtration.. 60

Fig 3.8 Mixture of PAO and *E. coli* at ratio of 1:1 was co-cultured with A549 cells and went 1through the DEP separation. Samples from both outlets were collected and plated .. 61

Fig 3.9 Proposed experimental flow on soil sample extraction/identification using lateral DEP separation device.. 64

Fig. 4.1 Schematic illustration of the in-droplet cell separation platform 73

Fig 4.2 Generated droplets containing bacterial cells and mammalian cells........................... 74

Fig. 4.3 Calculated real part of the Clausius-Mossotti factor ($Re[f_{CM}]$) of a mammalian cell and a bacterial cell, where the medium conductivity is set to 0.032 S/m 74

Fig. 4.4 Movement of Salmonella cells within a droplet as the droplet travels through the electrodes 80

Fig. 4.5 Split daughter droplets collected into two downstream collection chambers, where daughter droplet #1 were collected in the lower collection chamber and daughter droplet #2 were collected in the upper collection chamber 82

Fig. 4.6 Movement of macrophages within a droplet as the droplet travels through the DEP electrodes 83

Fig. 4.7 Movement of Salmonella cells and a macrophage inside a droplet 85

Fig. 4.8 COMSOL simulation results showing the x-directional electric field intensity (V/m) across the cell separation microchannel (COMSOL Multiphysics® 5.5) 87

Fig. 4.9 COMSOL simulation (COMSOL Multiphysics® 5.5) of internal circulation flow field at 33 μl/h flow rate.. 89

Fig. 4.10 Calculated x-directional DEP force acting on bacterial cell and mammalian cell based on the simulation result of x-directional electric field 90

Fig. 5.1 Working principle of the integrated droplet solution exchange platform and photographic image of the fabricated device.. 102

Fig. 5.2 Calculated real part of the polarization coefficient (Re[f_{CM}]) of *C. reinhardtii* cells suspended in TAP media as well as *S. enterica* cells in R2A media 103

Fig. 5.3 In-droplet solution exchange system validation using *C. reinhardtii* strain CC406 cells and color dye 109

Fig. 5.4 Characterization of the splitting and cleaving function using color dye 112

Fig. 5.5 Statical analysis of the cleaved droplet size 113

Fig. 5.6 In-droplet solution exchange workflow to assess the growth and lipid production of the microalga *C. reinhardtii* (CC406 strain) in droplet microfluidics format 114

Fig. 5.7 Solution exchange of a droplet containing *C. reinhardtii* CC-406 cells 116

Fig. 5.8 In-droplet solution exchange workflow to improve the fluorescent detection capability of droplet contents... 117

Fig. 6.1 Working principle of the air bubble trapping structure 125

Fig. 6.2 Bright field image of air bubbles being trapped at the end of the sloped microfluidic chamber where the ceiling is flat and fluorescent image of fluorescent beads continuously flowing out into the outlet channel without being hampered by the sloped microfluidic structure nor by the air bubbles trapped in the trapping region.... 130

Fig. 6.3 Microscopic images of the air bubble trapping/collection chamber with air removal process.. 131

Fig. 6.4 Microscopic images of the air bubble trapping/collection chamber showing air-free long-term cell culture.. 132

Fig. 6.5 Illustration of an alternative air bubble removal design. Instead of having a relatively steep slope that abruptly ends like a step-structure before connecting to the outlet microfluidic channel, in this design the structure gradually slopes down and connects to the main outlet microfluidic channel 134

Fig. 6.6 Simulation results of flow velocities inside the sloped microstructure design (this work) and the step-shaped microstructure (traditional design) 136

Fig. 7.1 The basic theory and working principle of the bandpass filter.................................. 146

Fig. 7.2 The structure of the bandpass filter and its working principle 148

Fig. 7.3 Fabrication steps of the bandpass filter devices 150

Fig. 7.4 The cone shaped PDMS chamber for droplet storage, cultivation, and reflow........... 154

Fig. 7.5 Proof of concept validation using a 120 μm – 80 μm bandpass filter 156

Fig. 7.6 Validation of proposed system using polydispersed droplets 158

Fig. 7.7 Biocompatible test of the IDE system using THP1 cells... 159

Fig. 7.8 Bandpass filter to remove the unsuccessfully merged and over-merged droplets from the upstream merging step 161

Fig. 7.9 Droplet-based IVTT workflow and gel electrophoresis validation 163

Fig. 7.10 Ideal and nonideal IDE alignment and corresponding performances....................... 165

LIST OF TABLES

Page

Table 2.1 Identified variant summary 26

Table 2.2 Summary of 20 nonsynonymous SNPs or indels that seen in functional genes which were considered candidates for mediating phenotypic changes 28

Table 2.3 Sensitivity test comparison between Naïve *E. coli* strain and evolved strain........... 33

Table 2.4 Sample timing of two rounds of evolutionary assay which controlled by central LabView program 37

Table 3.1 Composition of artificial bacterial community for mock screening assay 52

Table 3.2 Summary of sensitivity and selectivity test results 62

Table 3.3 Comparison of documented adhesion, identifications from microfluidic chip as well as conventional result. Here, red indicate high adherence phenotype, green indicate low adherence phenotype 63

Table 4.1 Parameters used in initial CM factor calculation 75

Table 4.2 Parameters used in COMSOL electric field simulation... 88

Table 5.1. Summary of the dielectric properties of cells used in the CM factor simulation 103

1. INTRODUCTION

1.1 Host-pathogen interaction study and current limitations

Just in year 2020, there have been 7 bacterial outbreaks in U.S., with various species such as *Salmonella, E. coli* or *Listeria*, negatively impacting the food industry, agriculture economy and most importantly public health system. Identification of pathogenic bacterial strains is very critical for current public health system as the technology advancement has brought more biocomplexities into people's range of contact, which subsequently posed an increasing risk of exposure to dangerous microbial pathogens[1-5]. For example, bacterial threats are currently very common in food industry and the outbreaks often occurs from the contaminated vegetables, infected poultry, frozen food, water supplies, to name a few. Additionally, the changes of climates, globalization, increasing population, as well as the expanding needs and accessibility of genetic engineering tools have also drastically lifted the likelihood of encountering unknown pathogens from other unexpected fields. Overall, the needs for evaluating the bacterial pathogenicity have dramatically increased in order to effectively combat the rinsing risks of pathogen exposure. Being able to predict the tendency microbial evolution and phenotypic development, as well as being able to identify bacterial pathogens from environmental samples can greatly benefit various fields of interests including pathogenetic genomic, antibiotic production, vaccine evaluation, public health prevention, ecology, and so on.

Deploying proactive approaches, such as experimentally tractable system for studying the evolution dynamic in the laboratory regarding how pathogen could gain intracellular parasitism or other key pathogenicity factors throughout the interaction of host cells, could become a great assistance for understanding the underlying correlation between the chromosol alternations and resulting evolved phenotypes. Additionally, a deep understanding of the evolution dynamic could also help to predict the tendency of the evolution, which might be able to better pose the strategies for outbreak prevention. If successful, these studies might uncover the hidden molecular mechanisms that drive the emergence and evolution of these pathogens, which can thereby benefit the development of preventative medicals or treatment strategies.

In terms of the reactive response and fast analysis of emerging pathogens, several strategies have been established to provide surveillances on invasive bacterial pathogens, aiming to support further investigation based on the real-time data and case evaluations. However, current existing strategies, including rapid diagnostic biology as well as metagenomics, are both leaning more on recognizing previously known bacterial strains, which is about 350 well-studied strains, which accounts for only a very small portion of bacteria spices considering the diversity of the Kingdom Bacteria. Gene sequencing technologies have also been developed in recent year buts still is relying on the existing understanding of genotype and the underlying relation between their driving gene and phenotype. Subsequently, majority of the bacterial diversity are currently remained obscure in terms of their pathogenicity determinations and won't be able to be analyzed by any of the mentioned tools.

A better solution to enhance the coverage of detectable spectrum can be as simple as directly characterizing bacterial pathogenicity of bacterial mixture. However, the direct testing often comes with a trade-off of throughput. First, previously mentioned bio-surveillance strategies can process many strains of bacteria at once, but conventional microbiology investigation were typically done at single strain basis. Having more types of cells tested together will increase the background noise and will have a hard time conclude phenotype of each strain if without effective labeling. Second, single isolates were typically obtained by plating which add more preparation time before actual conductance of experiments. Therefore, a platform that capable of phenotyping multiple strains at once is urged for the rapid determination of environmental bacterial pathogens.

1.2 Objectives and chapter outlines

To realize the functionality of those aforementioned key features, two microfluidic systems were developed. First, an enclosed *in vitro* microsystem that supports the study of the evolution of intracellular parasitism was developed and was deployed in the host-pathogen study using naïve *E. coli* strain and macrophages. Second, a microfluidics system that supports the quick identification of potential pathogens from environmental sample was developed and deployed in the soil sample analysis to find out the bacterial strains that with high adherence phenotypes.

The first developed microfluidic microsystem, SEER (System for Evaluating the Emergence of Replicating pathogens), exploited a novel porous membrane-based microfluidic system that can selectively trap and release bacterial cells and host cells using extremely simple structures and operations to automate a multi-step infection assay (total 11 steps). Here, chapter two covers all the relative materials for development of SEER platform. The second developed microfluidics microsystem, HiTAP (High-Throughput Adherence Phenotyping platform) will utilized the dielectrophoretic response that can selectively manipulate the target cells in a high-throughput manner without additional labeling to separate out the high binding bacterial cells from target community. Chapter 3 covers all the materials for development of HiTAP platform. The central hypothesis is that the SEER microfluidic lab-on-a-chip system can be used to evolve strains that harbor chromosomal alterations that confer enhanced intracellular survival, and the HiTAP microfluidics lab-on-chip system can be used to enable fast interrogation on adherence phenotypes of each individual strain from mixed community while holding high resolution and high accuracy.

On top of the successful development of two microfluidic systems for host-pathogen interaction study, several microfluidic technology advancements have also been achieved based on the utilization of cellular dielectrophoretic response to expand the applicability of microfluidic system on biological investigation.

First, the unique dielectrophoretic properties that utilized in separation of host and pathogen cells was transferred into a droplet microfluidic format, achieving the manipulation/separation of two different types of cells in the droplets. Such technology can unleash the droplet microfluidic technologies by bringing an important yet unavailable solution for in-droplet cell manipulation. The fourth chapter covers this in-droplet cell separation technology development.

Second, to realize the centrifugation-resuspension operation in the droplet microfluidic format, developed cell separation technologies were combined with droplet pairing and merging technologies to achieve in-droplet cell concentration – unwanted medium removal – addition of fresh medium, which essentially mimic the conventional cell rinsing steps. The fifth chapter covers this in-droplet solution exchange technology development.

Third, by upscaling the dielectrophoretic manipulation from cellular level to droplet level, the precise manipulation of droplets that with different sizes were achieved by utilizing the highly localized electric field. The entire droplet could be selectively manipulated with predefined size ranges and system was examined with highly diverse-sized droplet library. The seventh chapter covers relative materials for size-based droplet filtration and manipulation technology development.

Lastly, as a novel finding during the realization of SEER platform, the novel two-photon-polymerization photolithography tool could be utilized to unleash the z-axis limitation which typically accompanied with fabrication of master mold that used in soft-lithography process, thereby enabling the novel height-variant structures to be fabricated in a simple method. With the help of such novel tool, several novel microfluidic structures were fabricated and proved to have improved performance in various applications. The development of 2PP related novel fabrication structure is covered in chapter 6.

Overall, the development of these droplet microfluidic technologies could complete the lab-on-a-chip realization on most of the essential fundamental operations in conventional biological practice. In additional to the developed two microfluidic system that specialized on two specific biological investigation applications, as well as the utilization of novel three-dimensional microfluidic structure, we expect these advancements could enable numerous biological applications to be adapted in the microfluidic format in the near future.

2. MEMBRANED-BASED MICROFLUIDICS SYSTEM FOR MICROBIAL ENDOSYMBIOSIS EVOLUTION STUDY

2.1 Overview

Symbiosis, a status of “living together of unlike organisms”, plays a central role in the evolution of life. Many symbioses that involve interactions between microbes and eukaryotic cells, especially endosymbiosis in which microbes live inside eukaryotic cells, are critical to human health and disease. However, the molecular mechanisms that drive the emergence of inter-kingdom endosymbiosis remain obscure. Here, we describe the development of a microfluidic system, named SEER (System for the Evolution of Endosymbiotic Relationships), that automates the evolutionary selection of emergent inter-kingdom symbionts with enhanced intracellular survival and persistence within host cells. To demonstrate this concept, we show that a laboratory strain of *Escherichia coli* that initially possessed limited abilities to survive within eukaryotic host cells, when subjected to selection in the SEER system, the strain rapidly evolved to have capabilities for enhanced intracellular survival. Notably, molecular dissection of the evolved strains revealed that a single point mutation in the gene of envelope stress response regulator (*cpxR*) contributes substantially to the bacterial increased intracellular survival and persistence. Taken together, these results show the establishment of a microfluidic system for investigating the evolution of endosymbiosis, identification of cpxR as a genetic locus that contributes to this process, and set the stage for evolving other bespoke inter-Kingdom endosymbiotic systems with novel or emergent properties.

2.2 Introduction

Endosymbiosis is a major force driving the evolution of life. It is now appreciated that mitochondria and plastids, the classical membrane-bound organelles of eukaryotic cells, evolved from bacteria through endosymbiosis.[6,7] Inter-kingdom symbiotic interactions also play a central role in the evolution and physiology of land plants. For example, *Rhizobia*, endosymbiotic bacteria that fix atmospheric nitrogen, provide critical nutrients to many crops of agricultural importance, including legumes.[8] In another example, *Wolbachia*, which encompass a large group of endosymbiotic bacteria, play central roles in supporting the lifestyle of ecdysozoa species, including terrestrial arthropods.[9,10] Finally, emerging intracellular bacterial pathogens of humans and animals must acquire novel traits to survive, persist, or replicate within mammalian host cells, including immune cells like macrophages. As illustrated by these examples, endosymbiotic interactions are critical for the evolution and physiology of terrestrial living systems, including intracellular bacterial pathogens. Despite the importance of these interactions, surprisingly little is known about the mechanisms by which *de novo* emergence of endosymbiotic interactions occurs. This fact reflects, in part, the paucity of tractable experimental systems for interrogating the step-wise analysis of emergent endosymbiotic interactions.

To address this limitation, several reports described the development of synthetic systems in which synthetic, engineered, or evolved endosymbiotic interactions can be interrogated. For example, a pathogenic *Ralstonia solanacearum*, which is a typical root-infecting pathogen of plants, was engineered to carry a symbiotic plasmid pRalta containing nitrogen-fixation gene from a rhizobium. After inoculated the engineered bacteria in plant and grown in nitrogen-free conditions, the bacteria shown to establish productive symbiotic interactions with plants.[11] Interestingly, serial passaging of these recombinant strains in plants gave rise to variants with further enhanced symbiotic properties, linked to the suppression of virulence properties, thereby demonstrating that synthetic symbiotic interactions can be evolved when appropriate selective pressure is imposed on the system[12]. Genetic engineering of *Saccharomyces cerevisiae* toward synthetic symbiosis with bacteria has also been achieved, thereby setting the stage for the molecular dissection of genes that drive the evolution of organelles of endosymbiotic origin (e.g., mitochondria) or intracellular bacterial parasites.[13] Finally, serial passaging of bacterial pathogens in macrophages or propagation in animal models has been used to interrogate the evolution of virulence-associated adaptations.[14-16] These studies demonstrated the utility of laboratory models for evaluating mechanisms driving alterations in bacterial survival and fitness in the host.

Despite these advances, current understanding of the molecular drivers of the evolution of *de novo* endosymbiotic interactions remains incomplete. Previous studies had shown that laboratory systems for the analysis of evolution of a single bacterial species can provide important insights into fundamental biological mechanisms, including genome stability, metabolic regulation, and antibiotic resistance. In these systems, target bacteria were subjected to multiple rounds of mutagenesis, selection, and amplification, ultimately leading to the evolution of highly adapted strains. Importantly, the study of the evolution of antibiotic resistance, a trait which contributes to human disease by thwarting pharmacological intervention, has enabled the development of novel strategies for defeating resistance. Hence, the study of evolution of potentially pathogenic traits ultimately benefits countermeasure development. With these ideas in mind, we pursued a strategy to develop laboratory systems that enable the evolution of interactions between a laboratory strain of *Escherichia coli* (DH5a) and murine macrophages (J774A.1) to display hallmarks of inter-kingdom endosymbiosis and pathogenesis from *de novo*, in the form of intracellular survival of *E. coli* within the macrophages.

One of the major hurdles in laboratory studies that interrogate the evolution of inter-kingdom endosymbiosis is the necessity of repeatedly performing the evolutionary steps required for bacterial evolution and adaptation, as only by many rounds of evolutionary steps can such process result in the rise of endosymbiosis. Thus, despite the fact that such an evolutionary strategy can accelerate the identification of interesting inter-kingdom endosymbiotic interactions, the time-consuming and labor-intensive nature of these experiments have been a major bottleneck in the field. Cognizant that implementation of evolutionary strategy would greatly benefit from the reduced hands-on time and increased reproducibility afforded by automation, we developed a microfluidic lab-on-a-chip system to repeatedly execute the requisite manipulations of cells and reagents. Microfluidic lab-on-a-chip systems have the capability to precisely handle extremely small numbers of cells and reagents, and to conduct complex multi-step assays that are automated in a single microchip format. [17-19] Such systems have been extensively utilized for various microbial studies.[20-22] However, no system has been reported in which the evolution of bacterial species towards endosymbiosis is performed on-chip. Here, we describe an automated microfabricated microfluidic system named SEER (System for Evolving Endosymbiotic Relationships) that performed sequential multi-step cell- and reagent-handling processes that drive the evolution of microbes to acquire enhanced capacities to survive intracellularly. Finally, we show how the application of the novel system uncovered new single nucleotide polymorphisms (SNPs) in the cpxR gene,[23] a component of the cell's stress response pathway, that substantially contributes to intracellular survival, a hallmark of endosymbiosis and intracellular bacterial pathogenesis.

2.3 Evolutionary assay design

The central hypothesis of this study is that a system in which an interaction between bacterial and mammalian cells was evolved in the laboratory could provide insight into mechanisms of endosymbiosis. To verify the utility of this approach for measuring intracellular survival of bacteria, a laboratory strain of *E. coli* (DH5α) that does not have the capability of intracellular survival was first co-incubated with J774A.1 macrophage cell for 96 hours in the presence of gentamicin. Here, gentamicin was exploited because of its limited permeability across the plasma membrane of mammalian cells at low concentrations (e.g., 100 μg/ml). Therefore, gentamicin treatment in the evolutionary assay enables the development of an *in vitro* method for killing extracellular bacterial populations while protecting their intracellular counterparts from harm.[24] Following host cell lysis using Tween 20 buffer, the number of viable intracellular bacteria that remained in the incubation chamber was analyzed. The result showed that gentamicin/host cell system efficiently killed the intracellular *E. coli* population (**Fig. 2.1A**). However, a positive control *Ochrobactrum anthropi* strain, which replicates intracellularly, was efficiently recovered from infected host cells following application of the gentamicin protection regime, as expected (**Fig. 2.1A**).[25] Taken together, these data establish that this is a tractable biological system in which an analysis of the evolution of endosymbiotic properties could be conducted.

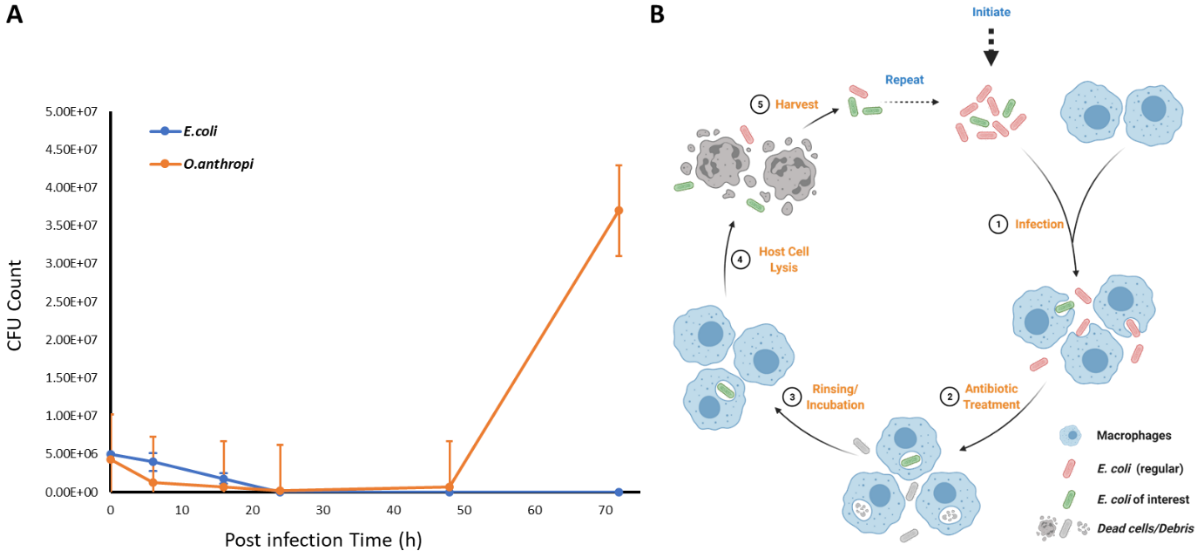

Fig 2.1 Evolutionary assay design and validation. **A**. Time serial intracellular survival population of *E. coli* and *Ochrobactrum anthropi* from infected host cells following application of the gentamicin protection regime. Intracellular *E. coli* population was efficiently killed, however, *O. anthropi* can successfully recovered from the proposed treatment; **B**. Proposed approach to analyzing the evolution of inter-Kingdom endosymbiosis. Bacterial population is incubated with macrophages for extended period of time, and released from host cells, then reamplified in rich culture. Such steps can be performed repeatedly to acquire mutated strains with higher intracellular survival capability.

To better understand how the endosymbiotic properties is evolved during this endosymbiosis interaction, specifically how bacterial cells with limited intracellular capability can acquire such ability during the interaction with host cells, *E. coli* (DH5α), which originally has limited intracellular survival, was selected to be the starting population to track the genetic alternation along with the evolution progression. The approach to analyzing the evolution of inter-Kingdom endosymbiosis was designed to involve the following steps (**Fig. 2.1B**). First, *E. coli* was co-incubated with macrophages (J774A.1) for one hour, during which time the bacteria were internalized into host cells. Next, the host cells after internalization were rinsed extensively with buffer solution to remove the extracellular bacterial cells. To kill any remaining residual extracellular bacterial population, especially those that may be adhering to the surface of macrophages, the infected host cells were further incubated with gentamicin-containing culture media. The lengths of incubation time were first set to be very short (one hour), then extended by each round of evolution (finally to 72 hours), aiming to select strains with better endosymbiosis phenotypes by gradually increasing the internal pressure applied on bacterial cells after they are exposed to intracellular environment. Afterwards, the infected macrophages were lysed to release the intracellular bacterial population. Finally, harvested bacterial population was quantified and then amplified in rich liquid media, and then used as the starting bacterial population for the next round of endosymbiosis assay.

2.4 Device design and fabrication

2.4.1 Membrane-based microfluidic cell trapping and release system

In order to conduct endosymbiosis evolutionary study in the lab-on-a-chip format, it is critical for the system to be able to mix, separate, and selectively retain two investigating cell types during the endosymbiosis process. The proposed membrane-based selective cell trapping and release unit is configured with two stacked milliliter-scale reaction chambers with a porous polycarbonate membrane sandwiched in the middle. The membrane-based method was selected because compared to the many different microfluidic-based cell manipulation method (both passive and active methods), the proposed method can be the easiest and most efficient in selective cell trapping and release as well as solution exchange. When the fluorescent bacterial cells [green fluorescent protein (GFP)-expressing *Salmonella enterica*] was used in the system, all microbes were effectively blocked by the 0.4 µm pore membrane (**Fig. 2.2**). Importantly, the membrane-based microfluidic structure can achieve the required key functions for the evolution assay (**Fig. 2.3**). The integrated unit is configured with two fluidic ports (serve as one inlet and one outlet) at the bottom chamber and one fluidic port (one outlet) at the top chamber, which enables both vertical flow and lateral flow operations. When applying a vertical flow from the bottom chamber to the top chamber through the membrane with cellular contents of interest, this configuration can selectively trap either only the bigger cell type or both cell types depending on the porosity of the membrane. For example, when host cells (10 – 15 µm size) and microbes (1.5 – 3.0 µm size) are used, applying a vertical flow carrying both cell types through the unit that configured with a 0.4 µm pore membrane can trap both cell types in the bottom chamber, enabling co-cultivation of the two cell types (**Fig. 2.3A**). This also allows solution exchange as well as washing/rinsing steps to be achieved by simply flowing a different solution vertically through the same 0.4 µm membrane. Such washing and solution exchange steps are needed in multiple intermediate steps in the proposed assay. When applying a vertical flow through a unit that configured with the 3.0 µm porosity membrane, only the host cells will be physically blocked and trapped in the bottom chamber, while the microbes can penetrate flow through the membrane due to their smaller dimensions. This will result in selective trapping of only host cells, which essentially achieves separation of the two cell types, where the top and bottom chamber will contain microbial cells and host cells, respectively. This manipulation step is needed when rinsing off the excessive extracellular microbes after microbial internalization into host cells, or when harvesting the intracellularly surviving microbes at the end of each round of the evolution assay (**Fig 2.3B**). Lastly, regardless of the porosity of the integrated membrane, when lateral flow is applied, all cells can be retrieved from the unit or the device chamber that can be cleaned to be ready for later usage (**Fig. 2.3C**). GFP-*S. enterica* and RAW264.7

macrophage were used to validate the proposed trapping and release system and successfully demonstrated the proper functionality of each key steps.

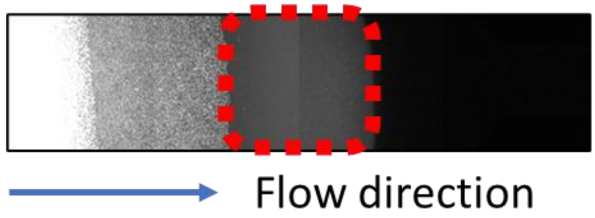

Fig 2.2 Side view of shaking culture carrying GFP-Salmonella cells flowing through porous polycarbonate membrane. GFP-Salmonella cells were successfully blocked and aggregated at the left side of the porous membrane.

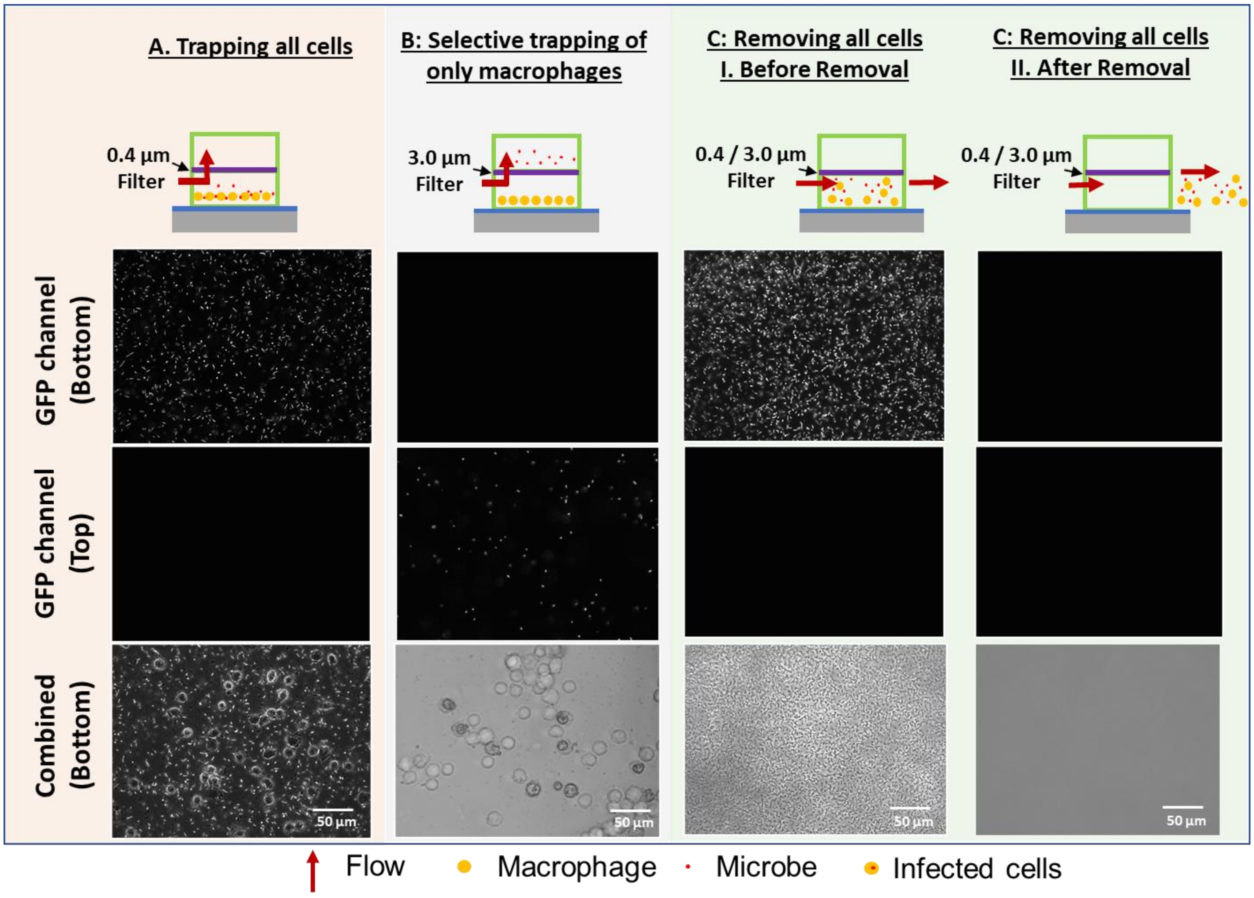

Fig 2.3. Functions of porous membrane-based microfluidics trapping unit with macrophages and bacterial cells. **A**. Vertical flow through 0.4 µm membrane can trap both types of cells; **B**. vertical flow through 3.0 µm can selectively trap mammalian cells while allowing bacterial cells to pass; **C**. Lateral flow can rinse off all types of cells from microfluidic system.

2.4.2 SEER microfluidic system design and validation

Based on the validation results of membrane-based functional unit, the SEER microfluidic system was designed to conduct the proposed multi-step evolutionary assay utilizing the developed membrane-based selective cell trapping/release structures (**Fig. 2.4A**). As shown in Fig. 2.4B, the basic unit has a top-bottom culture chamber with a porous membrane in between. Chamber #1 has a 0.4 µm pore membrane, and was used to trap and co-incubate both microbes and host cells in the bottom chamber by infusing a vertical flow carrying both cell types into the bottom chamber. After trapping and co-incubation, host cells along with the internalized microbes were seeded on the glass substrate (**Fig. 2.4C**). A lateral flow with buffer solution then extensively rinsed the entire bottom chamber so that the excessive extracellular bacterial cells can be removed from the system. Following, culture media with antibiotic gentamicin will be replenished into the system for long term culture by applying vertical flow. Afterwards, a lateral rinsing step will be applied to clean out the antibiotic culture and dead extracellular microbes (**Fig 2.4D**). Then, lysis buffer was applied with vertical flow and host cells will be lysed to release intracellular bacterial population, and the released bacteria were retained inside bottom chamber (**Fig. 2.4E**). Next, rich culture media was vertically introduced into the system to facilitate bacterial amplification, and the total bacterial population was monitored until sufficient for next cycle of evolutionary assay. Finally, harvested culture, which contains host cell, debris and bacterial cells, will be laterally retrieved from this 0.4 µm unit, then immediately introduced into the second interconnected unit that with a 3.0 µm membrane. At the second unit, harvested culture vertically went through the 3.0 µm membrane where the host cells and debris will be blocked/retained at bottom, while bacterial population passed through to the top chamber (**Fig. 2.4F**). Finally, filtered bacterial population was introduced into the third

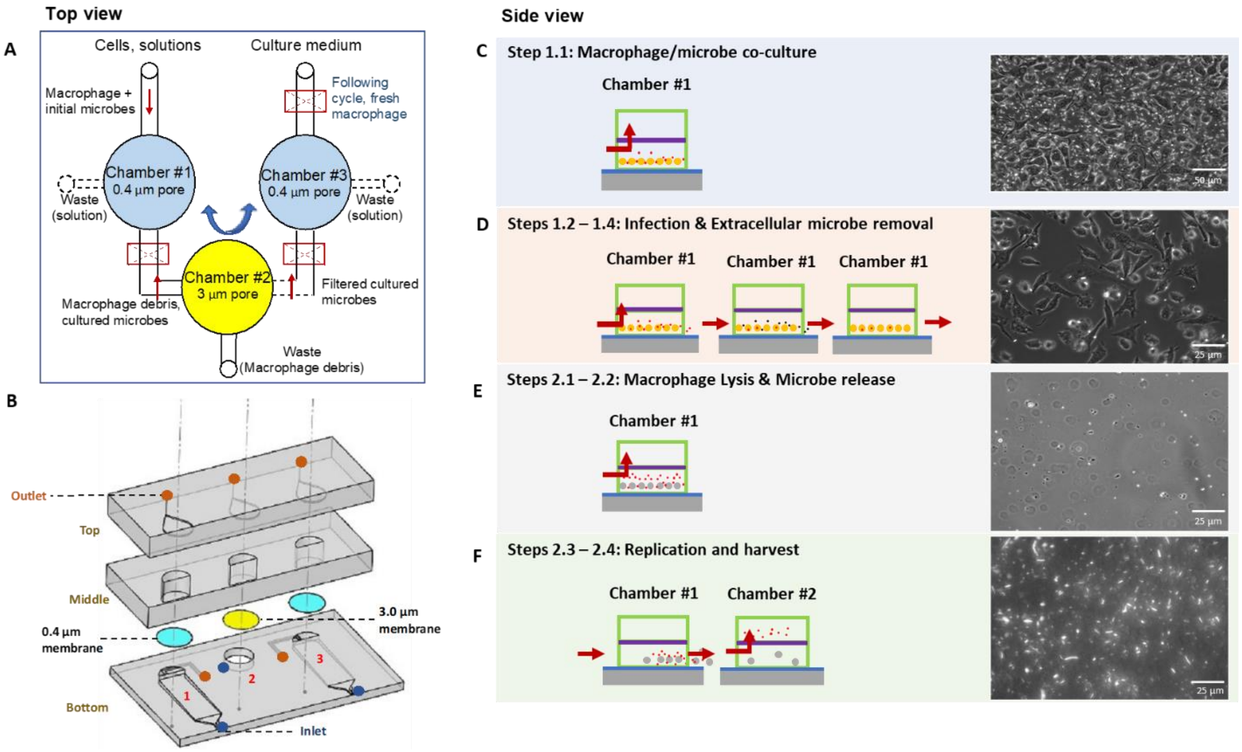

Fig 2.4. SEER platform configuration and validation. **A**. Interconnection of 3 porous membrane-based trapping unit. **B**. Explosion view of each chamber design. **C-F**. Step-by-step functions achieved by functional unit and validation results using GFP-*Salmonella* cells and macrophages.

interconnected unit that configured with 0.4 µm membrane. Bacterial cells, as the starting material of next repeated cycle, will mixed with fresh host cells and go through the evolutionary assay again. While the second cycle was being conducted and third unit was being utilized as incubation housing, the first and second unit can be fully rinsed with cleaning buffer so that they can be sterilized and ready for upcoming cycle. The detailed assay steps are further described in **Fig. 2.6**. Overall, this 3-unit system can handle the evolutionary assay to be conducted in a seamless manner with this back-and-forth fashion. Detailed design and dimensions are shown in **Fig 2.5**. To validate the functionality of proposed system, GFP-labeled *S. enterica* and RAW264.7 macrophages were again used here to visualize the dynamic of bacterial population during one evolutionary cycle. The functionality of each step as well as this entire system design was confirmed (**Fig. 2.4 C-F**).

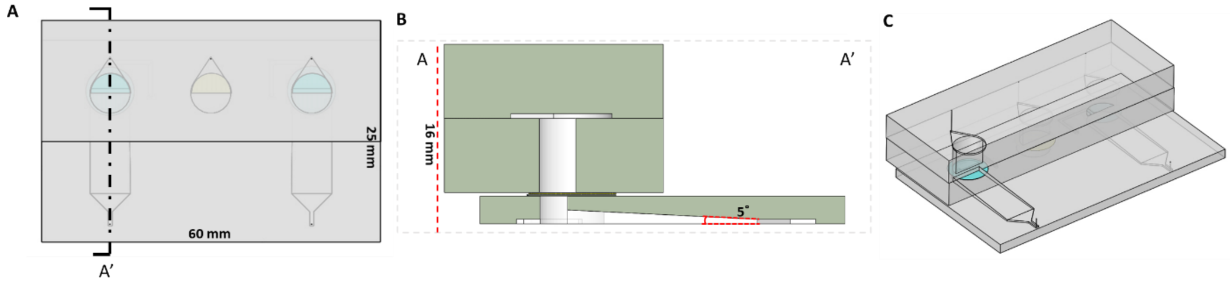

Fig 2.5 SEER platform design. **A**. Detailed dimension of SEER device. **B**. Assembled SEER platform and fabricated device.

2.4.3 Device design details and fabrication

The detailed dimensions of the entire microfluidics system are illustrated in **Fig. 2.5**. Here, chamber #1 and chamber #3, which were mainly used during the co-incubation steps, were designed to have around 800 µl to mimic volume of a single well from conventional well-plate-based handling. The surface area of bottom chamber was also intentionally designed to be as big as possible to enable more host cells to be seeded on glass substrate after cell loading step. Because of the relatively large chamber size, issues associated with air bubbles clogging inside these large chambers are highly likely. Therefore, the chamber is designed to have a sloped ceiling so that any air bubbles introduced into the chamber will be aggregated upwards towards the membrane due to its buoyancy and then be released through top outlet.[26] Chamber #2 was mainly served as a filtration and bacterial culture chamber, therefore was designed with smaller volume.

To fabricate the microfluidics device, 3D printer (Envision One) was first utilized to print out the master mold for polydimethyl siloxane (PDMS) soft lithography process. Printed 3D objects were baked and cured under UV light overnight to evaporate the resin residuals. Liquid-phase PDMS (Sylgard 184 Dow Corning, MI, USA) was acquired by mixing base and curing agent at a ratio of 10:1 and was poured onto the 3D printed master mold and cured for 4 h at 65°C, and then released from the master mold. Following, the PDMS layers were treated with O_2 plasma treatment and the bottom PDMS layer was bonded to the glass immediately afterwards. Next, the filter membranes (Isopore Membrane Filter, HTTP04700, MilliporeSigma, USA) with different porosities were trimmed and glued with liquid PDMS onto the top of the bottom PDMS layer, and sandwiched by the second PDMS stacking layer to create each functional unit. After final PDMS layer was bonded, entire device was baked at 85°C for 30 min. Before experiment, the entire device was rinsed with ethanol and then autoclaved to decontaminate.

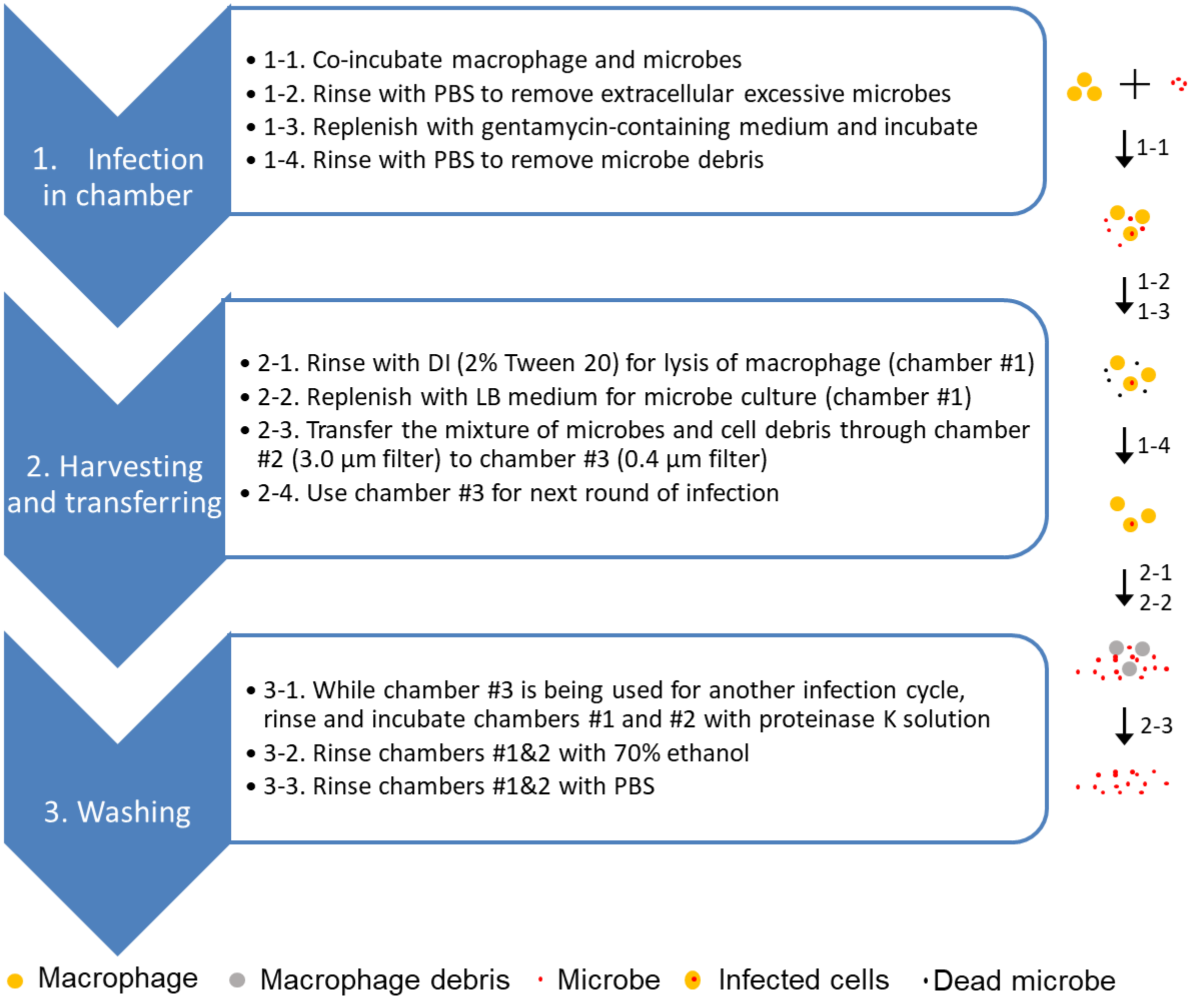

1. Infection in chamber

- 1-1. Co-incubate macrophage and microbes
- 1-2. Rinse with PBS to remove extracellular excessive microbes
- 1-3. Replenish with gentamycin-containing medium and incubate
- 1-4. Rinse with PBS to remove microbe debris

2. Harvesting and transferring

- 2-1. Rinse with DI (2% Tween 20) for lysis of macrophage (chamber #1)
- 2-2. Replenish with LB medium for microbe culture (chamber #1)
- 2-3. Transfer the mixture of microbes and cell debris through chamber #2 (3.0 µm filter) to chamber #3 (0.4 µm filter)
- 2-4. Use chamber #3 for next round of infection

3. Washing

- 3-1. While chamber #3 is being used for another infection cycle, rinse and incubate chambers #1 and #2 with proteinase K solution
- 3-2. Rinse chambers #1&2 with 70% ethanol
- 3-3. Rinse chambers #1&2 with PBS

Fig 2.6. Flow chart of SEER system operation.

2.4.4 Operations of on-chip evolutionary assay

Bacterial cells and host cells were initially mixed at an MOI of 10 and loaded into the chamber #1 with DMEM as carrier medium using syringe pump. The infusion rate was set as 1 ml/h for 1 h, and inlet at bottom chamber as well as outlet at top chamber were opened during the loading process. After cell loading, system was incubated at 37 °C for 1 h to allow host cell seeding and attaching on glass substrate. Next, PBS were introduced into system as a lateral flow at 1 ml/h for 30 min to rinse off the excessive extracellular microbes. Following, system was replenished with Gentamicin-containing DMEM (Lonza, 17-518L, USA, at 50 μg/ml) culture medium at 1 ml/h for 45 min with vertical flow setup and further incubated at 37 °C. The length of this incubation step was extended gradually as the evolutionary assay repeated, starting from 1 h to maximum 72 h. Afterwards, PBS flow at 3 ml/h were infused in lateral format to rinse off the gentamicin and dead microbe residuals. Following, lysis buffer (2% Tween 20 in DI water) was infused in vertical format at 1 ml/h for 30 min, and the system was incubated at 37 °C for 30 min. Next, PBS buffer was injected in vertical format at 1 ml/h for 30 min to rinse off the lysis buffer, and then LB broth medium were injected at 1 ml/h for 30 min as lateral flow to retrieve all released intracellular microbes and guide them into chamber #2. Within chamber #2, bacterial cells mixed with host cell debris were loaded in vertical setup and therefore all host debris were blocked and separated with target harvesting bacterial cells. Following, chamber #2 were incubated at 37 °C inside shaking incubator to amplify the population. Finally, harvested population were retrieved from chamber #2 with PBS, sampled for stocking purposes, and guided to chamber #3 to initiate the second round of evolutionary assay. In all the following cycles, the host cells were pre-seeded onto the glass substrate with a total population at $2x10^5$ before the introduction of bacterial population.

While the evolutionary assay is undergoing at one of the incubation chambers (chamber #1 or chamber #3), the other two chambers that potentially with some cell residuals from previous run, can be rinsed with Proteinase K (in 1 x PBS, pH = 7.4, at 1:200), incubated, and rinsed with 70% ethanol, then PBS all at 3 ml/h for 30 min to fully clean the existing residuals (**Fig. 2.7**).

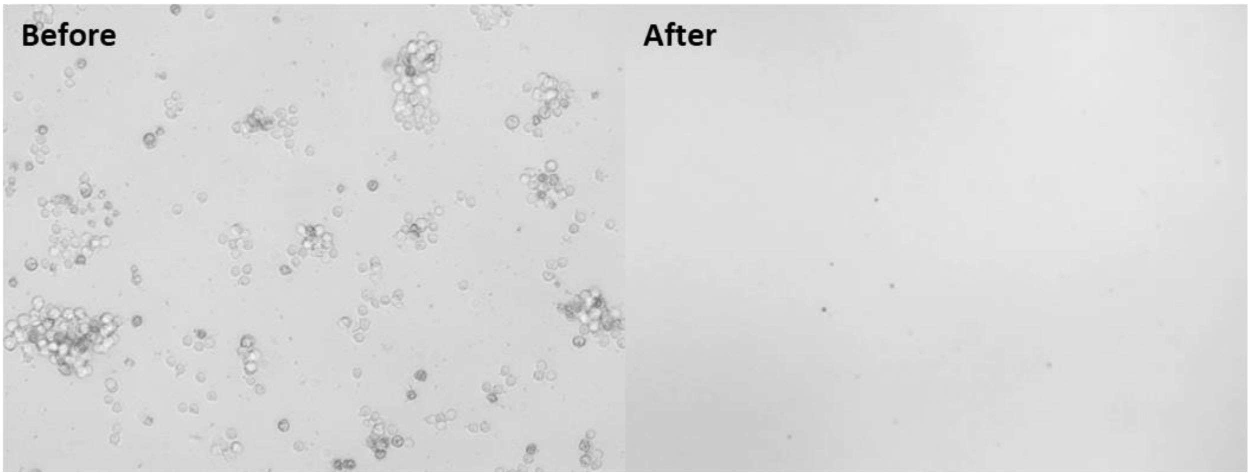

Fig 2.7. Cleaning of the standby chambers and comparison of remained residuals.

2.5 Biological material and methods

2.5.1 Cell preparation

J774A.1 (ATCC TIB67) or RAW 264.7 (ATCC SC6003) macrophages were thawed and grown on cell culture flask filled with DMEM containing 10% FBS and incubated at 37 °C in a 5% CO_2 atmosphere. Macrophages cells were detached by cell scraper prior to experiment and count the concentration by hemocytometer. Total number of injected macrophages were adjusted to $2x10^5$ cells to reach an estimate confluence of 70% after seeding. *Salmonella* typhimurium (strain ATCC 14028) cells that engineered with GFP plasmid (pCM18) were inoculated from a single colony and cultured in Lysogeny Broth (LB, GeneMate, USA) medium with 50 µg/ml erythromycin at 37 °C for 8 h. *E. coli* (DH5α, Thermo Fisher Scientific) strain was inoculated on LB agar plate, and single colony was picked and cultured in LB Broth for overnight. Right before experiment, the bacteria culture was centrifuged and washed with 1 x PBS (pH 7.4, unless otherwise indicated). Cell suspension medium was adjusted to OD of 1.0 and the total number of bacterial cells were adjusted to 2 x 10^6 to achieve multiplicity of infection (MOI) of 10.

2.5.2 Characterization of endosymbiosis phenotype

To validate the phenotypic alternations happens along with the evolutionary selection, 6 single colonies each that were picked at EcG0, EcG10, EcG20, EcG25 were characterized with plate assay and cross comparison. First, host cells (J774A.1) with total number of 2x10^5/well were loaded into 24-well plate and seeded overnight. For each picked bacterial colony, bacterial cells were inoculated and cultured in LB broth overnight and adjusted to OD 1.0 in the following day. Bacterial cells were added into the well at 2x10^6/well to keep MOI at 10. After bacterial cell loading, the mixture was incubated with antibiotic-free DMEM at 37 °C for 1 h to allow internalization. Following, host cells were rinsed with PBS thoroughly and culture medium was replaced to gentamicin containing DMEM (50 μg/ml). At 0, 24, 48, 72 and 96 h.p.i., host cells were rinsed with PBS, then lysed with 2% Tween 20 lysis buffer. Released bacterial cells were plated on agar plates for CFU analysis to figure out total survival of such strain at different time points and its relative survival phenotype when compared with naïve strain. To visualize such difference, colonies harvested at EcG25 were also engineered to have fluorescent tag and compared with EcG0. Microscopic images taken at different h.p.i. were also compared (**Fig. 2.8 C-D**). The isolates from each generation and original strain were further sequenced and analyzed to identify the mutation gene. After identification of mutant gene, a target gene, cpxR, were further evaluated using the complementary bacterial strains.

2.5.3 Stress response assay

Bacteria were grown in LB broth at 37 ℃ overnight, and 30 μg/ml of chloramphenicol was added in the LB medium for the bacteria carrying engineered plasmids. The overnight cultured cells were inoculated in fresh LB medium with 1:500 dilution, and let the bacteria grown until the early or mid-log phase (optical density at 600 nm [OD_{600}] ≤ 0.6). Adjust the concentration of the freshly cultured bacteria to $OD_{600} = 0.1$, and then 1:100 diluted and inoculated the bacteria in LB medium with different stress condition in a 96-well plate. Bacteria growth was monitored by recording OD_{600} every 30 minutes for 16 hours in a Cytation5 (BioTek) plate reader and incubator. The bacterial response to several stress conditions, including H_2O_2 (0.25, 0.5, 1.0 μM), sodium dodecyl sulfate (2.5, 5.0, 10.0%), gentamycin (1.25, 2.5, 5.0 μg/ml), and ampicillin (1.25, 2.5, 5.0 μg/ml) was tested. A same set of stress response was also tested in a M9 medium[27] with 0.2% glucose, which followed the same procedure as in the LB medium except of using M9 medium.

2.6 Results

2.6.1 Evolved strain characterization

To investigate the dynamic of genomic alternations and to find out their underlying correlation with the phenotypic changes during evolutionary endosymbiosis process, a naïve *E.*

coli strain (DH5α) which was previously confirmed to have limited intracellular capability was chosen to be the starting population. By utilizing proposed evolutionary assay and validated system, 25 rounds of infection and harvesting cycles were conducted in a serial manner. To minimize the random noises that happened during the selection process, therefore increase the possibility of discovering the gene alternations that are more critical and profound for endosymbiosis properties, this 25-round selection process was conducted twice separately for cross comparison. Two series of bacterial population were harvested throughout the process (henceforth denoted as EcG0-1 to EcG25-1, and EcG0-2 to EcG25-2, respectively, here "Gxx" stands for the corresponding cycles that has been completed when such sample was harvested from evolutionary assay).

This harvested two evolved stains were further examined with various biological assays to determine their phenotypic alternation compared to original strain. First, the relative intracellular survival capability was tested from 1 hour post-infection (h.p.i) to 96 h.p.i. to compare with the original strain, and significant enhancement of survival can be observed after 72 h.p.i, with both evolved strains (**Fig. 2.8A, 2.8B**). Notably, when comparing EcG25-1 against EcG0-1, a 55-fold increase of intracellular survival can be observed at 96 h.p.i. Additionally, a direct comparison of intracellular survival between naïve/evolved strains (EcG25-1 against EcG0-1) were conducted after GFP plasmid (pCM18) transfection, and significant increase of viable bacterial cells were found at EcG25-1 group at 96 h.p.i (**Fig. 2.8C, 2.8D**).

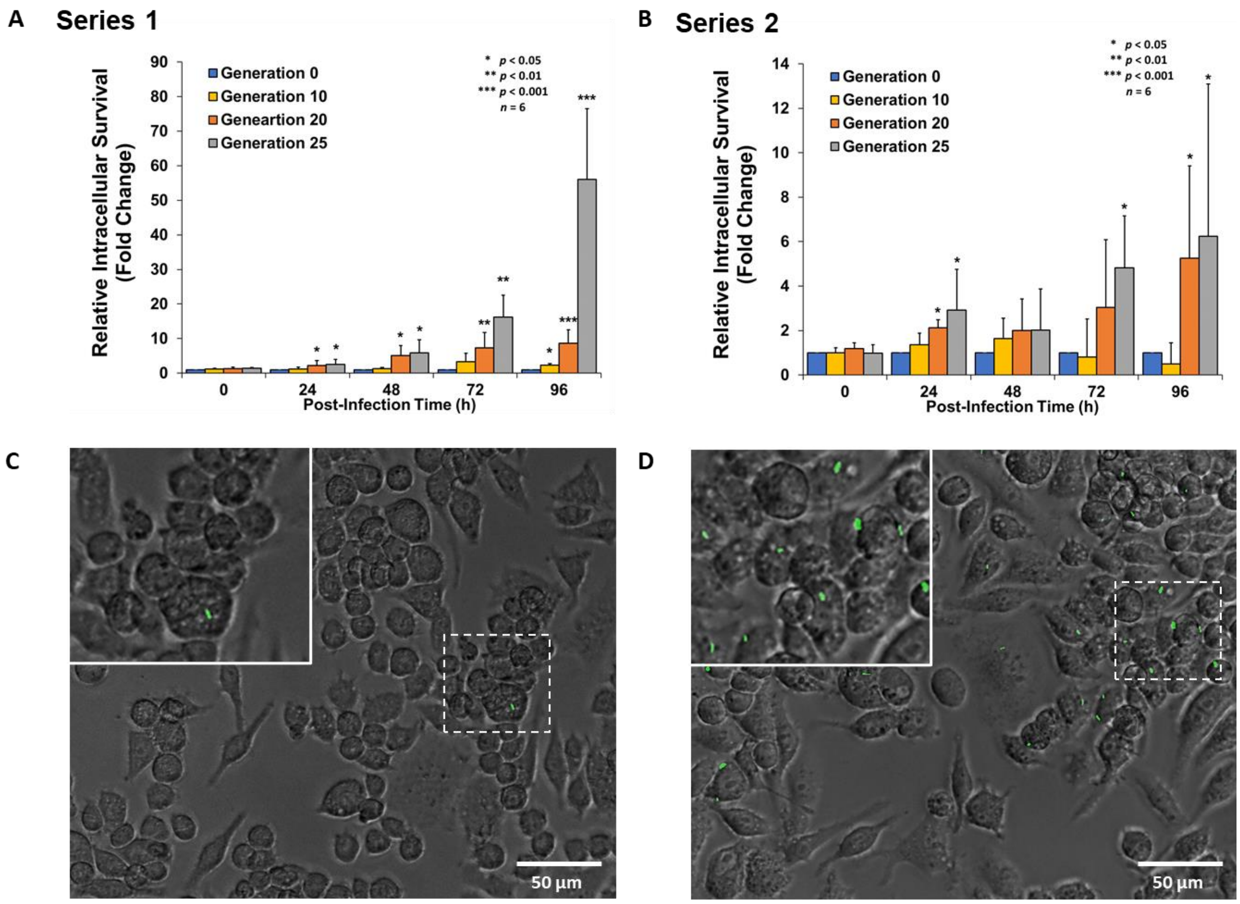

Fig 2.8. Validating survival capability of evolved strains. **A-B**. Relative intracellular survival of harvested strain from 2 independent series of evolution. Both evolved G25 strains demonstrated increased survival capability when compared with naïve strain. **C**. Survived GFP-transfected naïve *E. coli* at 96 h.p.i. **D**. Survived GFP-transfected evolved G25 *E. coli* at 96 h.p.i.

2.6.2 Gene mutation identification

To determine the specific mutations that conferred intracellular survival to EcG25, previous 2 independently evolved lineages were sequenced with Whole Genome Sequencing (WGS) technology, and then aligned with the sequence of EcG0 as control. A total of 203 variants were identified (**Table 2.1**). Of these, most were discounted for the following reasons: 100 mutations were found only in a single read, 48 were synonymous SNPs that had no impact on the protein sequence, 79 were in intergenic regions, 6 were in RNA genes, 11 occurred in genes associated with bacteriophages, 3 mutations occurred in transposase or mobile element proteins. A total of 20 nonsynonymous SNPs or indels were seen in functional genes which were considered candidates for mediating phenotypic changes (**Table 2.2**).

Table 2.1 Identified variant summary (result obtained by Dr. Fengguang Guo).

	Gen 10										Gen 20										Gen 25									
Samples	PE1	PE2	PE3	PE4	PE5	PE6	PE7	PE8	Sum	% mutation	PE9	PE10	PE11	PE12	PE13	PE14	PE15	PE16	Sum	% mutation	PE17	PE18	PE19	PE20	PE21	PE22	PE23	PE24	Sum	% mutation
1									0	0			PE11						1	12.5									0	0
1									0	0	PE9								1	12.5									0	0
3		PE2		PE4	PE5				3	37.5									0	0									0	0
4	PE1		PE3			PE6		PE8	4	50									0	0									0	0
1							PE7		1	12.5									0	0									0	0
1							PE7		1	12.5									0	0									0	0
1									0	0									0	0				PE20					1	12.5
1									0	0									0	0				PE20					1	12.5
1									0	0									0	0				PE20					1	12.5
18	PE1		PE3	PE4	PE5		PE7	PE8	6	75	PE9		PE11	PE12	PE13	PE14	PE15	PE16	7	87.5		PE18		PE20	PE21	PE23		PE24	5	62.5
2					PE5				1	12.5									0	0								PE24	1	12.5
4	PE1								1	12.5		PE10							1	12.5	PE17	PE18							2	25
1									0	0									0	0				PE20					1	12.5
1									0	0		PE10							1	12.5									0	0
21	PE1	PE2	PE3	PE4	PE5	PE6	PE7	PE8	8	100				PE12	PE13	PE14	PE15	PE16	5	62.5	PE17	PE18	PE19	PE20	PE21	PE22	PE23	PE24	8	100
1				PE4					1	12.5									0	0									0	0
1		PE2							1	12.5									0	0									0	0
1									0	0									0	0				PE20					1	12.5
1									0	0						PE14			1	12.5									0	0
7									0	0									0	0	PE17	PE18	PE19		PE21	PE22	PE23	PE24	7	87.5
1									0	0									0	0				PE20					1	12.5
1		PE2							1	12.5									0	0									0	0
6			PE3						1	12.5		PE10			PE13				2	25			PE19			PE22		PE24	3	37.5
6			PE3						1	12.5		PE10		PE12	PE13				3	37.5						PE22		PE24	2	25
1									0	0	PE9								1	12.5									0	0
2					PE5				1	12.5									0	0					PE21				1	12.5
1									0	0						PE14			1	12.5									0	0
19	PE1	PE2	PE3	PE4		PE6	PE7	PE8	7	87.5		PE10	PE11	PE12	PE13		PE15	PE16	6	75	PE17		PE18	PE19		PE22	PE23	PE24	6	75
3		PE2							1	12.5			PE11						1	12.5							PE23		1	12.5
13				PE4		PE6	PE7	PE8	4	50		PE10		PE12	PE13		PE15	PE16	5	62.5	PE17	PE18	PE19					PE24	4	50
1			PE3						1	12.5									0	0									0	0
3									0	0	PE9								1	12.5				PE20			PE23		2	25
1									0	0	PE9								1	12.5									0	0
2									0	0	PE9								1	12.5				PE20					1	12.5
1									0	0									0	0				PE20					1	12.5
1									0	0						PE14			1	12.5									0	0
1									0	0					PE13				1	12.5									0	0
1									0	0	PE9								1	12.5									0	0
1									0	0			PE11						1	12.5									0	0
1								PE8	1	12.5									0	0									0	0
1									0	0						PE14			1	12.5									0	0
10		PE2		PE3		PE5		PE8	4	50		PE10		PE12	PE13			PE16	4	50			PE19					PE24	2	25
1				PE4					1	12.5									0	0									0	0
1									0	0									0	0				PE20					1	12.5
10		PE2		PE4	PE5	PE6	PE7		5	62.5								PE16	1	12.5			PE19		PE21		PE23	PE24	4	50
3			PE13						1	12.5								PE16	1	12.5			PE19						1	12.5
6		PE2				PE6			2	25		PE10					PE15		2	25	PE17	PE18							2	25
9									0	0						PE14	PE15		2	25	PE17	PE18	PE19		PE21	PE22	PE23	PE24	7	87.5
4									0	0		PE10	PE12	PE13				PE16	4	50									0	0
1									0	0							PE15		1	12.5									0	0
1									0	0									0	0							PE23		1	12.5
13									0	0	PE9	PE10		PE12	PE13	PE14		PE16	6	75	PE17	PE18	PE19	PE20	PE21	PE22		PE24	7	87.5
3		PE2		PE4	PE5				3	37.5									0	0									0	0
1									0	0								PE16	1	12.5									0	0
1									0	0									0	0		PE18							1	12.5
1									0	0	PE9								1	12.5									0	0
1									0	0									0	0				PE20					1	12.5
1					PE5				1	12.5									0	0									0	0
1									0	0									0	0	PE17								1	12.5
19	PE1	PE2	PE3	PE4		PE6	PE7	PE8	7	87.5		PE10		PE12	PE13	PE14	PE15	PE16	6	75		PE18	PE19		PE21	PE22	PE23	PE24	6	75
1			PE3						1	12.5									0	0									0	0
1									0	0	PE9								1	12.5									0	0
1									0	0				PE12					1	12.5									0	0
21	PE1	PE2	PE3	PE4	PE5	PE6	PE7	PE8	8	100		PE10			PE13	PE14	PE15	PE16	5	62.5	PE17	PE18	PE19	PE20	PE21	PE22	PE23	PE24	8	100
22	PE1	PE2	PE3	PE4	PE5	PE6		PE8	7	87.5	PE9	PE10		PE12	PE13	PE14	PE15	PE16	7	87.5	PE17	PE18	PE19	PE20	PE21	PE22	PE23	PE24	8	100
1									0	0									0	0		PE18							1	12.5
1						PE6			1	12.5									0	0									0	0
1									0	0			PE11						1	12.5									0	0
1									0	0						PE14			1	12.5									0	0
1									0	0									0	0		PE18							1	12.5
22	PE1	PE2	PE3	PE4	PE5	PE6	PE7	PE8	8	100	PE9	PE10	PE11	PE12	PE13		PE15	PE16	7	87.5	PE17		PE19	PE20	PE21	PE22	PE23	PE24	7	87.5
22	PE1	PE2	PE3	PE4	PE5	PE6	PE7	PE8	8	100		PE10	PE11	PE12	PE13	PE14	PE15	PE16	7	87.5	PE17	PE18	PE19		PE21	PE22	PE23	PE24	7	87.5
2				PE4	PE5				2	25									0	0									0	0
1									0	0				PE12					1	12.5									0	0
1									0	0									0	0				PE20					1	12.5
1									0	0	PE9								1	12.5									0	0
1									0	0	PE9								1	12.5									0	0
1									0	0									0	0					PE21				1	12.5
4	PE1		PE3			PE6		PE8	4	50									0	0									0	0
6	PE1		PE3			PE6			3	37.5		PE10			PE13				2	25		PE18							1	12.5
1									0	0					PE13				1	12.5									0	0
4	PE1					PE6			2	25		PE10							1	12.5			PE19						1	12.5
1									0	0		PE10							1	12.5									0	0
1									0	0								PE16	1	12.5									0	0
1									0	0		PE10							1	12.5									0	0
22	PE1	PE2	PE3	PE4	PE5	PE6	PE7	PE8	8	100	PE9			PE12	PE13	PE14	PE15	PE16	6	75	PE17	PE18	PE19	PE20	PE21	PE22	PE23	PE24	8	100
1									0	0	PE9								1	12.5									0	0
1									0	0									0	0								PE24	1	12.5
1									0	0				PE12					1	12.5									0	0
1									0	0		PE10							1	12.5									0	0
3									0	0							PE15		1	12.5						PE22	PE23		2	25
1									0	0									0	0					PE21				1	12.5
22	PE1	PE2	PE3	PE4	PE5	PE6	PE7	PE8	8	100	PE9	PE10	PE11	PE12	PE13	PE14	PE15	PE16	7	87.5	PE17		PE19		PE21	PE22	PE23	PE24	6	75
4									0	0									0	0		PE18	PE19	PE20			PE23		4	50
6	PE1				PE5				2	25					PE13			PE16	2	25					PE21		PE23		2	25
2									0	0						PE14			1	12.5		PE18							1	12.5
1									0	0				PE12					1	12.5									0	0
14	PE1		PE3			PE6			3	37.5		PE10		PE12	PE13	PE14		PE16	5	62.5		PE18	PE19		PE21	PE22	PE23	PE24	6	75

13			PE3	PE4	PE5		PE7	PE8	5	62.5		PE10	PE11		PE13			PE16	3	37.5			PE19		PE21	PE22	PE23		4	50
1									0	0							PE15		1	12.5									0	0
11			PE3	PE4			PE7	PE8	4	50		PE10	PE11		PE13			PE16	4	50	PE17		PE19		PE21				3	37.5
6		PE2		PE4				PE8	3	37.5				PE12					1	12.5							PE23	PE24	2	25
1									0	0									0	0		PE18							1	12.5
13		PE2	PE3	PE4			PE7	PE8	5	62.5				PE12	PE13	PE14	PE15		4	50	PE17				PE21		PE23	PE24	4	50
9		PE2		PE4			PE7	PE8	4	50				PE12	PE13	PE14			3	37.5		PE18	PE19						2	25
10		PE2	PE3		PE5			PE8	4	50	PE9				PE13				2	25	PE17			PE20	PE21		PE23		4	50
4									0	0			PE11		PE13		PE15		3	37.5								PE24	1	12.5
2							PE7		1	12.5						PE14			1	12.5									0	0
2							PE7		1	12.5						PE14			1	12.5									0	0
1									0	0						PE14			1	12.5									0	0
1									0	0									0	0		PE18							1	12.5
1									0	0									0	0		PE18							1	12.5
1									0	0									0	0		PE18							1	12.5
5	PE1			PE4		PE6			3	37.5									0	0		PE18	PE19						2	25
2									0	0							PE15		1	12.5			PE19						1	12.5
3	PE1	PE2							2	25				PE12					1	12.5									0	0
5						PE6		PE8	2	25					PE13			PE16	2	25							PE23		1	12.5
2									0	0		PE10		PE12					2	25									0	0
3			PE3			PE6		PE8	3	37.5									0	0									0	0
1						PE6			1	12.5									0	0									0	0
3	PE1							PE8	2	25									0	0			PE19						1	12.5
3		PE2	PE3						2	25								PE16	1	12.5									0	0
1									0	0		PE10							1	12.5									0	0
1									0	0								PE16	1	12.5									0	0
1									0	0		PE10							1	12.5									0	0
1									0	0					PE13				1	12.5									0	0
1									0	0									0	0		PE18							1	12.5
3							PE7		1	12.5									0	0				PE20				PE24	2	25
1									0	0									0	0							PE23		1	12.5
2									0	0	PE9		PE11						2	25									0	0
3						PE6			1	12.5									0	0			PE19			PE22			2	25
1						PE6			1	12.5									0	0									0	0
3				PE4					1	12.5							PE15		1	12.5					PE21				1	12.5
12	PE1	PE2	PE3			PE6		PE8	5	62.5				PE12	PE13				2	25		PE18		PE20		PE22	PE23	PE24	5	62.5
16	PE1	PE2	PE3	PE4		PE6	PE7		6	75	PE9			PE12	PE13		PE15		4	50		PE18		PE20	PE21	PE22	PE23	PE24	6	75
5	PE1	PE2						PE8	3	37.5		PE10							1	12.5				PE20					1	12.5
3	PE1								1	12.5					PE13				1	12.5	PE17								1	12.5
1									0	0									0	0		PE18							1	12.5
1									0	0									0	0						PE22			1	12.5
13		PE2		PE4	PE5	PE6		PE8	5	62.5		PE10		PE12	PE13		PE15	PE16	5	62.5	PE17						PE23	PE24	3	37.5
1									0	0									0	0		PE18							1	12.5
2					PE5				1	12.5									0	0						PE22			1	12.5
1								PE8	1	12.5									0	0									0	0
1							PE7		1	12.5									0	0									0	0
2									0	0					PE13				1	12.5			PE19						1	12.5
1				PE4					1	12.5									0	0									0	0
17	PE1	PE2	PE3	PE4	PE5	PE6		PE8	7	87.5	PE9		PE11		PE13		PE15	PE16	5	62.5	PE17	PE18		PE20	PE21			PE24	5	62.5
17	PE1	PE2	PE3	PE4	PE5	PE6	PE7	PE8	8	100	PE9		PE11		PE13	PE14	PE15	PE16	6	75	PE17			PE20	PE21				3	37.5
10	PE1	PE2	PE3	PE4	PE5	PE6		PE8	7	87.5				PE12		PE14			2	25	PE17								1	12.5
13	PE1	PE2	PE3	PE4	PE5	PE6		PE8	7	87.5			PE11	PE12	PE13	PE14			4	50	PE17					PE23			2	25
1									0	0					PE13				1	12.5									0	0
1				PE4					1	12.5									0	0									0	0
9			PE3				PE7	PE8	3	37.5	PE9	PE10	PE11			PE14	PE15		5	62.5		PE18							1	12.5
10	PE1		PE3			PE6	PE7		4	50	PE9		PE11				PE15	PE16	4	50				PE20	PE21				2	25
1				PE4					1	12.5									0	0									0	0
1				PE4					1	12.5									0	0									0	0
3				PE4					1	12.5									0	0			PE19		PE21				2	25
16		PE2	PE3		PE5	PE6	PE7		5	62.5			PE11		PE13	PE14	PE15	PE16	5	62.5	PE17	PE18		PE20		PE22	PE23	PE24	6	75
3				PE4					1	12.5									0	0	PE17						PE23		2	25
3				PE4					1	12.5									0	0	PE17						PE23		2	25
1									0	0									0	0			PE19						1	12.5
1									0	0									0	0							PE23		1	12.5
1	PE1								1	12.5									0	0									0	0
1									0	0								PE16	1	12.5									0	0
1							PE7		1	12.5									0	0									0	0
4									0	0					PE13				1	12.5	PE17					PE22	PE23		3	37.5
1	PE1								1	12.5									0	0									0	0
2									0	0					PE13				1	12.5			PE19						1	12.5
1									0	0								PE16	1	12.5									0	0
1								PE8	1	12.5									0	0									0	0
2	PE1								1	12.5				PE12					1	12.5									0	0
7			PE3						1	12.5							PE15	PE16	2	25					PE21	PE22	PE23	PE24	4	50
3					PE5				1	12.5									0	0	PE17			PE20					2	25
5	PE1	PE2			PE5				3	37.5									0	0	PE17			PE20					2	25
6	PE1	PE2			PE5				3	37.5			PE11						1	12.5	PE17			PE20					2	25
23	PE1	PE2	PE3	PE4	PE5	PE6	PE7	PE8	8	100		PE10	PE11	PE12	PE13	PE14	PE15	PE16	7	87.5	PE17	PE18	PE19	PE20	PE21	PE22	PE23	PE24	8	100
1									0	0									0	0				PE20					1	12.5
2						PE6			1	12.5		PE10							1	12.5									0	0
2	PE1								1	12.5					PE13				1	12.5									0	0
1									0	0									0	0							PE23		1	12.5
21	PE1	PE2	PE3	PE4	PE5	PE6	PE7	PE8	8	100	PE9	PE10	PE11	PE12	PE13		PE15	PE16	7	87.5	PE17	PE18	PE19		PE21	PE22	PE24		6	75
1			PE3						1	12.5									0	0									0	0
14				PE4	PE5		PE7	PE8	4	50		PE10				PE14		PE16	3	37.5	PE17	PE18	PE19		PE21	PE22	PE23	PE24	7	87.5
5						PE6		PE8	2	25	PE9						PE15		2	25				PE20					1	12.5
5						PE6		PE8	2	25	PE9						PE15		2	25				PE20					1	12.5
7						PE6		PE8	2	25						PE14	PE15	PE16	3	37.5			PE19	PE20					2	25
8						PE6		PE8	2	25	PE9					PE14	PE15	PE16	4	50			PE19	PE20					2	25
1									0	0									0	0						PE22			1	12.5
1									0	0									0	0						PE22			1	12.5
5			PE3	PE4					2	25									0	0	PE17		PE19					PE24	3	37.5
2									0	0	PE9								1	12.5								PE24	1	12.5
1									0	0									0	0							PE23		1	12.5
1									0	0		PE10							1	12.5									0	0
4	PE1	PE2							2	25				PE12					1	12.5								PE24	1	12.5
1								PE8	1	12.5									0	0									0	0
1									0	0					PE13				1	12.5									0	0
3	PE1								1	12.5		PE10							1	12.5			PE19						1	12.5
3									0	0							PE15		1	12.5					PE21			PE24	2	25
15	PE1	PE2				PE6		PE8	4	50	PE9	PE10		PE12	PE13		PE15		5	62.5		PE18	PE19		PE21	PE22	PE23	PE24	6	75
2				PE4					1	12.5						PE14			1	12.5									0	0
2				PE4					1	12.5						PE14			1	12.5									0	0
2									0	0		PE10			PE13				2	25									0	0

Table 2.2 Summary of 20 nonsynonymous SNPs or indels that seen in functional genes which were considered candidates for mediating phenotypic changes (result obtained by Dr. Fengguang Guo).

Gene_ID	**Correspond DH5alpha GenBank ref**	**Gene Name**	**Protein change**	**Mutation type**	**G10 (%)**	**G20 (%)**	**G25 (%)**
fig|562.43589.peg.289	C1467_01695	Uncharacterized protein YbfC	Lys189fs	Deletion	37.5	0	0
fig|562.43589.peg.383	C1467_05430	Electron transfer flavoprotein, alpha subunit YgcQ	Leu220Arg	Nonsyn	50	0	0
fig|562.43589.peg.790	C1467_11775	DNA replication terminus site-binding protein	Pro160Thr	Nonsyn	100	62.5	100
fig|562.43589.peg.1604	None	core protein	Gln33Lys	Nonsyn	12.5	0	12.5
fig|562.43589.peg.1604	None	core protein	Gln33Lys	Nonsyn	87.5	75	75
fig|562.43589.peg.1602	None	Protein RhsA	Ala179Thr	Nonsyn	0	12.5	25
fig|562.43589.peg.1602	None	Protein RhsA	Lys262Thr	Nonsyn	0	12.5	12.5
fig|562.43589.peg.2517	C1467_23775	Copper-sensing two-component system response regulator CpxR	Gly89Ala	Nonsyn	0	25	87.5
fig|562.43589.peg.2518	C1467_23780	Copper sensory histidine kinase CpxA	Val174Ala	Nonsyn	0	50	0
fig|562.43589.peg.2518	C1467_23780	Copper sensory histidine kinase CpxA	Arg191His	Nonsyn	0	62.5	87.5
fig|562.43589.peg.2966	C1467_14890	FIG01269488: protein, clustered with ribosomal protein L32p	Gln154Leu	Nonsyn	100	87.5	87.5
fig|562.43589.peg.3014	C1467_15140	Major curlin subunit precursor CsgA	Val118Phe	Nonsyn	100	87.5	87.5

fig|562.43589.peg.3062	C1467_00900	Inner membrane protein YiaA	Ala88Thr	Nonsyn	25	0	0
fig|562.43589.peg.3586	None	PTS system, mannitol-specific IIABC component (EC 2.7.1.69)	Ser26Phe	Nonsyn	50	0	0
fig|562.43589.peg.3693	C1467_20280	Ferric hydroxamate outer membrane receptor FhuA	Val1_Leu2insValProLeu	Insertion	25	12.5	12.5
fig|562.43589.peg.4452	C1467_12280	Serine recombinase, PinQ/PinR-type	Ala159Val	Nonsyn	50	50	37.5
fig|562.43589.peg.4452	C1467_12280	Serine recombinase, PinQ/PinR-type	Arg3Gln	Nonsyn	50	37.5	25
fig|562.43589.peg.4451	C1467_12285	Uncharacterized protein, YnaE family	Thr51Lys	Nonsyn	62.5	50	50
fig|562.43589.peg.4469	C1467_01220	Glutamate decarboxylase (EC 4.1.1.15)	Lys1_Asn2insAspLeuSerIleAsnLys	Insertion	12.5	0	25
fig|562.43589.peg.4478	None	core protein	Lys189fs	Insertion	0	12.5	12.5

2.6.3 cpxR mutation promotes *E. coli* survival in J774A.1 macrophage

We predicted if a mutation benefits the bacterial intracellular survival, the bacteria with this mutation will be increased in the evolved population. To test this possibility, we examined generations 10, 20 and 25 and found a SNP in cpxR gene, resulting in a single amino acid change at position 89 from a Glycine to an Alanine, was accumulated in Generation 20 (12.5% of all reads) and 25 (87.5% of all reads) (**Fig. 2.9A and B, Table 2.2**). The cpxR is a member of the two-component regulatory system cpxA/cpxR which responds to envelope stress responses, such as heat shock, high pH, oxidative stress, and nutritional deprivation, by activating expression of downstream genes. To test if the cpxR mutant is involved in the bacterial intracellular survival, we constructed a bacterial expression plasmid to express either wild type cpxR or cpxR mutant (G89A) under original cpxR promoter separately (**Fig. 2.9C**). We found that cpxR knockout (ΔcpxR) *E. coli* showed significantly decrease in survival in J774A.1 at 24, 48, and 72 h.p.i. comparing to parent strain (**Fig. 2.9D**), indicating that cpxR is critical to the survive of *E. coli* in J774A.1 macrophage. In a complementary assay, we transformed blank, cpxR, or cpxR(G89A) plasmid into cpxR KO *E. coli* separately to generate three bacterial strains (P_{Blank}, P_{cpxR}, and P_{G89A}). The successfully transformation and cpxR expression was validated by western blot, and both P_{WT} and P_{G89A} strains showed equal growth rate in LB medium (**Fig. 2.10**). The intracellular survival phenotypes of the resultant strains were measured to compare with the KO strain that inserted with blank plasmid. The P_{G89A} showed enhanced survival in host cells at 1, 24, 48, and 72 h.p.i., thereby demonstrating the G89A in cpxR was necessary and sufficient to improve the intracellular survival of the bacterium (**Fig. 2.9E**).

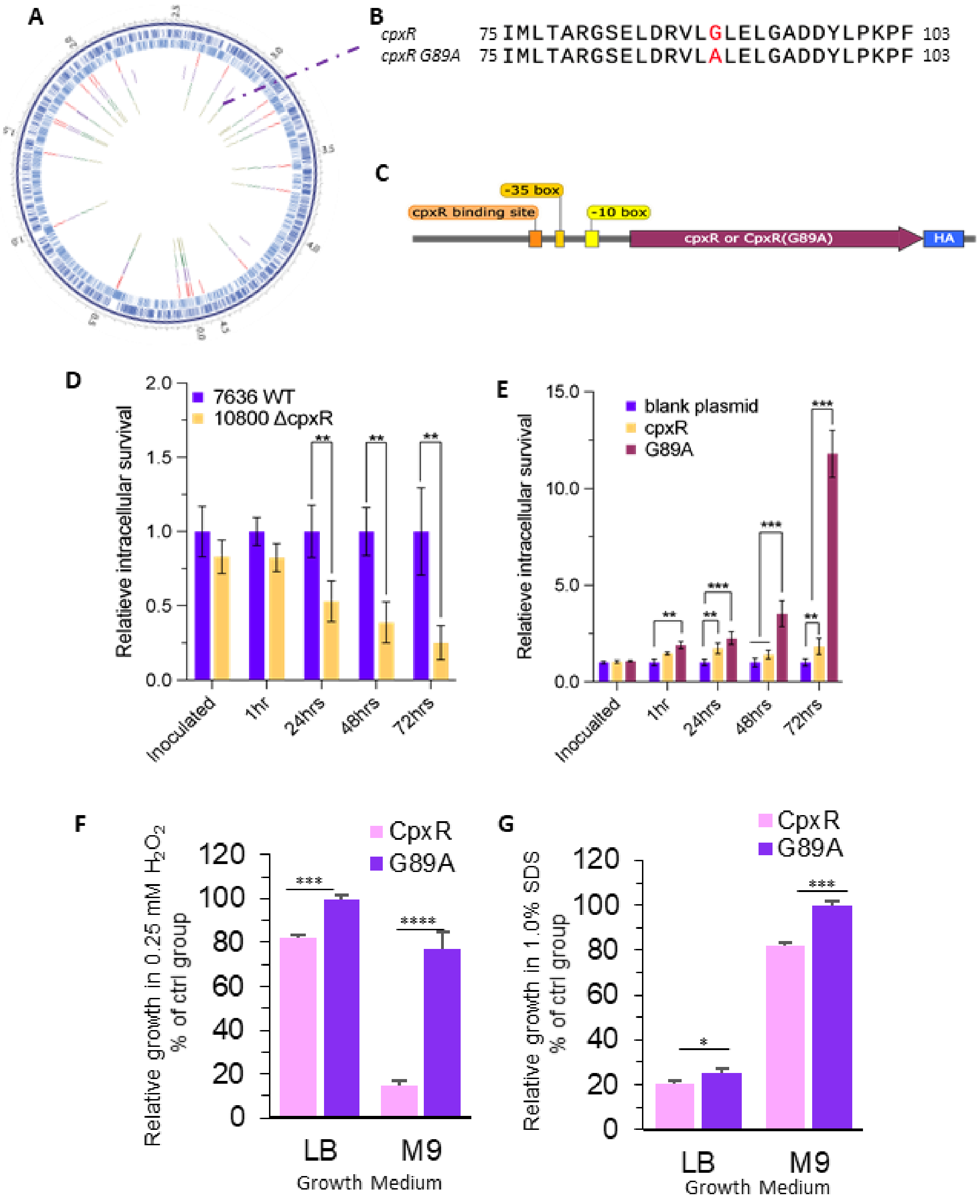

Fig 2.9. cpxR is critical for *E. coli* survival in J774A.1 macrophage. **A**. A circular diagram shows important SNPs in G10, 20, or 25 comparing to G0. **B**. A SNP causes the change of amino acid from glycine to alanine at position 89 of cpxR protein. **C**. Schematic of cpxR (WT) or G89A (cpxR mutant) expression cassette containing all engineering components. **D**. cpxR knock-out strain (10800) had low survival rate in J774A.1 macrophage comparing to wild type (7636) at 24, 48, and 72 hours of post inoculation time; **E-G**. Bacteria carrying cpxR mutant plasmid (G89A) had higher survival rate in J774A.1 macrophage than the one with wild type cpxR plasmid in J774A.1 cell, also exhibited an increased survival under high pressure culture condition, such as H_2O_2 and SDS exposure. (Result obtained by Dr. Fengguang Guo).

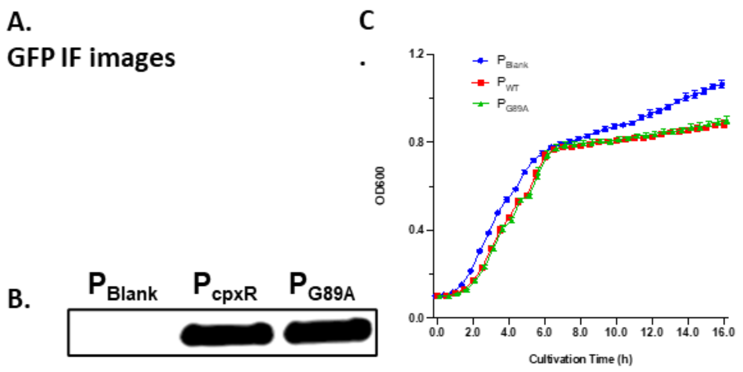

Fig. 2.10. A. GFP expressed in constructed *E. coli* strains, B. Western blot showed cxpR and cpxR (G89A) expressed in engineered *E. coli* strains P_{WT} and P_{G89A} separately introduced with plasmids, C. Bacteria expressed cpxR or cpxR (G89A) displayed same growth rate in LB broth medium, but they grow slower than the bacteria carrying a blank plasmid. (Result obtained by Dr. Fengguang Guo).

2.6.4 cpxR mutant resists to other stresses

cpxR function is related to different stress responses besides of bacterial intracellular survival. To investigate if the cpxR mutation (G89A) also affects the bacteria responding to other stresses, we tested the growth of P_{cpxR} and P_{G89A} at different stress conditions in both rich (LB) and minimal (M9 with 0.2% glucose) media. P_{G89A} showed better growth than P_{cpxR} under both H_2O_2 and SDS stress condition. LB or M9 medium containing 0.25 mM H_2O_2 separately had no or some effect on P_{G89A} growth, but significantly inhibited P_{cpxR} grow in both media (**Fig. 2.9F**). Similar result was observed in LB or M9 medium containing 1.0% SDS, in which P_{WT} growth was inhibited in both media and P_{G89A} growth was only suppressed in LB medium (**Fig. 2.9G**). Additionally, Table 2.3 summaries the comparison of sensitivity test results between Naïve *E. coli* strain and evolved strain under several treatment, including exposure of ampicillin, kanamycin, gentamycin, streptomycin, rifampin, SDS and hydrogen peroxide. The maximum resistant dosages of both strain against each treatment were determined, and significant increase of resistance over ampicillin, kanamycin, gentamycin and streptomycin can be observed.

Table 2.3 Sensitivity test result comparison between Naïve *E. coli* strain and evolved strain

Sensitivity	Naïve strain	Evolved strain	Differential
Ampicillin	2.5 µg/mL	5.0 µg/mL	**Yes**
Kanamycin	5.0 µg/mL	7.5 µg/mL	**Yes**
Gentamycin	0 µg/mL	1.25 µg/mL	**Yes**
Streptomycin	1.25 µg/mL	2.5 µg/mL	**Yes**
Rifampin	0.625 µg/mL	0.625 µg/mL	**No**
SDS	1.0% (v/v)	1.0% (v/v)	**No**
Hydrogen Peroxide	1mM	1mM	**No**

2.6.5 Other stress-related genes also affect *E. coli* intracellular survival

To test if other stress-related genes also important for *E. coli* intracellular survival, *cpxA* (a sensor histidine kinase, an envelope stress response gene) [28], *soxR* (a redox-sensitive transcriptional activator), and *CyoD* (Cytochrome oxidase subunit IV, a component of soxR regulon) [29] knock out *E. coli* strains from Keio collection [30] were tested for intracellular survival in J774A.1 macrophages. We found that all three stress related genes also played important role for the bacteria survival in macrophages. Knockout either of these genes, *E. coli* survival in J774A.1 significantly decreased (**Fig 2.11**).

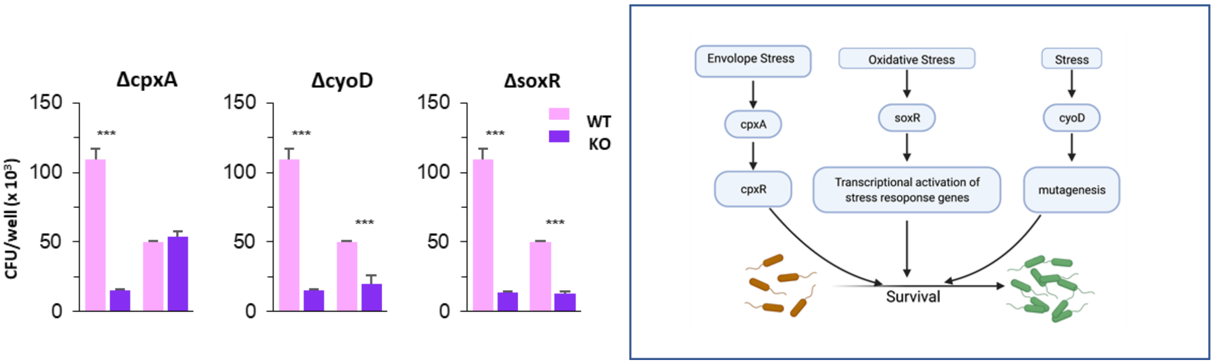

Fig 2.11. Stress related genes, cpxA, SoxR, and CyoD play important role in *E. coli* intracellular survival. The survival rate in J774A.1 is significantly decreased at 24h and 48h post inoculation for both SoxR and CyoD knockout *E. coli* strains, and at 24h for cpxA knockout *E. coli.* (Result obtained by Dr. Fengguang Guo).

2.7 Automation of the SEER platform

To fully operate the SEER platform with minimal manual input, the infusion of each reagent can be controlled by preset central program, and all types of the reagent (except for viable cells that required fresh from each round of evolution) could be loaded into a rack of loading vial at the initialization. Here, a block diagram (**Fig 2.12**) shows the overall control flow of the automated SEER platform. A pressure source will be control and timed by central LabView program so that the infusion can be paused during the steps. Pressure pump is connected to a solenoid valve unit, which is also controlled by same LabView program, is directly connected with regent loading vial. Pressure driven pump, once connected, will pump out the reagent and load them onto an intermediate assisting valve control chip (which controlled separately with another solenoid valve unit), to get the reagent ready before infusion. Finally, reagent will be loaded to the SEER chip.

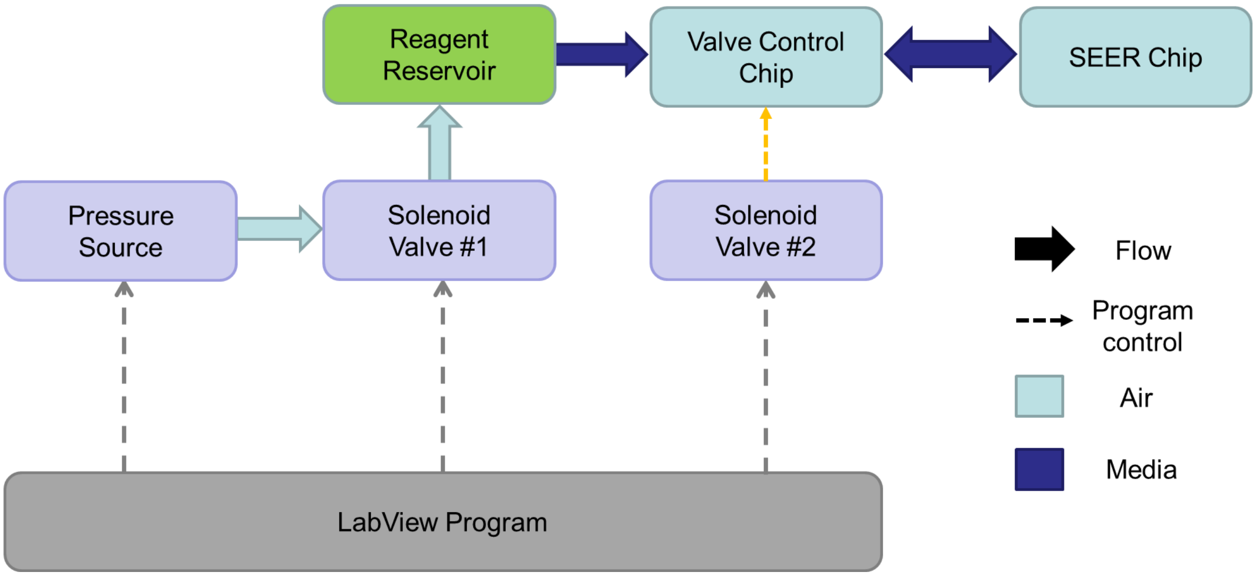

Fig 2.12. Block diagram of automated SEER platform.

In details, Fig 2.13 shows the configurations of the connection between each block. The pressure source is controlled by AMED flow controller, and is delivered to solenoid valve unit

(Purvis Industries), and the outlet is connected with 8 reservoirs that have been pre-loaded with experiment reagent, and together connected with the single outlet (**Fig. 2.13A**). During the time of operation, the reagent will be pumped out by air pressure source, into the intermediate network that connect the source and chambers (**Fig. 2.13B**). To avoid the unwanted infusion into operating chambers, pneumatic valve-controlled chip is fabricated to help close the connecting fluidic channel while infusing the reagent. Fabrication of the valve-controlled chip is also based

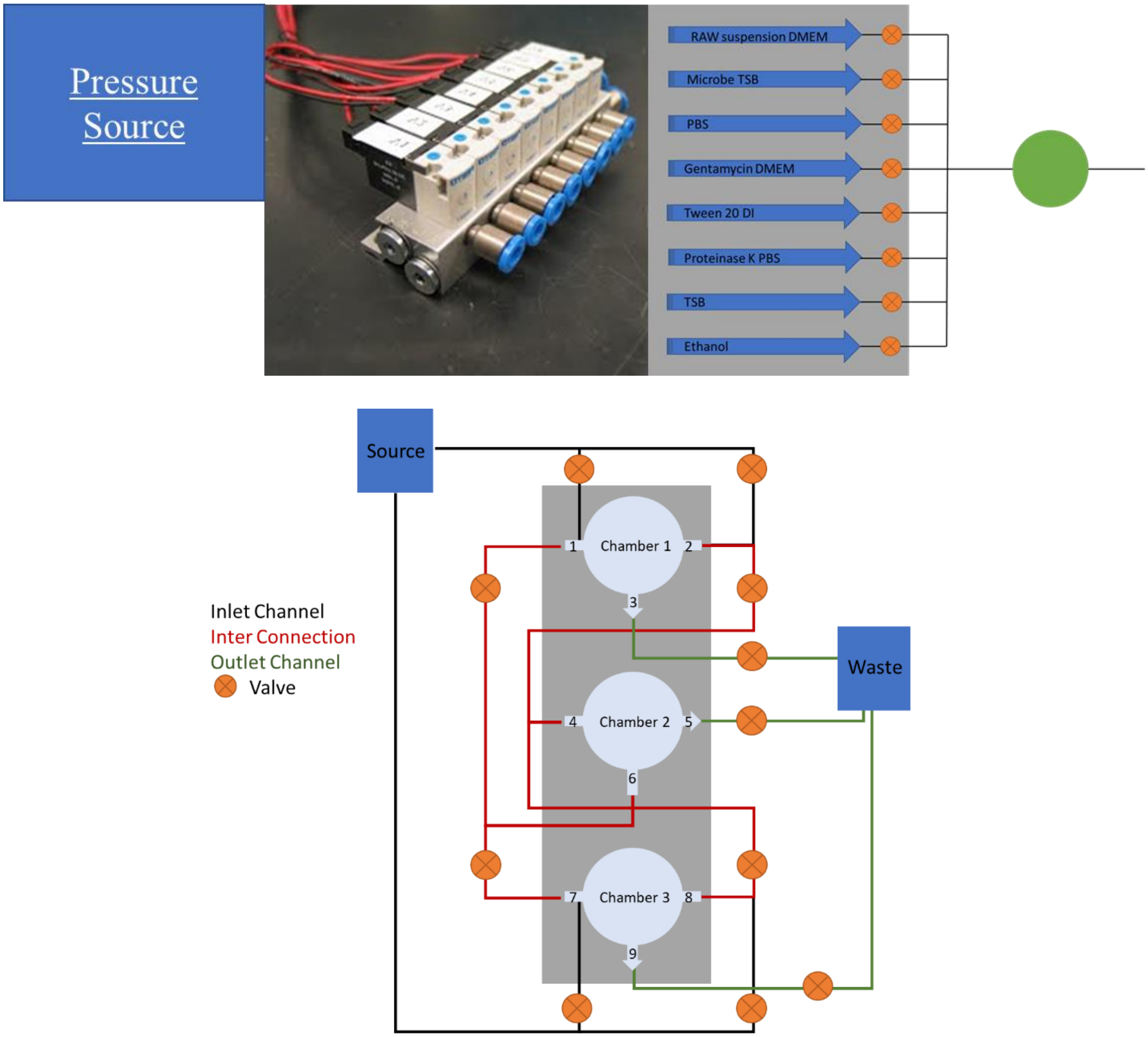

Fig 2.13. Illustration diagram showing connections between each functional block.

on the soft lithography of two PDMS layer, which is described in chapter 2.4, and after bonding together, the normally closed valve structure can be obtained.

Finally, a LabView program is configured to globally control the operation of all the valve units, which include the pressure-driven pump source, the pneumatic valve unit that controls the reagent reservoir loading, the pneumatic valve unit that controls the opening/closing of the normally closed microfluidic valve. The interface of that LabView program is shown in Fig 2.14. Specifically, this program is programmed so that the evolutionary assay can be conducted in a looped manner as described previously. The program is timed so that each valve control unit is coordinated to be operate at the time when they are supposed to. Table 2.4 shows a sample timing of two rounds of evolutionary assay, which starts from chamber 1, and is moved to chamber 3 after 1st round, then turned back to chamber 1 after 2nd round. Incorporated with the entire controlling system, the SEER platform finally could achieve the experiment conduct in a seamless manner.

Noted that this work is not completed. Future work includes testing with entire chip and functional validation using the *Salmonella* – macrophage system, and apply developed system to investigate additional host-pathogen models.

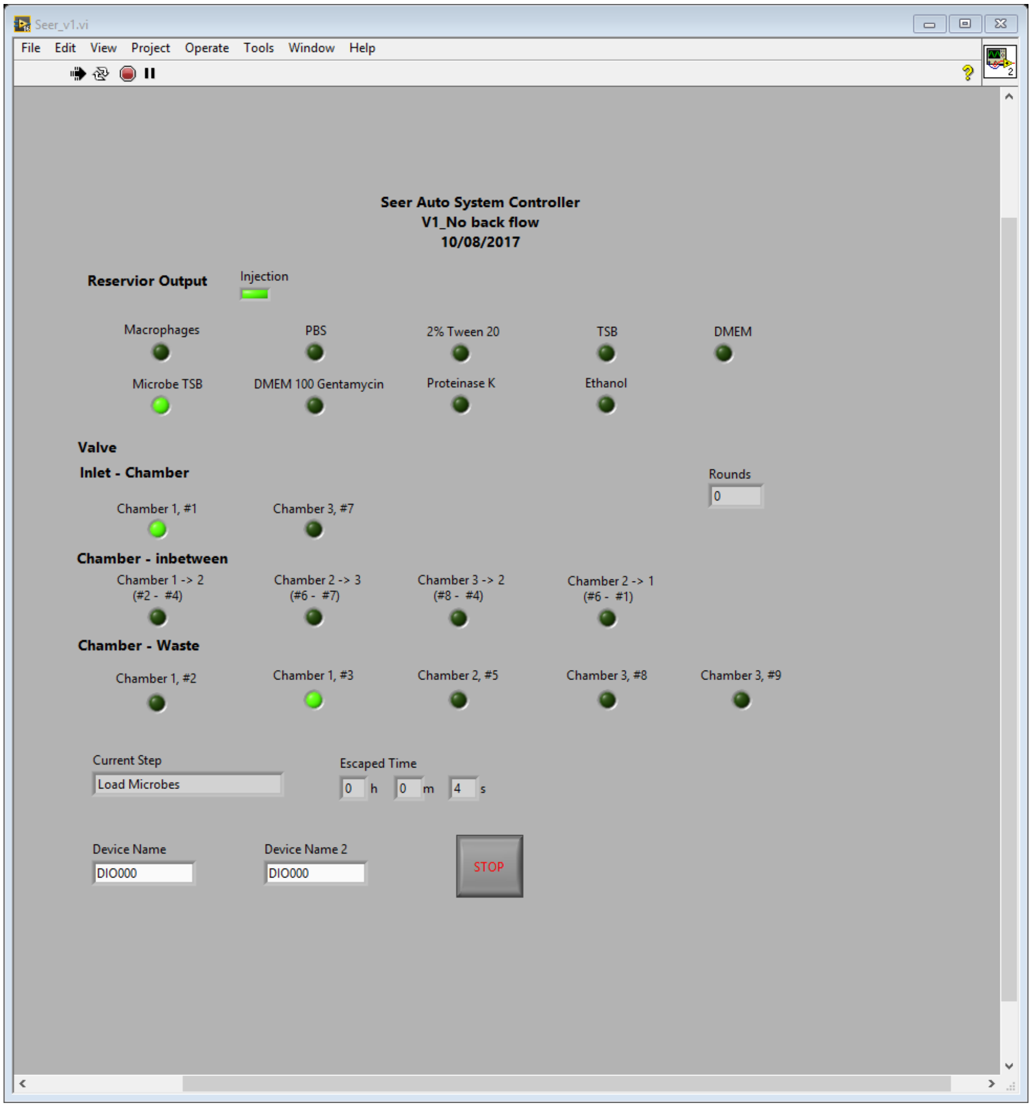

Rounds: 0

Current Step: Load Microbes

Escaped Time: 0 h 0 m 4 s

Device Name: DIO000

Device Name 2: DIO000

Fig 2.14. LabView controller interface, indicating the elapsed time as well as open/close status of each pneumatic controlled valve unit.

Table 2.4 Sample timing of two rounds of evolutionary assay which controlled by central LabView program

Steps	Medium	Inlet	Outlet	Pathway	Time	Rate	Interval
1.1	Raw cells DMEM	1	3	-	1 h	800 µL	0 min
1.1	Microbe TSB	1	3	-	10 min	800 µL	60 min
1.2	PBS	2	1	-	15 min	3000 µL	0 min

Table 2.4 Continued

Steps	Medium	Inlet	Outlet	Pathway	Time	Rate	Interval
1.3	Gentamycin DMEM	2	1	-	15 min	3000 µL	30 min
1.4	PBS	1	2	-	15 min	3000 µL	0 min
2.1	Tween 20 DI	1	3	-	15 min	3000 µL	30 min
2.2	TSB	1	3	-	15 min	3000 µL	36 h
2.3	TSB	1	9	2,4,6,7	30 min	3000 µL	0 min
2.4	Raw cells DMEM	7	9	-	1 h	800 µL	60 min
3.1	Proteinase K PBS	1	5	2,4	10 min	3000 µL	30 min
3.2	Ethanol	1	5	2,4	5 min	3000 µL	0 min
3.3	PBS	1	5	2,4	15 min	3000 µL	0 min

Steps	Medium	Inlet	Outlet	Pathway	Time	Rate	Interval
1.1	Raw cells DMEM	7	9	-	1 h	800 µL	0 min
1.1	Microbe TSB	7	9	-	10 min	800 µL	60 min
1.2	PBS	8	7	-	15 min	3000 µL	0 min
1.3	Gentamycin DMEM	8	7	-	15 min	3000 µL	30 min
1.4	PBS	7	8	-	15 min	3000 µL	0 min
2.1	Tween 20 DI	7	9	-	15 min	3000 µL	30 min
2.2	TSB	7	9	-	15 min	3000 µL	36 h
2.3	TSB	7	3	8,4,6,1	30 min	3000 µL	0 min
2.4	Raw cells DMEM	1	3	-	1 h	800 µL	60 min
3.1	Proteinase K PBS	7	5	8,4	10 min	3000 µL	30 min
3.2	Ethanol	7	5	8,4	5 min	3000 µL	0 min
3.3	PBS	7	5	8,4	15 min	3000 µL	0 min

2.8 Discussion

The developed evolutionary strategy is believed to provide a well coverage over the mutation events.[31-33] As one example demonstrated in this study, *E. coli* homogeneous cells were introduced into the proposed system. At end of each round of evolution, for a bacterium that divides about every half an hour (which is how quickly *E. coli* can grow when cultured with optimal conditions), a single bacterial cell can be amplified to a population with more than 2^{20} within 10 hours. Since *E. coli* has about 4 million nucleotide base pairs in its genome, if at a rate of 10^{-10} mutations per nucleotide base, a simple round of evolution can induce nearly 400 mutations even if just one single cell was survived/harvested after the pressure selection. Considering that *E. coli* contains about 3000 genes, that is about 13.3% possibility to have the alternation of any specific gene at this condition within one round. Thus, any gene that could theoretically mutated in the bacteria will have occurred somewhere in that population over 25 rounds of evolution at a chance with more than 97%. If the gene is highly correlated to the intracellular properties, such gene alternation is very likely to be preserved till the end of serial evolution.

Future work entails the further testification of identified gene mutations listed in Table 2.4. Biological pathway studies for those genes can provide detailed hypothesis on how the protein structure would altered therefore result the differential phenotype. Additionally, microfluidics system that proposed in this study could be further developed to be more flexible with other microbial models of interest such as *Ochrobactrum anthropi* and so on. Specifically, proposed system can be readily integrated with program interface to be controlled in a fully automatic manner. Such integration will require a central program to coordinate the operation of one facilitate pneumatic valve chip to control the opening/closing of interconnection channel between each step of operation, as well as a pressure-driven system to load/deliver reagents and cells. Under certain circumstances where exhaustion method is required to provide maximum coverage of possible mutations, ultra-violent or chemical exposure can also be embedded during the final amplification step at the top chamber of second unit to further accelerated the SNP mutation rate. The aforementioned fully automated system can also be deployed here to further extend the number of selection cycles while keeping the human labor input at the minimal level.

2.9 Conclusion

In this chapter, we have shown that an innocuous lab strain of *E. coli* can readily be evolved to acquire the capacity for enhanced intracellular survival, and that cpxR gene contributes to this process. In addition, we have shown that a novel microfluidic device (SEER) can be exploited to interrogate this process. This work opens up several new lines of investigation.

First, we develop a membrane-based microfluidic system (the SEER platform) that could facilitate the investigation intracellular parasitism of bacteria of interests, in an effortless and uninterrupted fashion. Second, this work also lay the groundwork for defining principles (and metrics) for evaluating the likelihood that a particular microbe (and/or classes of microbes) will evolve and/or acquire pathogenic properties. Finally, it provides a general method for predicting evolutionary outcomes before they arise (in the wild). Intracellular bacterial pathogens cause some of the deadliest infectious diseases known to humankind. Moreover, emerging diseases caused by intracellular pathogens pose a significant threat to human and animal health.[1-5] With this powerful evaluation tools in hand, high priority organisms can be subsequently tested in the SEER device to ascertain their pathogenic potential. Ultimately, the predictive capabilities of SEER will allow public health system to prepare in advance for the emergence of future microbial public health threats, thereby abandoning a reactive approach to public health or biodefense, and instead embracing a more anticipatory strategy.

3. MICROFLUIDIC SYSTEM FOR DIGITAL ANALYSIS OF ADHERENT BACTERIA TO IDENTIFIES EMERGENT PATHOGENS

3.1 Overview

There are enormous number of unknown microorganisms in nature, some of which have the potential to cause diseases. The identification of microorganisms that cause disease has conventionally relied on molecular or biochemical assays of material derived from cultivated microbes. While such methods provide reliable information about previously described infectious agents, they may offer limited utility for identifying emerging or novel pathogens. Phenotypic hallmarks of pathogenesis constitute an orthogonal information source about bacteria and their biological contexts. However, these hallmarks are infrequently examined for threat assessment as most phenotypical assays are complicated and labor-intensive. Adherence to host cells is one essential hallmark of the virulence programs of bacterial pathogens of humans. We therefore exploited this fact to develop and test a high-throughput microfluidic system in which bacterial adherence to host cells was used to identify microorganisms that are pathogenic to humans or that possess features that may confer emergent pathogenicity. The system features the use of continuous flow dielectrophoretic separation of bacteria that adhere to host cells at single cell (digital) resolution, and enables the sorting of 10^7 adherent microorganisms per hour, representing a comparable throughput with conventional flow cytometry systems however without pretreatment or any prerequisites of fluorescent labeling.

Although downstream biological investigation is still going on, the analysis of soil samples is expected to reveal several dozens of microbial species previously known to cause human disease, as well as novel strains that displayed hallmarks of emerging bacterial pathogens however yet to be studied. Taken together, the system would be able to provide an orthogonal approach for the rapid evaluation of bacterial adherence to host cells and dramatically expands the toolkit available for biological threat assessment and characterization of unknown or uncharacterized microorganisms.

3.2 Introduction

Rapidly changing climate, globalization, urbanization, and population dynamics have increased the likelihood of individuals encountering novel or previously unidentified microbial pathogens in nature. Therefore, improved strategies for identifying microbial pathogens are required to combat these rising risks. To date, pathogen identification strategies have featured the analysis of cellular components, including proteins, carbohydrates, or nucleic acids. Although several such analyses are routinely performed, they are fine-tuned for the identification of known pathogenic bacterial species, which account for only a very small portion of the total microbes that could potentially threaten public health.

DNA sequencing and serological technologies are typically employed to identify bacterial pathogens.[34-37] However, these routinely used approaches have several limitations. First, algorithms that predict bacterial pathogenic potential based on DNA sequence information alone revealed limitations in current approaches, especially when the analysis of phylogenetically diverse organisms is considered.[38] The continuing evolution of the genomes of bacterial pathogens further increases the challenge. Moreover, substantial cost and technical sophistication is required to generate high quality whole sequence genome sequence information from large numbers of microbes.[39] Finally, sequence-based approaches cannot accurately make predictions which show limited genomic similarity to the genomes of pathogens in the sequence databases. [40]

Given these limitations, and the need to develop orthogonal approaches for threat assessment, we are pursuing the development of alternative strategies that could be deployed in a high-throughput fashion to directly characterize phenotypes associated with bacterial pathogenicity. While conceptually attractive, the implementation of high-throughput phenotyping for large sample populations poses significant challenges, including the need to analyze many phylogenetically diverse microbes at single-cell resolution. This challenge is especially notable when sampling environmental bacteria, as the diversity is typically vast (varied from 10^2 – 10^9 CFU per gram of soil, with minimum 4000-7000 different types of bacterial genome per gram of soil)[41,42] and relatively few bacteria have been characterized. Till now, there are only about 200000 bacterial and archaeal complete or draft genomes uploaded to public databases, which accounts for the representations of about only 2% of the global prokaryotic taxa.[43] To address these limitations, we turned our attention to the unique high-throughput single-cell-resolution capabilities of microfluidic systems. Amongst the various phenotypic hallmarks of pathogenicity, we focused on bacterial adherence to host cells because it is essential for bacterial pathogenesis. In addition, a wide array of adherence mechanisms has been described, which renders the prediction of adherence phenotypes based on genome sequence data challenging.

Microfluidics systems have been extensively developed in the past two decades, and many different single-cell manipulation technologies are now available in various microfluidics formats.[44-49] In comparison with conventional methods, microfluidic platforms can investigate heterogenous biological samples at single-cell resolution and high precision, all at extremely high throughput, while requiring less reagent consumption and manual handling steps. Assaying bacterial adherence to host cells in microfluidics formats require separating bacterial cells that adhere to host cells from those that do not, ideally without any labeling requirements. To achieve this goal, we focused on the capability of dielectrophoretic cell separation that enables the separating of cells of different sizes.[50] The microfluidic system concept is to first co-incubate bacterial cells with host cells, and then separating all host cells from free-floating bacterial cells.

This procedure allows the highly selective harvesting of only the adherent bacterial cells that attached to host cells. The harvested host cells can then be plated at single-cell resolution, and the adherent bacterial cells subsequently recovered from these plates.

To demonstrate the utility of this on-chip adherence identification platform, we first examined the dielectrophoretic response of host cells and six types of bacterial strains that are commonly used as models for studying bacterial adherence to host cells,[51-54] including *Staphylococcus aureus*, *Bacillus subtilis, Pseudomonas aeruginosa* (PAO-1), *E. coli* and two mutant strains, a non-flagellated *Pseudomonas aeruginosa* strain[55] as well as mutant *Staphylococcus aureus* strain. Mixtures of host cells and each type of bacterial cell after a cultivation step were processed through the developed microfluidic system and the harvested samples were benchmarked to conventional adherence assay results. Next, system performance with multiple bacterial strains were first evaluated using *E. coli* and PAO-1 mixtures at different ratios, followed by an artificial microbe community that is composed of 30 different strains. Finally, upon successful validation of system performance, the developed microfluidics platform was deployed to investigate 2 soil bacterial samples having diverse compositions, and at least 10^3 strains were confirmed to be adherent to host cells.

Although downstream biological investigation is still going on, examined isolates are expected to contain several strains of which were not previously described to display adherence to host cells. Taken together, the developed high-throughput microfluidic bacterial adherence to host cell platform can be readily used under many on-field investigations to detect/characterize unknown microbial pathogens.

3.3 Working principle of the microfluidic device

Dielectrophoretic (DEP) force acting on cells is generated when they are positioned in a non-uniformed electric field. The received DEP force varies depending on their size and dielectric constant of cells as well as the applied voltage and frequency of the electric signal. The DEP force acting cells nearby a pair of planar electrode wires, and the resulting displacement of cells, $\Delta y'$, can be calculated by using the numerical simulation [56-58]:

$$\frac{d(\Delta y')}{dt} = \frac{F_{DEP}\cos\theta}{12\eta(S/l)} = \frac{\varepsilon_m V_c \cos\theta \, Re[f_{CM}] v_a^2}{32\eta\left(\frac{S}{l}\right)[\ln(8d/\pi a)]^2}\frac{\partial\left|\vec{A}\right|^2}{\partial x} \tag{1}$$

$$\vec{A} = \sum_{n=1}^{\infty}\left\{(-1)^{n+1}\frac{[x+(-1)^n(2n-1)d]\overrightarrow{a_x}+z\overrightarrow{a_z}}{[x+(-1)^n(2n-1)d]^2+z^2} + (-1)^{n+1}\frac{[x-(-1)^n(2n-1)d]\overrightarrow{a_x}+z\overrightarrow{a_z}}{[x-(-1)^n(2n-1)d]^2+z^2}\right\} \tag{2}$$

$$f_{CM} = \frac{\varepsilon_c^*(\omega)-\varepsilon_m^*(\omega)}{\varepsilon_c^*(\omega)+2\varepsilon_m^*(\omega)}, \text{where } \varepsilon^* = \varepsilon - j\frac{\sigma}{\omega} \tag{3}$$

The symbols used in the equation can be found in the Nomenclature section. Here, the lateral displacement of cells strongly depends on the magnitude of pDEP force, which is proportional to the real part of the Clausius-Mossotti factor determined by the dielectric properties of cells and the surrounding media.

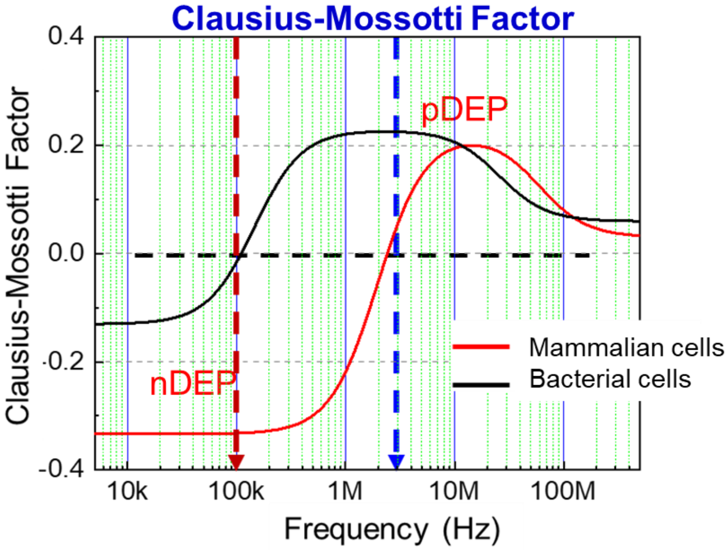

Fig 3.1 Calculated real part of Clausius-Mossotti Factor of mammalian cells and bacterial cells. From the calculation, at around 100 kHz to 200 kHz, bacterial cells receive neglectable DEP force when placed under electric field, however, the DEP force acting mammalian cells is maximized.

Specifically, the Clausius-Mossotti (CM) factor here is dependent with the applied frequency, so the DEP force acting on cells can be tuned depending on the frequency condition even when the parameters from physical dimension and surrounding medium is fixed. In the context of the bacterial adherence assay, the size and dielectric properties of bacterial cells and mammalian host cells are quite different. Through simulation as well as information from prior experiments, [50] we were able to find an optimal frequency where mammalian cells receive a large DEP force while bacterial cells are not impacted by any DEP force. Detailed information regarding the simulation of the CM factor can be found in the **Fig 3.1.** [50]

The overall design concept is the use of an angled DEP electrode pair to continuously move only one cell type from one side of the channel to the opposite side of the channel (**Fig. 3.2**), causing lateral displacement to separate out the two different cell population. In this study, instead of using one pair of electrodes, a planar interdigitated electrode array was used to induce and intensify the negative DEP force acting on the host cells (**Fig. 3.2**). The electrode array was tilted at an angle of 5.7° degree to the flow direction, pointing downwards to the lower outlet. The device has three inlets and two outlets. The middle inlet is for the cell loading, while the top-most inlet and the bottom-most inlet are for buffer reagent to shear the entire loaded cell stream to form the laminar flow. Co-flowing solution through these inlet forms a laminar flow, and thus without DEP force, both types of cells inside the co-culture media will flow directly towards the upper outlet. In contrast, when the DEP electric signal is applied, host cells receiving DEP force are guided by the tilted electrode array and gradually migrate to the lower part of the microchannel. Thus, any bacterial cells that are attached onto the host cells can be transferred along with the host cells and collected into the lower outlet. However, free-floating bacterial cells that are not attached to the host cells will continue to flow straight into the upper outlet since they are not affected by the DEP force. In summary, the proposed device can utilize DEP force to separate the host cells (along with the attached bacterial cells) from the unattached bacterial cells, consequently, achieve the selection of adherent bacterial cells from a mixed bacterial population.

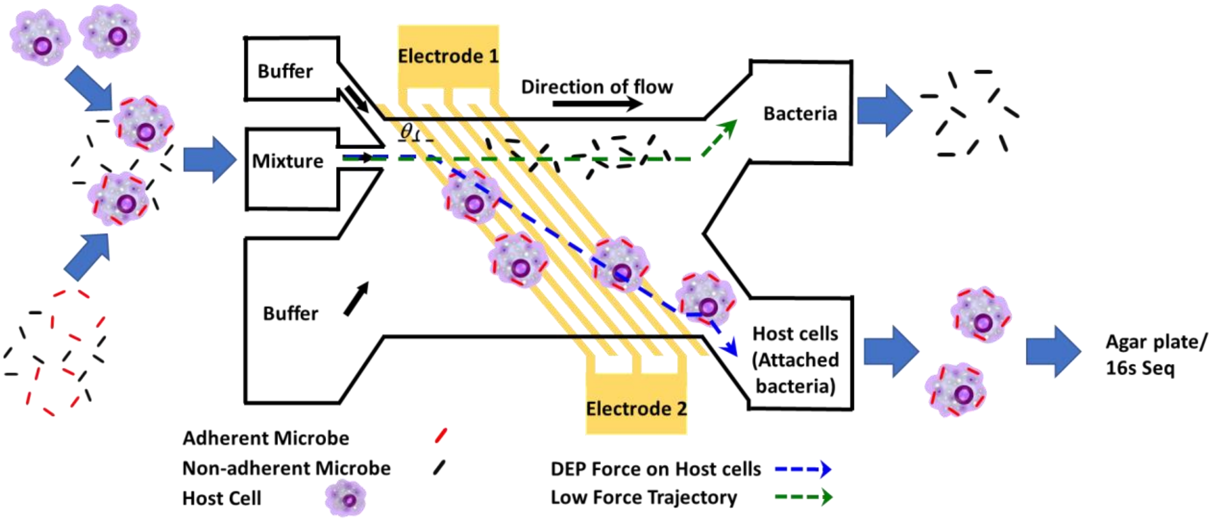

Fig 3.2 Proposed lateral dielectrophoretic screening microfluidic system.

3.4 Microfluidic device design and microfabrication

The developed microfluidics device was designed to have 3 inlets and 2 outlets. The inlet channel for bacteria/host cell co-culture solution (top-most inlet) is 50 μm wide, and the other two inlets for buffer media are designed to be 250 μm and 900 μm, respectively. The widths of the two outlets are both 900 μm, so that the co-culture sample, under laminar flow condition, will directly flow towards the upper outlet. The planar interdigitated electrode array is positioned at an angle of x to the flow direction at the main laminar flow region. Each electrode line has a width of 15 μm, and the distance between the electrodes is 15 μm. Finally, the entire device height is set to 26 μm, relatively shallow so that the electric field intensity generated by the planar electrode array can be sufficient to cover the entire channel height, while still being tall enough for the host cells to flow through without clogging the microchannel.

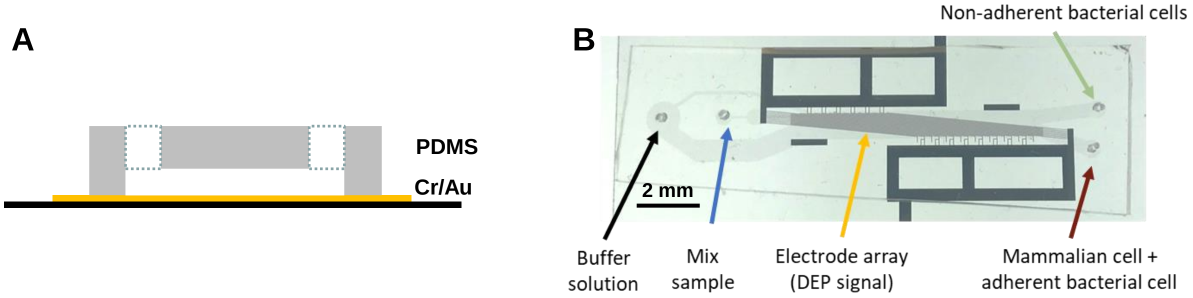

Fig 3.3 Device illustration. **A**. Cross-section view. **B.** Fabricated device.

The microfluidics device was fabricated on a patterned 0.7 mm thick borosilicate glass using a polydimethylsiloxane (PDMS) microchannel and a micropatterned planar electrode array. First, a 2x3 inch size borosilicate glass substrate (Swiftglass, Co., Inc., NY) was cleaned and deposited with Cr/Au (200 / 1000 Å) using an electron-beam evaporator, then patterned using AZ 1518 photoresist (AZ Electronic Material plc, NJ) with traditional photolithography process, and then the metal layers etched to create the interdigitated electrode array. Next, SU-8 2025 photoresist (Microchem, Inc., MA) was spun to obtain a 26 μm height master mold for soft lithography. The fabricated maser mold was then treated with tridecafluoro-1,1,2,2-tetrahydrooctyl-1-trichlorosilane (United Chemical Technologies, Inc., Bristol PA) to facilitate the PDMS layer release. The PDMS replica was made by pouring PDMS pre-polymer mixture (10 : 1, Sylgard 184, Dow Corning, Inc., MI) onto the treated master mold and cured in a 65˚C oven for 8 h. Finally, the PDMS replica and the metal-pattered glass substrate were treated with oxygen plasma, aligned, and bonded on an 85˚C hotplate for 24 h. Fabricated device is shown in **Fig. 3.3.**

3.5 Biological material and methods

3.5.1 A549 cell culture conditions

For host cells, A549 cells were selected because of its common usage in the adherence study.[59] The A549 cell line (ATCC CCL 185) was maintained in ATCC-formulated F-12K medium supplemented with 10% fetal bovine serum and incubated at 37°C in 5% CO_2. The cells were fed every 3 to 4 days and passaged at 85 - 95% confluency. Cells were briefly rinsed with PBS and treated with 0.25% Trypsin-0.53 mM EDTA solution submerging the cell layer about 5 min in 37°C. Additional complete growth medium was then added to stop the protease activity. The cells were then plated at the vessels using a sub cultivation ratio of 1:3 to 1:8.

3.5.2 A549 suspension cell adaptation

The attached A549 culture was adapted to suspension culture using a serum-free suspension by sequential 1:1 dilutions of the serum-containing medium with FreeStyle 293 expression medium (Thermo Scientific) supplemented with 0.1% pluronic F-68 non-ionic surfactant (Thermo Scientific) [59]. Each medium allowed the cells to adapt for suspension culture for 2 - 3 passages. Suspension cells were then cultured in a spinner flask using complete FreeStyle 293 expression medium. When needed, A549 were stained using SYTO 9 viability dye (ex/em 485/530 nm) prior to experiments.

3.5.3 Bacterial cell preparation.

Salmonella Typhimurium (strain ATCC 14028S) engineered with a GFP plasmid (pCM 18), *Staphylococcus aureus* (BEI NR-46543), mutant *Staphylococcus aureus* (USA300 JE2) *Pseudomonas aeruginosa* (PAK), mutant *Pseudomonas aeruginosa* (PAK ΔpilA), *Bacillus subtilis* (ATCC 6051), *Escherichia coli* (strain ATCC 25404), *Pseudomonas aeruginosa* engineered with an RFP plasmid, *and Escherichia coli* engineered with an RFP plasmid were inoculated on a trypticase soy agar plate, followed by incubation at 37°C overnight. The next day, single colonies were picked and cultured in Lysogeny Broth (LB) in a shaking incubator at 37 °C for 8 h. For each cell, write here, with reference, why we selected these cell types.

3.5.4 Bacterial community preparation

Artificial bacterial community was also provided by National Institute of Standards and Technology (NIST) for characterization of device performance. Details of the compositions of this microbial mixture can be found in **Table 3.1**.

Table 3.1 Composition of artificial bacterial community for mock screening assay

NIST ID	Species	strain	16s abundance
0011	*Acinetobacter baylyi*	TG19579	2.16%
0012	*Corynebacterium amycolatum*	NCTC7243	1.38%
0014	*Corynebacterium diphtheriae*	C7 (beta)	0.32%
0018	*Staphylococcus epidermidis*	1457	0.08%
0019	*Enterococcus faecalis*	OG1RF	0.10%
0020	*Staphylococcus aureus*	subsp. aureus UAMS-1	2.11%
0023	*Staphylococcus aureus*	subsp. aureus CIG1835	0.00%
0025	*Acinetobacter baumannii*	AB5075-UW	0.36%
0026	*Pseudomonas aeruginosa*	PAO1 strain 2017-A	0.25%
0027	*Pseudomonas aeruginosa*	43CFBRPA	0.08%
0032	*Deinococcus radiodurans*	ATCC 13939	51.12%
0045	*Klebsiella oxytoca*	NCTC13727	0.20%
0048	*Yersinia pseudotuberculosis*	PA3606 Pa3606	0.04%
0049	*Klebsiella pneumoniae*	k336	0.70%
0052	*Escherichia coli*	536	0.12%
0054	*Escherichia coli*	MOD1-EC5746	0.12%
0056	*Escherichia coli*	MUGSI_218	0.18%
0059	*Escherichia coli*	OLC2138	0.23%
0066	*Salmonella enterica*	subsp. enterica serovar Typhimurium str. DT104 strain H67	0.14%
0071	*Serratia rubidaea*	NCTC9419	3.81%
0073	*Bacillus cereus*	MOD1_Bc97	0.88%
0079	*Streptococcus agalactiae*	COH1	0.00%
0083	*Staphylococcus capitis*	subsp. capitis strain NCTC 11045	6.56%
0087	*Listeria innocua*	FSL S4-378	1.17%
0092	*Listeria monocytogenes*	CDPHFDLB-F14M01770.86-1	1.75%
0129	*Pseudomonas putida*	B001	0.20%
0139	*Elizabethkingia anophelis*	Elizabethkingia anophelis CIP111067	23.29%

Soil bacteria isolation and preparation: Two environmental soil samples (0–10 cm depth) were harvested at two sites, from Texas and Oklahoma. One is a loam soil taken from outside of the new warming experimental plots created in 2009 (34°58′45″ N, 97°31′15″ W), one is taken from feedlot where agricultural animals were raised (30°36'46.3"N 96°21'19.8"W).

To extract soil bacteria cells from soil sample, soil sample dispersion was first conducted using a blender with soil (5% w/v) mixed with Tween 20 (P9416, Sigma-Aldrich, USA) in PBS buffer (0.5% v/v) and rinsed with DI water and then isopropanol alcohol (70%). Following, cells were extracted from the soil dispersion by mixing it with the Nycodenz density gradient buffer (AXS-1002424, Cosmo Bio, 80% w/v in ultrapure water) and centrifuging the mixture at 15,000 ×g for 40 min at 4˚C. Finally, the layer containing cells were transferred and rinsed by PBS buffer to obtain the soil bacterial community. [60]

Prior to conducting the microfluidic adherence assay, A549 host cells were rinsed and resuspended in low-conductivity media, and the concentration of cells was adjusted to 1.0×10^6 cells/ml. Following, for each of the experiment, bacterial cells were mixing with A549 host cells at a multiplicity of infection (MOI) of 100 and mixture sample was co-incubated on rotary at 37˚C for 1 h.

3.5.5 Preparation of low-conductivity medium

Low conductivity medium used in the microfluidic experiment was made of 0.3 mM monopotassium phosphate (1551139, Sigma-Aldrich, USA), 0.85 mM of dibasic potassium phosphate (1151128, Sigma-Aldrich, USA), 2.5 mM of potassium chloride (P9333, Sigma-Aldrich, USA), and 280 mM of myo-Inositol (I5125, Sigma-Aldrich, USA) in de-ionized (DI) water, was described previously. [50]

3.5.6 Adherence assay on multi-well plate format

Approximately 2.5 x 10^5 A549 cells were seeded onto coverslips (20mm, Southern Labware, #801008) a day prior to the well-plate-format adherence assay so that the host cells attach to the coverslip surface. The cell monolayers were first washed three times with warmed 1xPBS. To determine the kinetics of bacterial association, the cells were overlaid with 500 µl of bacterial suspensions at MOI of 100. The bacteria were spun down at 1100 RPM for 10 min and incubated at 37°C for 1 h. The unbound bacteria were removed by washing the monolayers five times with warmed 1 x PBS (pH 7.4). The monolayers were then fixed for 15 min with 4% formaldehyde, then washed three time with PBS and stained with 50 ng/ml 4′,6-diamidino-2-phenylindole (DAPI). After 10 min of incubation, the coverslips were mounted using a MOWIOL (Sigma-Aldrich) mounting medium. The images were captured with BioTek Cytation 5. A demonstration of how it works is illustrated in **Fig. 3.4**.

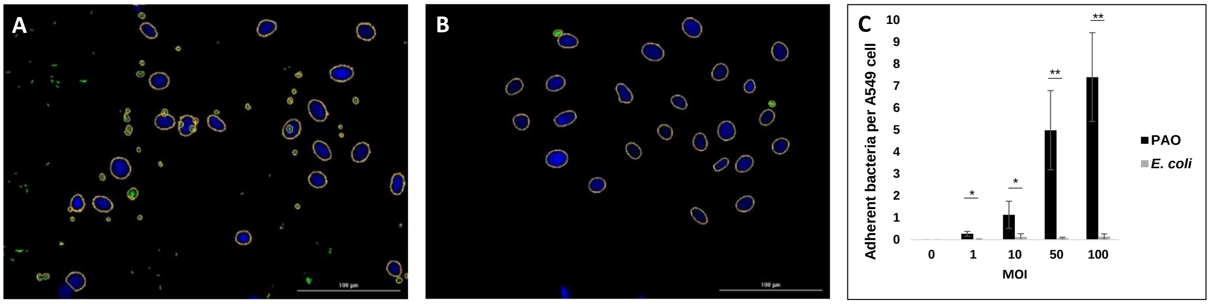

Fig 3.4 Example of the adherence assay on multi-well plate format. Here, (A) *P. aeruginosa*, and (B)*E. coli*, which typically used as positive and negative control in adherence study, is evaluated in well-plate format. The number of adherent bacteria per A549 cell at different MOI is summarized in (C). Scale bar: 100 µm. (Results provided by Dr. Jing Yang.)

3.5.7 Cell viability assay

Impacts of low-conductivity media and dielectrophoretic force on host cell viability were evaluated using SYTO 9 cell staining dye (ex/em 485/530 nm) and propidium iodide (PI) (ex/em 485/630 nm) (live/dead baclight bacterial viability kit, L7012, Invitrogen), mixed at 1:1 ratio. The fluorescence microscopic (Zeiss AXIO Observer 7) images, which were acquired before/after lateral dielectrophoretic cell separation experiment, were used for cell viability analysis. The entire experiment was conducted as same as previously described.[50]

3.5.8 Sequencing and analysis

Collected aliquots of environmental bacterial samples from both outlets were plated onto a blood agar plate (Fisher Scientific, R01200), harvested, amplified and sequenced for 16S rRNA analysis. The Taq DNA Polymerases (New England BioLabs Inc., M0273S) and E.Z.N.A Tissue DNA Kit (Omega Bio-Tek Inc., D3396), as well as forward primer (Sigma-Aldrich, primer-8F, Sequence 5’-3’: AGAGTTTGATCCTGGCTCAG) and reverse primer (Sigma-Aldrich, primer-U1492R, Sequence 5’-3’: GGTTACCTTGTTACGACTT) were used to extract and amplify the DNA for sequencing.

3.6 Microfluidic device operation

The developed microfluidic system was characterized using A549 host cells alone, GFP-labeled *Salmonella enterica* cells alone, A549 cells mixed with *Staphylococcus aureus* (MOI 1:100), A549 cells mixed with *Pseudomonas aeruginosa* (MOI 1:100), A549 cells mixed with *Bacillus subtills* (MOI 1:100), A549 cells mixed with *Escherichia coli* (MOI 1:100), A549 cells mixed with mutant *Pseudomonas aeruginosa*(MOI 1:100), A549 cells mixed with mutant *Staphylococcus aureus* (MOI 1:100), A549 cells mixed with *Pseudomonas aeruginosa* and *Escherichia coli* (MOI 1:50:50), A549 cells mixed with an artificial microbial library (MOI 1:100), and A549 cells mixed with soil-extracted microbial samples (MOI 1:100). Device operation was conducted under the same setup for all sample testing. The flow rates for buffer and low-conductivity media were set to 160 µl/h, and the flow rate of the cell sample was set to 40 µl/h. In addition, withdrawal through another syringe pump was also applied from both outlets at a flow rate of 100 µl/h, collecting the samples directly into syringes. During the entire operation, a sinusoidal signal of 200 kHz, 8 Volt peak-to-peak (V_{pp}) was applied to the electrode array to generate the DEP force for the host cells.

3.7 Results

3.7.1 DEP response of host cells and bacterial cells in the microfluidic system

To evaluate the DEP force acting on host cells and bacterial cells, each type of cells was loaded onto the developed microfluidic system and tested separately. To better monitor the trajectory of A549 host cells, A549 cells stained with SYTO 9 dye (green color) and GFP-*Salmonella* cells were used, and entire experiments were conducted under a fluorescence microscope (Zeiss AXIO Observer 7). For *Salmonella* cells, it can be seen that they flow straight and directly into the upper outlet regardless of whether applying DEP signal or not (**Fig. 3.5A, Fig. 3.5B**). For A549 cells, when DEP signal was off, cells flowed straight and into the upper outlet (**Fig. 3.5C**); however, when the DEP signal was turned on, cells can be seen following the angled electrode patterns and gradually moving downwards, and eventually flowing into the lower outlet

(**Fig. 3.5D**). The differential trajectories between the A549 cells and *Salmonella* cells demonstrated the feasibility of separating bacterial cells from host cells.

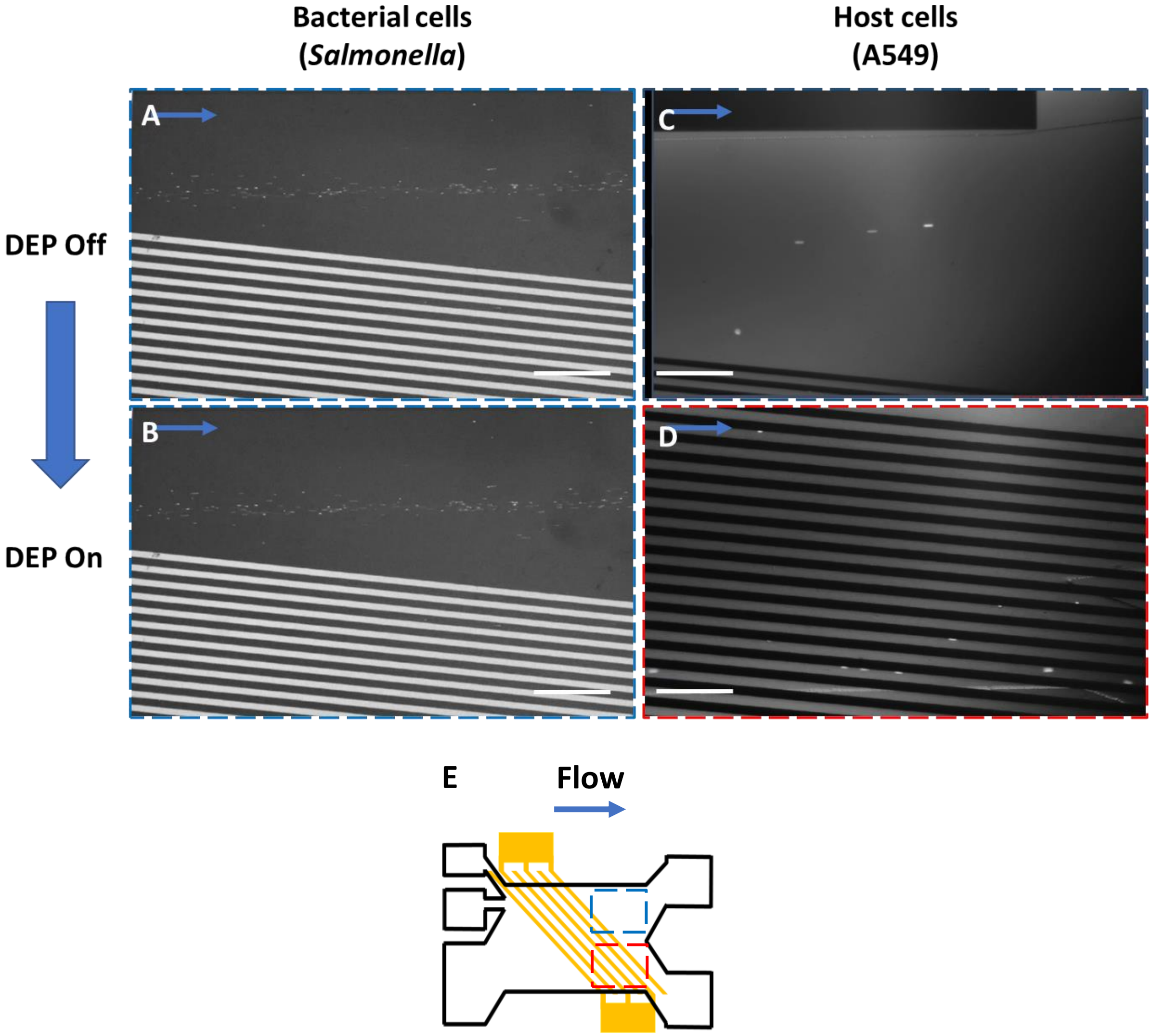

Fig 3.5 Trajectory comparison of bacterial cells and host cells when DEP turned on/off. (A-B) whether DEP was on or not, bacterial cells were streamed directly towards upper outlet. (C) when DEP was off, host cells behave similarly with bacteria cells. No host cells will be flow to the lower side. (D) When DEP was on, host cells where shifted due to experienced DEP force, therefore migrate towards lower outlet. Picture outline color corresponds to the dashed zone shown in (E). Scale bar: 200 µm.

3.7.2 Separating adherent bacterial cells using the microfluidic system

Following the characterization of DEP response of the host cells and bacterial cells, the developed device was evaluated using host/bacterial cell mixtures. The purpose here was to verify the functionality of the device using adherent and non-adherence bacterial cells, as well as gram-negative and gram-positive strains. Here, *S. aureus* (Gram positive, high adherence), *P. aeruginosa* (Gram negative, high adherence), *B. subtilis* (Gram positive, low adherence), and *E. coli* (Gram negative, low adherence), four well-studied bacterial cells that are known to exhibit canonical adherent phenotypes were individually tested with A549 host cells. Additionally, two mutant strains, *S. aureus* and *P, aeruginosa*, were also tested to validate the functionality of the proposed system against strains from same species. The co-cultured mixtures were introduced into the device and tested. Similar to the previous result, when the DEP signal was off, both host cells and free-floating bacterial cells flowed straight and into the upper outlet; when the DEP signal was turned on, while host cells were guided to the lower outlet the free-floating bacterial cells continued to flow straight and into the upper outlet.

The harvested cells were examined under a microscope and the average number of attached bacterial cells per host cells were measured using CFU counting. As can be seen in **Fig. 3.6 A-D**, a large number of *S. aureus* (**Fig. 3.6A**) and *P. aeruginosa* (**Fig. 3.6B**) cells can be seen attached onto the A549 cell surface. However, attachments of *B. subtilis* (**Fig. 3.6C**) and *E. coli* (**Fig. 3.6D**) cells onto A549 cell surface were rare. This result was further confirmed in comparison with those from a well-plate assay (indicated as off-chip assay in **Fig. 3.6E**). For example, *S. aureus* on

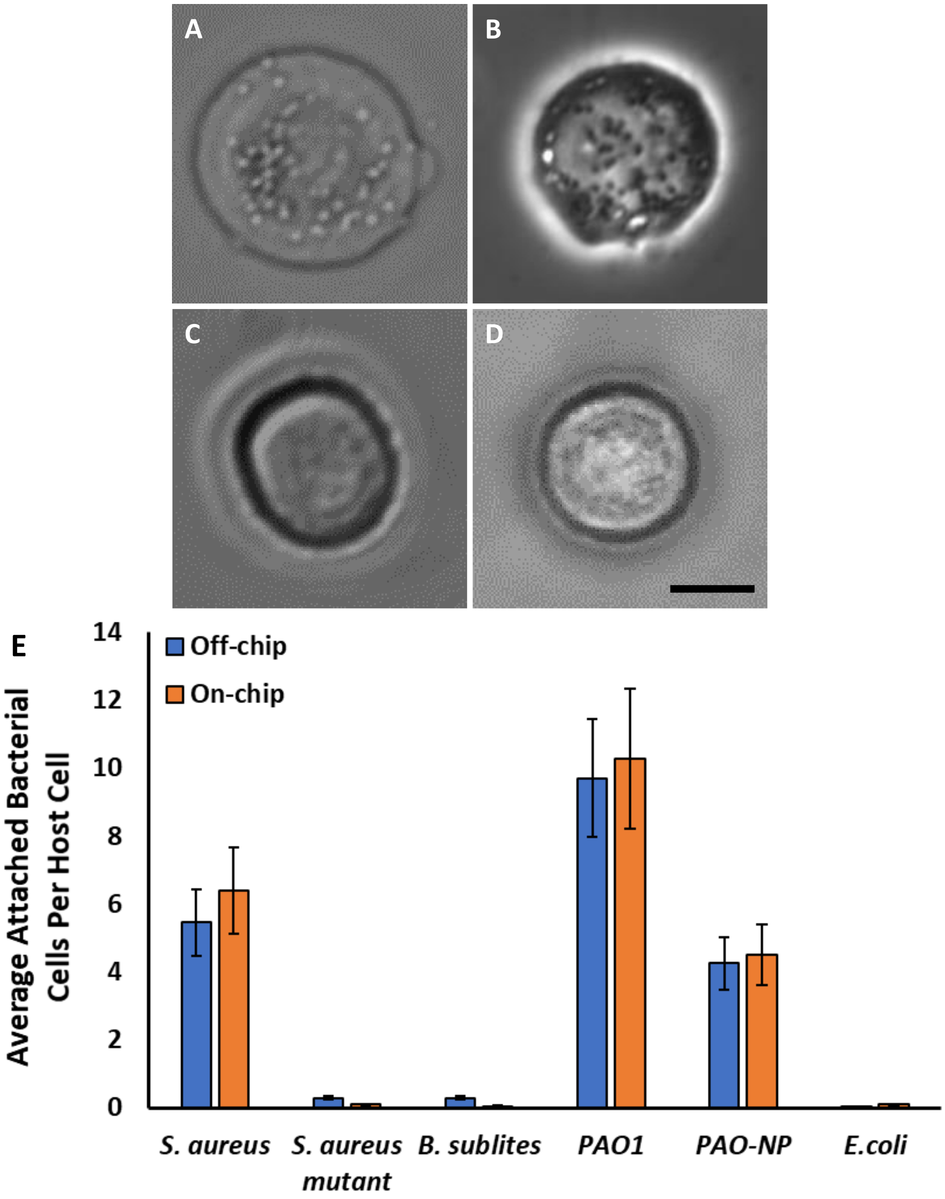

Fig 3.6 (A-D) Zoomed in picture shows that bacterial cells that attached on host cell surface were also successfully collected along with host cells during this process. **A.** *staphylococcus aureus* **B.** *Pseudomonas aeruginosa* **C.** *Bacillus cereus* **D.** *Escherichia coli.* **E.** Comparison between off-chip results vs. on-chip results.

average had 5.5 ± 1.0 adhering cells per host cells in a conventional plate assay, while having 6.4 ± 1.3 adhering cells per host cells in the microfluidic adherence assay. For flagellated *P. aeruginosa*, 9.7 ± 1.7 (off-chip) vs. 10.3 ± 2.1 (on-chip); *B. subtilis*, 0.3 ± 0.1 (off-chip) vs. 0.1 ±

0.0 (on-chip); *E. coli,* 0.0 ± 0.0 (off-chip) vs. 0.1 ± 0.0 (on-chip). These results showed that the developed microfluidic host-pathogen adherence interaction behaved similarly compared to a conventional assay, but These results showed that the developed microfluidic host-pathogen adherence interaction behaved similarly compared to a conventional assay, but with much fewer handling steps as well as equipment requirements. Lastly, the original mixture and harvested sample from lower outlet were directly compared **(Fig. 3.7)**. Most of the unattached bacterial cells from original mixture were successfully removed after DEP selection, which confirmed the collected samples from the lower outlet will only contains A549 cells and attached bacterial cells.

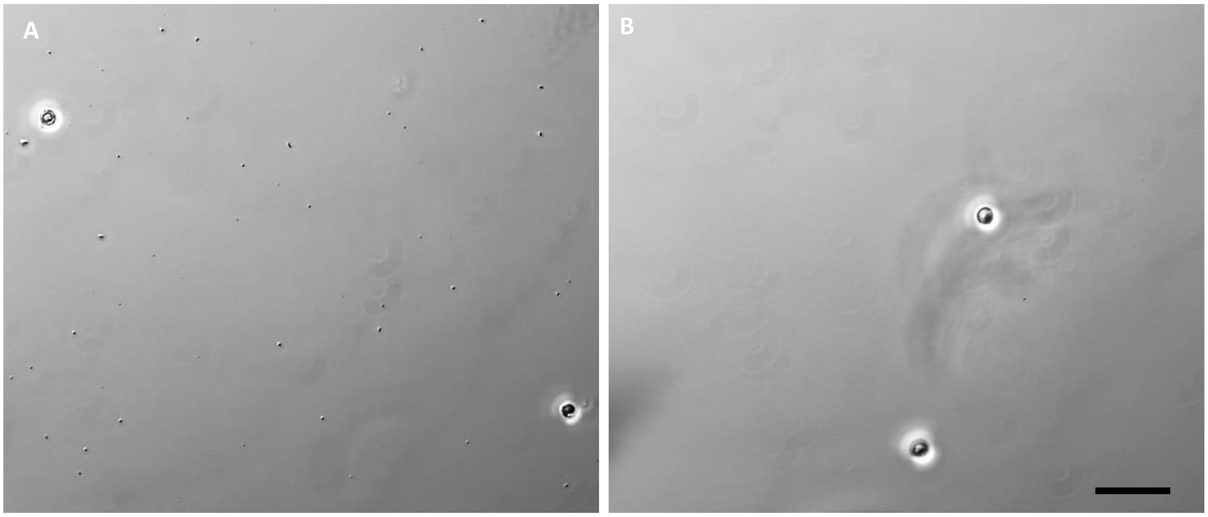

Fig 3.7 Comparison of mixture before/after the DEP filtration. (A) Before DEP separation, host cells were mixed with bacterial cells. (B) After DEP separation, host cells could be successfully recovered from collecting outlet, and effectively removed most of free-floating bacterial cells. Scale bar: 50 μm

3.7.3 Bacteria mixing community testing using lateral DEP device (Sensitivity and Selectivity)

To better evaluate the selectivity of proposed microfluidics device, GFP-*P. aeruginosa* and RFP-*E. coli* were mixed at 1:1, 1:10 and 1:100 mixing ratio to create three mixtures containing bacterial cells with high and low adherence phenotype. Mixture samples were then co-cultured with A549 cells and went through the lateral DEP separation separately. Similar with previous experiment, harvested samples from both outlets were plated on agar plate for CFU analysis **(Fig. 3.8)**. In the case of 1:1 mixing ratio, for upper outlet, both bacterial colonies can be found, and count of *E. coli* single colonies were as similar as that of *P. aeruginosa*; however, for lower outlet, *E. coli* colonies count were 115x less than *P. aeruginosa*. Compared with results from previous isolates testing as well as conventional results (ratio of average attached bacterial per cells can be calculated as 10.3/0.1 = 103x), it was clear that the difference of the adherence characteristics were well preserved during the entire on-chip experiment, and the proposed microfluidics device can successfully distinguish the adherent strains from an equally mixed sample. The samples collected from 1:10 and 1:100 mixture was also analyzed in the similar method, and all the results were summarized in **Table 3.2**.

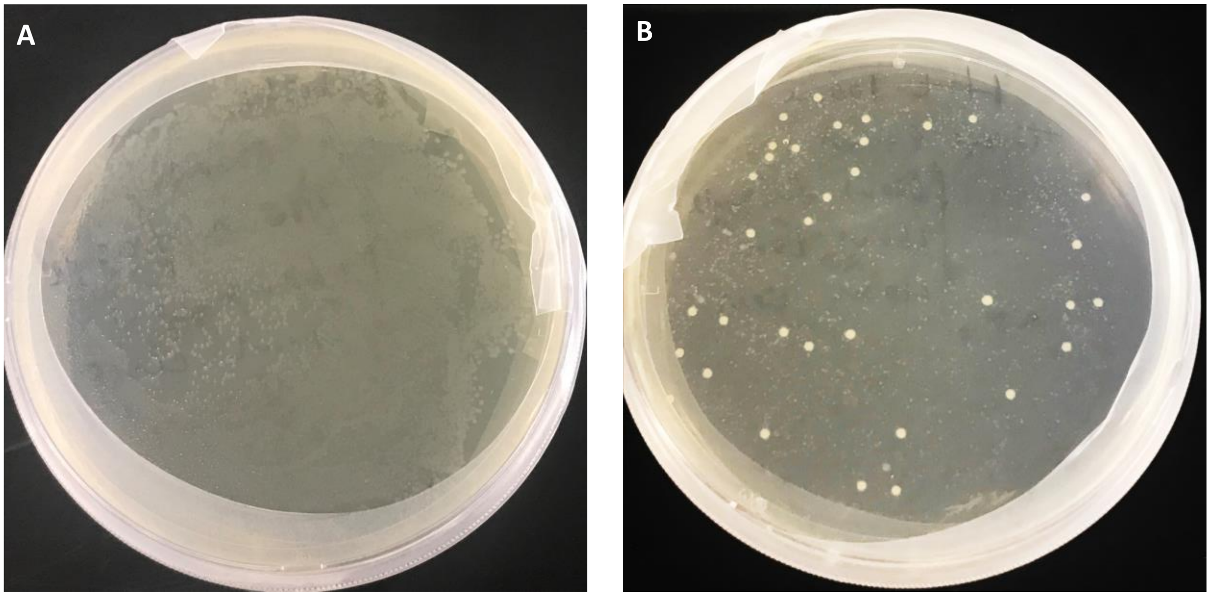

Fig 3.8 Mixture of PAO and *E. coli* at ratio of 1:1 was co-cultured with A549 cells and went through the DEP separation. Samples from both outlets were collected and plated. **(A)** from waste outlet, both bacterial gene were found, and *E. coli* were dominated in plate; **(B)** from collection outlet, *E. coli* (bigger white colonies) count were 115x lower than PAO, indicating difference of the degree of attachment for these two strains.

Table 3.2 Summary of sensitivity and selectivity test results

Mixing Ratio (+/-)	Original Abundancy	Final Abundancy	False Discovery Rate	Biological Noise (*projected*)
1:1	**50%**	**99.1%**	**0.9%**	**1.0%**
1:10	**9.1%**	**92.1%**	**7.9%**	**9.1%**
1:100	**1.0%**	**80.5%**	**19.5%**	**50.0%**

Furthermore, an artificial microbial community from NIST was used to benchmark and evaluate the performance of proposed device. The artificial community contains 30 types of microbes, which covers a wide range of bacterial diversity. Similar with the previous experiment, samples coming out from both outlets were collected and were sequenced to identify the types of the harvested strains. In parallel, isolates of all bacterial strains from this community were separately tested with conventional plate adherence assay to provide benchmark of adherence phenotypes of all tested strains. 16S rRNA sequencing results for all strains were summarized and the counts of reads for each strain at both outlets were cross compared to calculate the relative abundancy distribution after on-chip experiment **(Table 3.3)**. In the table, relative abundancy for each strain was calculated by dividing the count of reads from lower outlet to the sum of counts from both outlets. Higher the relative abundancy was, more percentage of bacterial cells were collected at the lower outlet, indicating a higher adherence phenotype for that specific bacterial strain. All strains were ranked based on their relative abundancy and have exhibited high similarities when benchmarked with conventional plate assay results from each isolate. Among 30 tested strains, 19 strains ended up with sufficient OTU reads that can support the data analysis. Notably, among these 19 strains, microfluidic system identifications of 17 strains were same with single-strain conventional well-plate assay results. Additionally, strain that with as low as 0.0002% original abundancy can be detected and characterized correctly (NIST 0023, *Staphylococcus* *aureus*). Here, comparing with conventional method were a soil sample needs to be isolated and picked colonies going through the well-plate assay for identification, this platform provides a powerful option where all contained soil bacterial strains can be analyzed altogether, in one run, with a fairly decent accuracy.

Table 3.3 Comparison of documented adhesion, identifications from microfluidic chip as well as conventional result. Here, red indicate high adherence phenotype, green indicate low adherence phenotype.

Strain ID	Strain name	Threat Level	Documented adhesins/ adherence	Microfluidics results	Conventional results
NIST0011	*Acinetobacter baylyi*	Low (Friend)	-	-	-
NIST0012	*Corynebacterium amycolatum*	Low (Friend)	-	+	-
NIST0014	*Corynebacterium diptheriae (⊿DT)*	Low (Friend)	+	+	+
NIST0018	*Staphylococcus epidermidis 1457*	Low (Friend)	+	-	Inconclusive
NIST0019	*Enterococcus faecalis OG1RF*	Low (Friend)	+	+	+
NIST0020	*Staphylococcus aureus subsp*	High (Foe)	+	+	+
NIST0023	*Staphylococcus aureus MW2*	High (Foe)	+	+	+
NIST0025	*Acinetobacter baumannii 5075*	Medium (Foe)	+	-	-
NIST0026	*Pseudomonas aeruginosa PA01*	High (Foe)	+	+	+
NIST0027	*Pseudomonas aeruginosa 8890-80*	High (Foe)	+	+	+
NIST0045	*Klebsiella oxytoca*	Low (Friend)	+/-	-	-
NIST0048	*Yersinia pseudotuberculosis*	High (Foe)	+	+	+
NIST0052	*Escherichia coli UPEC*	High (Foe)	+	-	-
NIST0056	*Escherichia coli*	Medium (Foe)	-	-	-
NIST0059	*Escherichia coli EHEC*	High (Foe)	+	-	-
NIST0071	*Serratia rubidaea*	High (Foe)	+	+	-
NIST0073	*Bacillus cereus*	High (Foe)	-	+	+
NIST0092	*Listeria monocytogenes*	High (Foe)	+	+	+

3.8 Current progress on environmental sample tests

To understand the performance and the capability of detecting high adherence bacterial strains from real environmental sample, bacterial mixtures was extracted from soil samples harvested from Oklahoma, Texas and were used as testing samples for proposed microfluidics device. Proposed workflow of this experiment is summarized in **Fig 3.9**.

Up to this point, the soil extraction has been extracted and microfluidic chip separation have been completed. The collected samples are being analyzed with off-chip phenotypic assay as well as WGS analysis to identify the accuracy of on-chip experiment.

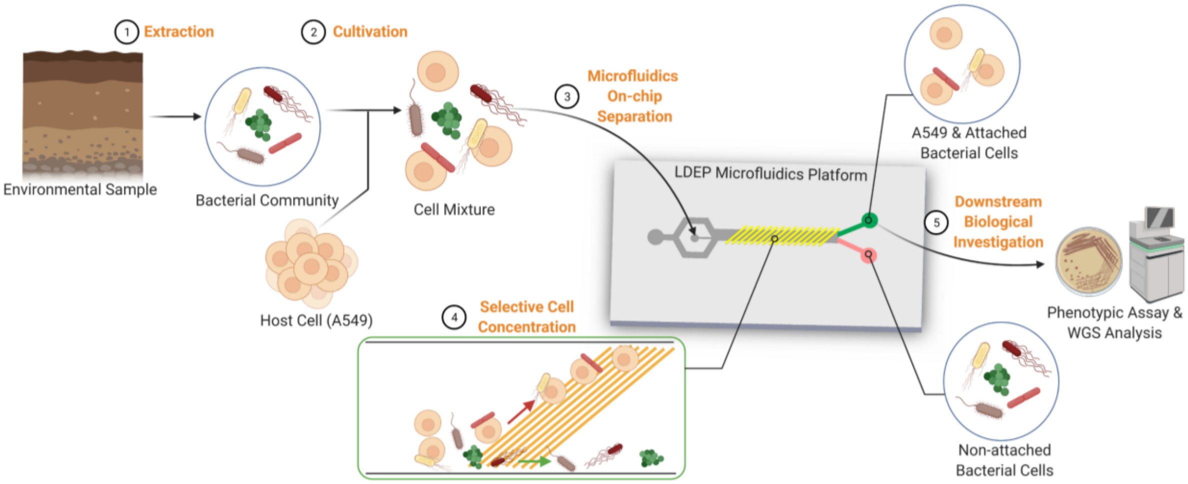

Fig 3.9 Proposed experimental flow on soil sample extraction/identification using lateral DEP separation device.

3.9 Conclusion

Overall, the lateral DEP microfluidics system has been validated for its functionality. Tests with mock communities have shown the system sensitivity of detecting the adherence strains with abundance of as low as 0.0002% in samples, while keeping high fidelity rate on its adherence characterization. The lateral DEP microfluidics system was able to characterize the adherence strains from mix samples with accuracy at 89.5 %, in comparison, conventional methods can only handle isolate colonies one at a time. Using conventional plate methods to test with each isolate could achieve comparable sensitivity and accuracy, but consider the cases such as screening environmental or synthetic microbial libraries, where large number of diverse heterogeneous strains were mixed and convoluted together, characterization on each isolates will be time-consuming and labor intensive. This system, once fully characterized and calibrated, can greatly improve the efficiency on current investigation of environmental emerging pathogen, and help to increase the capacity of health-related surveillance system, covering agriculture, food industry, national security and so on.

4. IN-DROPLET CELL SEPARATION BASED ON BIPOLAR DIELECTROPHORETIC RESPONSE TO FACILITATE CELLULAR DROPLET ASSAYS*

4.1 Overview

Droplet microfluidics have been developed to enable high-throughput biological investigation in the single-cell resolution, and most of the fundemental biological handling steps have been realized in the droplet microfluidic format. Precise manipulation of cells within water-in-oil emulsion droplets has the potential to vastly expand the type of cellular assays that can be conducted in droplet-based microfluidic systems, however, achieving such manipulation remains challenging. Here in this chapter, we present an in-droplet label-free cell separation technology by utilizing different dielectrophoretic responses of two different cell types. Two pairs of angled planar electrodes were utilized to generate positive or negative dielectrophoretic force acting on each cell type, which results in selective in-droplet movement of only one specific cell type at a time. A downstream asymmetric Y-shaped microfluidic junction splits the mother droplet into two daughter droplets, each of which contains only one cell type. The capability of this platform was successfully demonstrated by conducting in-droplet separation from a mixture of *Salmonella enterica* cells and macrophages, two cell types commonly used as a bacterial pathogenicity infection model. This technology can enable the precise manipulation of cells within droplets, which can be exploited as a critical function in implementing broader ranges of droplet microfluidics-based cellular assays, including droplet-based adherence assay, toxicity assay, antibiotic suseptability te[1]st, to name a few.

---

* Reprinted with permission from Han et al., 2020. Copyright 2020, Royal Society of Chemistry.

4.2 Introduction

In recent years, water-in-oil emulsion droplet-based microfluidics systems have demonstrated great potentials for broad ranges of biological assays and investigations. Due to its capability of handling extremely small volume of biological samples and liquid at very high-throughput, droplet-based microfluidics technology has become an ideal and powerful tool in facilitating cellular studies, and so far has been well established and widely utilized in high-throughput, single cell resolution assays, aiming to substitute time-consuming and labor-intensive conventional biotechnology laboratory methods.[61-64] Up until now, in order to transfer the conventional laboratory sample handling practices into a droplet microfluidics format, many different droplet microfluidics functions have been realized, such as cell encapsulation technology for creating isolated nano/pico-liter-scale bioreactors, droplet merging technology for mixing samples and reagents, droplet detection and sorting technology for analyzing assay results and retrieving samples.

Despite the fact that most liquid-handling technologies are now readily available in droplet microfluidics format, it still remains challenging to achieve in-droplet cell separation. There are many different applications that can benefit from in-droplet cell separation capabilities, of which one large application area being studying cellular interaction. For example, in broad ranges of microbiological studies, cellular interaction is one of the key topic area for obtaining insights into cellular mechanisms that drive cell-cell communication,[65] pathogenicity based on host-pathogen interaction,[66-68] immune responses,[69] to name a few. In conventional bulk-scale cellular interaction studies, different types of cells of interest are typically first mixed together and co-cultured for a certain period of time to allow the occurrence of cell-cell interactions, followed by analyzing the result and then ideally separating out the different cell types for further downstream investigation. Many researchers have successfully developed continuous-flow-based microfluidics platforms to achieve microfluidic pathogenicity studies, covering applications in studying cell-cell interactions, cytoadhesion, cytotoxicity, and immunological responses.[70-74] Performing these types of assays in droplet microfluidics platforms is highly desired, especially when large number of diverse heterogeneous cell samples have to be screened and tested, such as screening environmental or synthetic microbial libraries. For example, in host-pathogen adherence assay, in order to determine the degree of pathogenicity caused by microorganisms, bacterial cells are co-incubated with host cells, then free-floating bacterial cells are rinsed off to recover only microbes that adhere to the host cells.[75-77] Failure of effectively separating bacterial cells from host cells will lead to high false-positive rates as the degree of attachment will be misread when non-adherent microbes are remained during post analysis. Another example that requires in-droplet cell separation could be in drug screening applications, where in-droplet cell separation can lead to obtaining only pure cell samples of interest.

Overall, in the context of droplet microfluidics systems, in-droplet content manipulation technologies developed so far have been challenging to achieve selective cell separation and/or targeted content removal from within droplets. Thus, in -droplet cell separation techniques have the potential to further widen the bandwidth of droplet-based microfluidics technologies and extent broader ranges of cellular assays to be implemented in such format.

Several studies have been reported aiming to enable such in-droplet content manipulation technology. Aside from some passive methods,[78-80] active methods of in-droplet particle/cell manipulation require external force to be applied but can also achieve more precise manipulation. Several active manipulation methods have been realized by using magnetic beads,[61-64] acoustophoresis,[81-86] and dielectrophoresis (DEP).[87] Magnetic bead-based manipulation was exploited for target molecule separation such as human serum albumin,[88] mRNA,[89] and prostate-specific antigens in droplets to achieve drug analysis,[90] molecular detection, and immunoassays. However, since labelling step is essential in this method, this cannot be used when tagging cannot be performed at the beginning of the assay, or when the downstream assay is not compatible with magnetic beads. In addition, this extra labelling step limits its compatibility and makes it cumbersome to be implemented.

Acoustophoresis, a label-free particle/cell manipulation technique, has been used for in-droplet particle or cell manipulation. Fornell et al.[81-83] have demonstrated that particles and cells can be focused to the center of a droplet or to both sides of a droplet using first or second harmonic standing acoustic wave generated by bulk acoustic wave (BAW) due to their intrinsic positive acoustic contrast factor compared to carrying media. As all particles or all cells were moved to a particular location within the droplet, in-droplet particle/cell concentration was achieved with relatively high throughput (4 droplets/s) and high focusing efficiency (90%). In a follow-up study, they have further developed this into in-droplet particle separation based on different acoustic contrast factors (polystyrene vs polydimethyl siloxane (PDMS) particles).[84] However, this technology is somewhat limited when separating two different population of cells. Since all cells suspended in regular culture media have positive acoustic contrast factors, applying acoustic manipulation will result in all cells to move towards the same position within a droplet. Thus, these approaches are not suitable for selective manipulation of cells of interest from a cell mixture. Additionally, BAW device fabrication requires the use of hard materials, such as glass or silicon, to achieve acoustic wave propagation with low attenuation. An alternative approach in acoustophoresis is the use of surface acoustic wave (SAW). Park et al. have demonstrated in-droplet particle separation using travelling SAW based on different acoustic radiation force factors depending on the particle size.[85] Additionally, they have further demonstrated in-droplet particle washing by handling both droplets and particles using SAW, simultaneously.[86] However, so far SAW-based in-droplet separation has not been demonstrated with real biological samples such as cells. Thus, the feasibility of separating cells based on their different acoustic properties within droplets remains untested.

Dielectrophoresis (DEP) is an electrical field-based label-free cell manipulation method, which can be readily integrated in a microfluidic format, since only a simple patterned electrode placed on the bottom of a microfluidic channel is needed. Thus, DEP microfluidic technologies have been extensively used in particle and cell manipulation in free-flow microfluidics.[58,91-93] In DEP-based manipulation, cell experiences positive DEP force (pDEP, i.e., attracted to the electrode), negative DEP force (nDEP, i.e., repelled away from the electrode), or neutral response, depending on the frequency applied as well as the dielectric properties of cells and their surrounding media. Previously, we have successfully demonstrated in-droplet particle and cell manipulation using nDEP, where particles/cells could be accumulated to one side of the droplets and thus enriched into one of the daughter droplets.[87] However, in this case, all cells, regardless of the cell types, were concentrated towards the same side of the droplet. Therefore, this design could not be used to specifically manipulate a target cell population from mixing sample, thus in-droplet cell separation based on the cellular properties was not feasible under such setting.

In this chapter, we exploited, for the first time, the differences in DEP responses of different cell types under specific frequencies to achieve precise in-droplet cell separation of two different populations. Here, two sequential DEP electrode arrays were utilized so that one cell type experiences pDEP force and another cell type experiences nDEP force, resulting in the two different cell types to be moved to opposite sides within a given droplet. By splitting the droplet into two daughter droplets after the in-droplet DEP manipulation of cells, the different cell types could be separated into each of the two daughter droplets, respectively. Here, to better elucidate the capability as well as the applications of the proposed DEP-based in-droplet cell separation platform, mammalian host cells and bacterial cells were chosen to be used to mimic a common model system when studying host-pathogen interaction.

4.3. Working principle

Two pairs of planar parallel DEP electrodes were used to generate a high-gradient non-uniform electric field at the edges of the electrodes. The time-averaged $\boldsymbol{x}$-direction DEP force can be described by Equation 1.[94]

$$F_{dx} = 2\pi\varepsilon_m r^3{}_c Re[f_{CM}] \frac{\partial\left|\vec{E}\right|^2}{\partial x} \qquad (1)$$

According to this equation, the DEP force here is determined by ε_m, the permittivity of the surrounding solution, r, the cell radius, $Re[f_{CM}]$ ($f_{CM} = \frac{\varepsilon_c^*(\omega)-\varepsilon_m^*(\omega)}{\varepsilon_c^*(\omega)+2\varepsilon_m^*(\omega)}, \varepsilon^* = \varepsilon - j\frac{\sigma}{\omega}$), real part of the *Clausius-Mossotti* factor, and the applied voltage. Specifically, the DEP force is proportional to the real part of the *Clausius-Mossotti* factor, by which the magnitude of DEP force and DEP polarity are determined.

In this study, mammalian cells (J774A.1 macrophages) and bacterial cells (*Salmonella* Typhimurium) were used as a model system of bacterial cell – mammalian host cell interaction to demonstrate the feasibility of separating two different types of cells from a mixture depending on their different DEP responses inside a droplet. An in-droplet DEP cell separation system consists of a first DEP manipulation region for bacterial cells concentration (**Fig. 4.1**(**a**)), a second DEP manipulation region for mammalian cells concentration (**Fig. 4.1**(**b**)), and a droplet splitter (**Fig. 4.1**(**c**)). In front of the DEP separation units, a flow-focusing design droplet generator was placed to encapsulate bacterial cells and mammalian cells into a droplet (**Fig. 4.2**). Mammalian cell suspension and bacterial cell suspension were injected from two separate inlets, mixed at the first crossing, then went into the flow-focusing structure where droplets containing the cell mixture were generated. All generated droplets were flown through the DEP separation units having two sets of an angled DEP electrode pair placed at the bottom of a microfluidic channel.

Before reaching the DEP separation regions of the microfluidic channel, all cells in droplets have random distribution. As the droplets pass through the first pair of DEP electrodes, the upward-tilted electrodes function as a guiding track as bacterial cells affected by pDEP force are attracted to the electrode gap. Based on this simulation result of the *Clausius-Mossotti* factor (**Fig. 4.3**), by choosing a frequency (3 MHz) where mammalian cells receive no DEP force, only bacterial cells are accumulated to the upper half of the droplet by pDEP force, while leaving the mammalian cells randomly distributed within the droplet (**Fig. 4.1**(**a**)). Then, as the droplets pass through the second pair of DEP electrodes, since the bacterial cells have been already accumulated to the upper half of the droplet, by choosing a frequency (100 kHz) where bacterial cells have no DEP response, the bacterial cells remain within the upper half of the droplet due to the internal circulation flow in each half of the droplet. Meanwhile, mammalian cells experience nDEP force and are pushed away from the downward-tilted electrodes, always staying below the electrodes and thus gradually accumulating to the lower part of the droplet (**Fig. 4.1**(**b**)). Once the droplet reaches the asymmetric droplet splitting region, the mother droplet is split into two daughter droplets, where bacterial cells that remain in the upper half splits into a bacterial cell-only droplet, while mammalian cells that remain in the lower part of the droplet splits into a mammalian cell-only droplet (**Fig. 4.1**(**c**)).

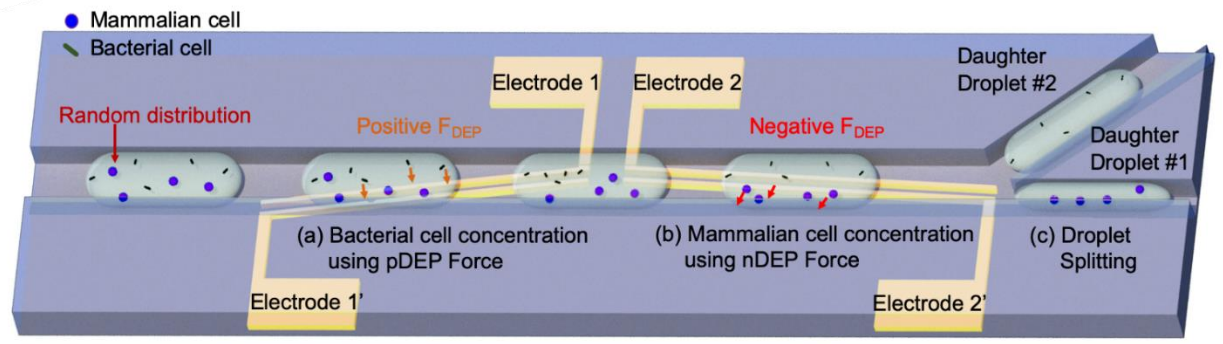

Fig. 4.1 Schematic illustration of the in-droplet cell separation platform composed of: (a) A first DEP electrode pair that tilts upwards for bacterial cell manipulation using pDEP force, resulting in accumulation of all bacterial cells to the upper part of the droplet; (b) A second downward-tilted DEP electrode pair for mammalian cell manipulation using nDEP force, resulting in concentration of all mammalian cells to the lower half of the droplet, while bacterial cells are unaffected and thus remain circulating within the upper half of the droplet by the internal circulation flow; (c) An asymmetric droplet splitter that divides the mother droplet into two daughter droplets, the upper split droplet (daughter droplet #1) containing only bacterial cells and the lower split droplet (daughter droplet #2) containing only mammalian cells. Reprinted with permission from Han et al., 2020. Copyright 2020, Royal Society of Chemistry.

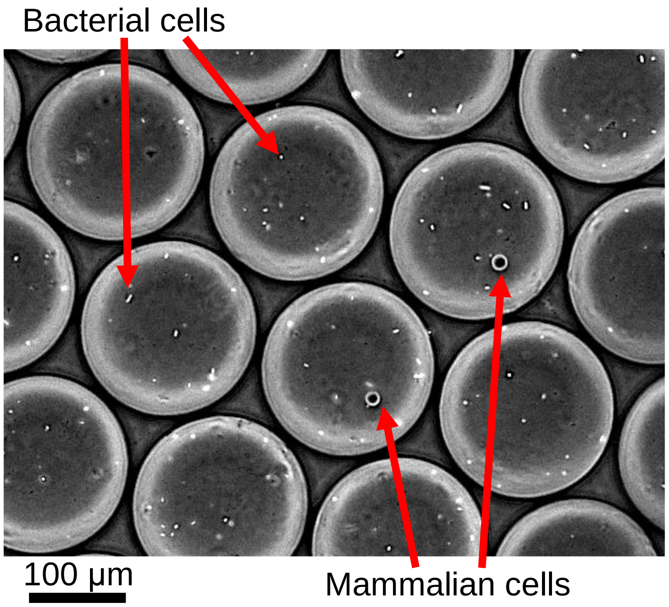

Fig. 4.2. Generated droplets containing bacterial cells and mammalian cells. Reprinted with permission from Han et al., 2020. Copyright 2020, Royal Society of Chemistry.

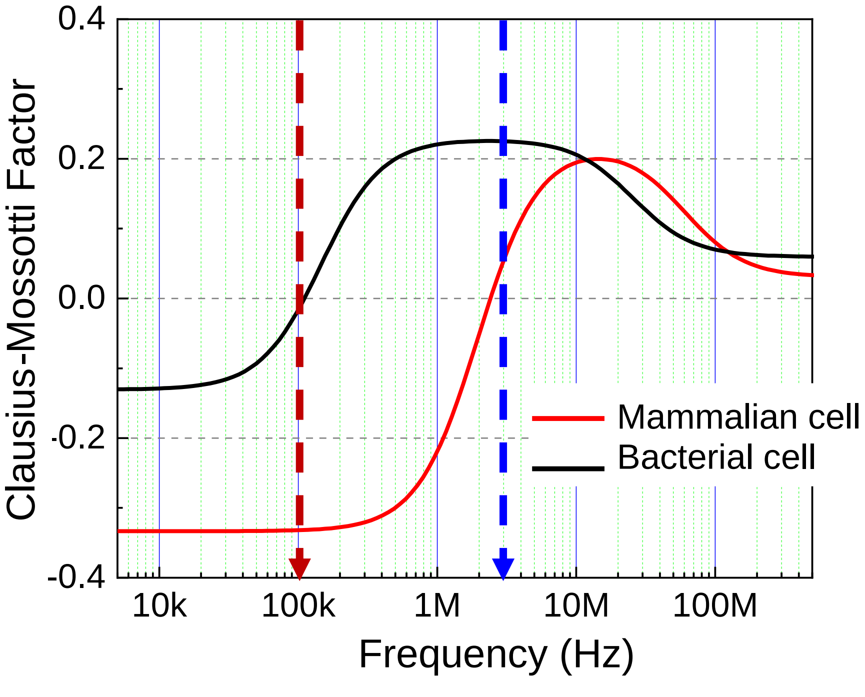

Fig. 4.3. Calculated real part of the *Clausius-Mossotti* factor ($Re[f_{CM}]$) of a mammalian cell and a bacterial cell, where the medium conductivity is set to 0.032 S/m. The diameter of the mammalian cell and the bacterial cell were set to 10 and 2 μm, respectively. The membrane capacitance and cytoplasm permittivity/conductivity used for this calculation are summarized in the table below.[95,96] Reprinted with permission from Han et al., 2020. Copyright 2020, Royal Society of Chemistry.

Table 4.1 Parameters used in initial CM factor calculation. Reprinted with permission from Han et al., 2020. Copyright 2020, Royal Society of Chemistry.

	Mammalian cell	**Bacterial cell**
Membrane capacitance (F/m^2)	1.8	1.4
Cytoplasm conductivity (S/m)	0.3	0.22
Cytoplasm permittivity (F/m)	$76\varepsilon_0$	$108\varepsilon_0$

4.4 Device design and fabrication

4.4.1 Device design

Microfluidic channels here were 200 µm wide and 26 µm high. For each electrode pair, the electrodes were parallel to each other, and tilted 0.05° with respect to the microfluidic channel. The width of each electrode was 15 µm and the gap between the electrodes was 10 µm. The first pair of DEP electrodes was tilted upwards, starting at the bottom side of the channel, to the point at the upper side where a 20 µm wide spacing was left without electrode coverage on the microfluidic channel. The second pair of electrodes starts 200 µm behind the first electrode pair with a downward tilt. At the splitting region, the widths of the upper and lower microfluidic channels were 130 µm and 70 µm, respectively.

4.4.2 Microfabrication

Cr/Au (200/1000 Å) layers were deposited by E-beam evaporation on 0.7 mm thickness of borosilicate glass substrates (Swiftglass, Co., Inc., NY). After photolithography patterning with AZ 5214 photoresist (AZ Electronic Material plc, NJ), the metal layers were etched. Finally, the photoresist was removed in AZ 400T stripper at 95°C for 5 min. The patterned master molds for PDMS replication were fabricated by SU-8™ photoresist (Microchem, Inc., MA) using conventional photolithography processes. A 26 µm height master mold was obtained by spin-coating SU-8™ 2025 at a speed of 2800 rpm, and was then coated with Tridecafluoro-1,1,2,2-Tetrahydrooctyl-1-Trichlorosilan (United Chemical Technologies, Inc., Bristol PA) to facilitate PDMS replication. Microfluidic channels were fabricated with PDMS (10:1 mixture, Sylgard 184, Dow Corning, Inc., MI) using conventional soft lithography techniques. PDMS and borosilicate substrates with Au patterning were aligned under a microscope using deionized water (DI water) as a lubricant layer and bonded right after 90 seconds of oxygen plasma treatment. The aligned device was placed on a hotplate at 95 °C for overnight baking to completely remove any vapor residues. Right before the experiment, the microfluidic channel was rinsed with precious metal surfactant (Aculon Inc., CA, USA), baked, followed by rinsing with filtered fresh Aquapel (Pittsburgh Glass Works, LLC., PA) to ensure the hydrophobicity of the microchannel.

4.4.3. In-droplet cell separation operation

The droplet microfluidic system was characterized using *Salmonella* cell suspension, macrophage suspension, and macrophage/*Salmonella* cell mixture, respectively. The total flow rate was varied from 27, 33 to 39 µl/h to find the optimal operating condition. For every test condition, the flow rate of carrier oil (Novec 7500, 2.5% Pico-Surf surfactant, 3200278, Dolomite, USA) was adjusted depending on the cell solution flow rate so that droplets having a diameter of 130 µm could be consistently generated. For *Salmonella*, the first DEP electrode pair signal was set to 3 MHz, 9, 12, and 15 V_{pp}, while the second DEP electrode pair signal was set to a constant 100 kHz, 8 V_{pp}. For macrophage, a constant sinusoidal signal of 3 MHz, 15 V_{pp} was applied to the first DEP electrode pair, and 100 kHz, 6, 7 and 8 V_{pp} signals were applied to the second DEP electrode pair. For the mixed cell experiment, droplets were generated using the flow-focusing structure at a speed of 30 µl/h for the carrier oil and 3 µl/h for the cell solution, and then pushed by 33 µl/h of carrier oil into the DEP cell manipulation/separation region.

4.5 Biological material and methods

4.5.1 Preparation of conductivity media

Low conductivity media was prepared in order to have greater relative displacement of cells within droplets. 0.3 mM of monopotassium phosphate (1551139, Sigma-Aldrich, USA), 0.85 mM of dibasic potassium phosphate (1151128, Sigma-Aldrich, USA), and 280 mM of myo-Inositol (I5125, Sigma-Aldrich, USA) were added into DI water to make the base media.[58,87] Potassium chloride (2.5 mM, P9333, Sigma-Aldrich, USA) was added into this base media to achieve a conductivity of 0.032 S/m.

4.5.2 Cell preparation

J774A.1 (ATCC TIB67) macrophage were thawed and grown in T75 culture flasks with Dulbecco's Modified Eagle Media (DMEM, D5648, Sigma-Aldrich, USA) containing 10% Fetal Bovine Serum (FBS, 16000044, Thermo Fisher Scientific, USA) in a 37°C, 5% CO_2 incubator. Prior to the experiment, cell culture media was removed, and macrophages were rinsed with low conductivity media by three times. Cell were then detached by cell scrapping, and the cell concentration was adjusted to 1.25×10^6 cells/ml, which results in about three macrophages encapsulated into each droplet (size: 130 µm diameter, volume: 1.15 nL). *Salmonella* Typhimurium (strain ATCC 14028S) engineered with a GFP plasmid (pCM 18) was inoculated on a trypticase soy agar plate containing 50 µg/ml erythromycin, followed by incubation at 37°C overnight. The next day, single colonies were picked and cultured in LB 50 µg/ml erythromycin broth in a shacking incubator at 37 °C for 8 h. The bacteria culture was centrifuged and rinsed with low conductivity media by three times before the experiment. For the initial in-droplet *Salmonella* manipulation experiment, the concentration of *Salmonella* culture was adjusted to an OD of 1.0 and then further diluted by 50 times to have around 20 *Salmonella* cells per microdroplet. For the final macrophage-*Salmonella* mixed sample separation experiment, the concentration of macrophages was diluted to 4.2×10^5 cells/ml, and the *Salmonella* culture with OD of 1.0 was diluted by 100 times to obtain around one macrophage and 10 *Salmonella* cells encapsulated in each droplet.

4.5.3 Cell viability assay

Cell viability for *Salmonella* cells was evaluated by calculating the percentage of dead cells in the population. SYTO 9 dye (ex/em 485/530 nm) was used to stain viable cells, while nonviable cells were stained with propidium iodide (PI) (ex/em 485/630 nm) (live/dead baclight bacterial viability kit, L7012, Invitrogen), both staining solutions were mixed 1:1 ratio before use. After droplet splitting, the daughter droplet #1 were collected from the lower side outlet and resuspended in 1 ml PBS solution. 6 µl of combined reagent mixture was added, followed by incubation for 15 min at room temperature. The fluorescence microscopic (Zeiss AXIO Observer 7) images, which were acquired before/after in-droplet cell separation experiment, were used for cell viability analysis. In the case of macrophages, Evans blue dye (E2129, Sigma Aldrich), which only stains nonviable cells, was used for cell viability evaluation. The daughter droplet #1 were collected from the lower side outlet and suspended in PBS solution. The collected cells were resuspended with 1 ml of 1% (w/v) stock solution of Evans blue and incubated for 5 min at room temperature. The sample was loaded into a hemocytometer and cell viability was measured using an inverted microscope.

4.5.4 Statistical analysis of separation efficiency

To analyze the separation efficiency, a high-speed camera (Phantom micro lab100, Vision Research, Inc.) was used to capture the trajectory of cell migration (60 frames per second (fps) for *Salmonella*, 200 fps for macrophage). The camera was set to image at the droplet splitting region, and cells within each daughter droplet were counted frame by frame before/after the droplet splitting to calculate the separation efficiency. For each case, approximately 100 images were analyzed. Additional statistic microscopic (Zeiss AXIO Observer 7) pictures of daughter droplets were obtained at downstream collection chambers for the purpose of verification.

4.6 Results

4.6.1 Characterization of in-droplet bacterial cell manipulation

Droplets containing only *Salmonella* cells were generated at a concentration of approximately 20 cells per droplet, and all *Salmonella* cells in the droplet show random

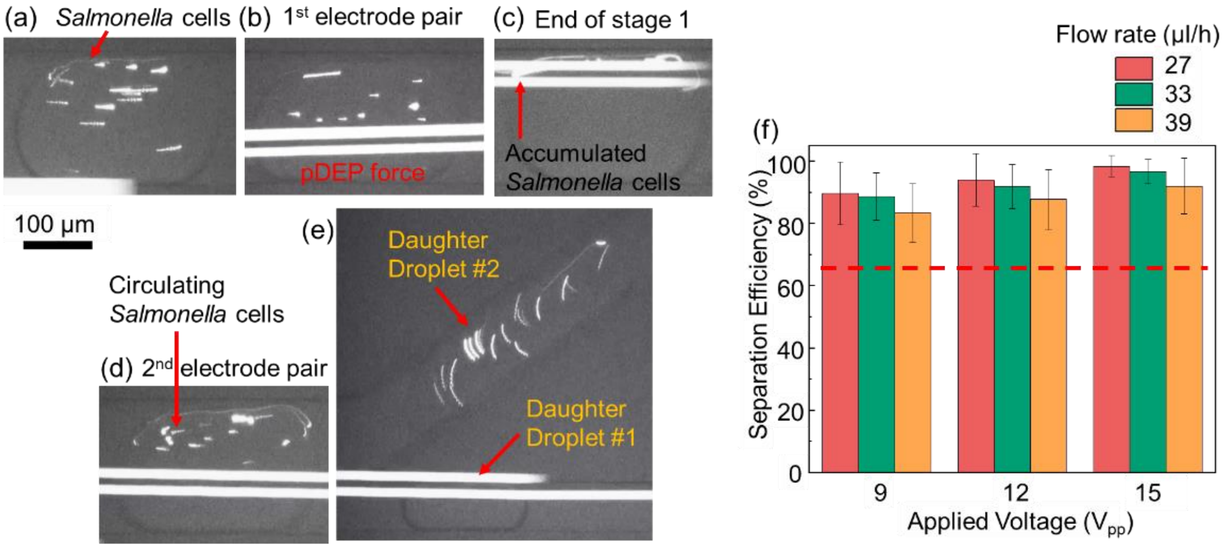

Fig. 4.4 Movement of *Salmonella* cells within a droplet as the droplet travels through the electrodes. (a) A droplet containing 17 *Salmonella* cells was generated and randomly distributed within the droplet. (b-c) As the droplet passes through the first DEP electrode pair, *Salmonella* cells were attracted to the angled electrodes due to pDEP force once they were close to the electrode, accumulating at the upper half of the droplet. (d) Even though *Salmonella* cells were not affected by any DEP force while passing through the second DEP electrode pair, they remain within the upper half of the droplet by the internal circulation flow. (e) The droplet was split into two daughter droplets, with the upper daughter droplet containing all the *Salmonella* cells. (f) *Salmonella* cell separation efficiencies into daughter droplet #2 at different flow rates and voltages tested. Flow rates were set to be 27, 33 and 39 µl/h, each with three applied voltages varying from 9, 12, to 15 V_{pp}. At 27 µl/h and 15 V_{pp}, the *Salmonella* cell separation efficiency reached 98%. Reprinted with permission from Han et al., 2020. Copyright 2020, Royal Society of Chemistry.

distribution (**Fig. 4.4**(**a**)). The droplets flow through the DEP cell separation region of the platform at a flow rate of 33 µl/h. As the droplets containing *Salmonella* cells travel through the first pair of DEP electrodes (3 MHz, 15 V peak-to-peak (V_{pp})), the *Salmonella* cells that came close to the tilted electrodes experienced pDEP force, resulting in attraction towards the electrodes (**Fig. 4.4**(**b**)). Since this electrode starts from the bottom side of the droplet, *Salmonella* cells circulating in the lower part of the droplet can be gradually moved to the upper part of the droplet by accumulating along the upward-tilted electrode. At the end of the first DEP electrode pair, all *Salmonella* cells were confined to the upper side of the droplet (**Fig. 4.4**(**c**)). As the droplet travelled through the second pair of DEP electrodes

(100 kHz, 8 V_{pp}), the accumulated *Salmonella* cells were released from the electrodes since bacterial cells experience no DEP force at this frequency. However, the *Salmonella* cells remained circulating within the upper half of the droplet due to the internal circulation of flow within the upper half of the droplet (**Fig. 4.4**(**d**)). When reaching the droplet splitting region, these accumulated *Salmonella* cells were split into the daughter droplet #2 (**Fig. 4.4**(**e**)). Comparison of the daughter droplets collected in the downstream chambers shows the successful concentration of *Salmonella* cells into the upper chamber (**Fig. 4.5**(**a**)). In this analysis, *Salmonella* cells, separated into daughter droplet #1 and #2, respectively, were manually counted under GFP filter condition (ex/em 495/519 nm), and then used to calculate the separation efficiency.

Next, further device characterization was conducted under three different DEP voltages applied (9, 12 and 15 V_{pp}) and at three different flow rates (27 µl/h = 1.2 droplets/s, 33 µl/h = 1.5 droplets/s, and 39 µl/h = 1.8 droplets/s) while keeping the droplet size the same. As expected, higher voltage and lower flow rate separate cells more efficiently, thus providing a higher separation efficiency (**Fig. 4.4**(**f**)). The optimal operation condition was found to be at 27 µl/h at 15 V_{pp}, and the maximum separation efficiency for *Salmonella* cells could reach 98±3%. However, even at 33 µl/h, the separation efficiency was still relatively high (97±4%), while the overall system throughput could be increased by 20%. The separation efficiency dropped to 92±9% at 39 µl/h. Thus, considering the overall trade-off, the flow rate of 33 µl/h and applied voltage of 15 V_{pp} was selected to be the ideal condition for the remainder of the experiments.

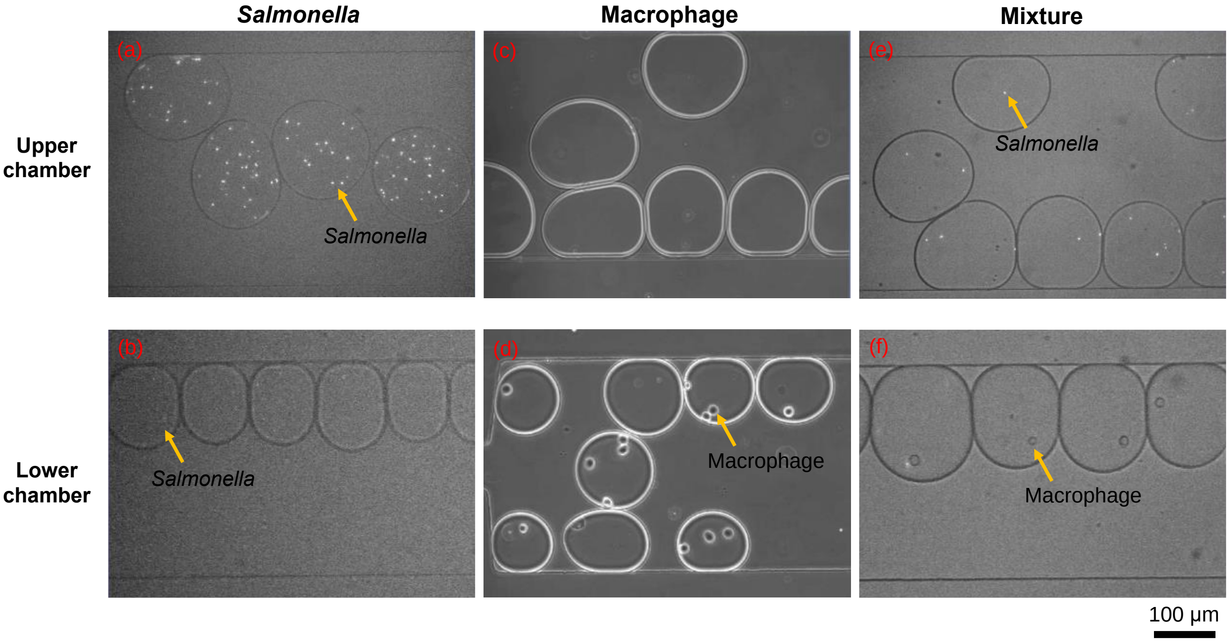

Fig. 4.5 Split daughter droplets collected into two downstream collection chambers, where daughter droplet #1 were collected in the lower collection chamber and daughter droplet #2 were collected in the upper collection chamber. (a-b) After in-droplet *Salmonella* cell manipulation, most *Salmonella* cells were separated into the daughter droplet #2, which were collected in the upper chamber. The daughter droplet #1, collected in the lower chamber, contained almost no *Salmonella* cells. (c-d) In the case of macrophage only, most macrophages were concentrated into the daughter droplet #1, which were collected in the lower chamber. The daughter droplet #2, collected in the upper chamber, were all empty. (e-f) In the case of mixture of *Salmonella* cells and macrophages, daughter droplet #2 collected in the upper chamber contained most of the *Salmonella* cells, while daughter droplet #1 collected in the lower chamber contained most of the macrophages. Reprinted with permission from Han et al., 2020. Copyright 2020, Royal Society of Chemistry.

4.6.2 Characterization of in-droplet mammalian cell manipulation

The number of macrophages encapsulated per droplet was around 4 as in most bacterial infection models the number of bacterial cells typically outnumber that of mammalian host cells. All conditions used here such as the DEP frequency and amplitude of voltage, as well as flow rate, were identical to those used for the in-droplet *Salmonella* cell manipulation characterization steps. Before the droplets reached the first pair of DEP electrodes, all macrophages were randomly distributed within the droplet (**Fig. 4.6**(**a**)). When passing through the first electrode pair, macrophages received no DEP force (**Fig.**

4.6(**b**)) and remain randomly distributed (**Fig. 4.6**(**c**)). As they pass through the second pair of DEP electrodes, macrophages experienced nDEP force and were repelled away from the electrode, therefore gradually confined below the electrode and into the lower half of the droplet (**Fig. 4.6**(**d**)). After droplet splitting, all macrophages were separated into the daughter droplet #1, while no macrophages were seen in the daughter droplet #2 (**Fig. 4.6**(**e**)). Comparison of the daughter droplets collected in the downstream chambers shows the successful concentration of macrophages into the lower chamber (**Fig. 4.5**(**d**)). The separation efficiency was analyzed using bright filed microscopy images.

Further device characterization was conducted under three different DEP voltages (6, 7 and 8 V_{pp}) and three different flow rates (total flow rate: 27, 33, and 39 µl/h). In the case of macrophages (**Fig. 4.6**(**f**)), the overall separation efficiency increased as the flow

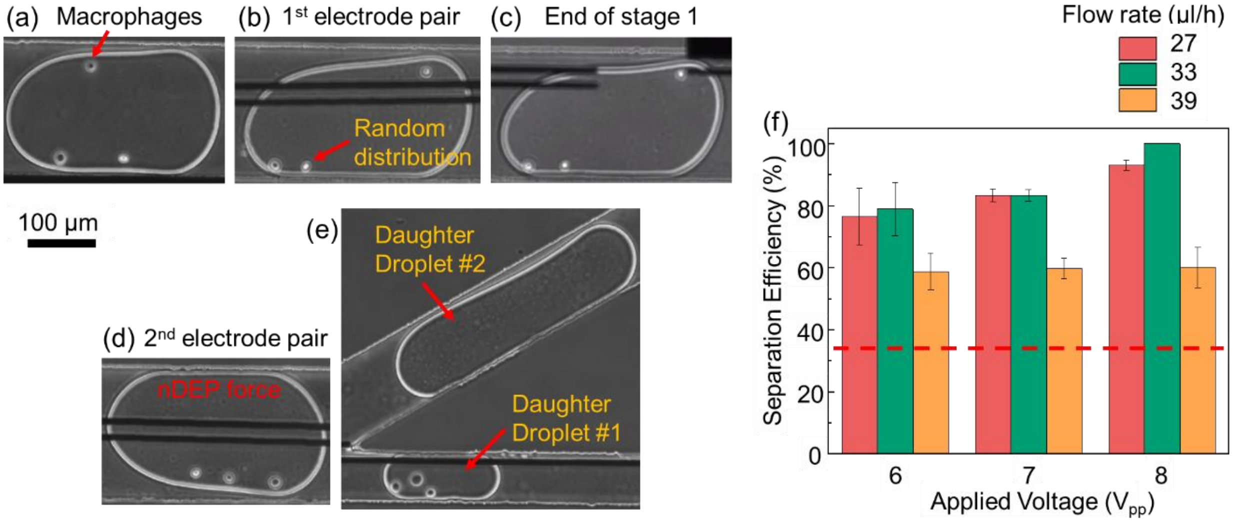

Fig. 4.6 Movement of macrophages within a droplet as the droplet travels through the DEP electrodes. (a) A droplet containing three macrophages is shown, randomly distributed. (b-c) The macrophages are not affected by the DEP force and remain randomly distributed while passing through the first DEP electrode pair. (d) As the droplet passed through the second DEP electrode pair, macrophages were repelled away from the electrode edges, resulting in all macrophages to be pushed towards the lower side of the droplet. (e) The droplet was split into two daughter droplets, with the lower daughter droplet containing all three macrophages. (f) Macrophage separation efficiencies into daughter droplet #1 at different flow rates and voltages tested. Flow rate was set to be 27, 33 and 39 µl/h, each with three applied voltages varying from 6, 7, to 8 V_{pp}. At 33 µl/h and 8 V_{pp}, the macrophage separation efficiency was 100%. Reprinted with permission from Han et al., 2020. Copyright 2020, Royal Society of Chemistry.

rate decreased or when the applied voltage increased. Even though the separation efficiency at the flow rate of 33 µl/h was somewhat higher than that at 27 µl/h, the separation efficiency with standard deviation was comparable to each other under the same applied voltage condition. When 8 V_{pp} was applied, the separation efficiencies at flow rates of 27 and 33 µl/h were 93±8% and 100%, respectively, demonstrating very efficient macrophage manipulation. However, a higher flow rate (39 µl/h) caused increase of the internal circulation flow force, thus the separation efficiency was about 60±7% among all voltage conditions tested, indicating that an even stronger DEP voltage is required to achieve sufficient force for in-droplet cell manipulation. Overall, by varying the voltage as well as the flow rate, an optimal condition was found to be at an applied voltage of 8 V_{pp} and at a flow rate of 33 µl/h.

4.6.3 In-droplet cell separation of cell mixture

To characterize the in-droplet separation efficiency between macrophage and *Salmonella*, a mixture of *Salmonella* cells and macrophages was encapsulated into droplets. After droplet generation containing this cell mixture (*Salmonella* cells vs. macrophage = 10 to 1 ratio), a macrophage and *Salmonella* cells can be seen randomly distributed within the droplets (**Fig. 4.7**(**a**)). As the droplets traveled through the first pair of DEP electrodes, *Salmonella* cells receiving pDEP force were attracted towards the electrode and accumulated along the tilted electrode, gradually moving to the upper half of the droplet, while the macrophage experiencing no DEP force remained randomly distributed (**Fig. 4.7**

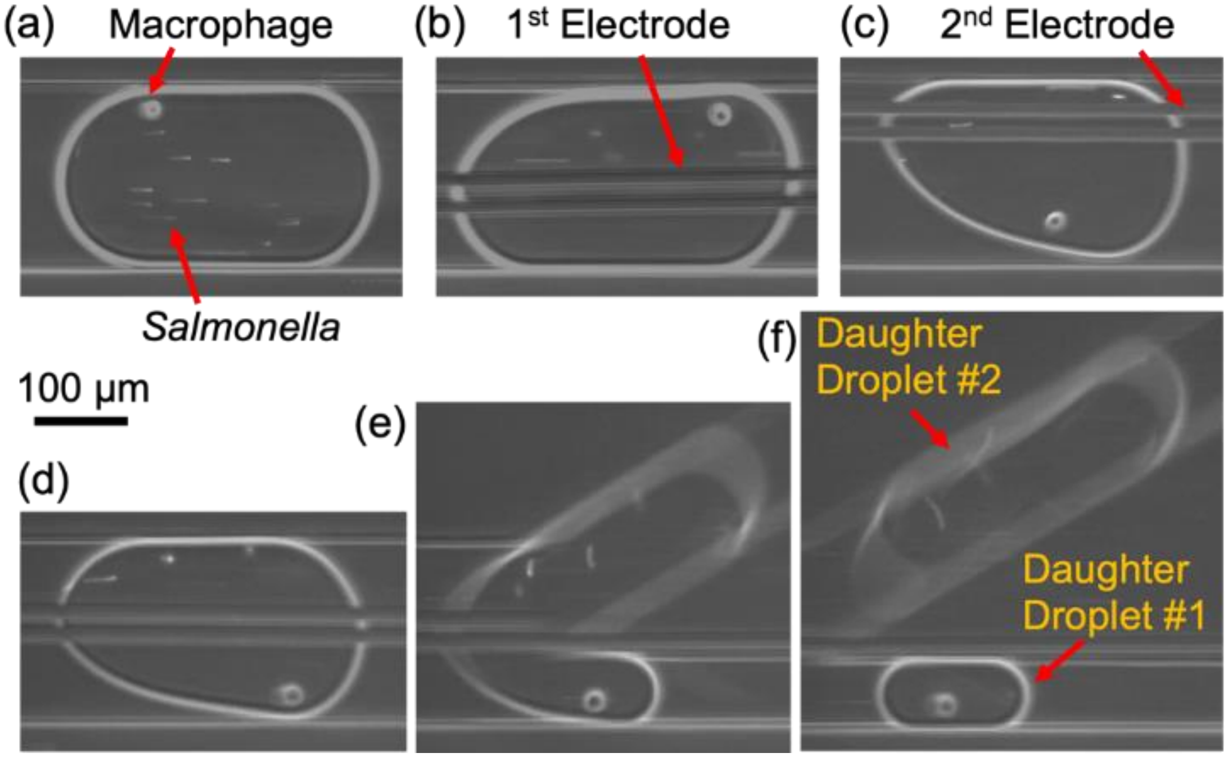

Fig. 4.7 Movement of *Salmonella* cells and a macrophage inside a droplet. The operation conditions were set to 100 kHz, 8 V_{pp} at the first DEP electrode pair and 3 MHz, 15 V_{pp} at the second DEP electrode pair. Flow rate was 33 µl/h. (a) Initially all cells are seen randomly distributed within the droplet. (b) *Salmonella* cells were attracted to the DEP electrodes that are tilted upwards due to the pDEP force, and eventually accumulated to the upper half of the droplet as the droplet reached the end of the first DEP electrode pair. (c-d) The macrophage experiencing nDEP force gradually migrated towards the bottom side of the droplet as the downward-tilted electrode position became lower within the droplet. Most *Salmonella* cells still remained within the upper half of the droplet due to the internal circulation flow. (e-f) After droplet splitting, the daughter droplet #2 contained most of the *Salmonella* cells, while the daughter droplet #1 contained the macrophage and few *Salmonella* cells that were not completely separated. Reprinted with permission from Han et al., 2020. Copyright 2020, Royal Society of Chemistry.

(**b**)). As the droplets traveled through the second pair of DEP electrodes, the cluster of *Salmonella* cells were released but remained circulating within the upper half of the droplet driven by the internal circulation flow force, while the macrophages receiving nDEP force gradually migrated to the lower portion of the droplet (**Fig. 4.7** (**c-d**)). At the droplet splitting region, majority of the *Salmonella* cells were separated into the daughter droplet #2, while the macrophages were separated into the daughter droplet #1 (**Fig. 4.7**(**e-f**)). When comparing the resulting daughter droplets, most of the host cells were successfully collected in the lower chamber, while most of the bacterial cells were successfully collected in the upper chamber, proving that the developed separation method can indeed be used in such cell mixture applications (**Fig. 4.6**(**e-f**)). Under the DEP voltage of 15 V_{pp} / 8 V_{pp} and flow rate of 33 µl/h, 74±8% of macrophages were successfully separated into the daughter droplet #1 (lower droplets), while 84±5% of *Salmonella* cells were successfully separated into the daughter droplet #2 (upper droplets).

4.7 Simulation analysis and comparison

4.7.1 Electric field simulation

The sorting efficiency is sensitive to the channel height due to the planar DEP electrode layout. Only cells that are close to the bottom side of the droplet are relatively close to the DEP electrode and will experience the maximum DEP force, which suggests that the channel height has to be carefully determined to ensure that the generated electric field can have good coverage over the entire z-axis of the microfluidic channel. The x-directional electric field across the cell manipulation microchannel was simulated under different channel height conditions (**Fig. 4.8**). The average electric field intensity at the ceiling of the channel was 2.6, 2.2, and 1.8 ($\times 10^5$ V/m) where the channel height was 22, 26, and 30 µm, respectively. With only 4 µm difference in channel height, the electric field intensity drops by about 20% under the same voltage condition, which can decrease the separation efficiency. To minimize the impact stemming from the channel height, mirrored DEP electrode pairs could be potentially patterned on the ceiling side of the channel, creating a top-bottom electrode design. **Fig. 4.8d** shows the electric field distribution in the case of a top-bottom electrode pair design so that the applied electric field can be intensified and be more uniform throughout the z-direction of the microfluidic channel.

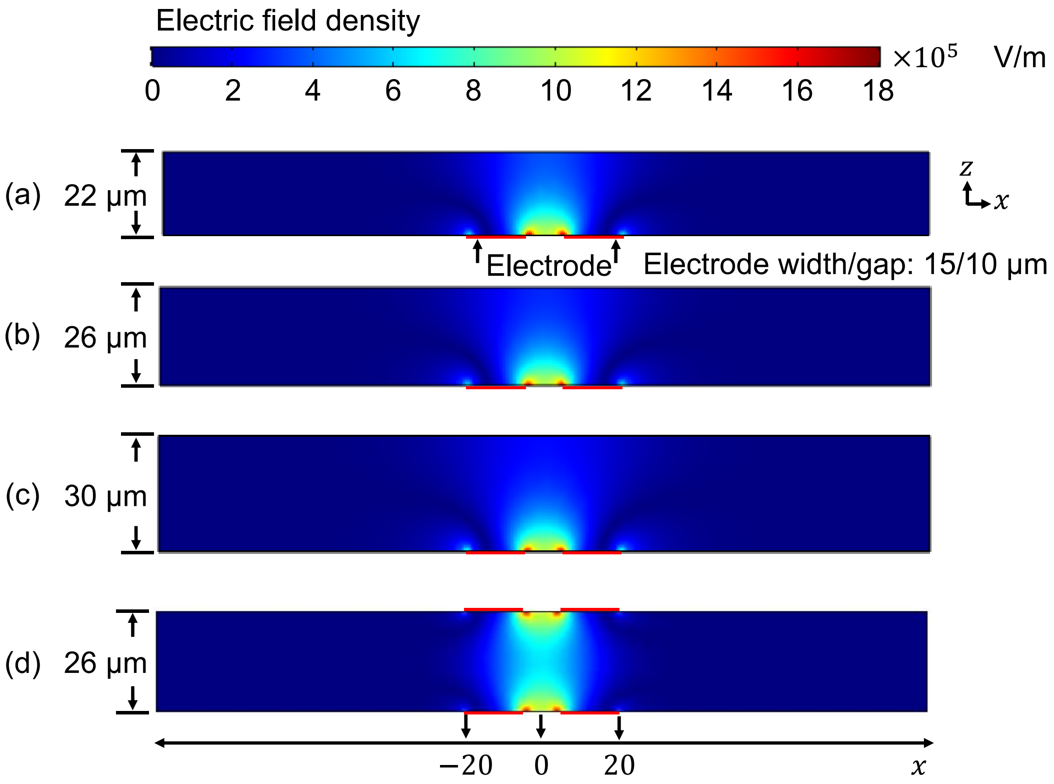

Fig. 4.8. COMSOL simulation results showing the x-directional electric field intensity (V/m) across the cell separation microchannel (COMSOL Multiphysics® 5.5). Carrier oil layer covers the electrode and the entire channel wall.[87] Cross sectional view where two electrodes have symmetric position in the cell separation microchannel, where the channel height is (a) 22, (b) 26, and (c) 30 μm, are shown. The applied voltage was set to 15 $V_{pp.}$ The electric field intensity at the edge of the electrode is strongest at about 18×10^5 V/m. Due to the planar electrode structure, the electric field intensity gradually decreases along the z-axis. With only 4 μm difference in channel height, the average electric field intensity at the ceiling of the microchannel ($-20 < x < 20$ μm) decrease about 20% as the height increase, meaning that the separation efficiency will be reduced by the weaker DEP force. (d) In the case of a top-bottom electrode design, having a 26 μm channel height, the electric field intensity is quite uniform along the z-axis, and also overall stronger compared to the planar electrode design. Thus, the top-bottom electrode design can reduce the effect of channel height on the separation efficiency. The parameters used in this simulation are summarized in the table below. Reprinted with permission from Han et al., 2020. Copyright 2020, Royal Society of Chemistry.

Table 4.2 Parameters used in COMSOL electric field simulation. Reprinted with permission from Han et al., 2020. Copyright 2020, Royal Society of Chemistry.

	Electrode	**Carrier oil layer**	**Suspending media**
Electrical conductivity (S/m)	4.1×10^{7}	2.5×10^{-15}	0.03
Relative permittivity	1	1.9	78

4.7.2 Calculation of Stokes drag force

First, to determine the types of the circulation flow that are presented inside droplets, the capillary number, Ca, is calculated by: $Ca = \mu_c v/\gamma$, where μ_c is the viscosity of the carrier oil (1.24 mPa·s), v is the droplet velocity (2 mm/s at 33 µl/h flow rate), and γ is the interfacial tension (3.5 ± 0.1) mN/m.[80] Thus, respective fluid constant, Ca, is calculated as 0.7×10^{-3} in this case, indicating that all particles and cells should exhibit random distribution along internal circulation flow within a droplet.[80,97] COMSOL simulation (COMSOL Multiphysics® 5.5) of internal circulation flow field, which can be used for the Stokes drag force calculation, was performed at the conditions of proposed channel geometry (width 200 µm, height 26 µm) and optimized flow rate (33 µl/h) (**Fig. 4.9**). Due to the fact that circulation flow in a droplet is axisymmetric, here we simplify all simulations in x-y plan (where z is 13 µm). Based on the result of COMSOL simulation, the Stokes drag force acting on cells is calculated by: $F_D = 6\pi\mu_f r v$, here μ_f is the viscosity of suspending media (0.89 mPa·s), r is the cell radius, v represent the simulated average circulation speed (0.73 mm/s) with respect to droplet at each point inside a droplet.[97]

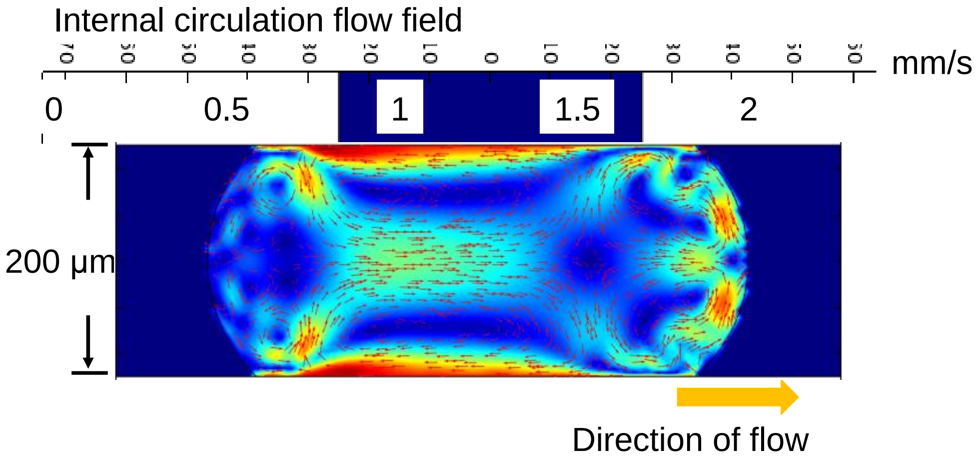

Fig. 4.9. COMSOL simulation (COMSOL Multiphysics® 5.5) of internal circulation flow field at 33 µl/h flow rate. Reprinted with permission from Han et al., 2020. Copyright 2020, Royal Society of Chemistry.

4.7.3 Calculation of dielectrophoretic (DEP) force

A non-uniform electric field, E, generated by a pair of tilted electrodes was simulated at the operation conditions of voltage and frequency (COMSOL Multiphysics® 5.5) used for each cell type manipulation (**Fig. 4.8b**). The x-directional DEP force, F_{dx}, is calculated by:[58,87,91,92]

$$F_{dx} = 2\pi\varepsilon_m r^{3}{}_{c} Re[f_{CM}]\frac{\partial\left|\vec{E}\right|^2}{\partial x}$$

Here x-directional is perpendicular to the edge of electrode, ε_m is the permittivity of the solution, r is the cell radius, $Re[f_{CM}]$ is the real part of the Clausius-Mossotti factor, and E is the x-directional root mean square magnitude of the electric field. According to **Fig. 4.3**, the $Re[f_{CM}]$ of bacteria cell is 0.22 at 3 MHz, while the $Re[f_{CM}]$ of mammalian cell is -0.33 at 100 kHz. Fig. 4.10 shows the simulated x-directional DEP force acting on cells when z is set as 13 µm (middle z plane of channel).

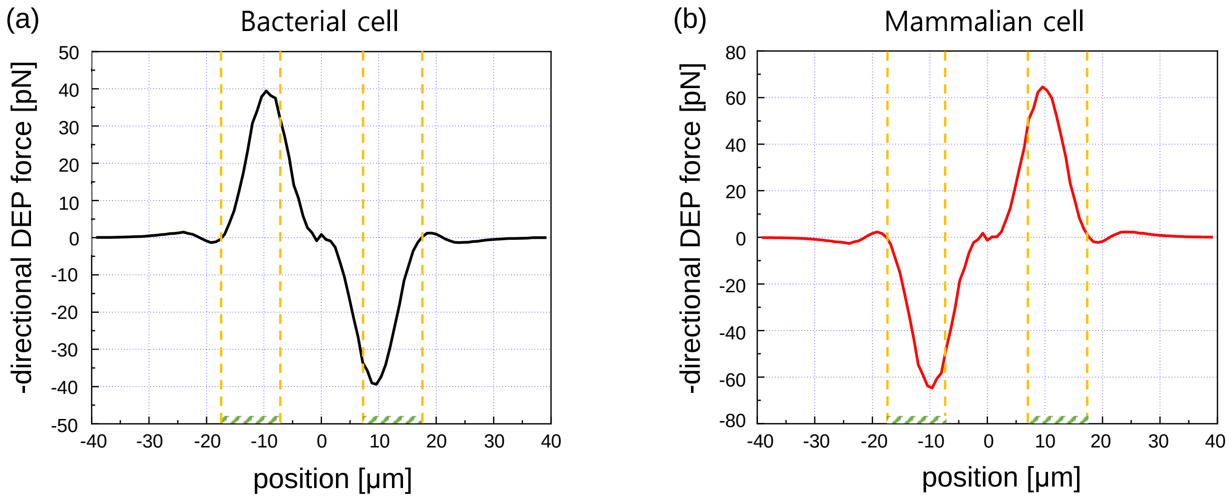

Fig. 4.10. Calculated x-directional DEP force acting on (a) bacterial cell and (b) mammalian cell based on the simulation result of x-directional electric field. The green color hatched bar on the x-axis represents an electrode element. Reprinted with permission from Han et al., 2020. Copyright 2020, Royal Society of Chemistry.

4.7.4 DEP force calculation and comparison

In order to compare the forces acting on in-droplet bacterial and mammalian cells while a droplet passing through the cell concentration regions, COMSOL simulations (COMSOL Multiphysics® 5.5) of internal circulation flow field as well as electric field were performed. The flow inside a droplet (seen in the middle x-y plane) shows uniform axisymmetric circulation pattern (**Fig. 4.9**). In addition, the capillary number, Ca, is 0.7×10^{-3} under the given conditions used here, indicates that cells within a droplet would exhibit random distribution,[80] which is coherent to our observation. The Stokes drag force was calculated based on average inertial circulation flow velocity obtained by the COMSOL simulation results. The x-directional DEP force for each cell type was calculated at the middle z plane (z = 13 μm) based on the simulation result of a non-uniform electric field. Based on this calculation, the DEP force on bacterial cells (**Fig. 4.10**(**a**)) increases as bacterial cells become closer towards the edge of the electrode. Compared to the received

Stokes drag force (12 pN), the pDEP force acting on bacterial cells can be as high as 39 pN when bacterial cells are right above the electrodes; therefore, pDEP force under this circumstance is high enough to overcome the Stokes drag force, enabling pDEP-based bacterial cell manipulation within a droplet. Similarly, the nDEP force (65 pN) acting on mammalian cell was greater than the Stokes drag force (61 pN), therefore can effectively repel cells from the electrodes. Additionally, we calculated that the Stokes drag force acting on mammalian cells reaches to 83 pN when the internal circulation flow field was simulated at total flow rate of 45 µl/h, which is larger than the calculated nDEP force for mammalian cell. Therefore, the Stokes drag force will dominate the trajectory of mammalian cells, where the DEP force in this case can no longer effectively manipulate the mammalian cells. These simulation and calculation results are indeed comparable to the experimental cell separation results under the three different flow rates (27, 33, and 39 µl/h), and may also explain the significant drop of mammalian cell separation efficiency that we observed at flow rate of 39 µl/h. Overall, these simulation and calculation can be utilized to select appropriate voltage, flow rate and channel dimension when applying the presented technology to other applications of interest.

4.8 Conclusion and Discussion

The developed in-droplet cell separation system enables the manipulation and separation of two different cell types within a droplet by utilizing their different DEP responses at different applied DEP frequencies. The proposed in-droplet cell manipulation platform was characterized using a bacterial-host cell interaction model with macrophage (representing mammalian host cell) and *Salmonella* cell (representing pathogenic bacterial cell). When encapsulated individually within droplets, macrophages and *Salmonella* cells were separated into daughter droplets #1 and #2 at 100% and 98% efficiency, respectively. However, when the two cell types were mixed, 74% of macrophages and 84% of *Salmonella* cells were successfully collected into the corresponding daughter droplets. This drop in separation efficiency is due to the fact that as macrophages move from the top portion of the droplet to the lower portion of the droplet, it was observed that these macrophages physically knock out some *Salmonella* cells accumulated along the DEP electrode, as well as some of these *Salmonella* cells hider the clean movement of macrophages to the lower part of the droplet.

Compared to our previous work of DEP-based in-droplet cell concentration,[87] there are several advancements, both from technological perspective as well as from application perspective. In continuous-flow microfluidics, cell separation using a single DEP electrode (either pDEP or nDEP) is possible since cells can be selectively trapped or separated based on their flow trajectory differences. This is not possible in droplet format due to the internal circulation flow, thus the use of a single DEP electrode and single polarity DEP force as shown previously[87] cannot achieve in-droplet separation. In this work, both pDEP and nDEP were utilized using an up-sloped and down-sloped electrodes to manipulate each cell type in a sequential manner, overcoming the complications streaming from the internal recirculation flow. From application perspective, this novel design resulted in the first demonstration of in-droplet cell separation, whereas our prior work demonstrated in-droplet cell concentration, essentially a centrifugation step in droplet format. Other technologies, such as BAW or SAW, have demonstrated in-droplet cell manipulation, but no cell separation. There are many biological applications where in-droplet cell separation is needed, such as for host-pathogen interaction studies or drug screening applications.

Overall, the new droplet application demonstrated here can benefit broad ranges of biological studies and enable more applications to be realized in droplet-based microfluidics platform.

In general, low conductivity media is used in order to manipulate particles or cells in DEP-based microfluidic systems. Since the magnitude of DEP force is proportional to the difference of dielectric properties between a cell and the surrounding solution, very weak DEP force is generated if cells are suspended in a normal culture media or Phosphate Buffered Saline (PBS) due to their similar dielectric properties with cells. To ensure that the use of low-conductivity medium do not affect the viability as well as functionality of cells, off-chip verification experiments were conducted using PBS as control. The result showed that more than 85% of the cells were viable over four hours of culture, which is in line with many other previous reports on DEP-based microfluidic system.[58,87,91,92] Considering that generally 1 to 3 h are required for most cell-cell interaction assays depending on multiplicity of infection (MOI),[98,99] we concluded that the use of low-conductivity media does not pose a great challenge to the viability of cells during the entire assay. In addition, we have conducted a cellular pathogenicity assay (adherence of bacterial cells to host cells) with cells in low-conductivity medium, and no differences were observed. Nevertheless, the fact that low conductivity solution is essentially needed in this DEP-based cell manipulation method is indeed a limitation in DEP-based cell manipulation applications.

After droplet splitting, the daughter droplets were collected and employed to examine cell viability (further details are described in the Experimental section). In-droplet *Salmonella* cells concentration was carried out under the conditions of 33 µl/h at 15 V_{pp}, and the collected daughter droplets #2 were used for the viability test with live/dead staining. The result showed that 93±0.5% of the cells after DEP manipulation were viable, compared to 94±2% viability before DEP manipulation. Next, the viability of macrophages was analyzed after in-droplet macrophage manipulation under the conditions of 33 µl/h at 8 V_{pp}. The daughter droplets #1 were collected and the viability was conducted with Evans blue staining. Compared to 95±1% viability before DEP manipulation, 90±3% of the cells were viable after DEP manipulation. Thus, it is clearly demonstrated that the cell viability was not drastically influenced by the applied voltage and the DEP force.

The maximum voltage generated by a conventional low-cost function generator is up to 20 V_{pp}, so to apply a higher voltage that may be required for some applications, a voltage amplifier may be necessary. For example, in the case of bacterial cell separation as shown here, their size is relatively small compared to mammalian cells, requiring a higher voltage applied compared to only mammalian cell manipulation. An alternative method is to use 3D electrodes[100] embedded in the bottom substrate that can generate stronger electric field than that generated by the planar electrode under the same voltage condition, allowing the use a generic low-cost function generator.

The overall system throughput achieved so far in this work is 2 droplets per second. Increasing the flow rate to increase the throughput is a possibility, however, this leads to stronger internal circulation flow force (as we discussed above), meaning that a higher DEP voltage is required to achieve a similar separation efficiency. Considering the potential functional damage that higher voltage may bring to the more susceptible mammalian host cells, such approach is less preferred from biological perspective, but might be useful when handling more robust cells (such as bacterial cells). Alternatively, if a higher throughput is needed, a multi-channel parallel approach can readily achieve higher system-level throughput.

For further applications, DEP based separation is typically not possible when the *Clausius-Mossotti* factors of the two cells of interest are close to each other. However, cell size is also a main factor affecting DEP force. Thus, if the size of the two cell types are different enough, a well-optimized voltage condition should be able to manipulate only one target cell type with DEP force, which can then be separated from the mixture using a subsequent droplet splitting structure. Since there is no DEP force acting on undesired cells, they will be randomly distributed in the droplet and thus not fully discarded even after separation. In this case, removal efficiency is decided by the ratio of the width of Y-shaped splitting channels. In the device shown here, the width of each splitting channel is 130 and 70 µm, respectively, so ideally 65% of undesired cells where no DEP force is exerted on can still be removed. In such a scenario, the lower channel width can be adjusted depending on the application to maximize the separation efficiency.

Since DEP-based systems can be readily integrated into most microfluidic devices, the use of DEP for in-droplet cell manipulation opens up large number of possible applications where this system can be integrated into. These include integrating impedance and optical analysis systems for in-droplet cell counting and hit discrimination, electric field-based or pneumatic-based droplet sorting systems, and droplet merging systems for realization of droplet solution exchange, which is to perform more systematic assays on a single chip, to name a few. The droplet solution exchange system development will be further explained in the following chapter.

5. CELL WASHING AND SOLUTION EXCHANGE IN DROPLET MICROFLUIDIC SYSTEMS*

5.1 Overview

Following the discussion in Chapter 4, water-in-oil emulsion droplet microfluidic systems have been extensively developed, and currently almost all cell handling steps can be conducted in this format. An exception is the cell washing and solution exchange step, which is commonly utilized in many conventional cell assays. This chapter presents an in-droplet cell washing and solution exchange technology that utilizes dielectrophoretic (DEP) force to move all cells to one side of a droplet, followed by asymmetrically splitting the droplet to obtain a small daughter droplet that contains all or most of the cells, and then finally merges this cell-concentrated droplet with a new droplet that contains the desired solution. These sequential droplet manipulation steps were integrated into a single platform, where up to 88% of the original solution in the droplet could be exchanged with the new solution while keeping cell loss to less than 5%. Two application examples were demonstrated using the developed technology. In the first example, green microalga *Chlamydomonas reinhardtii* cells were manipulated using negative DEP force to exchange the regular culture medium to a nitrogen-limited medium to induce lipid production. In the second example, *Salmonella enterica* cells were manipulated using positive DEP force to replace fluorescent dye that models fluorescent cell stains that contribute to high background noise in fluorescence-based droplet content detection to fresh buffer solution, significantly improving the droplet content detection sensitivity. Since the cell washing step is one of the most frequently utilized steps in many cell biology assays, we expect

---

* Reprinted with permission from Huang et al., 2021. Copyright 2021, American Chemical Society

the developed technology can significantly broaden the type of assays that can be conducted in droplet microfluidics format.

5.2 Introduction

Droplet microfluidics technologies have been extensively developed in the past decade, including various functions, [48,49,101,102] as well as many different cell biology assays.[58,103] In conventional cell biology assays, solution exchange is an extremely commonly utilized step for multiple purposes, such as to adjust cell concentrations, wash cells, exchange solutions in which cells are suspended, and remove cell debris, to name a few. These steps are typically performed using centrifugation to pelletize the suspended cells, remove most of the solution through a pipetting step, and resuspend the pelletized cells in a new solution. However, achieving solution exchange in a droplet-based microfluidics system remains very challenging. Adding or removing solution to a droplet can be easily conducted by merging a droplet with the target droplet containing the desired solution or splitting the droplet, respectively. However, simply splitting a droplet to remove unwanted solution also results in significant loss of droplet content, in this case cells. A better strategy for in-droplet solution exchange is by mimicking the conventional centrifugation step, namely to concentrate all cells within the droplet to one side of the droplet before removing the unwanted solution by droplet splitting, followed by merging the split droplet that contains most of the cells with a new droplet that contains the desired solution. These three steps are essentially same as the centrifugation-based cell washing and solution exchange. Here, the key to achieving successful in-droplet solution exchange function is to remove the unwanted solution from the existing droplet as much as possible while keeping most of the desired in-droplet cellular contents, as well as to add the new desired solution at precise quantity, all in a highly efficient manner.

There are now a few developed technologies that can achieve in-droplet solution exchange. One method is to use bulk acoustophoresis, which has been demonstrated to conduct solution exchange using polystyrene beads and cells.[45,104] However, bulk acoustophoretic cell manipulation utilizes acoustic wave to generate acoustophoretic force acting on cells, and therefore requires the use of hard materials (e.g., silicon or glass) that can support acoustic wave propagation with minimum loss, as well as precise control of the microchannel dimensions that determine the acoustic resonance frequency. These requirements significantly reduce the number of applications in which this method can be utilized. Importantly, cells are focused either to the center of the droplet or to both sides of the droplet regardless of the frequency applied, resulting in low solution exchange efficiency or high cell loss. The use of magnetic cell manipulation is another method that has been utilized to achieve in-droplet solution exchange.[105] However, this method requires the target cells to be labeled with magnetic beads, therefore limiting its applicability or sometimes not even possible to do so if cells are already inside droplets.

Here, we developed an in-droplet cell washing and solution exchange microfluidic platform that combines a high-accuracy dielectrophoretic (DEP)-based cell concentration function, an asynchronous droplet splitting function, and a high-efficiency droplet cleaving/pairing/merging function. The DEP-based in-droplet cell concentration technique can concentrate all cells to one side of the droplet, and thus by splitting the droplet into two daughter droplets, one daughter droplet can contain all (or most) of the cells while the other daughter droplet contains most of the original solution.[50,87] This enables removing the unwanted solution without any cell loss (or minimum loss). Here, both negative DEP (nDEP) and positive DEP (pDEP) force can be utilized so that broad ranges of cell types can be manipulated within droplets. Another advantage of using DEP-based cell manipulation is its non-invasive and label-free nature, which allows the entire solution exchange steps to be conducted without any cell labeling step. Following the droplet splitting step, the split daughter droplet containing most of the cells can cleave a continuous-phase fresh solution flow to generate a pair of droplets (the daughter droplet with all/most cells and a newly cleaved droplet with the new solution). Such droplet cleaving and merging method can automatically synchronize the paired droplets, therefore enabling a high-efficiency (>99%) droplet merging step, as demonstrated previously.[106] The presented cell washing and solution exchange platform, which was enabled by integrating these two techniques, can be readily integrated into most droplet microfluidics systems to significantly broaden the type of cell assays that can be conducted in droplet microfluidics format.

To demonstrate the utility of this in-droplet cell washing and solution exchange platform, we selected two application examples. The first example is for microbial library screening applications,[47] where typically cells are first encapsulated in droplets at single-cell resolution and cultured to expand them into clonal populations, followed by downstream characterizations that often require (or can benefit from) exchanging the solution in which the cells are originally suspended in. We picked the example of microalgae growth and lipid production assay since several droplet microfluidics assays for this application have been previously developed. [58,107,108] Here, we first cultured the droplet-encapsulated microalgae in a regular culture medium, followed by exchanging the culture medium to a nitrogen-limited medium to induce lipid production in the microalgae to allow lipid productivity of cells to be measured. The second example we selected is cell staining and detection applications, where in-droplet fluorescent cell staining is desired, but where such staining solutions typically have high fluorescent background noise that impedes droplet content detection and analyses. Here, reducing the high optical background noise coming from the cell staining fluorescent dye when conducting droplet detection and sorting[109-111] can lead to significant improvement in in-droplet cell analyses efficiencies. Such cell washing steps after fluorescent cell staining is commonly utilized in conventional cell staining assays, where the staining solutions are typically removed through a centrifugation step before imaging/analyzing the cells. Overall, achieving the cell washing and solution exchange functions in droplet format can enable many sophisticated cellular assays to be performed in droplet microfluidics format.

5.3 Microfluidic system design

5.3.1 Device design and operating principle

The design of first part of solution exchange platform is based on the previous in-droplet cell separation design. In the DEP-based in-droplet cell concentration unit, one pair of tilted planar electrodes is aligned and placed below the droplet microfluidic channel. The electrode pair is tilted upward (2.5° angle), starting from the lower side of the microchannel towards the upper side of the microchannel. The end of the electrode aligns to the vertex of the downstream Y-junction asymmetric droplet splitting region. A sinusoidal signal with a specific frequency is applied to generate either nDEP or pDEP force acting on cells, determined depending on the dielectric properties of cells and the surrounding solution. When cells experience nDEP force, cells are repelled away from the electrodes, therefore are gradually concentrated towards the upper side of the droplet. When cells experience pDEP force, cells are attracted to the electrodes, which results in concentration of all the cells to the electrode surface. In either case, all or most of the cells in the moving droplet are gradually concentrated to the upper side of the droplet along the tilted electrode regardless of the DEP polarity. Splitting this droplet results in all or most of the cells moving into the upper daughter droplet, while the unwanted solution is split into the other daughter droplet. Here, the asymmetric droplet splitting ratio[112] determines how much of the original solution will be removed from the cell-containing upper daughter droplet. Next, the daughter droplet containing all or most of the concentrated cells is flown into a continuous-phase flow stream that contains the desired target solution. Cleaving this flow stream will generate a droplet that is automatically paired with the cleaving droplet. The paired two droplets (the cell-concentrated daughter droplet and the cleaved new solution droplet) are then further guided through a straight channel so that the two droplets can become in close contact before entering the droplet merging region. Finally, the paired droplets are merged under an electric field generated by a NaCl saltwater electrode, resulting in the final droplet that contain all or most of the cells from the original droplet but now suspended in the new solution. This entire process is illustrated in **Fig. 5.1A**.

The optimal frequency to achieve in-droplet DEP-based cell manipulations can be determined by the dielectric properties of cells and their surrounding solution within the droplet. The time-averaged x-directional DEP force received by a cell can be expressed as:

$$F_{dx} = 2\pi\varepsilon_m r^3 Re[f_{CM}]\frac{\partial\left|\vec{E}\right|^2}{\partial x}$$

Here, the conductivity of the surrounding solution, ε_m, the radius of cells, r, the electric field, *E*, as well as the real part of Clausius-Mossotti (CM) factor, Re$[f_{CM}]$, can affect the polarity and the magnitude of the DEP force acting on cells.[94] The CM factor in relation to the applied voltage frequencies can be calculated based on the dielectric properties of cells (**Fig. 5.2, Table 5.1**). In our demonstrating applications, to maximize the magnitude of DEP force acting on the target cells, 200 kHz was chosen to generate an nDEP force on *Chlamydomonas reinhardtii* (*C. reinhardtii*) cells, and 3 MHz was selected for manipulating *Salmonella enterica* (*S. enterica*) cells with pDEP force.

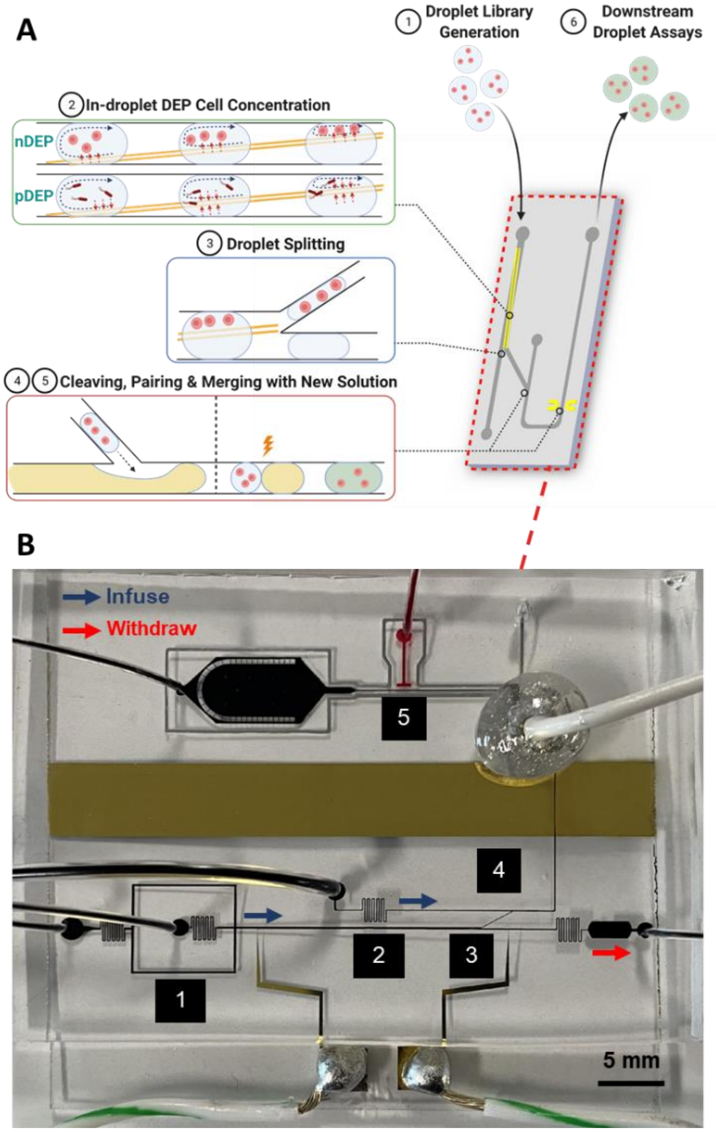

Fig. 5.1. (A) Working principle of the integrated droplet solution exchange platform and (B) photographic image of the fabricated device. Number marking in the device shown in B corresponds to number marking in A. Reprinted with permission from Huang et al., 2021. Copyright 2021, American Chemical Society.

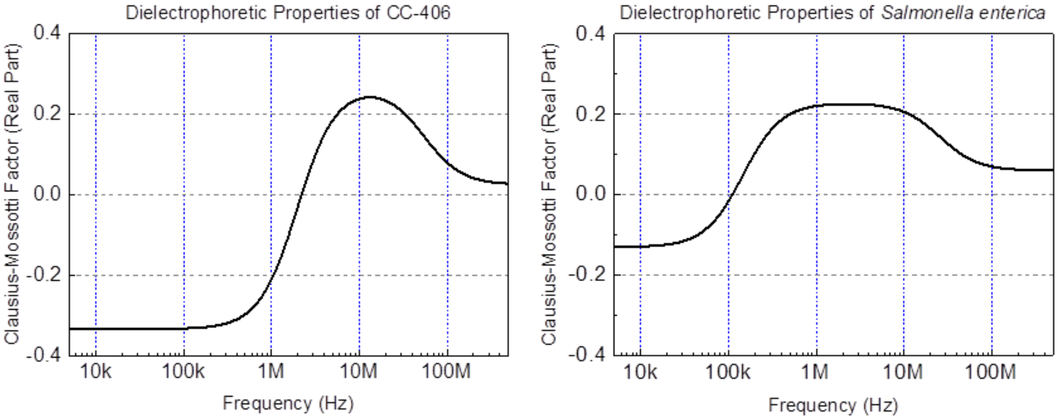

Fig. 5.2. Calculated real part of the polarization coefficient (Re$[f_{CM}]$) of *C. reinhardtii* cells suspended in TAP media as well as *S. enterica* cells in R2A media. The membrane capacitance and cytoplasm permittivity/conductivity used for this calculation are summarized in Table 5.1 below. Reprinted with permission from Huang et al., 2021. Copyright 2021, American Chemical Society.

Table 5.1. Summary of the dielectric properties of cells used in the CM factor simulation. Reprinted with permission from Huang et al., 2021. Copyright 2021, American Chemical Society.

	C. reinhardtii	***S. enterica***
Membrane capacitance (mF/m^2)	1.24	1.4
Cytoplasm conductivity (S/m)	0.5	0.22
Cytoplasm permittivity (F/m)	$70\varepsilon_0$	$108\varepsilon_0$

5.3.2 Device fabrication

The device was fabricated by conventional soft lithography and metal patterning processes. [95,113,114] The angled electrode pair was prepared by conventional microfabrication techniques, including Cr/Au (20 nm/ 100 nm) deposition on the glass substrate, patterning of an etch mask using AZ1518 photoresist (AZ Electronic Materials, USA), selective metal etching of the Cr and

Au layers, followed by etch mask removal using AZ400T (AZ Electronic Materials, USA). SU-8^{TM} 2025 photoresist (Microchem, USA) was used to fabricate a 25/40 µm thick double-layer SU-8 master mold for the soft lithography process. Liquid-phase polydimehtyl siloxane (PDMS, Sylgard 184 Dow Corning, MI, USA, mixed at a ratio of 10:1 base and curing agent) was poured onto the SU-8 master mold and cured for 30 min at 85°C, and then released from the master mold.[115,116] Then, the PDMS layer was bonded to the 0.7 mm thick borosilicate glass substrate on which the electrodes were patterned using O_2 plasma treatment. In this step, after oxygen plasma treatment of both the electrode-patterned glass substrate and the PDMS microchannel layer, they were aligned and bonded together at 85°C for 24 hr. Before the experiment, the Cr/Au electrode surface was treated with Precise Metal Surfactant (Aculon Inc., CA, USA), baked dry, followed by rinsing with filtered fresh Aquapel (Pittsburgh Glass Works, LLC., PA), to make the entire microchannel surface hydrophobic.

5.3.3 Experimental setup for evaluating the droplet cleaving, pairing, and merging functions

The top split daughter droplets flow into a continuous aqueous flow, which is the desired new solution, at an angle of 45°. This causes the carrier oil of the first droplet train to physically cleave the aqueous stream and create a new droplet from this aqueous solution. Since the carrier oil surrounding the first droplet is what cleaves this aqueous flow, these two droplets (droplet that cleaves the aqueous solution and the newly generated droplet) are automatically paired one-to-one at extremely high efficiency.[106] The widths of the droplet reflow channel and the continuous aqueous phase flow channels were 50 µm and 100 µm, respectively, with the height of both channels being 25 µm. The original droplets with a diameter of 130 µm were generated and collected first using a separate droplet generator and were then reflown with spacer oil (Novec

7500, 2.5% Pico-Surf surfactant, Dolomite, USA) to cleave the aqueous stream. The flow rates of these three streams (droplet reflow, marked as "1" from **Fig. 5.4A;** oil spacing, marked as "1" from **Fig. 5.4A;** and continuous aqueous infusion, marked as "3" from **Fig. 5.4A**) were set to be 10 µl/h, 60 µl/h, and 7 µl/h, respectively. Additionally, to increase the stability of the droplet operation, a withdrawal function from a syringe pump was applied to the lower right outlet (see red arrow in **Fig. 5.1B**) after droplet splitting, at a flow rate of 50 µl/h. The overall throughput of this function can be adjusted readily by proportionally adjusting the flow rates. Syringe pumps (Fusion 400, Chemyx Inc.) were used to control the volumetric flow rates of all input streams. Images and videos were captured through a microscope using a CMOS camera (C11440, Hamamatsu). For the droplet merging part, a NaCl (1 M) liquid electrode pair was utilized to provide a stable electrical field.[117] A function generator (DG4102, Rigol) and a high-voltage power amplifier (Model 2210-CE, TREK) were used to apply an electrical field for droplet merging. In most cases, a square wave with a 300 V peak-to-peak (V_{pp}) signal at 10 kHz was used for generating this droplet merging electric field.

5.4 Cells and reagent preparation for the two cell biology assays

For the first application, *C. reinhardtii* strain CC-406 cells were cultured in Tris-acetate-phosphate (TAP) media at 22°C under continuous illumination (60 µmol photons$\cdot$m$^{-2}\cdot$s^{-1}). Cells were collected during the exponential growth phase and centrifuged, then resuspended in fresh TAP media to adjust the cell concentration to $3\text{x}10^6$ cells/ml before droplet encapsulation. The conductivity of culture media was measured to be 0.1 S/m, and this measured conductivity was used when simulating the DEP response of CC-406 cells. For the second application, *S. enterica* cells were inoculated from a single colony and cultured in Lysogeny Broth (LB) media with 50 μg/ml erythromycin at 37 °C for 8 h. The bacteria culture was centrifuged and rinsed with Reasoner's 2A (R2A) medium (0.08 S/m). The concentration of *S. enterica* culture was adjusted to 4x10^7 cells/ml and mixed with FITC-dextran (1 μM, Sigma-Aldrich, 53379) to simulate fluorescent cell staining dye before droplet generation.

5.5 Experiment setup

5.5.1 Application demonstration using nDEP force for microalga *C. reinhardtii* culture solution exchange

The unicellular microalga *C. reinhardtii* (strain CC-406), which is known to accumulate lipid under stressed conditions such as nutrient deprivation (e.g., nitrogen), was used to demonstrate the utility of the developed in-droplet cell washing and solution exchange microfluidic system using nDEP force manipulation. In this case, the starting droplets contained on average four microalgal cells suspended in normal TAP medium. The continuous phase flow, which is the new solution, was nitrogen-depleted TAP (TAP-N) medium. Both the starting droplets and the solution-exchanged droplets were incubated in the culture chamber of the microfluidic device at 22°C under continuous light illumination (60 μmol photons$\cdot$m$^{-2}\cdot$s^{-1}) for 3 days. On each day, droplets were imaged (Zeiss AXIO Observer 7) to count the average number of cells per droplet. Additionally, cells were harvested from the droplets and stained with a lipid-staining fluorescent dye (4,4-Difluoro-1,3,5,7,8-Pentamethyl-4-Bora-3a,4a-Diaza-s-Indacene [BODIPY^{TM}], Thermofisher, D3922, ex/em 493/503 nm), and imaged (LED 475nm, ex/em 495/519 nm, 10 ms) to quantify the relative amount of induced intracellular lipid.[107] The NIH ImageJ software was used for post-processing the microscopic images to analyze the percentage of lipid in cells by calculating the measured area ratio of BODIPY fluorescence (lipid indicator, green emission) over chlorophyll autofluorescence (growth indicator, red emission). For nDEP manipulation of the cells, the applied electrical signal was set to 200 kHz, 15 V_{pp}.

5.5.2 Application demonstration using pDEP force with GFP-*S. enterica* for in-droplet cell detection with higher sensitivity

Salmonella enterica strain ATCC 14028S with GFP plasmid pCM 18 was used to demonstrate the utility of the developed in-droplet solution exchange platform in improving in-droplet fluorescent cell detection, where *S. enterica* was manipulated utilizing pDEP force. The starting droplets encapsulating *S. enterica* cells with a high fluorescent background (FITC-dextran) suspended in R2A medium were first generated to have approximately 55 *S. enterica* cells per droplet. The continuous phase flow, which is the new solution, was fresh R2A medium containing no fluorescent dye. The starting droplets, solution-exchanged droplets, as well as droplets containing only blank media were imaged (LED 475nm, ex/em 495/519 nm, 300 ms) to compare the in-droplet GFP cell detectability under the presence of different levels of fluorescent background that can be controlled by the different degree of solution exchange. The NIH ImageJ software was used for post-processing the images to obtain the signal-to-noise ratio (SNR) of GFP-*S. enterica* compared to the background fluorescence. For pDEP manipulation of *S. enterica*, the applied electrical signal was set to 3 MHz, 20 V_{pp}.

5.6 Results and discussion

5.6.1 Testing and characterization of the droplet microfluidics platform

The cell washing and solution exchange droplet microfluidics platform is composed of three interconnected microfluidic units: an in-droplet DEP-based cell concentration unit, a droplet splitting unit, and a droplet cleaving/pairing/merging unit (**Fig. 5.1A**). Detailed device design and working principles are described in the above method section. **Fig. 5.1B** shows the microfabricated platform, with key functional parts marked with numbers that correspond to the numbers shown in the conceptual design illustration of **Fig. 5.1A**.

The functionality and operation of the in-droplet cell washing and solution exchange functions were first characterized using *C. reinhardtii* cells to test the DEP-based in-droplet cell manipulation step, followed by using color dye droplets for fluidic functionality testing. **Fig. 5.3A-D** shows the DEP-based in-droplet cell concentration step (area marked as #2 in **Fig. 5.1**). Initially, cells inside the droplet are seen randomly distributed (**Fig. 5.3A**), and then can be seen being concentrated to the top part of the droplet as the nDEP force pushes all cells away from the paired electrodes (**Fig. 5.3B-C**). Splitting this droplet into two daughter droplets results in the top daughter droplet having all (or most) of the cells (**Fig. 5.3D**). The details of these in-droplet DEP-based cell manipulation steps will be further discussed in chapter 2.2 and chapter 2.3. Starting from **Fig. 5.3E**, for easier visualization of the overall droplet microfluidic operation, the original droplets were made of black color dye (to be washed away with the new transparent solution), and the fresh solution (to be added as the new solution) was PBS (transparent). **Fig. 5.3E** shows the original color droplet splitting into two daughter droplets at the asymmetric droplet splitting junction. The daughter droplet flowing into the upper channel can then be seen cleaving the fresh solution (PBS) flow, creating automatically synchronized paired droplets (**Fig. 5.3F**). We have previously demonstrated that this droplet cleaving and auto-synchronization method results in extremely high droplet merging efficiency even when relatively large droplet sizes (e.g., hundreds of micrometers in diameter) are used as needed by various cell biology applications, especially those requiring in-droplet cell culture.[106] The DEP region of the

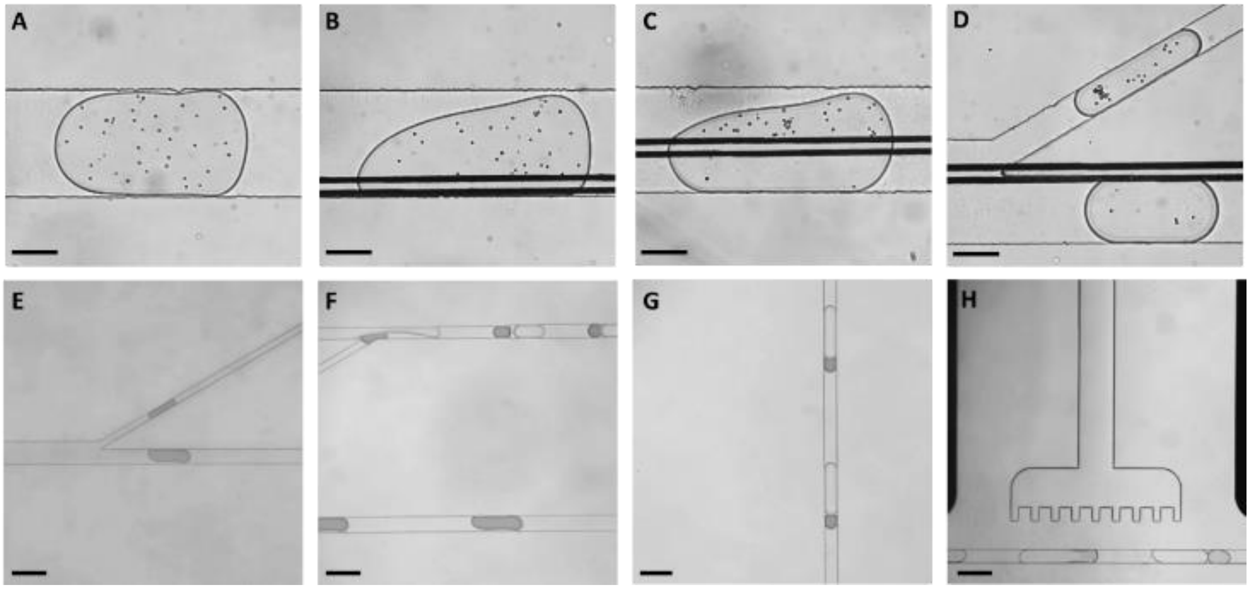

Fig. 5.3. In-droplet solution exchange system validation using *C. reinhardtii* strain CC406 cells and color dye. (A-D) In-droplet trajectory of microalgae cells when DEP signal was applied. Most microalgal cells were successfully concentrated and split into the top daughter droplet; Scale bar: 100 µm. (E-H) Droplet microfluidics system characterization using transparent and darkcolor solution. A droplet can be seen splitting at a ratio of 3 to 7 at the splitting junction (E); the top daughter droplet (dark color) cleaves the continuous stream of fresh solution (transparent), resulting in one-to-one droplet pairs (F); droplet pairs are guided into the margining region (G), and merged downstream under an electric field (H). Scale bar: 200 µm. Reprinted with permission from Huang et al., 2021. Copyright 2021, American Chemical Society.

microfluidic channel has a relatively shallow height of 25 µm to maximize the DEP force applied to cells.

Since such a shallow height is not needed in the other regions of the droplet microfluidics platform, to minimize the downstream flow resistance the fluidic channel height is increased to 40 µm after the droplet cleaving/pairing junction. The automatically paired and synchronized droplets (**Fig. 5.3G**) were then flown into the downstream droplet merging region where they were merged by applying an external electrical field (**Fig. 5.3H**). The final cleaving and merging efficiency achieved was 98% (49 out of 50 droplets). The overall system throughput tested was 1.5 droplets/s, where the throughput was mainly limited by the in-droplet DEP-based cell concentration step since DEP force is a relatively weak force.

5.6.2 Identifying parameters that affect the degree of cell washing and solution exchange

In the developed droplet microfluidics platform, the degree of cell washing and solution exchange can be easily adjusted by the flow rates. The degree of solution exchange is mainly dependent on the splitting ratio of the two daughter droplets as well as the size of the new solution droplet the split daughter droplet is merged with. These two parameters can be controlled by the inlet flow speed (marked as "1" in **Fig. 5.4A**, kept here as constant), the withdrawal flow speed (marked as "2" in **Fig. 5.4A**), and the flow rate of the aqueous stream (marked as "3" in **Fig. 5.4A**). First, the volumetric ratio of the top split daughter droplet against the mother droplet can be simply controlled by adjusting the withdrawal flow rate, as summarized in **Fig. 5.4B**. Here, the mother droplet size was 104 µm ± 2.1 µm. By adjusting the flow rate ratio (withdrawal flow rate at outlet #2 / flow rate at inlet #1) from 0.36 to 0.77, the resulting split top daughter droplet to mother droplet volumetric ratio can be controlled from 45.0% ± 4.3% to 12.5% ± 2.1%. At a flow rate ratio of 0.82 and above, droplets do not split anymore for the given design, and thus cannot achieve any solution exchange. **Fig. 5.4C-D** shows an example of a droplet splitting at a 4:6 volumetric ratio, and **Fig. 5.4E-F** shows an example of a droplet splitting at a 2:8 volumetric ratio. Size variation in the cleaved droplets was also analyzed and summarized in **Fig. 5.5**. In summary, the droplet splitting ratio can be easily adjusted, which we consider as the primary parameter in controlling the degree of washing and solution exchange.

Second, adjusting the new solution volume to which the top daughter droplet is merged with provides the second control over the degree of washing and solution exchange, and also controls the final cell concentration in the newly merged droplet. For example, when a 4:6 droplet splitting ratio was utilized (**Fig. 5.4E**), the length of the cleaved and paired new solution droplet could be controlled from approximately 100 µm to 250 µm in diameter[106] by adjusting the inlet flow rate from 10 µl/h to 20 µl/h. In another example, when a 2:8 splitting ratio was utilized (**Fig. 5.4F**), the volume of the cleaved and paired new solution droplet could be controlled from 100 µm to 250 µm in diameter by adjusting the inlet flow rate from 5 µl/h to 12 µl/h. Cleaving and merging with a smaller new solution droplet results in less dilution of the original sample and higher concentrated of cells. In contrast, cleaving and merging with a larger new solution droplet results in higher dilution of the original sample and lower concentration of cells. Combined with the droplet splitting ratio control, this results in controllability over how much of the original solution to remove and how much new solution to add, providing broad flexibility depending on the cell assay need.

In almost all droplet microfluidics systems, the dimension of the microfluidic channels and flow rates are optimized to fit a particular droplet size. Any change in this droplet size typically requires recharacterization of the droplet microfluidic system. Thus, it is ideal for the final droplet size after the in-droplet solution exchange step to be the same as the original droplet size, eliminating the need for re-characterizing and re-optimizing the system. By utilizing the above-mentioned control, here we have demonstrated that regardless of the initial droplet splitting ratio, the final droplet size can be made almost identical (**Fig. 5.4G, 5.4H**). In this case, where the final droplet size is the same as the original droplet, the solution exchange ratio can be as high as 83.3%, when the original droplet is split at 16.7% vs 83.3% volumetric ratio followed by merging the split droplet with a 5X larger new solution droplet. However, due to the volume limitation of the top daughter droplet, such a high droplet splitting ratio may result in cell loss if not all cells can be concentrated to within that 16.7% of the original droplet solution. In the case when absolutely no cell loss is desired, a more conservative splitting ratio could be 28% vs. 72%, achieved by using flow rates of 10 µl/h (reflow droplet), 60 µl/h (spacing oil), 50 µl/h (withdrawal), and 7 µl/h (aqueous stream). Such an operation condition results in approximately 72% of the original solution being removed from the original droplet. These optimal flow rates were used for the following two cellular applications.

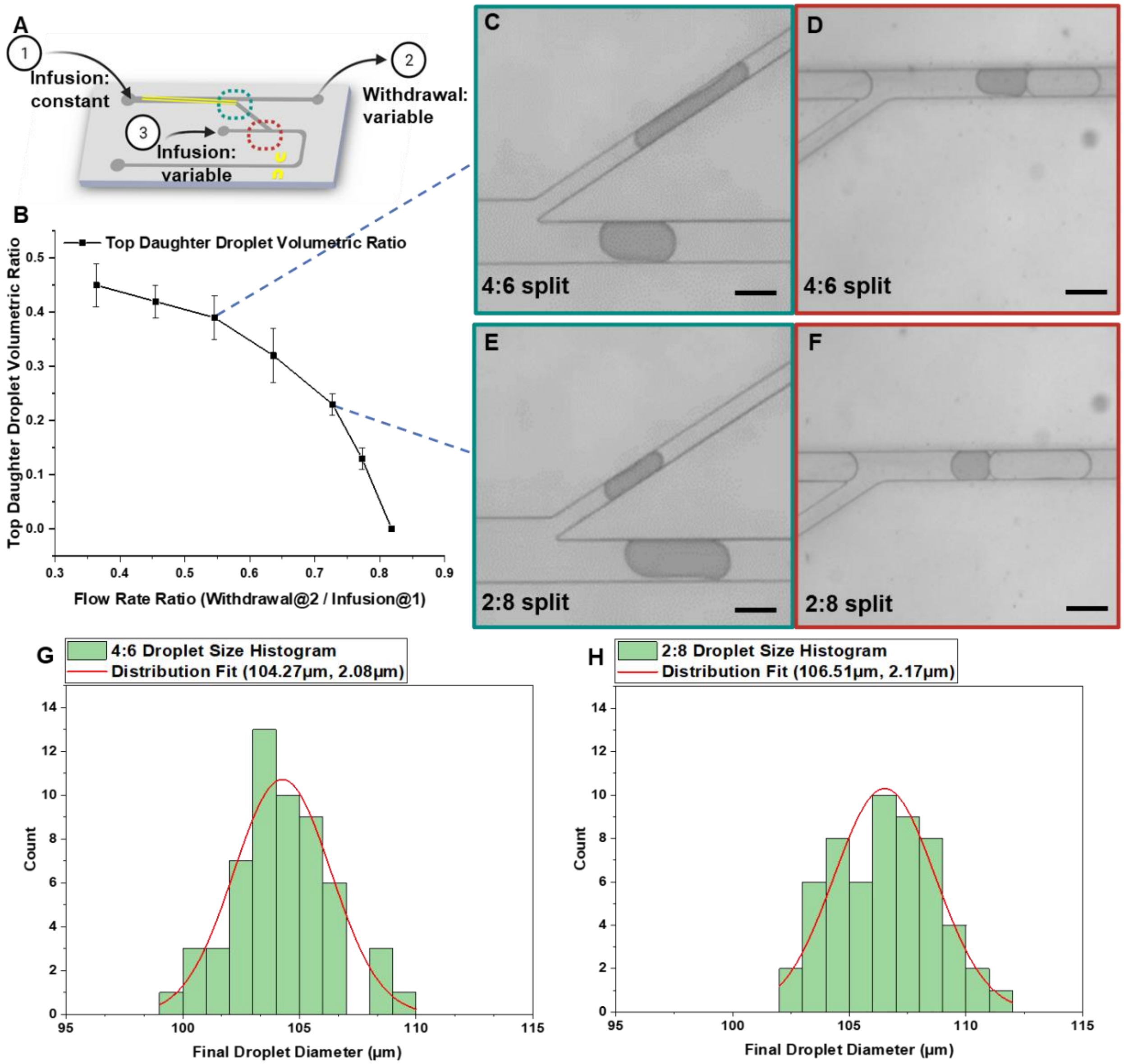

Fig. 5.4. Characterization of the splitting and cleaving function using color dye. (A) Illustration of the overall system. (B) The effect of flow rate ratio on volume of spitted daughter droplet. (C-F) Achieving same overall droplet volume of the paired droplet when using different droplet splitting ratios (4:6 (C-D) and 2:8 (E-F)) by controlling the infusion and withdraw flow rates, (G-H). The resulting overall volume of the paired and merged droplets are shown. Reprinted with permission from Huang et al., 2021. Copyright 2021, American Chemical Society.

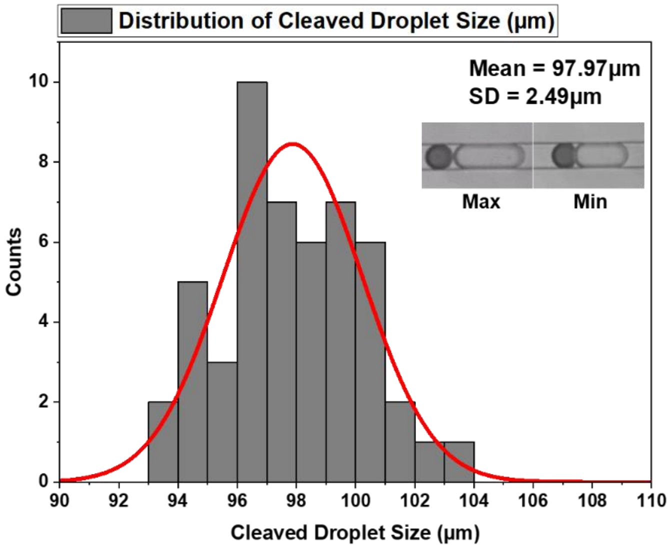

Fig. 5.5. Statical analysis of the cleaved droplet size. The size variation of the cleaved droplet was evaluated using a fixed size cleaving droplet. The relative standard deviation (RSD) of the cleaved droplet length is 0.07, with minimum and maximum droplet length being 93.03μm and 103.87μm, resulting in a final droplet diameter of 97.97μm ± 2.49μm. Upper right inset images show the minimum and maximum cleaved droplet sizes compared. Reprinted with permission from Huang et al., 2021. Copyright 2021, American Chemical Society.

5.6.3 Cellular application 1 – Detecting lipid induction after exchanging microalgae culture media

The intention of this application here is to demonstrate that the developed system can be utilized when the cell culture medium in the droplet needs to be exchanged during an experiment. We picked microalgae culture as an example for several reasons: their lipid-producing capability is of high interest as green biofuel,[118] they grow rapidly under normal media conditions but then have to be cultivated in nitrogen-limited conditions to induce lipid production and hence require solution exchange to be able to assess both their growth and lipid production capability.[58,119] Importantly, screening of microalgae for their growth and lipid production have been conducted in many different microfluidic systems, including droplet microfluidic systems.[46,120] The entire experiment flow is illustrated in **Fig. 5.6A**. *C. reinhardtii*-

encapsulated droplets were generated in normal TAP medium, followed by solution exchange to nitrogen-limited medium (TAP-N), and then cultivated for 72 h to monitor their lipid production.

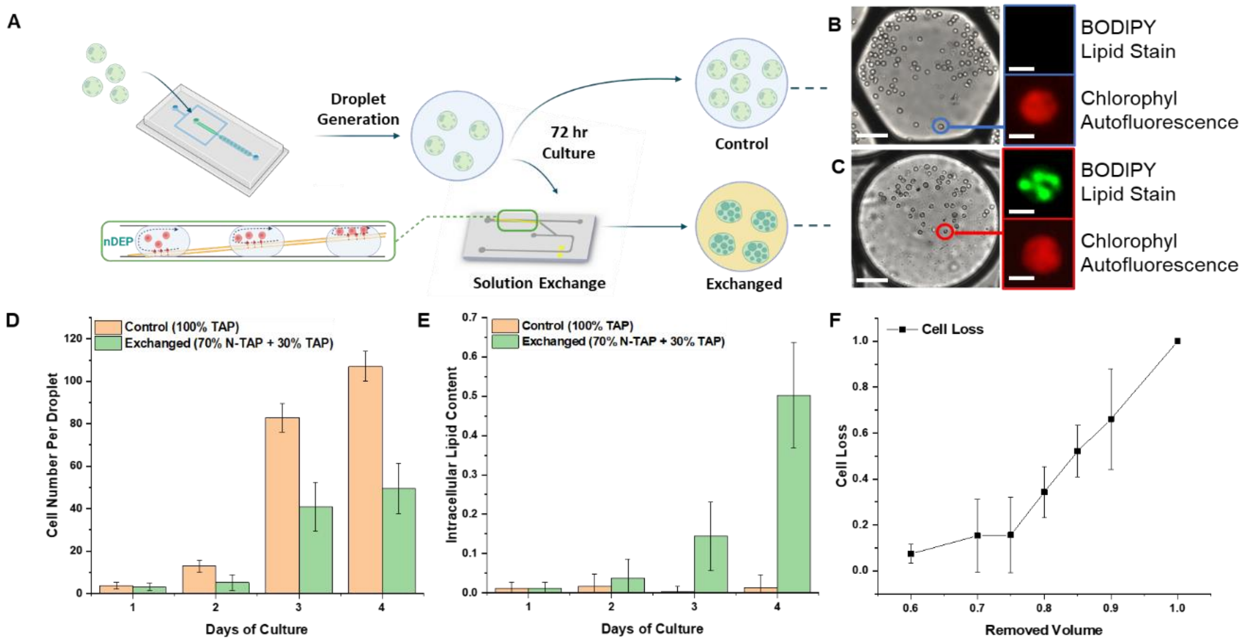

Fig. 5.6. In-droplet solution exchange workflow to assess the growth and lipid production of the microalga *Chlamydomonas reinhardtii* (CC406 strain) in droplet microfluidics format. (A) Droplet microfluidics workflow. (B) Microscopic images of cells after being cultured for 72 h in the original droplet compared to when their culture media was changed to nitrogen-limited media. Scale bar: 25 µm, inset: 5 µm. (C) Comparison of cell growth in the two different droplets. (D) Comparison of lipid content of cells in the two different droplets. Reprinted with permission from Huang et al., 2021. Copyright 2021, American Chemical Society.

As a control, droplets without solution exchange were also cultivated for 72 h. **Fig. 5.6B** shows a droplet without solution exchange, where robust growth of cells can be observed (initial cell number was around 4 cells, expanded to about 107 cells after 72 h of culture). Fluorescent image of an individual cell clearly shows chlorophyl autofluorescence (red fluorescence), while no lipid in the cell can be observed (no green fluorescence after BODIPY lipid stain). In contrast, **Fig. 5.6C** shows a droplet after solution exchange, where the resulting droplet contains 28% of TAP medium and 72% of TAP-N medium. The expectation is that the presence of TAP medium will result in some cell growth but significantly lower than the case of 100% TAP medium (no solution exchange), while the limited nitrogen will induce lipid production. As expected, this can indeed be seen by a large amount of intracellular lipid production (**Fig. 5.6C**, green fluorescence). Next, the differences in both growth, and lipid production during the 72 h culture period were compared. Initially, on average 4 cells were encapsulated per droplet, which in the control group case expanded to around 107 ± 12 cells after 72 h of culture (**Fig. 5.6D**), while their intracellular lipid content was less than 1.3% ± 3.2% of the cell volume (**Fig. 5.6E**). However, the droplets after solution exchange had an average of only 49 ± 7 cells showing significantly slower growth due to the limited amount of nitrogen in the droplet (**Fig. 5.6D**), whereas the amount of lipid production increased to around 50.3% ± 13.4% of the cell volume (**Fig. 5.6E**). These drastic differences between their cell culture profiles validate the functionality of the in-droplet cell washing and solution exchange microfluidic system as well as demonstrate the utility of this new droplet microfluidics technology.

It is to be noted that in this application nDEP force was utilized. In the DEP-based cell concentration unit, microalgal cells encapsulated in the droplets experienced nDEP force and thus were repelled away from the electrode pair and gradually concentrated to the upper side of the droplet because of the tilted angle electrode geometry. **Fig. 5.7** shows that a split droplet that contains most of the cells flows into the droplet cleaving/pairing unit to create paired droplets containing TAP-N medium and then merged together under an electric field (10 kHz, 300 V_{pp}). Further reducing the top split daughter droplet size shown here could increase the solution exchange efficiency, but it could also result in significant cell loss. This can be seen in **Fig. 5.6F**, where as the upper droplet volumetric ratio increased, cell loss also increased. In this particular example, if the top daughter droplet size is smaller than 25% of the original droplet volume, the cell loss ratio remained less than 15.7%. The relationship between the cell loss and removed solution volume is dependent on the specific cell type used, as the DEP-based in-droplet cell

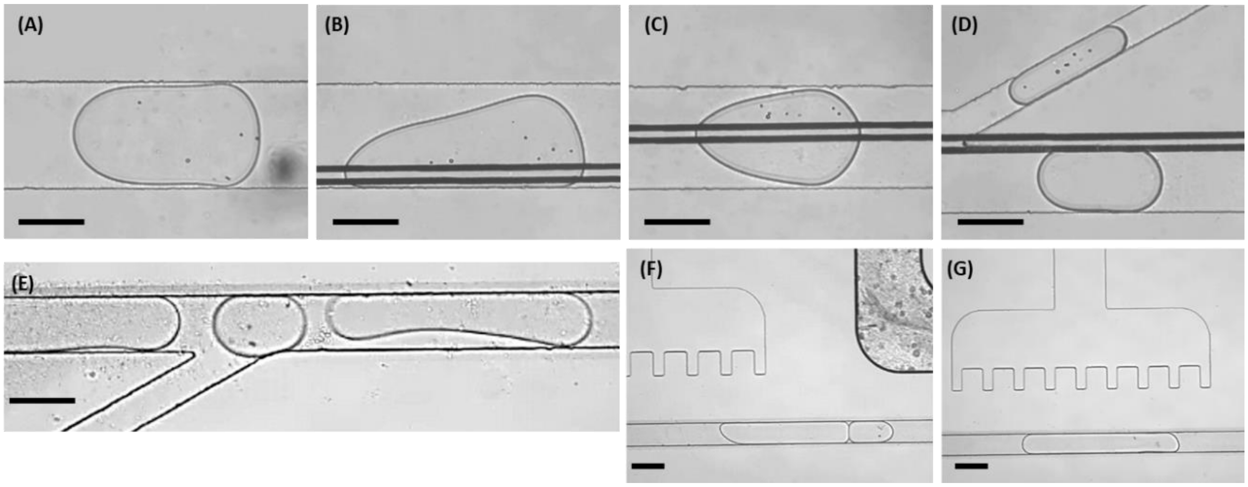

Fig. 5.7. Solution exchange of a droplet containing *C. reinhardtii* CC-406 cells. (A-D) A droplet containing six CC-406 cells pass through the DEP manipulation zone, where all cells were concentrated by nDEP to the upper daughter droplet after droplet splitting. (E) Following droplet splitting, the daughter droplet containing all cells was guided to the droplet cleaving part, where it cleaved the continuous stream of fresh media (coming from left), resulting in one-to-one automatic pairing of droplets. (F-G) Droplet pairs being merged under an electric field. Scale bar: 100 µm. Reprinted with permission from Huang et al., 2021. Copyright 2021, American Chemical Society.

manipulation step is highly dependent on the cell types due to their different dielectric properties.

5.6.4 Cellular application 2 – Improved fluorescent detection of cells in droplets

In droplet microfluidics, it is very common to utilize laser-based fluorescence detection of fluorescent cells (labeled or are expressing fluorescent proteins) inside droplets, where the droplets are sorted based on their measured fluorescent intensity. Here, the fluorescent signal may come from the fluorescently labeled cells or fluorescent protein-expressing cells, autofluorescence of cells, and autofluorescence of culture media. For optical detection, a high signal-to-noise ratio (SNR) is desired. Unfortunately, it is common to have a strong background signal from fluorescent staining dye or culture media itself, which can greatly decrease this SNR, limiting the detectability of the target cells. In conventional laboratory assays, such background noise is typically not an issue since multiple centrifugation steps followed by resuspending the cells in low-background-signal medium is commonly used before imaging. In this application,

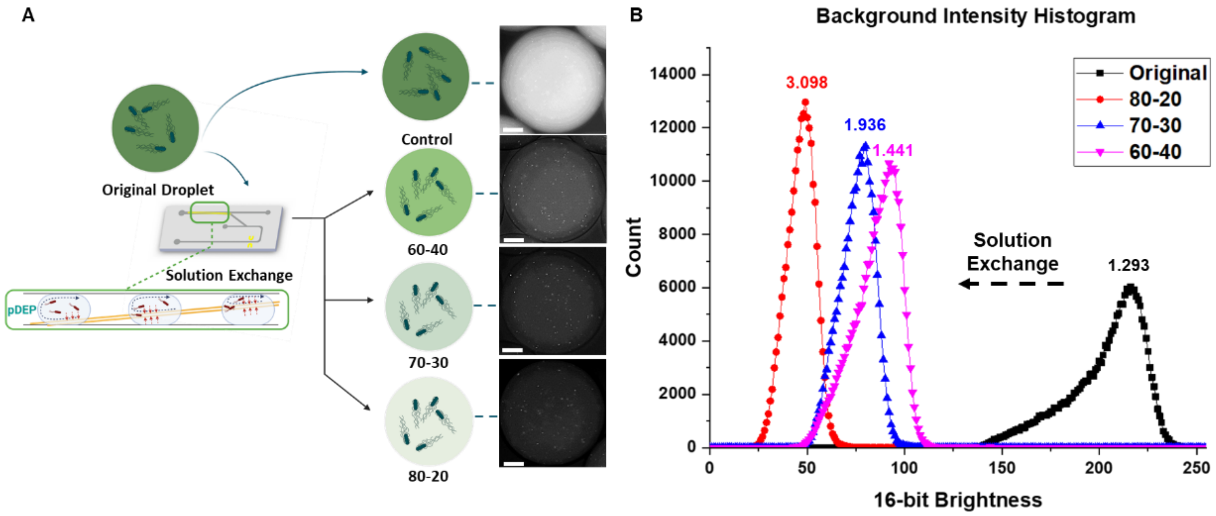

Fig. 5.8. In-droplet solution exchange platform workflow to improve the fluorescent detection capability of droplet contents. (A) Illustration of the entire solution exchange process and microscopic images of the original and solution-exchanged droplets under same exposure condition. (B) Background noise histogram of solution-exchanged droplets at different solution exchange efficiencies, compared to the original droplet. Scale bar: 25 µm. Reprinted with permission from Huang et al., 2021. Copyright 2021, American Chemical Society.

droplets encapsulating approximately 55 GFP-*Salmonella* cells along with fluorescent dye (FITC) were used to generate the initial droplets. Then, fresh medium containing no fluorescent dye was used to replace the original solution as much as possible to reduce the background noise during optical detection. To manipulate GFP-*Salmonella* cells, pDEP force was utilized. Three different solution exchange ratios were tested, aiming to remove 60%, 70%, and 80% of the original droplet solution (**Fig. 5.8A**). Droplets before and after solution exchange were imaged under the same settings and their background noise histograms compared (**Fig. 5.8B**). Through this in-droplet solution exchange step, the average background noise intensity of droplets reduced from 197.1 ± 20.5 to 85.4 ± 12.0, 75.4 ± 8.9, and 46.5 ± 7.3 when 60%, 70%, and 80% of the original solution was exchanged, respectively (**Fig. 5.8B**). This resulted in SNR increasing from 1.29 (i.e., fluorescent cells barely detectable) to 3.10 (i.e., fluorescent cells easily detectable). Similar to the previous microalgae culture medium exchange application, we also evaluated the cell loss vs. different solution exchange rates. Here, a maximum solution exchange rate of 88% could be achieved while minimizing the cell loss to less than 5%. In terms of the throughput, the system could be operated at up to 5 droplets/s, beyond which cell loss increased to 10% and more. For example, when operating the system at 15 droplets/s, the cell loss was around 50%. It is envisioned that depending on the application need, a lower throughput with minimum cell loss or a higher throughput even if quite a bit of cells are lost may be selected. It is to be noted that the solution exchange rate, cell loss, and maximum throughput are all dependent on how efficient the DEP-based cell concentration step is, which is cell type-dependent.

5.7 Future works

The current in-droplet solution exchange efficiency can be varied based on the specific application need and can achieve up to 88% of solution being exchanged with less than 5% cell loss. Since the droplet size can be kept the same after solution exchange, such platform can also be connected in a serial manner to further improve the solution exchange efficiency. A >97% solution exchange efficiency is expected when using two devices in series connection, which will result in near-complete solution replacement. Many conventional assays are difficult to perform inside droplets due to the requirement of washing steps, such as enzyme-linked immunosorbent assay (ELISA) and nanoparticle-based Surface Enhanced Raman Spectroscopy (SERS), in which reagents from the first reaction must be removed before the next reagents are introduced. Such assay can be realized using the developed in-droplet solution exchange technology.

5.8 Conclusions

In this chapter, an in-droplet cell washing and solution exchange platform that integrates DEP-based cell concentration and droplet splitting/cleaving/merging functions were successfully demonstrated. The current solution exchange efficiency can be varied depending on the specific application need, and can achieve up to 88% of solution being exchanged with less than 5% cell loss. In terms of the throughput, the developed system can be operated at 5 droplets/s under minimum cell loss condition, and at 15 droplets/s if ~50% cell loss is acceptable. Additionally, since the droplet size can be kept same after solution exchange, such a platform can also be easily connected in series to further improve the solution exchange efficiency to potentially up to 97%. Such repeated washing step is commonly applied in conventional centrifugation assays, where three washing steps are commonly utilized. The utility of the developed system was demonstrated in two different cell biology assays using *S. enterica* and *C. reinhardtii* as the target cells, utilizing either pDEP or nDEP force, demonstrating that any cell that can be manipulated with DEP force regardless of their polarity can be utilized in the developed platform. In summary, considering that a cell washing step is extremely commonly utilized in conventional cell assays, we expect that this new droplet manipulation technique, which is one alternative replacement method for conducting conventional centrifugation and cell washing steps in droplet format, can enable more complicated cellular assays to be performed in droplet microfluidics format.

6. ELIMINATING AIR BUBBLE IN MICROFLUIDIC SYSTEMS UTILIZING INTEGRATED IN-LINE SLOPED MICROSTRUCTURES*

6.1 Overview

This chapter includes the extension work based on Chapter 2, the development of SEER platform. In most microfluidics systems, formation and accumulation of air and other gas bubbles can be detrimental to their operation. Air bubbles in a microfluidic channel induce a pressure profile fluctuation and therefore disturb the stability of the system. Once an air bubble is generated, its also extremely difficult to remove such bubbles from the microfluidic systems. In tissue and cell culture microfluidic systems, a single air bubble can completely shear off cells that are being cultured in such systems. Air bubbles can be especially problematic in microfluidic systems that have to operate for long period of time, since completely eliminating the generation of air bubbles for prolonged periods of time, where a single air bubble can ruin an entire multi-day/multi-week experiment, is extremely challenging. Several in-line and off-chip bubble traps have been developed so far, but cannot completely eliminate air bubbles from the system or are relatively difficult to integrate into microfluidic systems. Recent advancements in two-photon polymerization (2PP)-based microfabrication method eliminates the restriction in Z-axis control in conventional two-dimensional microfabrication, and thus enables complex 3D structures to be fabricated at sub-micrometer resolution. In this work, by utilizing this 2PP technique, we refer to the SEER device design and developed a sloped microfluidic structure that is capable of both trapping and real-time removal of air bubbles from the system in a consistent and reliable manner. The novel structures and designs developed in this work present a unique opportunity to overcome

---

* Reprinted with permission from Huang et al., 2020. Copyright 2020, Springer Nature.

the many limitations of current, state-of-the-art solutions in air bubble removal and enable a multifunctional microfluidic device to operate seamlessly free from air bubble disruption. The microfabricated system was tested in both droplet microfluidics and continuous-flow microfluidics applications, and demonstrated to be effective in preventing air bubble aggregation over time. This simple sloped microstructure can be easily integrated into most microfluidics devices to minimize bubble introduction, which will contribute to creating a stable and bubble-free microfluidic platform amenable for long-term operation.

6.2 Introduction

One of the most commonly observed problem in any microfluidic systems, despite how meticulous a microdevice and experiment are designed, are the introduction of air bubbles, which can be detrimental to their operation and outcome. Depending on their sizes, air bubbles will either partially or completely clog the microchannel or flow stream. Small air bubbles can be easily lodged in areas typically found in local, low-pressure niches, and remain there for long periods of time, continuously disrupting the flow. Since air bubbles are compressible and flexible, the degree of disruption is dynamic, further causing difficulties in managing the operation of the microfluidic system. In addition, these unwanted air bubbles introduce additional liquid-gas interfaces in fluidic channels, which present interfacial tension and often cause the aggregation of particles/cells/droplets that would normally be uniformly distributed throughout the microfluidic channel. Unfortunately once introduced, such bubbles are extremely difficult to remove, and thus if such phenomena happen at the beginning of an experiment, most commonly the entire system is flushed out and the experiment needs to be restarted. The biggest impact of these air bubbles is for applications where microfluidic systems have to operate for long periods of times (days to weeks). For example, in cell culture microfluidic systems,[121-125] where often times the presence of CO_2 is needed to maintain cell culture, air bubbles can be easily generated and/or introduced. In these applications, a single air bubble can shear off the cells from the surfaces on which they are being cultured and ruin the entire multi-day/multi-week experiment. In the case of droplet microfluidic systems that require on-chip culture and imaging of droplet content,[108,126,127] an air bubble can put pressure to the water-in-oil emulsion droplets, causing droplet merging or significantly moving the position of droplets that are being imaged. As a result of the summation of these aforementioned issues, a highly efficient novel solution that can be seamlessly integrated into broad ranges of microfluidic devices can enable many microfluidic-based platforms and protocols to run in a reproducible and robust manners.

The introduction of air bubbles into microfluidic systems can be caused by many different sources.[128-130] These include: incomplete sealing at tubing-device interfaces, small air pockets left from the very beginning even after microfluidic channel priming processes, dissolved air in solution forming air bubbles during thermal treatment of solutions for various biochemical reactions, and in certain applications caused by piezoelectric actuation or electrolysis at sensing/actuation electrode surfaces. One of the most commonly used microfluidic device material, polydimethyl siloxane (PDMS), is more prone to such problems, as the material is gas permeable, a requirement for many cell culture microfluidic systems and why they are used so extensively in microfluidic systems. Air bubble generation is especially severe when the microfluidic systems have to operate at elevated temperature (e.g., 37^{o}C for cell culture), involve cell culture where degassing of solution is not desired, and when operating over a long period of time where any small problem can eventually cause air bubble generation over time.

Common methods of avoiding air bubble generation include priming the microfluidic channel with solvents first to remove all air bubble, followed by filling the microfluidic channel with aqueous solution, placing cell culture microfluidic systems underwater or under oil, vacuum degassing the PDMS device prior to experiment, and the use of hydraulic pressure to actuate microvalves instead of pneumatic pressure, to name a few. Beyond such laboratory tricks, several other methods and devices have been developed to minimize the presence of air bubble in microfluidics channels. Some methods utilize the permeability of PDMS and directly apply vacuum through a thin PDMS layer to remove incoming air bubble.[131,132] However, such methods typically cannot remove air bubbles that are generated later within the system, and can also be sensitive to pressure dynamics across the membrane. Open-air structures that utilize ambient air pressure have been also reported to achieve passive air removal,[133-135] but have the potential for contamination due to the exposure of aqueous contents to external environment. Microstructures that can achieve air trapping and air removal have been also developed, where a multi-layer PDMS device was fabricated so that the buoyancy of air was utilized to achieve bubble trapping. However, due to the complexity of the structure, these systems can normally only be fabricated through complicated microfabrication approaches.[136-139] In addition, typically these macroscale solutions cannot be integrated directly into in-line microfluidic channels, thus creating additional channel-to-tubing interfaces that are prone to air bubble introduction themselves, or cannot be made into a compact integrated system. Importantly, none of these systems can completely remove air bubbles from the microfluidic systems. In addition, most of these systems have been developed for continuous-flow (ie., single-phase flow) microfluidics systems, but not for water-in-oil droplet microfluidics systems despite the fact tht such air bubbles also disrup the operations in droplet microfluidic systems. Thus, there is a need for developing a better solution that can easily be integrated into microfluidic channels and can address the presence of undesired air bubbles in both continuous flow and droplet microfluidic platforms. Such an approach can have extremely broad utility in almost all types of microfluidic systems. The work presented here aims to provide a solution that meets these design criteria, further advancing the potential, functionality, and application of microfluidic systems. The novel microstructures developed in this work provide an unequaled solution for the traditional problem of unwanted air bubbles infiltrating microfluidic channels. The work presented herein efficiently prevents the passages of air bubbles through the collection regions, can readily be integrated into the overall schematic footprints of any microfluidic channel design, and has been demonstrated in successful operation over an extended assay duration.

In this chapter, a microfluidic channel where the ceiling of the channel slopes upward, essentially creating a microfluidic channel that becomes wider in the vertical direction, was created so that air bubbles that naturally float upwards due to their buoyancy will move to the ceiling part of the microfluidic channel and accumulate there. This allows the aqueous solution to flow unimpeded since the air bubbles do not occupying the direct path of the liquid flow. This sloped air bubble trapping microstructure can be coupled with a negative pressure chamber located on top of the air bubble accumulation area, allowing for the system to achieve air bubble trapping and removal over an extended period of assay time without over-accumulation of trapped air bubbles. A challenge in this design concept is that conventional 2D microfabrication steps cannot easily create such microstructures where the Z-direction height changes gradually within the same device. Recent development and commercialization of two-photon polymerization (2PP) technique allows creating true 3-dimensional microstructures within the same device with sub-micrometer resolution, where this microfabrication capability is now relatively widely available. Several recent works have achieved fabrication of complex 3D structures utilizing 2PP techniques, which vividly demonstrate the potential of applying these techniques to microfluidics field[140,141]. Here, the Z-direction sloped microstructure was fabricated by creating a master mold using a commercially available 2PP instrument. The novel microstructures designed and developed for this work provide a solution to a traditional microfluidic obstruction to robust platforms by harnessing the powerful spatial control of a 2PP approach paired with a deep understanding of the physical phenomena governing fluid and air flow within microchannels. The simplicity in the fabrication and relatively small footprint of the structures allow for demonstration of a true microscale air bubble filtration system that can be combined into most existing microfluidic platforms and devices. The developed air bubble trapping and removal microstructure was evaluated in both continuous-flow and droplet microfluidics configurations in several scenarios, including carrier oil inlet air bubble prevention, aqueous media inlet air bubble prevention, as well as demonstration of long-term cell culture with no air bubble introduction. The extremely simple microstructure also enables integrating such a structure directly into many microfluidic device schemes and applications as an in-line air bubble removal solution, and thus has broad utility in almost all types of microfluidic systems.

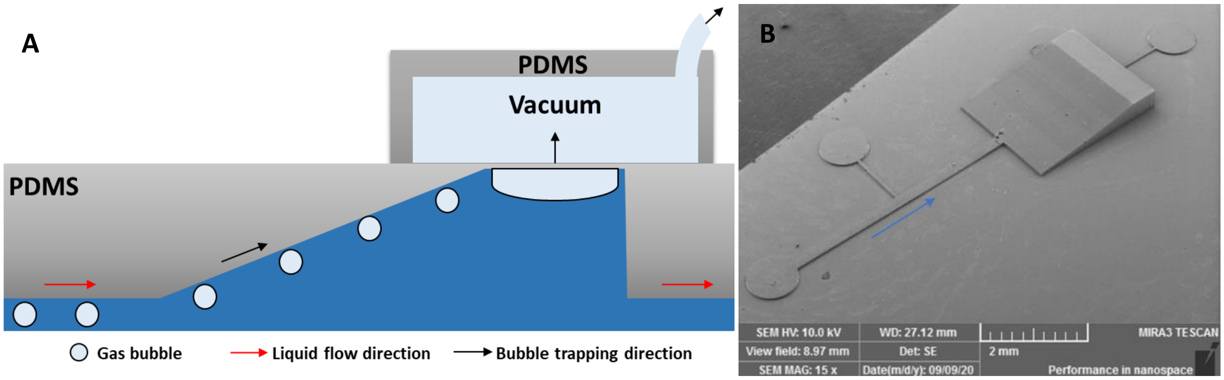

Fig. 6.1 (A) Working principle of the air bubble trapping structure. Air bubbles in the microfluidic channel gradually climb up to the air bubble trapping region due to their buoyancy. Negative pressure applied across the thin PDMS membrane placed on top of the trapping region continuously remove the collected air bubbles. (B) SEM image of the air bubble trapping structure. Reprinted with permission from Huang et al., 2020. Copyright 2020, Springer Nature.

6.3 Device design and working principle

The device working principle is illustrated in **Fig. 6.1**. The air bubble trapping and removal unit is composed of an incoming microfluidic channel, a downstream chamber that has an upward-sloped ceiling, a thin gas-permeable membrane ceiling region where the air bubbles can be collected and removed, and a downstream microfluidic outlet channel. Due to the buoyancy of air bubbles in aqueous solution or fluorinated oil, air bubbles that flow in the microfluidic channel will float upward along the sloped channel and accumulate at the top right side of the chamber. This removal of air bubbles from the main flow channels allows the liquid flow to continue into the outlet channel, which has the same height as the inlet microfluidic channel. Negative pressure applied to the chamber through a thin gas-permeable polydimethyl siloxane (PDMS) membrane allows for the continuous removal of air bubbles from the air bubble collection region without impacting the liquid flow in the main flow channel or other conditions in the microfluidic channel. The height of the main flow channel used here is 30 µm. The slope structure has an arc length of 2.03 mm with a constantly changing point-by-point curvature until reaching the total chamber height of 350 µm, at which point the channel remained at this height for 500 µm long to allow for the negative pressure chamber to be placed on the top side of the air bubble collection region. This design allows trapping of up to 1.08 µl of air at a given time. Since any accumulated air bubble can be continuously removed from this air bubble trapping region through the negative pressure applied, this is more than sufficient in most applications. The air bubble removal speed can be tuned by changing the PDMS membrane thickness as well as the applied vacuum pressure to ensure that any air bubble accumulated can be quickly removed from the chamber without obstructing the liquid flow in the main microfluidic channel.

6.4 Device Fabrication

The microdevice was fabricated using a conventional soft lithography method. However, to create the sloped microstructure, instead of using a conventional two-dimensional photolithography-based master mold fabrication process, the master mold was fabricated using a commercially available two-photon photolithography (2PP) tool (Nanoscribe Photonics Professional GT, IP-S photoresist). This instrument allows essentially 3D printing of microstructures with sub-micrometer resolution, hence ideal to create microstructures where the Z-directional height can vary freely within a single master mold. The fabrication process follows that as described in previous soft lithography works that use Nanoscribe for master mold fabrication.[140] Briefly, a 4-inch silicon wafer was pretreated to ensure enhanced adhesion of the photoresist to the substrate. The wafer was then submerged into solution contains 1 % (v/v) 3-(trimethoxsilyl)propyl methacrylate (440159, Sigma-Aldrich, USA) diluted into 25 ml of ethanol for 10 h. This wafer was then washed in dH_2O and dried using a N_2 gun. Next, a 3-dimensional computer aided drawing (CAD) was prepared using Solidworks 2018 (Dassault Systemes SolidWorks Corp, MA) and transcribed for writing using Describe (Nanoscribe GmbH, Germany) and uploaded onto the 2PP tool. The master mold was fabricated out of IP-S negative photoresist (Nanoscribe GmbH, Germany) using the 25X objective print field at a power scaling of 1.0, tetrahedron inner scaffold, base scan speeds of 50,000, base laser power of 60%, shell/scaffold scan speeds of 100,00, and shell/scaffold laser power intensities set at 70%. Following the print job, the unpolymerized resist was set to develop in propylene glycol monoethyl ether acetate (PGMEA, Millipore Sigma, MA) for 6 min followed by a 10 min fine development step in 99% Isopropyl alcohol (IPA, VWR, PA). The patterned master mold was then coated with (tridecafluoro-1,1,2,2 tetrahydrooctyl) trichlorosilane (United Chemical Technologies, Inc., Bristol, PA) to enhance PDMS release. PDMS mixture (1:10, Dow Sylgard 184) was then poured on the 2PP-fabricated master mold, cured at 85˚C for 4 hour, released from the master mold, and then bonded on a glass substrate after oxygen plasma treatment. PDMS was poured only up to slightly above the master mold height, resulting in the air bubble aggregation region to have only a 300 µm thick membrane as the ceiling. Finally, a small PDMS chamber (surface area: 4.38 mm^2) was bonded on top of the air bubble trapping region to allow applying vacuum pressure through the thin PDMS membrane ceiling for air bubble removal. The microfabricated 2PP master mold was sputter-coated with a thin Au layer, and the microstructures were examined with SEM (TESCAN MIRA3) (**Fig. 6.1B**).

6.5 Experiment setup

For testing purposes, to intentionally introduce air bubbles into the chamber, a second inlet perpendicular to the main flow channel, forming a T-junction, was utilized. Through this side channel, = air bubbles were introduced by continuously actuating a syringe containing only air while in the main channel aqueous solution was continuously introduced, resulting in the periodic generation of air bubbles in the microfluidic channel. For easy visualization of the main fluidic flow, fluorescent microbeads (4.8 µm diameter, Thermofisher, Inc.) were flown through the microfluidic channels and imaged using a fluorescent microscope (AxioObserver, Zeiss, Inc.). Next, to demonstrate that no air bubble flows past the air bubble collection chamber and into a microfluidic cell culture chamber over a multi-day culture period, mammalian cells were cultured in the microfluidic device. This multi-day, cell culture experiment is to further demonstrate the utility of the presented air bubble trapping and removal microstructure since the existence of air bubbles flowing through such a system can be detrimental during extended cell culture experiments where cell-shearing and cell toxicity due to the presence of air bubbles can be observed. A549 (ATCC CCL-185^{TM}) epithelial cell were thawed from a cryostock and grown in T75 culture flasks with Dulbecco's Modified Eagle Media (DMEM, D5648, Sigma-Aldrich, USA) containing 10% Fetal Bovine Serum (FBS, 16000044, Thermo Fisher Scientific, USA) in a 37°C, 5% CO_2 incubator. Prior to the experiment, A549 cells were detached using trypsin and the cell concentration was adjusted to 2×10^6 cells/ml, which results in about 20% confluency after loading the cells into the device chamber. Cells were cultured in the microfluidic chamber for up to 5 days, while being periodically monitored under a microscope. Cell viability during culture was examined by staing the cells using YOYO™-1 Iodide (491/509) cell viability dye.

6.6 Results

6.6.1 Air bubble accumulation and trapping using the sloped microchamber

Air bubble accumulation in the sloped microchamber was first tested through microscopy, followed by measuring the air bubble collection efficiency under a continuous flow condition. Air bubbles were intentionally introduced into the chamber using the second inlet of the T-junction structure. As expected, air bubbles gradually moved upward towards the air bubble trapping/aggregation region (**Fig. 6.2A**, right side flat top part). Here, some small air bubbles accumulated and merged into a much larger air bubble, while no air bubble was seen flowing through the outlet microfluidic channel.

To assess whether this sloped microfluidic structure impedes the aqueous solution flow and whether the accumulated and merged large air bubble in the air bubble trapping region interfere with the aqueous solution flow, aqueous solution containing fluorescent beads (size: 4.8 μm) for easy visualization of the fluid flow was flown through the microfluidic channel. These fluorescent beads also mimic situations where microparticles or cells need to flow through microfluidic channels without being disrupted by air bubbles or any microstructures being added to a microsystem. Even when a relatively large aggregated air bubble exists in the air bubble trapping region (**Fig. 6.2B**, air bubble diameter: 442 µm), it was confirmed that the fluorescent bead-containing flow could continuously flow out into the outlet microfluidic channel without any major disruption.

Similarly, to evaluate whether this structure could trap air bubbles in droplet microfluidics applications and if the accumulated air bubbles interfere with the droplet delivery, water-in-oil emulsion droplets were generated and flown through the microfluidics channel. Carrier oil (Light Mineral Oil, VWR, with 2.5% Span 80, Sigma-Aldrich) flow rate was set to 150 µl/h and aqueous solution (DI water with blue color dye for visualization) flow rate was set to be 100 µl/h. It was confirmed that the droplets could continuously flow out into the outlet microfluidic channel without any major disruption (**Fig. 6.2C**).

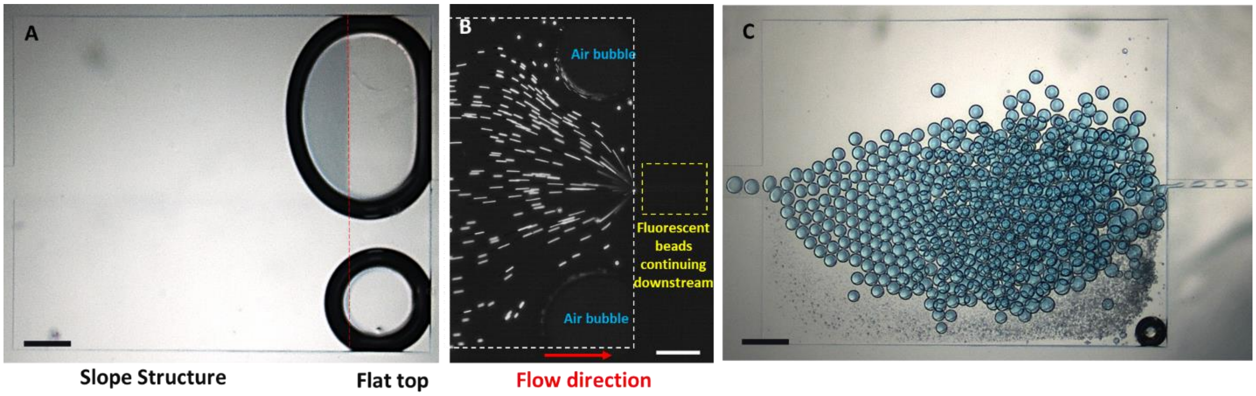

Fig. 6.2 (A) Bright field image of air bubbles being trapped at the end of the sloped microfluidic chamber where the ceiling is flat. (B) Fluorescent image of fluorescent beads continuously flowing out into the outlet channel without being hampered by the sloped microfluidic structure nor by the air bubbles trapped in the trapping region. (C) Water-in-oil emulsion droplets can be seen continuously flowing out into the outlet channel without being hampered by the sloped microfluidic structure. Scale bar: 250 µm. Reprinted with permission from Huang et al., 2020. Copyright 2020, Springer Nature.

6.6.2 Removal of accumulated air bubbles

For long-term operation of a microfluidic system, the accumulated air bubbles have to be removed continuously from the system to prevent the eventual overflow of air bubbles into the main microfluidic channels. The air bubble removal functionality was tested by applying negative pressure through the thin PDMS membrane ceiling of the air bubble trapping/accumulation chamber. For this, after a large number of air bubbles were trapped and accumulated in the chamber (**Fig. 6.3A**), all fluid flow was stopped and 92 kPa negative pressure was applied. After 0.5 hr of applying vacuum, almost all air bubbles can be seen removed from the chamber (**Fig. 6.3B**), and after another 30 min of applying vacuum, all air bubbles were removed from the chamber (**Fig. 6.3C**). This results in an air bubble removal rate of around 17 nL/min. Considering that the amount of air bubbles seen accumulated in **Fig. 6.3A** is quite a lot (0.70 µl volume, equivalent to approximately 10,000 of 50 µm diameter air bubbles), considering a typical microfluidic system operation, such an air bubble removal rate (3 of 50 µm diameter air bubbles/sec) is sufficient for almost all applications.

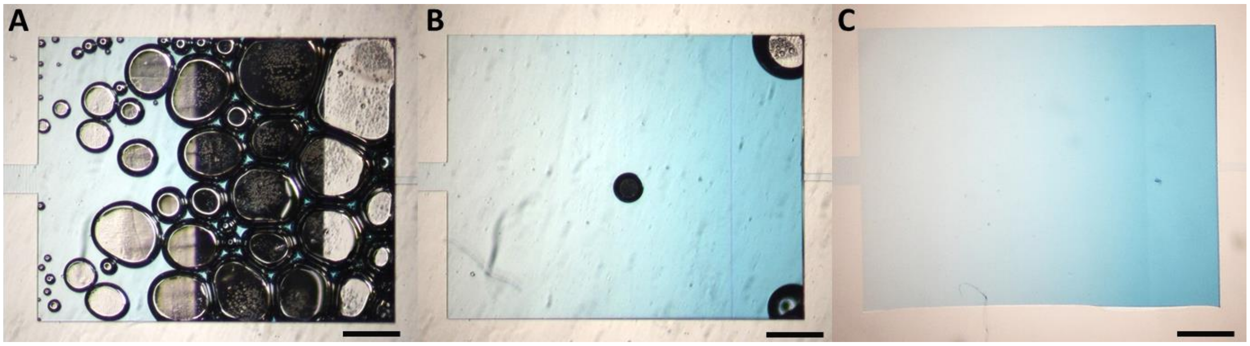

Fig. 6.3 (A-C) Microscopic images of the air bubble trapping/collection chamber showing: (A) Large number of air bubbles initially accumulated in the collection chamber. (B) An almost empty chamber after applying negative pressure for 0.5 hr. (C) A completely empty chamber after applying negative pressure for 1 hr. Scale bar = 500 µm. Reprinted with permission from Huang et al., 2020. Copyright 2020, Springer Nature.

6.6.3 Long-term cell cultivation in the microfluidic chamber without disruption by air bubbles

To demonstrate the utility of the proposed air bubble removal microstructure in enabling long-term cell culture without disruption by air bubbles, A549 cells were seeded into the microfluidic chamber at 20% confluency. Following the initial cell loading step, culture media was perfused into the chamber at a rate of 5 μL/h. As can be seen in **Fig. 6.4**, cells can be loaded and seeded into the microfluidic chamber without the presence of any air bubble. Similar with previous results, in the presence of vacuum pressure applied to the air bubble removal microstructure upstream of the microfluidic cell culture chamber, no air bubble accumulation was observed throughout the 5-day culture period and no cell shearing was observed. The number of cells gradually increased and finally reached 70% confluency by end of the 5-day culture period. Cell viability was tested at the beginning and end of the culture period to ensure that the microfluidic chamber and the applied operating condition have minimal impact on cell viability. Contrary to this, if air bubbles were flowing through the microfluidic system, even occasionally, such air bubbles would have sheared off large number of cells being cultured in the microchamber. This experiment validates that the presented air bubble removal microstructure design could be used in many microfluidic cell culture systems to provide long-term bubble-free culture conditions, which is expected to have broad utility.

Fig. 6.4 Microscopic images of the proposed trapping/collection chamber showing: (A) initial cell loading into the trapping chamber. (B) cell can be successfully seeded and have nearly 100% viability after overnight culture. (C) cells remained over 95% viability after 5 days of culture. Reprinted with permission from Huang et al., 2020. Copyright 2020, Springer Nature.

6.7 Alternative sloped microstructures for air bubble trapping and removal

Utilizing the basic concept of a sloped microstructure along which air bubbles can float up due to buoyancy and be removed from microfluidic channels, various other designs can be considered. **Fig. 6.5** shows another sloped air bubble removal microstructure, where the orientation of the slope differed from the original design by flipping the curvature from a concave to convex, and also has a micropillar array positioned in the middle of the slope in order to guide the air bubbles into two adjacent air bubble collection chambers while the fluidic stream can directly go straight to the outlet. Such design could be useful where microscopy of microfluidic channels are important, so that the air bubble removal vacuum application port do not impede imaging of this area. In addition, the end part of the sloped microstructure then gradually slopes downward to the main flow channel region, instead of the step-height drop seen in Fig. 1. This can minimize dead volume or prevent any issue stemming from abrupt changes in fluid flow. To test this design, fluidic flow rate was set to 3 ml/h while air bubbles were intentionally introduced through the T-junction air bubble generation structure. As can be seen in **Fig. 6.5B-C**, air bubbles could be seen trapped along the micropillar structure and then guided towards the two outer air bubble removal ports. This again shows that the concept of a sloped microstructure-based air bubble removal can be utilized in various design concepts as needed by the specific microfluidic system requirements.

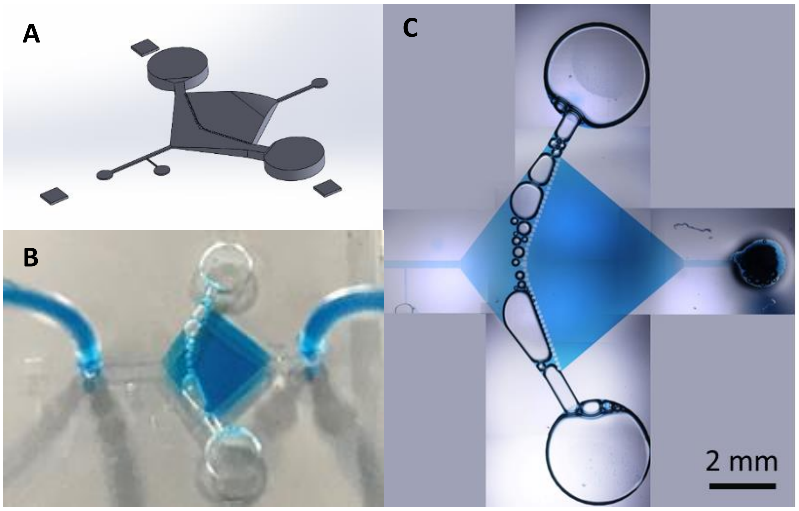

Fig. 6.5 (A) Illustration of an alternative air bubble removal design. Instead of having a relatively steep slope that abruptly ends like a step-structure before connecting to the outlet microfluidic channel, in this design the structure gradually slopes down and connects to the main outlet microfluidic channel. (B-C) Air bubbles trapped in the trapping chamber were guided to the side chambers following the slope. In addition, the upside-down hanging micropillar array further prevented the air bubbles from flowing into the main outlet channel. Reprinted with permission from Huang et al., 2020. Copyright 2020, Springer Nature.

6.8 Discussion

In this work, we demonstrated the utility of a simple yet effective method of trapping undesired air bubbles from microfluidic systems utilizing a microfluidic channel structure where the ceiling slopes in both concave and convex shapes, without impeding the solution and particle flow in the main microfluidic channel. Furthermore, we demonstrated that incorporating a negative pressure vacuum chamber to the air bubble trapping region can remove the accumulated air through the thin gas-permeable membrane ceiling, enabling long-term operation of microfluidic systems without any air bubble issues. The sloped microstructure was enabled by utilizing a commercially available sub-micron resolution 3D printer utilizing 2PP technology, where such sloped microstructures cannot be fabricated using conventional 2D photolithography methods.

To directly compare the fludic dynamics of the presented structure to that of a traditional 2D-lithography fabricated step-shape structure, a COMSOL simulation (COMSOL Multiphysics® 5.5) has been performed to show the flow profile at the middle x-z plane of the microfluidic structures, with the flow rate set as 300 µl/h (**Fig. 6.6**). The result shows that without a slopped structure, the sudden expansion at the chamber inlet introduce a large interference of the laminar flow, resulting a significantly higher z-directional flux at the inlet side of the air trapping chamber. In contrast, smoother transitioning of pressure and flow velocity can be observed in the sloped microchannel design. Additionally, the isosurface of flow velocity indicates that this novel sloped structure can help distribute the aqueous flow across the y axis. Such enhanced uniformity in flow velocity distribution can greately benefit the cell loading or air bubble trapping process since target cells or unwanted air bubbles have higher likelihood to bypass through the sides of chamber. Overall, these improvements lead to higher air trapping efficiency in the sloped microchannel design since air bubbles will be easier to be trapped and less disturbed once trapped in the upper side of the venting chamber.

The developed device was first successfully utilized to demonstrate the capability of trapping air bubbles at the intended air bubble trapping region without impeding the delivery of fluid or solid content in the solution. The theoretical capacity of an air trapping chamber can be determined by the total volume that spans above the incoming microfluidic flow channel, which in our case was around 0.83 µl. As a result of the buoyancy force between the air bubble and the carrier fluid phase, air bubbles float toward the microfluidic channel ceiling and aggregate at the ceiling of said chamber. However, during the priming process and especially at relatively high flow rates (15 ml/h or higher), the local pressure profile within the chamber did not equilibrate, which led to air bubbles tending to stay in the low-pressure regions. When looking at the cross section, air bubble aggregation nearest to the outlet channel has a larger cross-sectional area and therefore the local fluidic flux would be less when compared to the inlet region, resulting in a

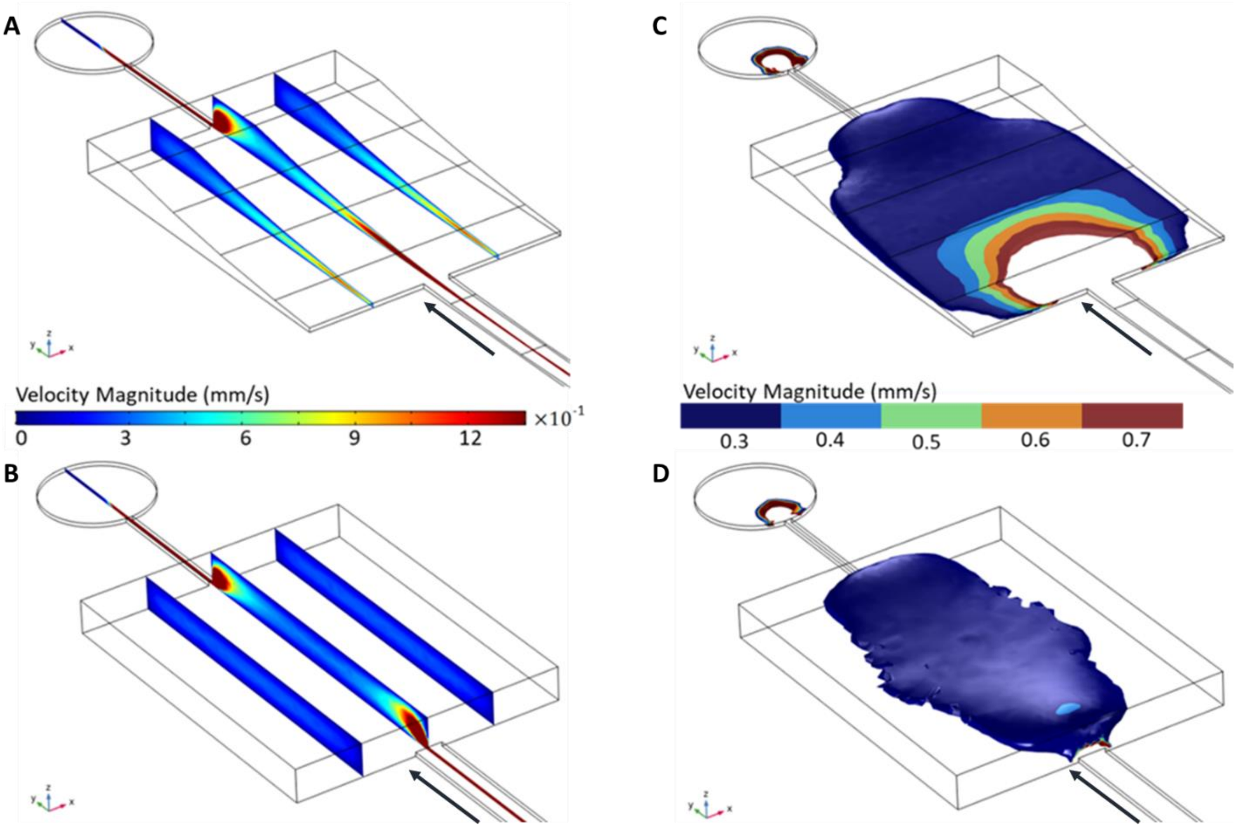

Fig. 6.6 (A-B) Simulation results of flow velocities inside the sloped microstructure design (this work) and the step-shaped microstructure (traditional design). (C-D) Isosurface showing the boundary of flow velocity at 0.3 mm/s inside each design. The sloped structure design shows more uniformity in terms of flow distribution. Carried particles/cells or unwanted air bubbles can have more exposure to the side of chamber, increasing the trapping efficiency and effective volume of trapping. Reprinted with permission from Huang et al., 2020. Copyright 2020, Springer Nature.

gradual pressure drop across the chamber. Therefore, bubble would tend to stay nearby the outlet, which led to air bubbles occasionally escaping from the air bubble trapping chamber and into the outlet channel. Thus, the actual air trapping capacity is slightly less than that of theoretical calculation. This can be resolved by applying a higher negative pressure. Alternatively, as shown in the alternative design (**Fig. 6.5**), a sloped microstructure with an almost isosceles trapezoidal cross-sectional geometry can be utilized so that the air will be moved further away from the downstream outlet microfluidic channel, minimizing the risk of air bubble escape into the main flow channel. Another possible modification to enhance the trapping efficiency and minimize the error rate is further optimizing the angle of the slope as well as the dimension of the chamber depending on the application needs. Lastly, this air bubble trapping microstructure, combined with continuous air bubble removal through the application of negative pressure through a thin gas-permeable membrane ceiling, was successfully utilized to demonstrate long-term operation of a microfluidic cell culture system. Compared to several previously developed air bubble trapping and removal structures[131,133-139], the advantage of the presented system is its simplicity and scalability in design, easy fabrication and integration into any microfluidic channels, contamination-free, and applicable to both continuous-phase microfluidic systems as well as droplet microfluidic systems.

Several potential immediate applications for this air bubble trapping and removal microstructure exist. For example, the presented strategy could be utilized where there is a need for fluid transfer between serially connected microfluidic devices, where each tubing junction enhances the risk for accidental air bubble introduction. The design could also be integrated just downstream of an inlet of an aqueous media, an inlet for reinjected and reflowed water-in-oil emulsion droplets, an inlet for carrier oil used in droplet microfluidic systems, as well as in front of any cell culture microfluidic chambers where any introduction of an air bubble could be detrimental, to remove any air bubble that may come from such inlets. In addition, this proposed device could also be utilized as a stand-alone device that can be integrated into any tubing systems for air bubble removal. In summary, the simple yet highly efficient air bubble trapping and removal system can have broad applicability in ranges of microfluidic systems in minimizing error rates stemming from air bubble introduction.

6.9 Conclusion

In this chapter, an integrated in-line air bubble trapping and removal microstructure based on a sloped microstructure has been successfully developed. The developed sloped microstructure includes features that support operation of broad ranges of microfluidics systems while maintaining effective trapping and removal of air bubbles that are difficult to completely prevent in any microfluidic systems. The microsystem features include: i) efficient trapping and removal of air bubble in both continuous-flow microfluidic system as well as droplet microfluidic system, ii) easy microfabrication step and simple microstructure, iii) easy integrability into any microfluidic channels and systems, iv) flexibility in scaling up or scaling down capacity based on the application need, v) long-term stability, and vi) no concern for contamination since no microfluidic parts are directly exposed to external environment. The air bubble trapping and removal function was confirmed with the help of fluorescent beads and color-dye based visualization in both continuous-flow microfluidics and droplet microfluidics and demonstrated trapping of all air bubbles while causing no obstruction to the fluidic delivery. Air bubble removal rate were evaluated under extreme cases and it was confirmed that the speed of removal is sufficient for most microfluidic applications. Long-term operation stability was tested through a cell culture microsystem operating over a 5-day culture period, where cells could be cultured and proliferated without any air bubble issue. Furthermore, an improved alternative structure was proposed with smoother transition in microstructure that contributed to more efficient air bubble removal. The air bubble trapping and removal sloped microstructures presented here can be applied as a general method in eliminating air bubbles in most forms of microfluidics systems and applications, thus are expected to have broad applicability.

7. SIZE-BASED BANDPASS FILTER FOR DROPLET MICROFLUIDIC SYSTEM USING INTERDIGITATED ELECTRODE ARRAY

7.1 Overview

Additional functional module for droplet QC can greatly enhance the quality of droplet-based biological assay with minimal noises. This chapter presents a high-sensitivity microfluidic droplet size-based bandpass filter. The method couples natural buoyancy phenomena with localized interdigitated electric field beneath the microfluidic channel for droplet sorting. In such microfluidic channel, only droplets that are large enough and closely approach the electrode will be sorted out by dielectrophoretic (DEP) force. The bandpass filtration can be achieved by combining two of such high-pass filter units. The method and concept have been proven by sorting out 80 μm droplets from a library containing three different sizes of droplets (40 μm 80 μm and 160 μm). The output results showed the filtration efficiency was larger than 99% (false negative and false positive cases <1%) at a variety of different throughputs (5 to 100 droplets/sec). A sonication-generated polydispersed droplets library was employed for characterizing the features of the filter. The passband and bandwidth can be adjusted by tuning applied voltages and the combination of two-channel heights. The droplet filter is capable of distinguishing droplets differing in diameter by approximately 7 μm. To demonstrate its application in conjunction with other droplet manipulations, we apply this droplet filter downstream of a droplet PCR and droplet merger. The filter was able to remove the most (>98%) unsuccessful droplets on the merging step and droplets damaged during droplet PCR thermal cycling. With tuning of geometry dimension, such design can be utilized under various droplet microfluidic systems, achieving functions such as quality control of droplet sizes, filtering out the desired droplets after droplet handing steps that can cause unwanted droplet size variations.

7.2 Introduction

Droplet microfluidics has shown promise in various fields including cell biology,[142-144] drug screening,[145-147], and nucleic acid analysis,[148,149], to name a few. Active manipulation of droplets serves as one crucial component in droplet-based microfluidics systems. owing to the recent technological advancements in sample control and handling techniques, individual droplets can nowadays be transported, merged, dispersed, trapped, and sorted within microfluidic platforms with decent efficiency and accuracy, in a high-throughput manner.[150] In most of the applications, high quality of monodisperse droplets is required for all aforementioned active manipulations as devices are designed for operating with droplets of specific size. Having input droplets with various sizes will cause unwanted turbulence of flow, malperformance in functions such as droplet reflow, merging, picoinjection, and sorting, which eventually lead to degraded performance of the entire microfluidics platform.[10, 11] However, abnormally sized droplets are quite difficult to completely avoid, and the presence of these droplets seems to be evitable after droplet transporting, merging, splitting steps which often comes with slight deficiency. In this context, having a readily available method to actively remove droplets with unwanted size becomes one of great interest for further pushing the limit of droplet microfluidic systems, as removal of abnormal-sized droplets can greatly increase the accuracy and efficiency of functionality of microfluidic platforms.

Abnormally sized droplets can be produced from a variety of sources, which including (1) fluctuation of flow speed during the droplet generation caused by mechanical errors of pumps and/or presence of compressible air bubbles in the system; (2) unsuccessful droplet pairing and merging; (3) split of large droplets or fusion of small droplet during the droplet transition or reflow process; (4) broken droplets or over-merged droplets due to the periodic change of physical environment (e.g. droplet PCR). Recently, several sized-dependent droplet separation techniques have been reported based on deterministic lateral displacement (DLD),[151,152] physical filtration,[153] guiding tracks[154,155], and hydrfodynamic methods.[156,157] Separation of droplets using the DLD method was first reported by Joensson *et al*.[152] DLD devices are typically space-consuming due to their pillar array geometries. Furthermore, this method can only separate two batches of droplets with at least two-fold volumetric difference, and also have difficulties to sort larger size droplets (>100 µm) that are commonly used for cellular functional assay due to the compression and deformation of large droplets when hitting the pillars. Thus, it is quite challenging to utilize such method to perform highly sensitive size-based droplet separation, especially with large-size droplets. Another selective size-based droplet separation method relies on physical filtration features. Ding *et al*.[158] used the cross-flow filtration features to prevent the flow of unwanted larger droplets and was able to distinguish droplets with only 20% difference in volume. However, this method was only applicable for separating small droplets from large droplets (can be considered as either a high-pass or low-pass filter). In addition, the cut-off size of filtered droplets is dependent on flow conditions, which makes the quality control of such filtration system quite difficult. The guiding track separation method combines Laplace’s trapping mechanism with the hydrodynamic drag force. This method implies the use of structured features located at the top or bottom of the microchannel to guide the confined droplets through the use of continuous[159] or “dotted” guiding tracks.[154,160] The use of hydrodynamic on-rail filters can achieve sensitive separation by size.[154] However, this method is usually limited by its low throughput nature, and also requires the fabrication of complicated multi-layered devices. Hydrodynamic methods, such as pinched flow fractionation[157,161], and inertial force microfluidics were also reported for sized-based droplet sorting. Maenaka *et al.*[157]

has demonstrated that by utilizing the pinched flow method, droplet shear-force-induced migration in a parabolic flow could separate small “satellite” droplets from target droplets that are more than 5 times larger. Overall, this method is relatively low sensitivity to droplet size and therefore is inapplicable for accurate sorting applications. In addition, microfluidic devices based on the balance of inertia and fluidic force for separation of hydrogel droplets were developed by Li *et al*.[156] Droplets varying in size migrate to different size-dependent dynamic equilibrium positions across fluid streamlines under the combined effects of inertial forces of shear-gradient lift force and a wall effect lift force. The drawbacks of this technique are its low sorting efficiency (around 90%) and the sorting of a polydispersity population could lead to the device design being extremely complicated.

Interdigitated electrode array has been widely utilized in manipulation in microfluidic systems and has achieved functions such as droplet merging, particle manipulation, cell screening, to name a few.[162-164] Despite recent advances in the IDE-based manipulation technologies, the full potential of this manipulation method has not been well exploited. The interdigitated electrode pairs can provide a highly localized and fine controlled electric field compared to 3D electrode designs that are currently widely utilized in droplet microfluidic systems, and such characteristics could greatly benefit precise control of droplets in ultra-high-throughput systems.

In this chapter, by coupling with natural buoyancy phenomena, we proposed an IDE-based droplet microfluidic design that can generate localized electric field beneath microfluidic channel, therefore resulting in fine manipulation on target droplets with specific sizes. Target droplets that mostly fill the cross-section of microfluidic channel will be affected by the generated electric field, therefore sorted by received dielectrophoretic (DEP) force. Meanwhile, droplets with a smaller diameter will be floating on the top of the microfluidic channel, receiving minimal DEP force from bottom IDE manipulation and flow straight to the other outlet. This method is the first of its kind and the demonstrated device can separate droplets that are only 7 µm different in diameter. The filtration efficiency is larger than 99% under a variety of throughputs (5 – 100 droplets/sec). The overall performance of the device is better than the aforementioned published works. With adjusting of geometry dimension, such design can be utilized under various droplet microfluidic systems, achieving functions such as quality control of size, sorting out the desired droplets after active manipulation steps that can cause undesired droplet size variations. The proposed microfluidic system unit can be served as an inserting unit and can be readily implemented into most currently available droplet microfluidic systems to assure quality controls of input droplets. In summary, we expect such proposed technology can be widely utilized in various types of droplet-based microfluidics assays.

The utility of the bandpass filtration system was demonstrated in two real scenarios. The first example is for droplet merging quality control, where typically merging is not always performed with high efficiency, and unmerged/over-merged droplets will cause huge performance downgrade at downstream biological assays. Being able to exclude unwanted droplets from the library right after droplet merging step can significantly reduce the false cases at later detection/sorting steps. In this application, for better visual representation, droplets with two different sizes are labeled with two colors, and droplets were merged with a conventional droplet merger. Afterward, merged droplets, as well as unmerged droplets, were introduced to the proposed IDE manipulation unit and unwanted droplets were filtered out, achieving efficiency that is larger than 99%. In the second application, the proposed IDE unit was integrated into a classic Droplet Digital PCR (ddPCR) workflow, to help achieve cell-free in vitro transcription/translation (IVTT) assay in the droplet format. The proposed unit here serves as a quality control unit to 1) filter out all off-sized droplets/micelles right after thermal cycling steps, and 2) exclude unmerged droplets after the IVTT droplet merging step. The integration of these units ensured the proper conduct of the entire droplet-based IVTT workflow. A significant improvement in droplet quality was confirmed after implementing the aforementioned IDE units, and the proposed system is proven not to cast any biological interference during on-chip manipulations. Overall, we believe the proposed functional unit can enable many sophisticated and precise assays to be performed in droplet microfluidics format.

7.3 Theory and simulation

The presented device is designed to utilize the buoyancy phenomena effects on different sized droplets, so that the droplet at different z positions can be affected by differential magnitudes of DEP manipulation force, therefore resulting in completely different droplets trajectories (**Fig. 7.1a**). To provide sufficient buoyancy, such design requires the density of carrier oil to be greater than that of the droplet aqueous medium. Fluorinated oil as the most frequently used oil in droplet microfluidic field meets this requirement. Planar interdigitated electrodes were fabricated underneath the microfluidic channel and generated localized electric field along z-axis. When droplet diameter is close to channel height, the buoyant droplet is approximate to IDE surface. As a result, stronger DEP force can be induced by localized electric field and droplet trajectory will be affected with the design of IDE pattern; however, when droplet size is less than channel height, the buoyant droplet will be far to IDE surface, therefore, receives neglectable DEP force (**Fig. 7.1b**). Droplets at this size will approximately follow the guide from Stokes' drag force and follow the flow of carrier oil. With fine control of channel height, droplets with smaller sizes can be guided directly to the opposite channel while bigger droplets affected by DEP force can be collected to the IDE guided channel.

Droplets posed in uniformed electric field experiences DEP force based on their position and diameter. Equation 1 describes the time-average DEP force that each droplet received.

$$F_{DEP} = 2\pi\varepsilon R^3 Re[f_{CM}]\nabla\left|\vec{E}\right|^2 \qquad (1)$$

Here, the conductivity of the surrounding solution, ε, the radius of cells, R, the electric field, E, as well as the real part of Clausius-Mossotti (CM) factor, Re$[f_{CM}]$, can affect the polarity and the magnitude of the DEP force acting on droplets.[94] Approximately, the CM factor remains the same when droplet size is not far too different. In our case, the CM factor is treated as constant during comparison.

According to COMSOL simulation result (**Fig. 7.1c**), the electric field generated by the IDE electrode was calculated. As a direct comparison, the intensity of the electric field posed at 1 µm beyond IDE electrodes is approximately 55 times higher than that at 60 µm beyond IDE electrode surface. Based on the calculation, when the droplet size is comparable with the cross section of the microfluidics channel, the base cap of droplet is still approximate to the IDE surface. In contrast, when the droplet size is smaller than the height of the channel, the droplet will be lifted by the buoyancy and therefore distanced from the IDE surface. Droplet size vs. received DEP force is calculated and standardized to the case of 100 µm size droplets and plotted in **Fig. 7.1d**. As an example, when a droplet with 80 µm and a droplet with 100 µm flow through the IDE patterned microfluidic channel with a height of 100 µm, according to simulation and calculation results, droplets with the size of 100 µm receives approximately 0.16 mN total DEP force when posed about such IDE patterns, which is about 31 times greater than that acting on 80 μm droplets. The great difference of received DEP force between two droplet sizes provides distinct manipulation effects.

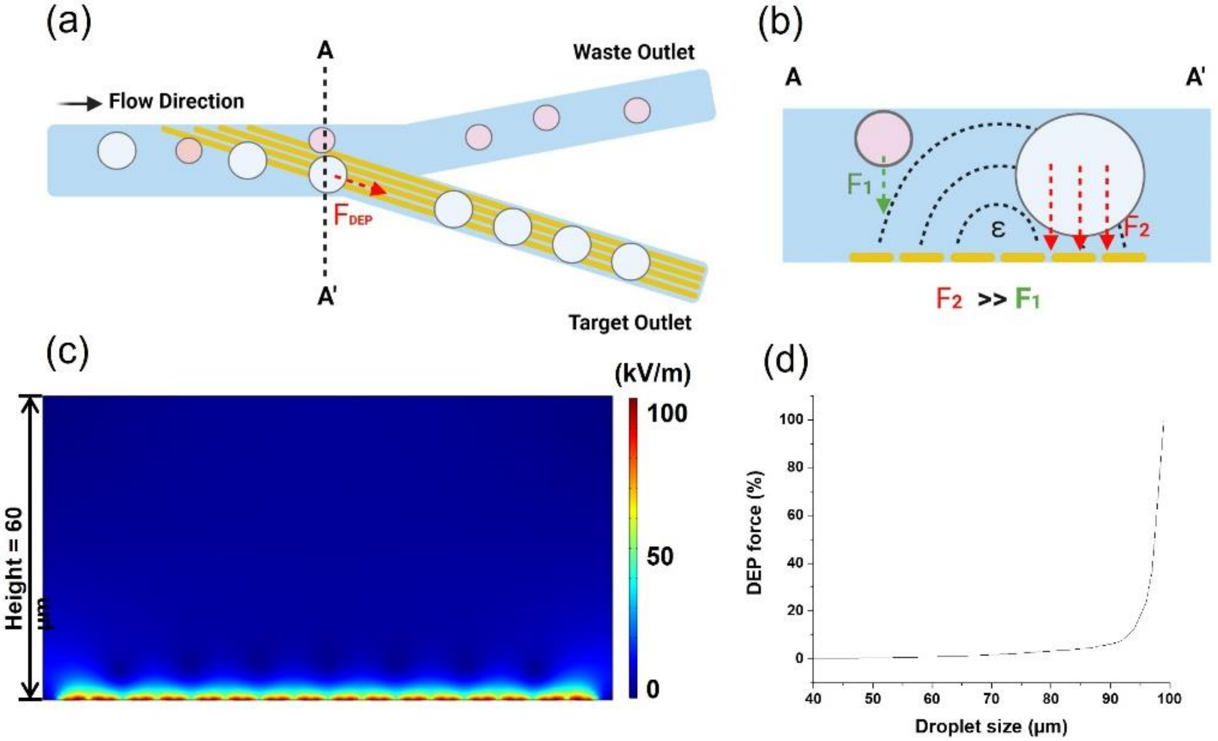

Fig. 7.1. The basic theory and working principle of the bandpass filter. (a) Schematic top view of the sorting region. (b) Cross-section view of the sorting region. (c) Cross-section view of COMSOL simulated electrical field generated by the proposed IDE design. (d) Subjected DEP force of different droplets in size in a 100 μm height channel.

7.4 Design and operating principle

Fig. 7.2a is the schematic graph of the proposed droplet size bandpass filter. The device consists of three sections: (1) droplet reflow and lifting section; (2) large droplets removal section (solely as a low-pass filter); (3) small droplets removal section (solely as a high-pass filter). In the droplet reflow and lifting section, the polydisperse droplet population was reinjected from the droplet reflow inlet. Different from conventional oil spacing after droplet reflow, here, the height of oil flow focusing channels was intentionally designed to be half (60 μm) of the droplet reflow channel (120 μm) (**Fig. 7.2b**). The purpose of this design is to create an underneath sheath flow while spacing out the reflow droplets, thus lifting the droplet to the ceiling of the microfluidic channel before approaching to IDE patterned region. When the droplets are delivered to the second section, where the first IDE (6 µm finger width and 6 µm spacing, **Fig. 7.2c**) array is patterned, due to the highly localized electrical field generated by IDE array, the large droplets (>100 µm) are affected by DEP force and are sorted out to Outlet 1. To prevent the unwanted attachment of droplets on the IDE electrode surface, the height of the exit channel is slowly increased from 120 µm to 160 µm starting from sorting junction and within a length of 500 µm, while the width of this channel is also designed to be gradually expanded by 2 times (**Fig. 7.2d**). The height of the main channel is then decreased to 80 µm (**Fig. 7.2e**) before entering the small droplet removal section (section 3). Similar to the large droplet removal section, this section allows DEP force to pull out all the droplets of the desired size. By adjusting the channel height at the sorting junction. Same as section 2, the height of the exit channel is slowly expanded from 80 µm to 120 µm within a length of 400 µm (**Fig. 7.2d**), consequently, droplets with target size range are sorted to Outlet 2 and the unwanted small droplets are then biased toward the waste Outlet 3. The bias flows applied here are to ensure all the reflow droplets stay on the opposing side of the IDE sorting exit channels before DEP manipulation, so that the overall sorting control can be less tricky to maintain. **Fig. 7.2f** and **Fig. 7.2g** here show the microscopic images of the fabricated microfluidic device and enlarged IDE patterns. To reduce the flow speed of sorted droplets, a circular expansion chamber is placed in front of each outlet for observation and measurement purposes (OB, in **Fig. 7.2f**).

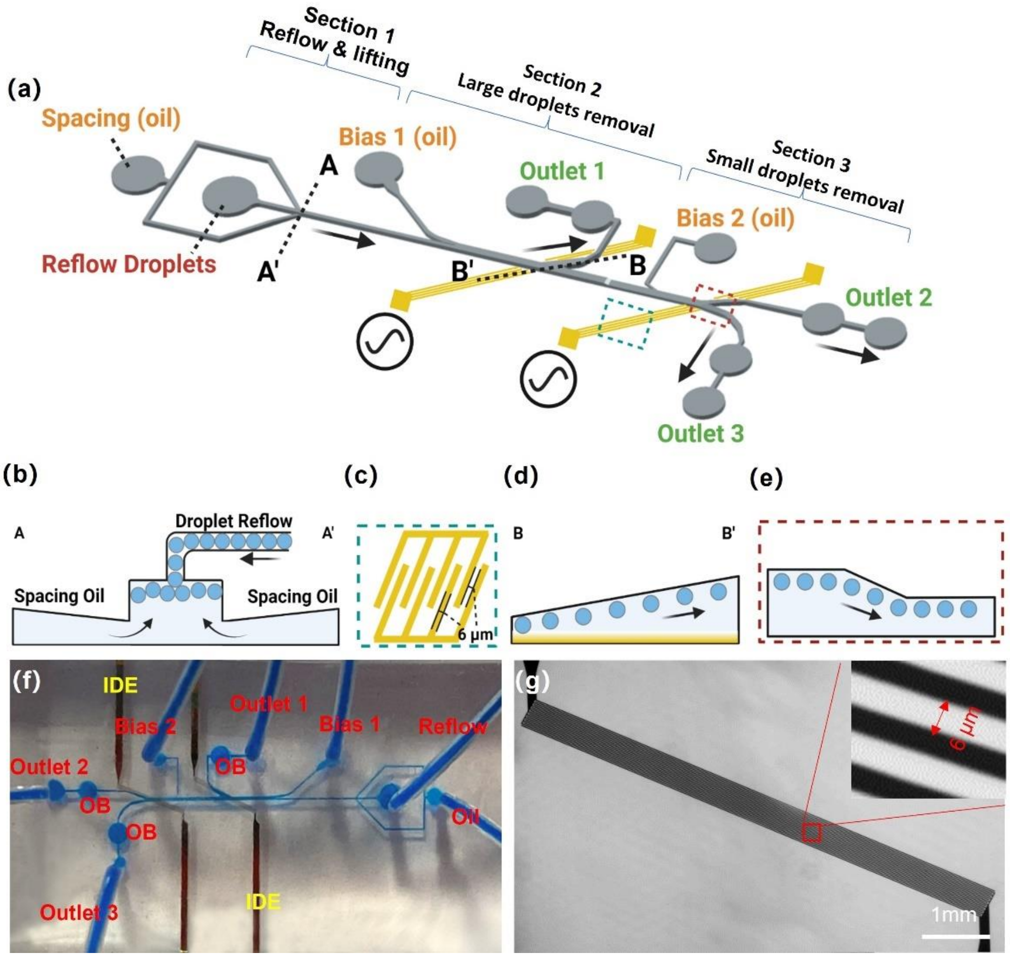

Fig. 7.2. The structure of the bandpass filter and its working principle (a) The schematics showing the three functional sections of the bandpass filter. (b) the cross-section view (A to A') of the reflow, spacing, and lifting junction. (c) IDE design with 6 μm finger width and 6 μm spacing. (d) The channel with an expansion of height and width at B to B'. (e) The height of the main channel was reduced from 120 μm to 80 μm. (f) Microscopic images of the fabricated microfluidic device and (g) enlarged IDE patterns.

7.5 Device fabrication

The device was replicated from master mold by the conventional soft lithography process. The replication master mold was prepared by a two-photon-polymerization (2PP) equipment (Nanoscribe Photonics Professional GT, IP-Q photoresist). 2PP printing technology here perfectly facilitated the fabrication of sloped structures, allowing smooth height transition between different regions.[165,166] Polydimehtyl siloxane (PDMS, Sylgard 184, Dow Corning, USA, mixed at a ratio of 10:1 base and curing agent) was poured onto the 2PP fabricated master mold and cured for 30 min at 85°C, and then released from the master mold. IDE electrode pattern was prepared by conventional microfabrication techniques. A Ti/Au (20 nm/ 100 nm) E-beam evaporation deposition was first performed on the 0.7 mm thick borosilicate glass substrate (Swiftglass, USA), followed by patterning of an etch mask using AZ1518 photoresist (AZ Electronic Materials, USA), selective metal etching of the Ti and Au layers, and finished with etching mask removal using AZ400T (AZ Electronic Materials, USA). To isolate and protect the IDE metal layer from direct contact with reagents flow in the microfluidic channel, a 100 nm SiN_x layer was deposited using plasma-enhanced chemical vapor deposition (PECVD) equipment (Oxford PlasmaLab 80Plus). Then, the released PDMS layer was bonded onto the SiN_x coated glass substrate on which the IDE design was patterned using O_2 plasma treatment. The PDMS microfluidic channel was aligned with the IDE pattern and bond together at 85°C for overnight. Right before the experiment, the fabricated device was rinsed with filtered fresh Aquapel (Pittsburgh Glass Works, LLC., USA), to make the entire microchannel surface hydrophobic. The schematic of the entire fabrication procedure is shown in **Fig. 7.3.**

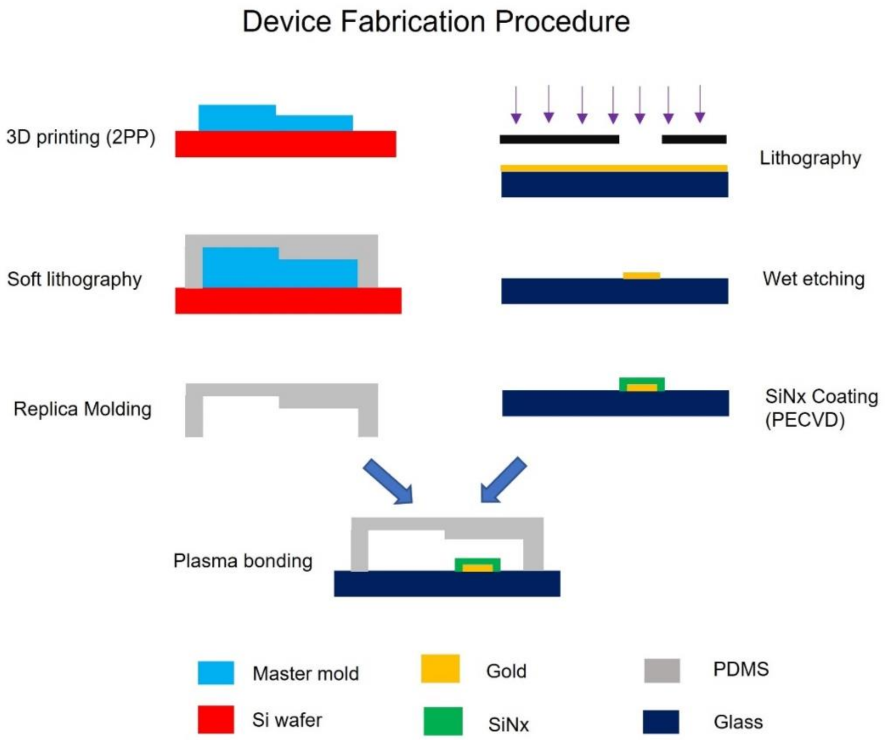

Fig. 7.3. Fabrication steps of the bandpass filter devices

7.6 Experiment setup

7.6.1 Droplet preparation

For proof-of-concept validation, droplets with three different sizes were first generated separately using DI water mixed with different food color dyes. Novec 7500 with 2% Pico-surf was used as the carrier oil. These droplets were then completely mixed before the test. The size of generated droplets was approximately 40 µm (black), 80 µm (blue), and 160 µm (red), respectively. For the system characterization experiment, the highly polydisperse droplet population was generated by sonicating (Ultrasonic Cleaner, BRASON 2800) the mixture of Novec 7500 (2% Pico-surf) with color dye (blue) at a volume ratio 1:1 in a 1ml syringe for 10 mins, the prepared droplet library was then directly reflowed into the bandpass filter platform for testing. For the demonstration of perfect merger application, the merged and unmerged droplets were prepared using a conventional merging method[163] with a resulting efficiency of approximately 80%. Two reflow droplets population were generated at the sizes of around 60 µm and 70 µm, targeting the successfully merged droplet size being around 82 µm, the over-merged droplets can be much larger than 90 µm. The prepared droplets were then reflowed to the bandpass filter for enrichment assay.

7.6.2 Cell preparation and cultivation after collection

THP1 cells (cell line info) were cultured in RPMI media (Sigma-Aldrich, St. Louis, USA) in an incubator under a 5% CO_2, 37 ˚C environments. After 3-day culture, the cells were then concentrated to 1×10^6 cells/ ml for generation of cell encapsulated droplets (120 µm in diameter). After generation, each droplet should contain approximately 7 cells on average. When operating the bandpass filter, flow rates were set to 50µl/h, and voltage was set at 240 V at 100 kHz. The initial viability of cells was evaluated before on-chip operation. Following, these droplets were divided into two groups, and one-half of the droplets were then reflowed through the bandpass filter microfluidic device. Afterward, both groups were collected and cultured in a microfluidic basket culture chamber for a second viability check at 4 h time point. The cells were stained with both HOCHEST (Sigma-Aldrich, St. Louis, USA) for counting of overall cell number and YOYO1(Sigma-Aldrich, St. Louis, USA) for counting of dead cells.

7.6.3 Experimental setup for proof-of-concept experiment

The bandpass filter system was first evaluated using a prepared droplet library containing droplets of three different sizes, 40 µm (black), 80 µm (blue), and 160 µm (red). The main channel heights for the bandpass filter were designed to be 120 µm (Section 2) and 80 µm (Section 3), aiming to sort out the 160 µm (red) and 80 µm (blue) from outlet 1 and outlet 2, respectively. The width of the reflow channel was designed to be 100 µm. The flow rates for the droplet reflow, spacer oil, bias oil infused from port 1 and bias oil infused from port 2 were set to 30 μl/ h, 200 μl/h, 400 μl/h, and 200 μl/h, respectively. The throughput under this flow condition was between 15-20 droplets/sec. The overall throughput can be adjusted readily by proportionally adjusting the flow rates. Syringe pumps (Fusion 400, Chemyx Inc.) were used to control volumetric flow rates of all input flows. The color images and videos were captured through a microscope using Nikon FI3 color camera (5K). A function generator (DG4102, Rigol) and a high-voltage power amplifier (Model 2210-CE, TREK) were used to apply an electrical field. In this experiment, a 240 V_{pp} 100 kHz square wave was used for generating the electric field for droplet sorting.

7.6.4 Experimental setup for device characterization using sonication generated droplets

To investigate the sensitivity and selectivity of the proposed sorting method, generated polydisperse droplets library which contains droplets with all different sizes (ranges from several microns to hundreds of microns) were employed. Two different designs were fabricated to examine the correlation of channel height and resulting passband. In this experiment, the channel height combinations for device 1 and device 2 were set to be 100 μm (Section 2)-90 μm (Section 3), and 100 μm (Section 2) - 80 μm (Section 3), respectively. In theory, both bandpass filters should sort droplets that size smaller than 100 μm with bandwidths of around 10 μm and 20 μm. The initial voltages were set to 240 V_{pp} (100 kHz square wave). When investigating the effect of voltage on the resulting passband, the voltage applied at the second IDE was gradually decreased to 120 V_{pp} with a decrement of 60 V_{pp}. In addition, the minimum voltages need to achieve ~100% sorting efficiency for different droplet sizes at different throughputs were also evaluated using a similar setup.

7.6.5 In-droplet IVTT workflow

IVTT of green fluorescent protein (GFP) was carried out to demonstrate the functionality of the proposed system in one biological assay. The plasmid pJL1-sfGFP was a gift from Michael Jewett (Addgene plasmid # 102634). The plasmid was extracted using the ZymoPURE plasmid miniprep kit (Zymo Research, CA, USA). Forward primer 5'GCG AAT TAA TAC GAC TCA CTA TAG GG 3' and reverse primer 5' TTC TAA TCA GAA TTG GCT TTC AGC 3' were used to amplify the GFP sequence to generate DNA template for NEB PURExpress *In vitro* protein synthesis (NEB#E6800L). Droplet generation (80 μm) and PCR amplification were carried out using the protocol described by Sukovich et.al.[167], (without the addition of Tween 20). PCR product generated using high fidelity Q5 polymerase was cleaned and concentrated using the Zymo Research DNA clean and concentration (DCC) kit and used as a positive control. To carry out IVTT of GFP, PCR amplified droplets are reflown and merged with droplets (100μm) containing the NEB PURExpress protein synthesis kit, which included NEB PURExpress solution A (55% v/v), of NEB PURExpress solution B (42%), and RNasin® Ribonuclease Inhibitor (3%). The merged IVTT droplets were collected in a 3D printed cultivation chamber (**Fig. 7.4**) and incubated at 37 ˚C for 3 h. The fluorescent intensity of expressed GFP was measured by excitation at 479 nm and emission at 520 nm. GFP expression was also confirmed by comparison of SDS-PAGE bands with the control group that was conducted in well-plate.

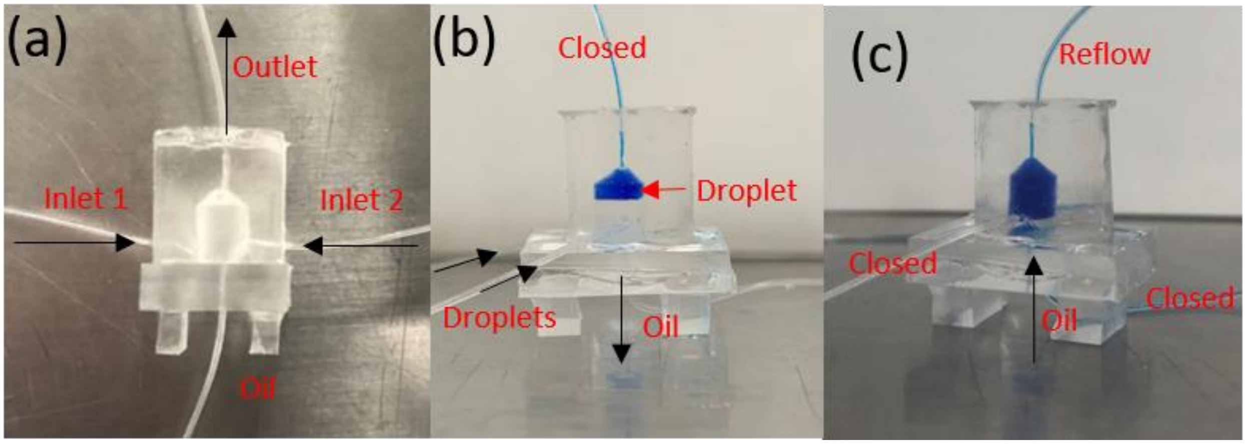

Fig. 7.4. The cone shaped PDMS chamber for droplet storage, cultivation, and reflow. (a) Empty chamber, (b) after blue color dye-encapsulated droplet collection, and (c) during droplet reflow into the outlet tubing. Generated droplets are collected from either or both inlets 1 and/or 2. At the droplet collection phase, the outlet is pinched, and the oil tube is open to discharge extra oil. At the droplet reflow phase, the inlet 1 and 2 are pinched, and oil flows into the chamber from the bottom oil tube to push the droplets out from the top side.

7.6.6 Data collection and analysis

The sizes of collected droplets are measured at the circular observation chambers. A workflow was developed in Fiji/ImageJ to calculate the size of the droplets and then applied to all the acquired images. The bright-field images were first converted to binary masks based on an arbitrary intensity threshold. Holes in the resulting droplet masks were filled and the bounding boxes of all the droplets were extracted. The height and width of each droplet's bounding box serve as two measurements of its diameter. An average of the two was taken as the final measurement. A scaling of 1 µm/px was determined for the objective and camera being used and based on this, the unit of the diameter measurement was converted from pixels to micrometers. At least 200 droplets were counted and measurement for each statistical analysis. The images of the observation chamber were saved and then analyzed using the build-in measurement tool of the camera software to obtain the droplet size accordingly.

7.7 Results

7.7.1 Proof of concept validation

The reflow droplet population consists of three sizes of droplets: 40 µm (black), 80 µm (blue), and 160 µm (red). Based on our sorting theory, the 160 µm and 80 µm sized droplets should be sorted out from outlet 1 and outlet 2, respectively. The 40 µm sized droplets should be not affected by IDE electric field thus flow directly toward outlet 3 (**Fig. 7.5a**). The experimental results shown in **Fig. 7.5b** and **Fig. 7.5c** agreed with the proposed theory. The performance of the 120 µm -80 µm bandpass filter device was then evaluated under various throughputs (5, 20, and 100 droplets/second), and the operation efficiency was calculated. 500 droplets of each color were count for analysis of false-positive (FP) and false-negative (FN) rates at each outlet, and the statistic is illustrated in **Fig. 7.5d**. The FNs and FPs for all outlets and throughputs were less than 1%, at all three throughput conditions. It can be seen that the percentages of FPs are larger than FNs. The major cause of this is likely to be the collision of targeted droplets with non-targeted droplets, which pushes the non-target droplet towards unmatched outlet channels. Moreover, a higher flow rate or larger throughput could lead to a slightly higher FN rate, but causing no significant increase to the FP rate. Overall, the system efficiency is greater than 99% with throughputs less than 100 droplets/sec.

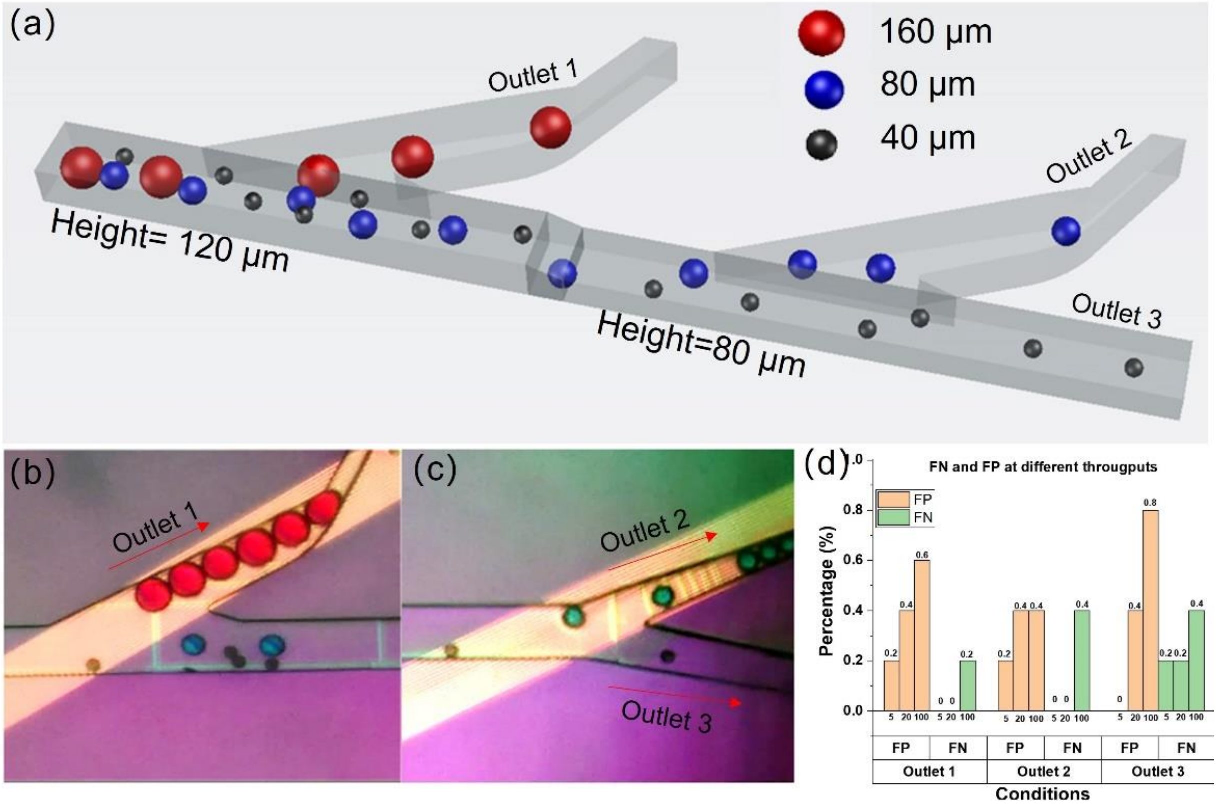

Fig. 7.5. Proof of concept validation using a 120 µm – 80 µm bandpass filter. (a) schematics of the expected result based on the theory and working principle. The experimental result at sorting junction of (b) section 2 and (c) section 3. (d) Sorting efficiency at all outlets with a variety of throughputs (*N*=500)

7.7.2 Characterization using sonication generated droplets

The top view of the entire bandpass filter device (100 µm - 90 µm) is shown in **Fig. 7.6a**. The prepared polydispersed droplets (**Fig. 7.6b**) were reflowed to the system and resulting droplets were collected at each outlet to find out the passband of the 100 µm - 90 µm combination device. The collected droplets from outlets 1, 2, and 3 are demonstrated in **Fig. 7.6c**, **Fig. 7.6d**, and **Fig. 7.6e**, respectively. It can be seen that the bandpass pass filter was able to target droplets with a very specific size. The size of collected droplets (*N* = 320) was measured at the circular observation chamber to calculate the performance of the proposed bandpass filter. The passband (0dB) for this device is approximately from 74 µm to 78 µm (**Fig. 7.6f**, dark blue), while having a bandwidth (-3dB) from 71 µm to 81 µm. (**Fig. 7.6f**, light blue). The result also indicates that for a complete separation of two groups of droplets, the size difference needs to be no less than 7 μm. In addition, the size distribution of the collected droplets from different outlets is shown in **Fig. 7.6g**.

To evaluate how the change of channel geometry will affect the performance of bandpass filter, **Fig. 7.6h** compares the size distribution of droplets collected from outlet 2, between results from 100 μm-90 μm filter and 100 μm-80 μm filter. In total, more than 300 droplets were collected from outlet 2 from each design, and data analysis has shown that the smallest size of droplets that were collected from outlet 2 from 100 μm-80 μm bandpass filter was about 60 μm. Compared with the results from 100 μm-90 μm bandpass filter design which collected a minimal 70 μm size droplet, the lower bound of the bandpass filter was extended by about 10 μm by simply reducing the main channel height of the third section by 10 μm.

Besides, the effect of voltage on passband was also investigated by adjusting the voltage applied on the second IDE pattern (Voltage applied on first IDE remained constantly at 240 V_{pp}). As can be seen, the filter tended to sort out larger droplets (75 μm -82 μm) when the applied voltage decreased. The width of the passband under 120 V_{pp} was almost shrunk to half compared to the case of 240 V_{pp}.

To evaluate the impact from different types of carrier oil, another commonly used fluorinated oil, FC40, was used to substitute Novec 7500 and evaluated. FC40 has relatively higher density than Novec 7500 (1.85 g/ml vs 1.61 g/ml). Based on our theory, heavier oil provides greater buoyancy force, which supports more firmly hugging of droplets to the microchannel ceiling. The result is presented in **Fig. 7.6j**. Although the mean droplet size of the FC40 group is slightly larger than the Novec 7500 group, no statistically significant difference was found ($p>0.05$). Both types of carrier oil are believed to be suitable in this application.

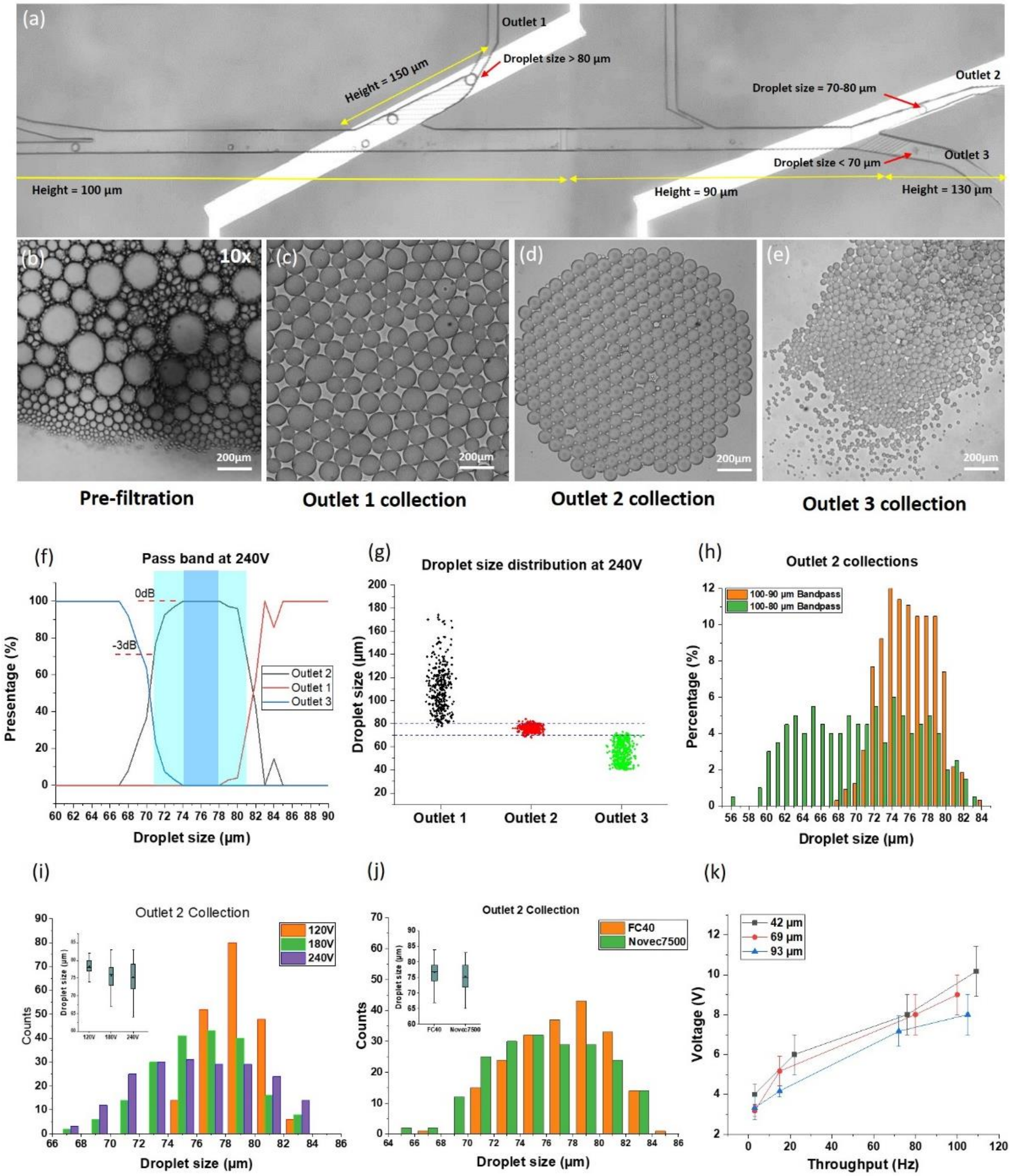

Fig. 7.6. (a) The top view of a working 100 µm - 90 µm bandpass filter device. (b) sonication generated droplets for reflow. (c) Collected large droplets from outlet 1. (d) Collected bandpass-filtered droplets from outlet 2. (e) Collected small droplets from outlet 3. (f) Passband of 100 µm - 90 µm filter under an applied voltage of 240 V for both IDE. (g) Size distribution of collected droplets from three outlets (*N*=200). (h) Comparison of droplet size distribution bandpass-filtered by 100 µm - 90 µm device and 100 µm - 80 µm device. (i) The effect of Voltage on the filtered droplet size. (j) The effect of density of carrier oil on the filtered droplet size. (k) The effect of through to applied voltage for different sizes of droplets.

The minimal voltage required for sorting three sizes of droplets (24 μm, 69 μm, and 93 μm) under various throughputs is illustrated in **Fig. 7.6k**. The correlation of throughputs and voltages is positively related. Moreover. Pulling of smaller droplets required a higher voltage than larger droplets.

7.7.3 Biocompatibility of the IDE system

Droplets containing THP1 cells were utilized in the presented bandpass droplet filter system as an example to evaluate the biocompatibility of the proposed IDE system. Droplets that before manipulation, from the first outlet, second outlet, and the third outlet were each collected, and the viability of cells was examined. Overall, 90% of cells were viable 4 h after manipulation, compared with 90% that without manipulation, we believed that such a system will not affect cellular viability under our determined operating conditions. Our experiment finding is also matched with previously published results.[50] The detailed information can be found in **Fig. 7.7**.

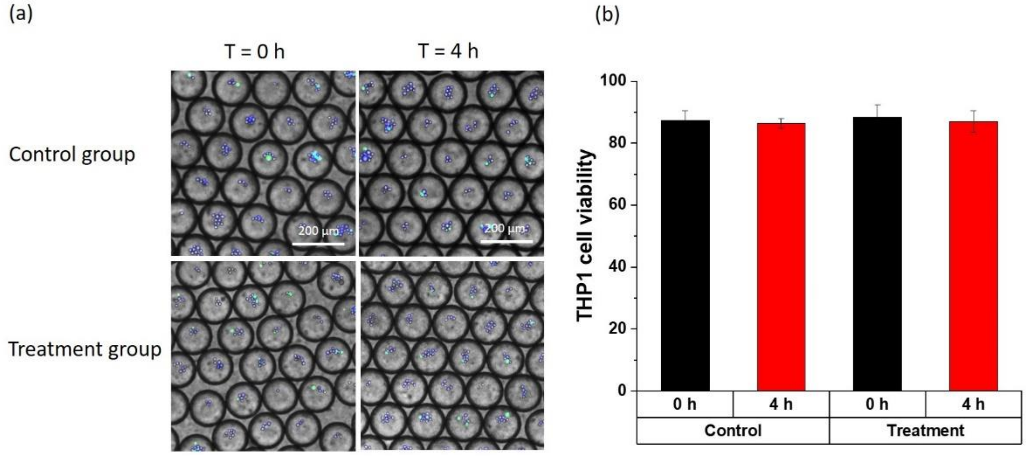

Fig. 7.7 Biocompatible test of the IDE system using THP1 cells (a) Viability stain of the cell for control and treatment groups at 0 h and 4 h time point (blue = HOCHEST stain, green = YOYO1 strain). (b) Comparison of the THP1 cell viability of control and treatment group at 0h and 4h.

7.7.4 Application 1: exclude the unmerged and over-merged droplets

Typically, when two droplets (carrying different cells/reagent) need to be merged into one single droplet, droplet pairing before merging is the most critical step to ensure all droplets are merged at a one-to-one ratio. Among almost all the previously published methods, the droplet merging efficiency remains in the range of 80–95% Considering an optimum droplet library screening scenario which is of 95% pairing/merging efficiency, when processing a library of 1 million droplets, there are still about 50000 droplets that will potentially be mispaired or over-merged, and later contribute to the false positives and/or false negatives in droplet screening. With the combination of the proposed bandpass filter, such malperformance can be greatly alleviated by removing unpaired/unmerged droplets as well as over-merged droplets (**Fig. 7.7a** and **Fig. 7.7b**).

In this application, a droplet population with around 20% "false" droplets was prepared by a conventional droplet merging microdevice. Here, 100 μm-80 μm design was used and the experiments were conducted under throughput of 20 droplets/second, with 240 V_{pp} for both IDEs. After the removal of unwanted droplets, the collected droplet group contains more than 99% of the target droplet. The merger can also be further integrated with the bandpass filter as a two-in-one device. A major limitation of this application is that the filtration requires a few microns different in diameter. In this case, it is expected that 60 μm droplet will be merged with 70 μm droplet to get 82 μm droplet, so the original droplet library contains droplets of quite different sizes (60 μm, 70 μm, 82 μm, > 91 μm). In the case in which a giant droplet is merged with a tiny droplet, the size change of the resulting droplet may not large enough for distinguishment. In this case, the false-positive rate could significantly increase.

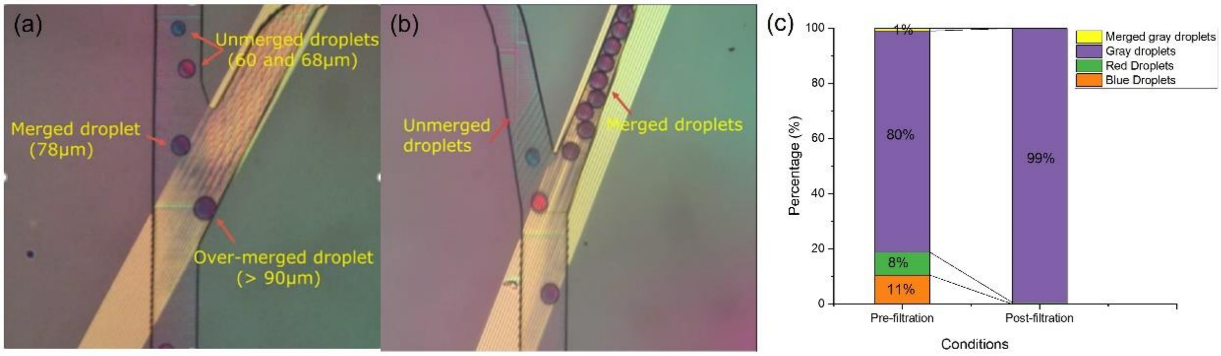

Fig. 7.8 Bandpass filter to remove the unsuccessfully merged and over-merged droplets from the upstream merging step. (a) Section 2 at sorting junction showing removal of the over-merged droplets. (b) Section 3 at sorting junction showing removal of the unsuccessfully merged droplets. (c) Comparison of droplet components pre and post-bandpass filtration.

7.7.5 In-droplet IVTT

IVTT assay itself provides a promising alternative method for in vivo expression of heterogeneous proteins and could be utilized to generate a combinatorial synthesis protein library for functional screening. On the other hand, droplet microfluidic systems have been extensively utilized to perform functional library screening for their high-throughput nature, and various functional screening assays have already been achieved. It is a natural match to incorporate microfluidics technologies to achieve IVTT library functional screening, however, several issues will have to be resolved for reliable performance. First, although droplet digital PCR has been realized in previous studies, it was essential to add surfactants such as Tween 20 and/or 80[167,168] into the reagent buffer to ensure the uniformity of droplets after thermal cycling. However, the addition of such surfactants and detergents could significantly impact cell viability, which becomes unacceptable for cellular functional assays. Another option here is to not add these surfactants into the reagent buffer, however, the resulting droplets will become quite diverse in size. For compensation, a critical droplet size control method needs to be added here to remove unwanted droplets/micelles. Second, IVTT protein synthesis kits need to be added into droplets after thermal cycling for GFP express, so another droplet merging step is required. Here, droplet size variation after droplet merging becomes problematic again. The droplet size variation will cause improper concentration/expression of IVTT and cause false downstream detection/sorting performance. Here, as a biological application demonstration, we examined whether it is feasible for us to realize IVTT assay in droplet microfluidic format under the help of the IDE size-based droplet sorting technique.

Based on the previous discussion, a droplet-based IVTT workflow is proposed (**Fig. 7.9a**). IVTT templates were first used to generate a single-encapsulated droplet library (step ①) and then went through thermocycling to complete ddPCR amplification (step ②). Afterward, an IDE filtration unit was introduced here to remove droplets with unwanted sizes (step ③). Following, the remaining droplet library was merged with IVTT substrate by droplet merger (step ④). Then, a second IDE filtration unit was utilized here to remove over-merged or unmerged droplets (step ⑤). Finally, IVTT protein expression was completed in droplet format (step ⑥), and the droplet library was ready for downstream detection/sorting. Here, the IVTT template library that contains different levels of GFP protein expression was used to generate a visualized mock droplet library. Throughout the entire process, droplets were collected and imaged under microscope and their size distribution was analyzed. A significant improvement of uniformity was confirmed when comparing the droplet size distribution before/after the IDE filtration unit. As a control, when skipping both IDE filtration steps, harvested droplet library was composed of droplets with different sizes (varied from tens of µm to hundreds of µm), as well as droplets without GFP expression (incorrectly merged droplets). Around 66% of droplets were confirmed to be properly expressed and with the correct size. In contrast, when adding those two IDE filtration steps, 97.5% of droplets were confirmed to be flawless. Proposed IDE filtration units indeed improved the efficiency of droplet digital IVTT assays.

Finally, to validate whether implementing such IDE size-based sorting technology will impede the proper expression of the IVTT template, the expressed GFP proteins were examined by serum protein electrophoresis (**Fig. 7.9b**). Results showed that all types of proteins were expressed in the same manner both in terms of quantity and abundance. The IDE filtration unit did not affect the template and downstream expression.

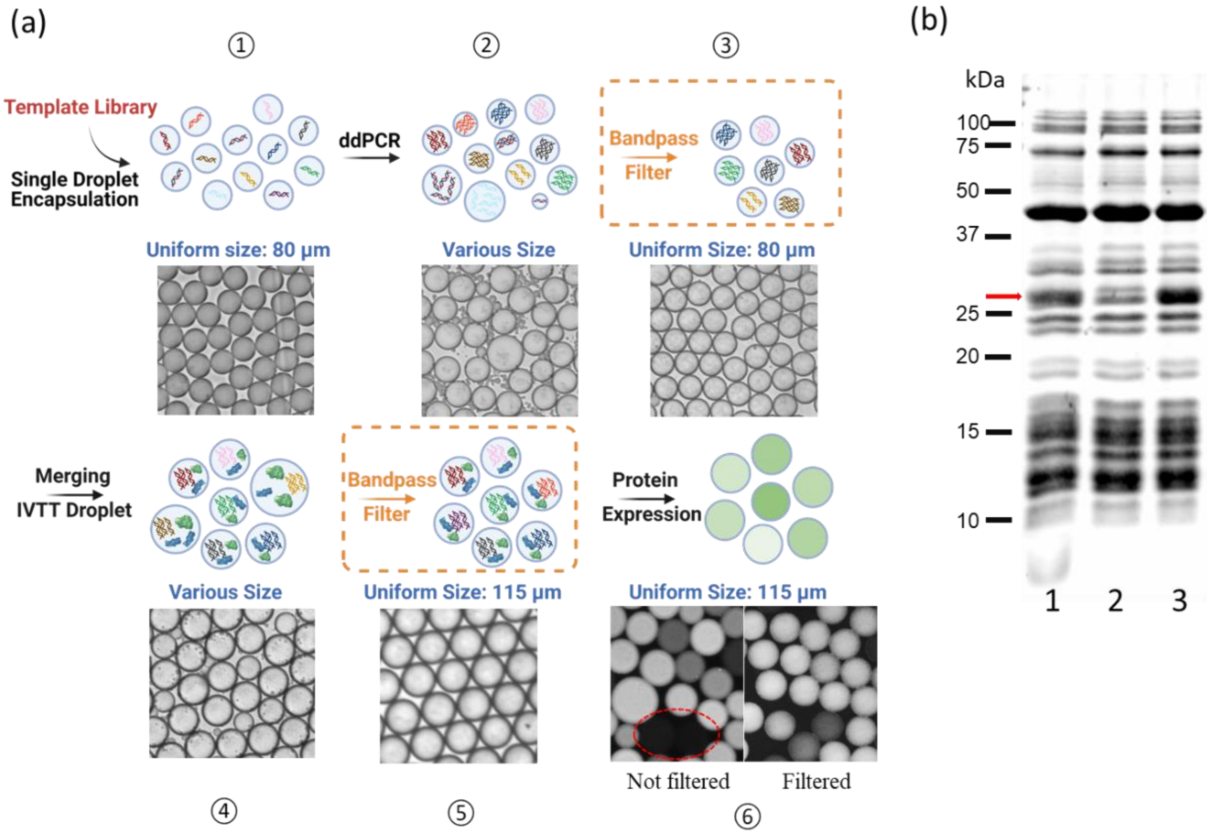

Fig. 7.9 Droplet-based IVTT workflow and gel electrophoresis validation. (a) Droplet-based IVTT workflow with the integration of bandpass filter for droplet size quality control. (b) Gel electrophoresis result comparison with well-plate negative and positive controls.

7.8 Discussions

In the previous result section, we have demonstrated several factors that can affect the performance of the IDE filtration unit. The applied voltage can greatly affect the width of passband/filtration, as they can provide extra/less DEP force acting on all droplets. As an example, when using 90-100 bandpass configuration, Base on **Fig. 7.6i**, the minimum sort size is negatively related to the applied voltage. The lower boundary of filtered droplet size range shifted from 67 µm to 74 µm when applied voltage decreased from 240 V to 120 V, which mean reducing voltages of both IDEs could cause a shift of passband from 70 µm - 80 µm to 70 + λ1 µm - 80 + λ2 µm. Here the λ1 and λ2 are passband shifts by microns. The minimum and maximum working voltage for throughput 20 droplets/sec were 120 V and 300 V. Too high voltage for a relatively low throughput could potentially slow down the sorted droplets and cause merging when they contact one another. Serval other factors can also affect the performance of this bandpass filter system. Design with different channel heights will drastically result in two distinct collection profiles (**Fig. 7.6h**). Additionally, when using different types of carrier oil, specifically FC 40 (density 1.85g/cm3) and Novec 7500 (1.61g/cm3), the density difference also results in a slight variation on the collected droplet size profile (**Fig. 7.6j**). Denser carrier oil (FC 40) will provide better buoyancy force acting on droplets, therefore further isolate smaller droplet size to be apart from IDE localized electric field. Also, when the flow rate increases, Stokes' force acting on droplets will be increased accordingly, therefore a higher DEP force (thereby a higher applied voltage) will be required to manipulate/diverge the droplet towards the hit outlet (**Fig. 7.6k**). Overall, based on the application requirement, the first and second pairs of IDE manipulation can be turned on/off accordingly, to achieve a high-pass filter, low-pass filter, or bandpass filter. Additionally, the lower bond, higher bond of such filter can be tuned by increase/decrease the applied voltage, change of channel heights, and choice of carrier oil, throughput, or a combination of all listed above.

This bandpass method is only suitable for the cases in which carrier oil density is higher than that of the dispensed aqueous solution. Fortunately, fluorinated oil such as HFE (1.6-1.7 g/ml), Novec (1.6-1.7 g/ml) and FC series (1.8-2.0 g/ml) as the most popular oil family selected for droplet microfluidic applications meet this requirement. Fabrication error from SiNx coating could to some extent affect to minimum voltage and a voltage range that need for the sorting. Thicker SiNx coating normally requires a higher working voltage. The unideal alignment of IDEs with fluidic channels could potentially lead to a droplet trapping issue. There is a small chance that some medium-size droplets are trapping on the edge of the IDE at the vertex of the two split channels. **Fig. 7.10** shows the idea alignment and nonideal alignment with droplet trapping near the vertex.

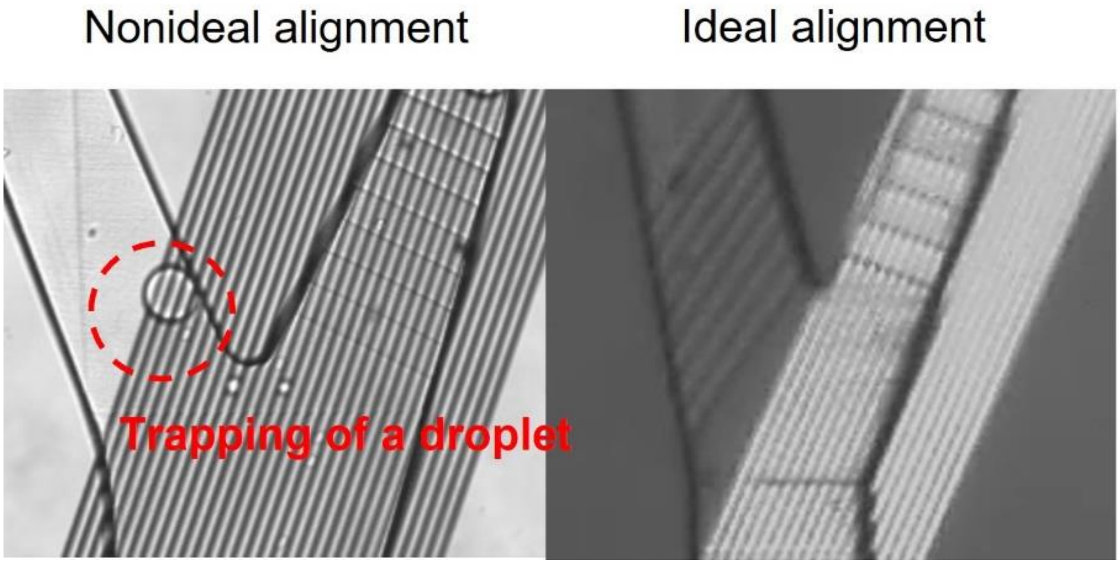

Fig. 7.10 Examples of nonideal and ideal alignment of IDE to the microfluidic channel. (a) The droplet is trapped at the edge of IDE before exiting. (b) An example of an ideal alignment.

7.9 Conclusion

In this chapter, a passive droplet size-based bandpass filter platform that utilizing a combination of natural buoyancy phenomena and localized interdigitated electric field for DEP sorting of the droplet by size was designed and successfully demonstrated. The system efficiency of sorting 80 µm droplets out from 40 µm and 160 µm droplets was larger than 99% at the throughput of 100 droplets/sec. A higher voltage is needed to sort out droplets at higher throughput. The passband can be adjusted by changing the combination of channel heights and applied voltages. Based on the resulting bandwidth, the device successfully separated droplets that are only 7 µm different in diameter. The utility of the developed system was demonstrated in two real scenarios. The results indicate that our bandpass filter was able to remove more than 98% of the unwanted or false droplets from the droplet merging step and droplet PCR. The developed bandpass filter system can be potentially used in combination with other parts of the microfluidic manipulation systems to significantly improve the overall performance of these systems.

8. OVERALL REVIEW AND CONCLUSIONS

The aim of this thesis is to enable multiple biological assays, specifically on host-pathogen interaction study, to be realized in the microfluidic platform, following, to use calibrated system to facilitate/replace conventional investigations, which are typically low-throughput and labor-intensive. Progresses have been made in both microfluidic technology advancements as well as biological assay realizations. Major achievements are as following:

a. Development of SEER platform for investigating evolutionary stress response

Developed SEER platform can carry evolutionary host-pathogen interaction study in the seamless manner. Utilizing porous membrane and the physical dimension differences between host and bacterial cells, SEER platform can effectively achieve selective trapping/releasing of target cell types, and can provide contamination-free chamber for host-pathogen interaction. The evolutionary assay was realized in the lab-on-a-chip format, with the effort in automated system development, SEER platform can minimize the human input throughout the repetitive operations. Lastly, by analyzing the harvested evolved strain from SEER system, we reveal that cpxR gene, which found as a SNP mutation site throughout the evolution process, contributes to the intracellular pathogen survival phenotype.

b. Development of adherent bacterial cell identification system

To detect the pathogen from unknown environmental sample, a microfluidic system focusing on isolation of adherent bacterial cells was developed. The developed platform utilized dielectrophoretic force acting on host cells to fish out the adherent bacterial cells after co-incubation steps. This simple all-in-one platform allows the examination of all extracted bacterial strains at single run without necessarily investigate each isolated strain one at a time. The system was first characterized with 6 types of standard adherence cellular model, followed up with performance test on one artificial mock community and two soil samples. The performance of developed platform was validated, and the dramatic increase of overall throughput and no request of cell labeling make this developed platform a very attractive option for real-time environmental pathogen outbreak surveillance.

c. Development of droplet microfluidics technologies

In terms of fundamental microfluidic technology advancements, three major aspects have been investigated. First, a droplet microfluidic technology which can effectively separate two different types of cells within the droplet was proposed and developed. With such technology, cells inside the same droplet can be separated due to their different dielectrophoretic response, resulting two daughter droplets each containing only one type of the cells.

Second, with the previously developed in-droplet DEP concentration function, by incorporating with a downstream pairing and merging unit, we proposed an integrated droplet microfluidic platform which can systematically concentrate the cellular content, remove unwanted droplet reagent, pair and merge with fresh reagent, all in a serial manner, which essentially achieve in-droplet centrifugation and resuspension. The system was validated with two common application scenarios, and can achieve up to 88% of solution exchange efficiency.

Lastly, inspired by the use of interdigitated electrode pattern in the adherent bacterial cell study, a DEP based droplet selection unit was developed utilizing the highly localized electric field that generated from IDT design. Such technology utilizes the droplet buoyancy and localized electric field to achieve high precision selection of droplets that with specific droplet sizes. Developed platform was tested with polydisperse droplet library and proved its high selectivity and accuracy.

d. Development of microfluidics fabrication methods using novel lithography tools

Using two-photon-polymerization tools, the master molds that typically used in traditional soft lithography process now can be fabricated with additional freedom on z axis, with high precision. This technology therefore enables fabrication of more complicated structure, especially with multiple/gradual height transitions. By incorporating this novel lithography tool, several novel microfluidic structures have been developed to resolve existing microfluidic challenges, covering from air bubble aggregation, droplet transitions and so on.

Remaining works entail the completion of biological investigation for SEER platform, the sample analysis of aliquots from adherent bacterial cells platform collection.

REFERENCES

1 Zarember, K. A. *et al.* Innate immunity against Granulibacter bethesdensis, an emerging gram-negative bacterial pathogen. *Infection and immunity* **80**, 975-981, doi:10.1128/IAI.05557-11 (2012).

2 Audic, S., Lescot, M., Claverie, J. M. & Scholz, H. C. Brucella microti: the genome sequence of an emerging pathogen. *BMC genomics* **10**, 352, doi:10.1186/1471-2164-10-352 (2009).

3 Morris, J. G., Jr. & Southwick, F. S. Brucella, voles, and emerging pathogens. *The Journal of infectious diseases* **202**, 1-2, doi:10.1086/653085 (2010).

4 Rabozzi, G. *et al.* Emerging zoonoses: the "one health approach". *Safety and health at work* **3**, 77-83, doi:10.5491/SHAW.2012.3.1.77 (2012).

5 Seleem, M. N., Boyle, S. M. & Sriranganathan, N. Brucellosis: a re-emerging zoonosis. *Veterinary microbiology* **140**, 392-398, doi:10.1016/j.vetmic.2009.06.021 (2010).

6 Gray, M. W., Burger, G. & Lang, B. F. Mitochondrial Evolution. *Science* **283**, 1476-1481, doi:10.1126/science.283.5407.1476 (1999).

7 Moustafa, A. *et al.* Genomic Footprints of a Cryptic Plastid Endosymbiosis in Diatoms. *Science* **324**, 1724-1726, doi:10.1126/science.1172983 (2009).

8 Laloum, T. *et al.* Two CCAAT-box-binding transcription factors redundantly regulate early steps of the legume-rhizobia endosymbiosis. *The Plant Journal* **79**, 757-768, doi:https://doi.org/10.1111/tpj.12587 (2014).

9 Scholz, M. *et al.* Large scale genome reconstructions illuminate Wolbachia evolution. *Nat Commun* **11**, 5235, doi:10.1038/s41467-020-19016-0 (2020).

10 Lefoulon, E. *et al.* Breakdown of coevolution between symbiotic bacteria Wolbachia and their filarial hosts. *PeerJ* **4**, e1840, doi:10.7717/peerj.1840 (2016).

11 Marchetti, M. *et al.* Experimental Evolution of a Plant Pathogen into a Legume Symbiont. *PLOS Biology* **8**, e1000280, doi:10.1371/journal.pbio.1000280 (2010).

12 Marchetti, M. *et al.* Shaping bacterial symbiosis with legumes by experimental evolution. *Mol Plant Microbe Interact* **27**, 956-964, doi:10.1094/mpmi-03-14-0083-r (2014).

13 Waite, A. J. & Shou, W. in *Engineering and Analyzing Multicellular Systems: Methods and Protocols* (eds Lianhong Sun & Wenying Shou) 27-38 (Springer New York, 2014).

14 Mackaness , G. B. Cellular resistance to infection. *Journal of Experimental Medicine* **116**, 381-406, doi:10.1084/jem.116.3.381 (1962).

15 Mackaness , G. B. The immunological basis of acquired cellular resistance. *Journal of Experimental Medicine* **120**, 105-120, doi:10.1084/jem.120.1.105 (1964).

16 Murray, E. G. D., Webb, R. A. & Swann, M. B. R. A disease of rabbits characterised by a large mononuclear leucocytosis, caused by a hitherto undescribed bacillus Bacterium monocytogenes (n.sp.). *The Journal of Pathology and Bacteriology* **29**, 407-439, doi:https://doi.org/10.1002/path.1700290409 (1926).

17 Fidalgo, L. M. & Maerkl, S. J. A software-programmable microfluidic device for automated biology. *Lab on a Chip* **11**, 1612-1619, doi:10.1039/C0LC00537A (2011).

18 Dittrich, P. S. & Manz, A. Lab-on-a-chip: microfluidics in drug discovery. *Nat Rev Drug Discov* **5**, 210-218, doi:10.1038/nrd1985 (2006).

19 Yager, P. *et al.* Microfluidic diagnostic technologies for global public health. *Nature* **442**, 412-418, doi:10.1038/nature05064 (2006).

20 Han, A., Hou, H., Li, L., Kim, H. S. & de Figueiredo, P. Microfabricated devices in microbial bioenergy sciences. *Trends in Biotechnology* **31**, 225-232, doi:https://doi.org/10.1016/j.tibtech.2012.12.002 (2013).

21 Rusconi, R., Garren, M. & Stocker, R. Microfluidics Expanding the Frontiers of Microbial Ecology. *Annual Review of Biophysics* **43**, 65-91, doi:10.1146/annurev-biophys-051013-022916 (2014).

22 Kaminski, T. S., Scheler, O. & Garstecki, P. Droplet microfluidics for microbiology: techniques, applications and challenges. *Lab on a Chip* **16**, 2168-2187, doi:10.1039/C6LC00367B (2016).

23 Masi, M., Pinet, E. & Pagès, J. M. Complex Response of the CpxAR Two-Component System to β-Lactams on Antibiotic Resistance and Envelope Homeostasis in Enterobacteriaceae. *Antimicrob Agents Chemother* **64**, doi:10.1128/aac.00291-20 (2020).

24 Hand, W. L. & King-Thompson, N. L. Contrasts between phagocyte antibiotic uptake and subsequent intracellular bactericidal activity. *Antimicrob Agents Chemother* **29**, 135-140, doi:10.1128/aac.29.1.135 (1986).

25 Prokesch, R. C. & Hand, W. L. Antibiotic entry into human polymorphonuclear leukocytes. *Antimicrob Agents Chemother* **21**, 373-380, doi:10.1128/aac.21.3.373 (1982).

26 Huang, C., Wippold, J. A., Stratis-Cullum, D. & Han, A. Eliminating air bubble in microfluidic systems utilizing integrated in-line sloped microstructures. *Biomedical Microdevices* **22**, 76, doi:10.1007/s10544-020-00529-w (2020).

27 M9 minimal medium (standard). *Cold Spring Harb. Protoc.*, doi:10.1101/pdb.rec12295. (2010).

28 Weatherspoon-Griffin, N., Yang, D., Kong, W., Hua, Z. & Shi, Y. The CpxR/CpxA two-component regulatory system up-regulates the multidrug resistance cascade to facilitate Escherichia coli resistance to a model antimicrobial peptide. *J Biol Chem* **289**, 32571-32582, doi:10.1074/jbc.M114.565762 (2014).

29 Pomposiello, P. J., Bennik, M. H. & Demple, B. Genome-wide transcriptional profiling of the Escherichia coli responses to superoxide stress and sodium salicylate. *J Bacteriol* **183**, 3890-3902, doi:10.1128/jb.183.13.3890-3902.2001 (2001).

30 Baba, T. *et al.* Construction of Escherichia coli K-12 in-frame, single-gene knockout mutants: the Keio collection. *Mol Syst Biol* **2**, 2006.0008, doi:10.1038/msb4100050 (2006).

31 Wielgoss, S. *et al.* Mutation rate dynamics in a bacterial population reflect tension between adaptation and genetic load. *Proceedings of the National Academy of Sciences* **110**, 222-227, doi:10.1073/pnas.1219574110 (2013).

32 Toprak, E. *et al.* Evolutionary paths to antibiotic resistance under dynamically sustained drug selection. *Nature genetics* **44**, 101-105, doi:10.1038/ng.1034 (2012).

33 Wielgoss, S. *et al.* Mutation rate dynamics in a bacterial population reflect tension between adaptation and genetic load. *Proceedings of the National Academy of Sciences of the United States of America* **110**, 222-227, doi:10.1073/pnas.1219574110 (2013).

34 Quainoo, S. *et al.* Whole-Genome Sequencing of Bacterial Pathogens: the Future of Nosocomial Outbreak Analysis. *Clinical Microbiology Reviews* **30**, 1015-1063, doi:10.1128/CMR.00016-17 (2017).

35 Oniciuc, E. A. *et al.* The Present and Future of Whole Genome Sequencing (WGS) and Whole Metagenome Sequencing (WMS) for Surveillance of Antimicrobial Resistant

Microorganisms and Antimicrobial Resistance Genes across the Food Chain. *Genes* **9**, doi:10.3390/genes9050268 (2018).

36 Rossen, J. W. A., Friedrich, A. W. & Moran-Gilad, J. Practical issues in implementing whole-genome-sequencing in routine diagnostic microbiology. *Clinical Microbiology and Infection* **24**, 355-360, doi:https://doi.org/10.1016/j.cmi.2017.11.001 (2018).

37 Tagini, F. & Greub, G. Bacterial genome sequencing in clinical microbiology: a pathogen-oriented review. *European Journal of Clinical Microbiology & Infectious Diseases* **36**, 2007-2020, doi:10.1007/s10096-017-3024-6 (2017).

38 Maistrenko, O. M. *et al.* Disentangling the impact of environmental and phylogenetic constraints on prokaryotic within-species diversity. *The ISME Journal* **14**, 1247-1259, doi:10.1038/s41396-020-0600-z (2020).

39 Bishara, A. *et al.* High-quality genome sequences of uncultured microbes by assembly of read clouds. *Nature Biotechnology* **36**, 1067-1075, doi:10.1038/nbt.4266 (2018).

40 Rossi-Tamisier, M., Benamar, S., Raoult, D. & Fournier, P.-E. Cautionary tale of using 16S rRNA gene sequence similarity values in identification of human-associated bacterial species. *International Journal of Systematic and Evolutionary Microbiology* **65**, 1929-1934, doi:https://doi.org/10.1099/ijs.0.000161 (2015).

41 Zhou, J. *et al.* Spatial and Resource Factors Influencing High Microbial Diversity in Soil. *Applied and Environmental Microbiology* **68**, 326-334, doi:10.1128/AEM.68.1.326-334.2002 (2002).

42 Ranjard, L., Poly, F. & Nazaret, S. Monitoring complex bacterial communities using culture-independent molecular techniques: application to soil environment. *Research in Microbiology* **151**, 167-177, doi:https://doi.org/10.1016/S0923-2508(00)00136-4 (2000).

43 Zhang, Z., Wang, J., Wang, J., Wang, J. & Li, Y. Estimate of the sequenced proportion of the global prokaryotic genome. *Microbiome* **8**, 134, doi:10.1186/s40168-020-00903-z (2020).

44 Qin, N., Zhao, P., Ho, E. A., Xin, G. & Ren, C. L. Microfluidic Technology for Antibacterial Resistance Study and Antibiotic Susceptibility Testing: Review and Perspective. *ACS Sens* **6**, 3-21, doi:10.1021/acssensors.0c02175 (2021).

45 Gerlt, M. S. *et al.* Manipulation of single cells inside nanoliter water droplets using acoustic forces. *Biomicrofluidics* **14**, 064112, doi:10.1063/5.0036407 (2020).

46 Kim, H. S., Devarenne, T. P. & Han, A. Microfluidic systems for microalgal biotechnology: A review. *Algal Research* **30**, 149-161, doi:https://doi.org/10.1016/j.algal.2017.11.020 (2018).

47 Sesen, M., Alan, T. & Neild, A. Droplet control technologies for microfluidic high throughput screening (μHTS). *Lab on a Chip* **17**, 2372-2394, doi:10.1039/C7LC00005G (2017).

48 Guo, M. T., Rotem, A., Heyman, J. A. & Weitz, D. A. Droplet microfluidics for high-throughput biological assays. *Lab on a Chip* **12**, 2146-2155, doi:10.1039/C2LC21147E (2012).

49 Joensson, H. N. & Andersson Svahn, H. Droplet Microfluidics—A Tool for Single-Cell Analysis. *Angewandte Chemie International Edition* **51**, 12176-12192, doi:https://doi.org/10.1002/anie.201200460 (2012).

50 Han, S.-I., Huang, C. & Han, A. In-droplet cell separation based on bipolar dielectrophoretic response to facilitate cellular droplet assays. *Lab on a Chip* **20**, 3832-3841, doi:10.1039/D0LC00710B (2020).

51 Byrd Matthew, S. *et al.* The Pseudomonas aeruginosa Exopolysaccharide Psl Facilitates Surface Adherence and NF-κB Activation in A549 Cells. *mBio* **1**, e00140-00110, doi:10.1128/mBio.00140-10.

52 Sato, H., Okinaga, K. & Saito, H. Role of Pili in the Pathogenesis of <i>Pseudomonas aeruginosa</i> Burn Infection. *MICROBIOLOGY and IMMUNOLOGY* **32**, 131-139 (1988).

53 Cole, G. W. & Silverberg, N. L. The Adherence of Staphylococcus aureus to Human Corneocytes. *Archives of Dermatology* **122**, 166-169, doi:10.1001/archderm.1986.01660140056017 (1986).

54 Torres Alfredo, G., Zhou, X. & Kaper James, B. Adherence of Diarrheagenic Escherichia coli Strains to Epithelial Cells. *Infection and immunity* **73**, 18-29, doi:10.1128/IAI.73.1.18-29.2005 (2005).

55 Kilmury Sara, L. N., Burrows Lori, L. & Harwood Caroline, S. The Pseudomonas aeruginosa PilSR Two-Component System Regulates Both Twitching and Swimming Motilities. *mBio* **9**, e01310-01318, doi:10.1128/mBio.01310-18.

56 Han, S.-I., Lee, S.-M., Joo, Y.-D. & Han, K.-H. Lateral dielectrophoretic microseparators to measure the size distribution of blood cells. *Lab on a Chip* **11**, 3864-3872 (2011).

57 Han, K.-H., Han, S.-I. & Frazier, A. B. Lateral displacement as a function of particle size using a piecewise curved planar interdigitated electrode array. *Lab on a Chip* **9**, 2958–2964 (2009).

58 Han, S.-I., Kim, H. S., Han, K.-H. & Han, A. Digital quantification and selection of high-lipid-producing microalgae through a lateral dielectrophoresis-based microfluidic platform. *Lab on a Chip* **19**, 4128-4138, doi:10.1039/C9LC00850K (2019).

59 Robert Longley, J. *et al.* Development of a Serum-free Suspension Process for the Production of a Conditionally Replicating Adenovirus using A549 Cells. *Cytotechnology* **49**, 161-171 (2005).

60 Ouyang, Y. *et al.* Direct cell extraction from fresh and stored soil samples: Impact on microbial viability and community compositions. *Soil Biology and Biochemistry* **155**, 108178, doi:https://doi.org/10.1016/j.soilbio.2021.108178 (2021).

61 Brouzes, E. *et al.* Droplet microfluidic technology for single-cell high-throughput screening. *Proc. Natl. Acad. Sci. U.S.A.* **106**, 14195-14200, doi:10.1073/pnas.0903542106 (2009).

62 Guo, M. T., Rotem, A., Heymanab, J. A. & Weitz, D. A. Droplet microfluidics for high-throughput biological assays. *Lab on a Chip* **12**, 2146-2155, doi:10.1039/c2lc21147e (2012).

63 Mashaghi, S., Abbaspourrad, A., Weitz, D. A. & Oijen, A. M. v. Droplet microfluidics: A tool for biology, chemistry and nanotechnology. *TrAC Trends in Analytical Chemistry* **82**, 118-125, doi:10.1016/j.trac.2016.05.019 (2016).

64 Barea, J. S., Lee, J. & Kang, D.-K. Recent Advances in Droplet-based Microfluidic Technologies for Biochemistry and Molecular Biology. *Micromachines* **10**, 412, doi:10.3390/mi10060412 (2019).

65 Chen, M.-T. & Weiss, R. Artificial cell-cell communication in yeast Saccharomyces cerevisiae using signaling elements from Arabidopsis thaliana. *Nat. Biotechnol.* **23**, 1551-1555, doi:10.1038/nbt1162 (2005).

66 Klement, Z. Rapid Detection of the Pathogenicity of Phytopathogenic Pseudomonads. *Nature* **199**, 299-300, doi:10.1038/199299b0 (1963).

67 Sanford, B. A., Shelokov, A. & Ramsay, M. A. Bacterial Adherence to Virus-Infected Cells: A Cell Culture Model of Bacterial Superinfection. *J. Infect. Dis.* **137**, 176-181, doi:10.1093/infdis/137.2.176 (1978).

68 Shattock, R. J. & Griffin, G. E. Cellular adherence enhances HIV replication in monocytic cells. *Res. Virol.* **145**, 139-145 (1994).

69 Wang, R., Kobayashi, R. & Bishop, J. M. Cellular adherence elicits ligand-independent activation of the Met cell-surface receptor. **93**, 8425-8430, doi:10.1073/pnas.93.16.8425 (1996).

70 Antia, M., Herricks, T. & Rathod, P. K. Microfluidic Modeling of Cell−Cell Interactions in Malaria Pathogenesis. *PLoS Pathogens* **3**, e99, doi:10.1371/journal.ppat.0030099 (2007).

71 Wang, Z., Kim, M.-C., Marquez, M. & Thorsen, T. High-density microfluidic arrays for cell cytotoxicity analysis. *Lab Chip* **7**, 740, doi:10.1039/b618734j (2007).

72 Xu, T. *et al.* Real-time monitoring of suspension cell–cell communication using an integrated microfluidics. *Lab Chip* **10**, 2271, doi:10.1039/c004844e (2010).

73 Herricks, T. *et al.* A microfluidic system to study cytoadhesion of Plasmodium falciparum infected erythrocytes to primary brain microvascularendothelial cells. *Lab Chip* **11**, 2994, doi:10.1039/c1lc20131j (2011).

74 Yang, J., Chen, Z., Ching, P., Shi, Q. & Li, X. An integrated microfluidic platform for evaluating in vivo antimicrobial activity of natural compounds using a whole-animal infection model. *Lab Chip* **13**, 3373, doi:10.1039/c3lc50264c (2013).

75 Katz, S., Izhar, M. & Mirelman, D. Bacterial Adherence to Surgical Sutures. *Ann. Surg.* **194**, 35-41, doi:10.1097/00000658-198107000-00007 (1981).

76 Ogawa, S. K., Yurberg, E. R., Hatcher, V. B., Levitt, M. A. & Lowy, F. D. Bacterial Adherence to Human Endothelial Cells In Vitro. *Infect. Immun.* **50**, 218-224 (1985).

77 Boyle, E. C. & Finlay, B. B. Bacterial pathogenesis: exploiting cellular adherence. *Curr. Opin. Cell Biol.* **15**, 633-639, doi:10.1016/s0955-0674(03)00099-1 (2003).

78 Kurup, G. K. & Basu, A. S. Field-free particle focusing in microfluidic plugs. *Biomicrofluidics* **6**, 022008 (2012).

79 Sun, M., Khan, Z. S. & Vanapalli, S. A. Blood plasma separation in a long two-phase plug flowing through disposable tubing. *Lab Chip* **12**, 5225, doi:10.1039/c2lc40544j (2012).

80 Hein, M., Moskopp, M. & Seemann, R. Flow field induced particle accumulation inside droplets in rectangular channels. *Lab Chip* **15**, 2879-2886, doi:10.1039/c5lc00420a (2015).

81 Fornell, A. *et al.* Controlled Lateral Positioning of Microparticles Inside Droplets Using Acoustophoresis. *Anal. Chem.* **87**, 10521-10526, doi:10.1021/acs.analchem.5b02746 (2015).

82 Fornell, A., Ohlin, M., Garofalo, F., Nilsson, J. & Tenje, M. An intra-droplet particle switch for droplet microfluidics using bulk acoustic waves. *Biomicrofluidics* **11**, 031101, doi:10.1063/1.4984131 (2017).

83 Fornell, A. *et al.* An acoustofluidic platform for non-contact trapping of cell-laden hydrogel droplets compatible with optical microscopy. *Biomicrofluidics* **13**, 044101 (2019).

84 Fornell, A., Cushing, K., Nilsson, J. & Tenje, M. Binary particle separation in droplet microfluidics using acoustophoresis. *Appl. Phys. Lett.* **112**, 063701, doi:10.1063/1.5020356 (2018).

85 Park, K. *et al.* In-droplet microparticle separation using travelling surface acoustic wave. *Biomicrofluidics* **11**, 064112 (2017).

86 Park, J., Destgeer, G., Kim, H., Cho, Y. & Sung, H. J. In-droplet microparticle washing and enrichment using surface acoustic wave-driven acoustic radiation force. *Lab on a Chip* **18**, 2936-2945, doi:10.1039/C8LC00733K (2018).

87 Han, S.-I., Kim, H. S. & Han, A. In-droplet cell concentration using dielectrophoresis. *Biosensors and Bioelectronics* **97**, 41-45 (2017).

88 Lombard, D. & Dittrich, P. S. Droplet microfluidics with magnetic beads: a new tool to investigate drug–protein interactions. *Analytical and Bioanalytical Chemistry* **399**, 347-352, doi:10.1007/s00216-010-4302-7 (2011).

89 Brouzes, E., Kruse, T., Kimmerling, R. & Strey, H. H. Rapid and continuous magnetic separation in droplet microfluidic devices. *Lab on a Chip* **15**, 908-919 (2015).

90 Gao, R., Cheng, Z., deMelloc, A. J. & Choo, J. Wash-free magnetic immunoassay of the PSA cancer marker using SERS and droplet microfluidics. *Lab on a Chip* **16**, 1022-1029 (2016).

91 Han, K.-H., Han, S.-I. & Frazier, A. B. Lateral displacement as a function of particle size using a piecewise curved planar interdigitated electrode array. *Lab Chip* **9**, 2958, doi:10.1039/b909753h (2009).

92 Han, S.-I., Lee, S.-M., Joo, Y.-D. & Han, K.-H. Lateral dielectrophoretic microseparators to measure the size distribution of blood cells. *Lab on a Chip* **11**, 3864-3872, doi:10.1039/c1lc20413k (2011).

93 Jubery, T. Z., Srivastava, S. K. & Dutta, P. Dielectrophoretic separation of bioparticles in microdevices: A review. *ELECTROPHORESIS* **35**, 691-713, doi:10.1002/elps.201300424 (2014).

94 Gascoyne, P. R. C. & Vykoukal, J. V. Dielectrophoresis-based sample handling in general-purpose programmable diagnostic instruments. *Proc. IEEE* **92**, 22-42 (2004).

95 Bai, W., Zhao, K. S. & Asami, K. Dielectric properties of E. coli cell as simulated by the three-shell spheroidal model. *Biophysical Chemistry* **122**, 136-142 (2006).

96 Han, S.-I., Joo, Y.-D. & Han, K.-H. An electrorotation technique for measuring the dielectric properties of cells with simultaneous use of negative quadrupolar dielectrophoresis and electrorotation. *Analyst* **138**, 1529-1537 (2013).

97 Kurup, G. K. & Basu, A. S. in *Proceedings of the IEEE Engineering in Medicine and Biology Conference (EMBC).* 4034-4037.

98 Timpe, J. M., Holm, M. M., Vanlerberg, S. L., Basrur, V. & Lafontaine, E. R. Interaction of *Pseudomonas aeruginosa* with A549 pneumocyte cells. *Infect. Immun.* **59**, 822-828 (1991).

99 Timpe, J. M., Holm, M. M., Vanlerberg, S. L., Basrur, V. & Lafontaine, E. R. Identification of a moraxella catarrhalis outer membrane protein exhibiting both adhesin and lipolytic activities. *Infaction and Immunity* **71**, 4341-4350, doi:10.1128/iai.71.8.4341-4350.2003 (2003).

100 Guzman, A. R., Kim, H. S., de Figueiredo, P. & Han, A. A three-dimensional electrode for highly efficient electrocoalescence-based droplet merging. *Biomedical Microdevices* **17**, 35, doi:10.1007/s10544-014-9921-x (2015).

101 Abate, A. R., Hung, T., Mary, P., Agresti, J. J. & Weitz, D. A. High-throughput injection with microfluidics using picoinjectors. *Proceedings of the National Academy of Sciences* **107**, 19163-19166, doi:10.1073/pnas.1006888107 (2010).

102 Agresti, J. J. *et al.* Ultrahigh-throughput screening in drop-based microfluidics for directed evolution. *Proceedings of the National Academy of Sciences* **107**, 4004-4009, doi:10.1073/pnas.0910781107 (2010).

103 Kim, H. S. *et al.* Raman spectroscopy compatible PDMS droplet microfluidic culture and analysis platform towards on-chip lipidomics. *Analyst* **142**, 1054-1060, doi:10.1039/c6an02221a (2017).

104 Liu, Z., Fornell, A., Barbe, L., Hjort, K. & Tenje, M. On-chip background dilution in droplets with high particle recovery using acoustophoresis. *Biomicrofluidics* **13**, 064123, doi:10.1063/1.5129256 (2019).

105 Lee, H., Xu, L. & Oh, K. W. Droplet-based microfluidic washing module for magnetic particle-based assays. *Biomicrofluidics* **8**, 044113, doi:10.1063/1.4892495 (2014).

106 Zhang, H. *et al.* An ultra high-efficiency droplet microfluidics platform using automatically synchronized droplet pairing and merging. *Lab on a Chip* **20**, 3948-3959, doi:10.1039/D0LC00757A (2020).

107 Kim, H. S. *et al.* A High-throughput Droplet Microfluidics Screening Platform for Selecting Fast Growing and High Lipid Producing Microalgae from a Mutant Library. *Plant Direct* **1**, 1-13 (2017).

108 Kim, H. S., Guzman, A. R., Thapa, H. R., Devarenne, T. P. & Han, A. A Droplet Microfluidics Platform for Rapid Microalgal Growth and Oil Production Analysis. *Biotechnology and Bioengineering* **113**, 1691-1701 (2016).

109 Khorshidi, M. A., Rajeswari, P. K. P., Wählby, C., Joensson, H. N. & Andersson Svahn, H. Automated analysis of dynamic behavior of single cells in picoliter droplets. *Lab on a Chip* **14**, 931-937, doi:10.1039/C3LC51136G (2014).

110 Cho, S. *et al.* Droplet-Based Microfluidic Platform for High-Throughput, Multi-Parameter Screening of Photosensitizer Activity. *Analytical Chemistry* **85**, 8866-8872, doi:10.1021/ac4022067 (2013).

111 Mary, P., Chen, A., Chen, I., Abate, A. R. & Weitz, D. A. On-chip background noise reduction for cell-based assays in droplets. *Lab on a Chip* **11**, 2066-2070, doi:10.1039/C1LC20159J (2011).

112 Cheng, W. L., Sadr, R., Dai, J. & Han, A. Prediction of Microdroplet Breakup Regime in Asymmetric T-Junction Microchannels. *Biomedical Microdevices* **20**, 72, doi:10.1007/s10544-018-0310-8 (2018).

113 Siebman, C., Velev, O. D. & Slaveykova, V. I. Alternating Current-Dielectrophoresis Collection and Chaining of Phytoplankton on Chip: Comparison of Individual Species and Artificial Communities. *Biosensors* **7**, 4 (2017).

114 Chen, H. *et al.* Cardiac-like flow generator for long-term imaging of endothelial cell responses to circulatory pulsatile flow at microscale. *Lab on a Chip* **13**, 2999-3007, doi:10.1039/C3LC50123J (2013).

115 Chen, B. *et al.* Microfluidic bioassay to characterize parasitic nematode phenotype and anthelmintic resistance. *Parasitology* **138(1)**, 80-88 (2011).

116 Zhang, H. *et al.* Use of Surface-Enhanced Raman Scattering (SERS) Probes to Detect Fatty Acid Receptor Activity in a Microfluidic Device. *Sensors* **19**, 1663 (2019).

117 Clark, I. C., Thakur, R. & Abate, A. R. Concentric electrodes improve microfluidic droplet sorting. *Lab on a Chip* **18**, 710-713, doi:10.1039/C7LC01242J (2018).

118 Unkefer, C. J. *et al.* Review of the algal biology program within the National Alliance for Advanced Biofuels and Bioproducts. *Algal Research* **22**, 187-215, doi:https://doi.org/10.1016/j.algal.2016.06.002 (2017).

119 Kim, H. S., Guzman, A. R., Thapa, H. R., Devarenne, T. P. & Han, A. A Droplet Microfluidics Platform for Rapid Microalgal Growth and Oil Production Analysis. *Biotechnology and Bioengineering* **113 (8)**, 1691-1701 (2016).

120 Kim, H. S. *et al.* High-throughput droplet microfluidics screening platform for selecting fast-growing and high lipid-producing microalgae from a mutant library. *Plant Direct* **1**, e00011, doi:10.1002/pld3.11 (2017).

121 EW, Y. & DJ, B. Fundamentals of microfluidic cell culture in controlled microenvironments *Chemical Society reviews* **39 (3)**, 1036-1048 (2010).

122 Jeong, S. H. *et al.* A Three-Dimensional (3D) Arrayed Microfluidic Blood-Brain Barrier (BBB) Model with Integrated Electrical Sensor Array. *IEEE Transactions on Biomedical Engineering* **62 (2)**, 431-439 (2018).

123 Kim, H. S., Weiss, T. L., Thapa, H. R., Devarenne, T. P. & Han, A. A microfluidic photobioreactor array demonstrating high-throughput screening for microalgal oil production. *Lab on a Chip* **14**, 1415-1425, doi:10.1039/C3LC51396C (2014).

124 Han, S.-I., Kim, H. S., Han, K.-H. & Han, A. Digital quantification and selection of high-lipid- producing microalgae through a lateral dielectrophoresis-based microfluidic platform. *Lab on a Chip* **19**, 4128-4138 (2019).

125 Han, S.-I., Huang, C. & Han, A. In-droplet cell separation based on bipolar dielectrophoretic response to facilitate cellular droplet assays. *Lab on a Chip*, doi:10.1039/D0LC00710B (2020).

126 Wippold, J. A. *et al.* PRESCIENT: platform for the rapid evaluation of antibody success using integrated microfluidics enabled technology. *Lab on a Chip* **20**, 1628-1638, doi:10.1039/C9LC01165J (2020).

127 Zhang, H. *et al.* An ultra high-efficiency droplet microfluidics platform using automatically synchronized droplet pairing and merging. *Lab on a Chip*, doi:10.1039/D0LC00757A (2020).

128 Prakash, M. & Gershenfeld, N. Microfluidic Bubble Logic. *Science* **315**, 832-835, doi:10.1126/science.1136907 (2007).

129 Garstecki, P., Gitlin, I., DiLuzio, W. & Whitesides, G. M. Formation of monodisperse bubbles in a microfluidic flow-focusing device. *Appl. Phys. Lett.* **85**, 2649 (2004).

130 Gordillo, J. M., Cheng, Z., Ganan-Calvo, A. M. & M Marquez, D. W. A new device for the generation of microbubbles. *Physics of Fluids* **16**, 2828-2834 (2004).

131 Xu, J., Vaillant, R. & Attinger, D. Use of a porous membrane for gas bubble removal in microfluidic channels: physical mechanisms and design criteria. *Microfluid Nanofluid* **9**, 765-772 (2010).

132 Kohlheyer, D., Eijkel, J. C. T., Schlautmann, S., Berg, A. v. d. & Schasfoort, R. B. M. Bubble-Free Operation of a Microfluidic Free-Flow Electrophoresis Chip with Integrated Pt Electrodes. *Anal. Chem.* **80, 11**, 4111-4118 (2008).

133 Liu, C., Thompson, J. A. & Bau, H. H. A membrane-based, high-efficiency, microfluidic debubbler. *Lab Chip* **11** (2011).

134 Johnson, M., Liddiard, G., Eddings, M. & Gale, B. Bubble inclusion and removal using PDMS membrane-based gas permeation for applications in pumping, valving and mixing in microfluidic devices. *J. Micromech. Microeng.* **19** (2009).

135 Cheng, D. & Jiang, H. A debubbler for microfluidics utilizing airliquid interfaces. *Appl. Phys. Lett.* **95** (2009).

136 Sung, J. H. & Shuler, M. L. Prevention of air bubble formation in a microfluidic perfusion cell culture system using a microscale bubble trap. *Biomedical Microdevices* **11**, 731-738 (2009).

137 Zheng, W., Wang, Z., Zhang, W. & Jiang, X. A simple PDMS-based microfluidic channel design that removes bubbles for long-term on-chip culture of mammalian cells. *Lab Chip* **10**, 2906-2910 (2010).

138 Wang, Y. *et al.* Systematic prevention of bubble formation and accumulation for long-term culture of pancreatic islet cells in microfluidic device. *Biomedical Microdevices* **14**, 419-426 (2012).

139 Kang, E., Lee, D. H., Kim, C.-B., Yoo, S. J. & Lee, S.-H. A hemispherical microfluidic channel for the trapping and passive dissipation of microbubbles. *J. Micromech. Microeng.* **20** (2010).

140 Wippold, J. A., Huang, C., Stratis-Cullum, D. & Han, A. Enhancing droplet transition capabilities using sloped microfluidic channel geometry for stable droplet operation. *Biomedical Microdevices* **22:15** (2020).

141 Mayer, F. *et al.* Multimaterial 3D laser microprinting using an integrated microfluidic system. *Sci Adv* **5**, eaau9160-eaau9160, doi:10.1126/sciadv.aau9160 (2019).

142 Yu Fen Samantha, S., Hongxing, H. & Christoph, A. M. Microfluidic single-cell technology in immunology and antibody screening. *Molecular Aspects of Medicine* **59**, 47-61, doi:https://doi.org/10.1016/j.mam.2017.09.004 (2018).

143 Segaliny, A. I. *et al.* Functional TCR T cell screening using single-cell droplet microfluidics. *Lab on a Chip* **18**, 3733-3749, doi:10.1039/C8LC00818C (2018).

144 Wang, Y. *et al.* High-throughput functional screening for next-generation cancer immunotherapy using droplet-based microfluidics. *Science Advances* **7**, eabe3839, doi:10.1126/sciadv.abe3839 (2021).

145 Samaneh, M., Alireza, A., David, A. W. & Antoine, M. Droplet microfluidics: A tool for biology, chemistry and nanotechnology. *TrAC Trends in Analytical Chemistry* **82**, 118-125, doi:https://doi.org/10.1016/j.trac.2016.05.019 (2016).

146 Wong, A. H.-H. *et al.* Drug screening of cancer cell lines and human primary tumors using droplet microfluidics. *Scientific Reports* **7**, 9109, doi:10.1038/s41598-017-08831-z (2017).

147 Ding, Y., Howes, P. D. & deMello, A. J. Recent Advances in Droplet Microfluidics. *Analytical Chemistry* **92**, 132-149, doi:10.1021/acs.analchem.9b05047 (2020).

148 Tewhey, R. *et al.* Microdroplet-based PCR enrichment for large-scale targeted sequencing. *Nature biotechnology* **27**, 1025-1031, doi:10.1038/nbt.1583 (2009).

149 Rotem, A. *et al.* High-Throughput Single-Cell Labeling (Hi-SCL) for RNA-Seq Using Drop-Based Microfluidics. *PLOS ONE* **10**, e0116328, doi:10.1371/journal.pone.0116328 (2015).

150 Pit, A. M., Duits, M. H. G. & Mugele, F. Droplet Manipulations in Two Phase Flow Microfluidics. *Micromachines* **6**, 1768-1793 (2015).

151 Bowman, T., Frechette, J. & Drazer, G. Force driven separation of drops by deterministic lateral displacement. *Lab on a Chip* **12**, 2903-2908, doi:10.1039/C2LC40234C (2012).

152 Joensson, H. N., Uhlén, M. & Svahn, H. A. Droplet size based separation by deterministic lateral displacement—separating droplets by cell-induced shrinking. *Lab on a Chip* **11**, 1305-1310, doi:10.1039/C0LC00688B (2011).

153 RuihuaDing, Ung, W. L., Heyman, J. A. & Weitz, D. A. Sensitive and predictable separation of microfluidic droplets by size using in-line passive filter. *Biomicrofluidics* **11**, 014114, doi:10.1063/1.4976723 (2017).

154 Yoon, D. H., Numakunai, S., Nakahara, A., Sekiguchi, T. & Shoji, S. Hydrodynamic on-rail droplet pass filter for fully passive sorting of droplet-phase samples. *RSC Advances* **4**, 37721-37725, doi:10.1039/C4RA08354G (2014).

155 Rehman, A. U. *et al.* Size-Based Sorting of Emulsion Droplets in Microfluidic Channels Patterned with Laser-Ablated Guiding Tracks. *Analytical Chemistry* **92**, 2597-2604, doi:10.1021/acs.analchem.9b04308 (2020).

156 Li, M., van Zee, M., Goda, K. & Di Carlo, D. Size-based sorting of hydrogel droplets using inertial microfluidics. *Lab on a Chip* **18**, 2575-2582 (2018).

157 Maenaka, H., Yamada, M., Yasuda, M. & Seki, M. Continuous and size-dependent sorting of emulsion droplets using hydrodynamics in pinched microchannels. *Langmuir* **24**, 4405-4410 (2008).

158 Ding, R., Ung, W. L., Heyman, J. A. & Weitz, D. A. Sensitive and predictable separation of microfluidic droplets by size using in-line passive filter. *Biomicrofluidics* **11**, 014114 (2017).

159 HyunáYoon, D. Hydrodynamic on-rail droplet pass filter for fully passive sorting of droplet-phase samples. *RSC advances* **4**, 37721-37725 (2014).

160 Yoon, D. H., Tanaka, D., Sekiguchi, T. & Shoji, S. Size-Dependent and Property-Independent Passive Microdroplet Sorting by Droplet Transfer on Dot Rails. *Micromachines* **9**, 513 (2018).

161 Tan, Y.-C. & Lee, A. P. Microfluidic separation of satellite droplets as the basis of a monodispersed micron and submicron emulsification system. *Lab on a Chip* **5**, 1178-1183 (2005).

162 Crews, N., Darabi, J., Voglewede, P., Guo, F. & Bayoumi, A. An analysis of interdigitated electrode geometry for dielectrophoretic particle transport in micro-fluidics. *Sensors and Actuators B: Chemical* **125**, 672-679 (2007).

163 Zagnoni, M. & Cooper, J. M. On-chip electrocoalescence of microdroplets as a function of voltage, frequency and droplet size. *Lab on a Chip* **9**, 2652-2658 (2009).

164 Han, P. *et al.* Continuous Label-Free Electronic Discrimination of T Cells by Activation State. *ACS nano* **14**, 8646-8657 (2020).

165 Huang, C., Wippold, J. A., Stratis-Cullum, D. & Han, A. Eliminating air bubble in microfluidic systems utilizing integrated in-line sloped microstructures. *Biomedical Microdevices* **22**, 1-9 (2020).

166 Zhang, H. *et al.* An ultra high-efficiency droplet microfluidics platform using automatically synchronized droplet pairing and merging. *Lab Chip* **20**, 3948-3959, doi:10.1039/d0lc00757a (2020).

167 Sukovich, D. J., Lance, S. T. & Abate, A. R. Sequence specific sorting of DNA molecules with FACS using 3dPCR. *Scientific Reports* **7**, 39385, doi:10.1038/srep39385 (2017).

168 Williams, R. *et al.* Amplification of complex gene libraries by emulsion PCR. *Nature methods* **3**, 545-550 (2006).

APPENDIX A

FILM MASKS, 3D PRINTING AND 2PP DESIGN

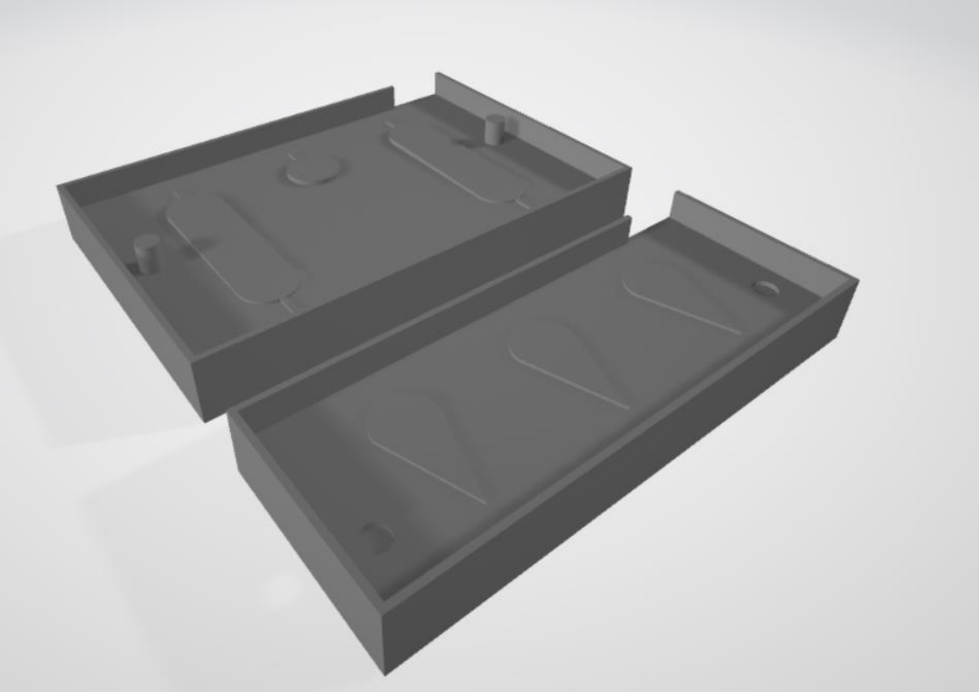

Fig. A.1 (Chapter 2) 3D printing master mold design (two pieces) for SEER device.

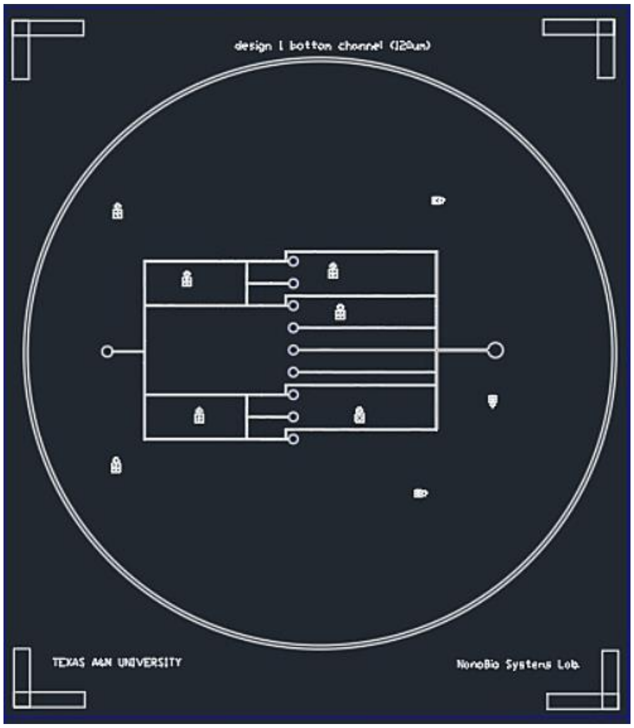

Fig. A.2 (Chapter 2) Fluidic layer design for SEER device, automatic controller chip.

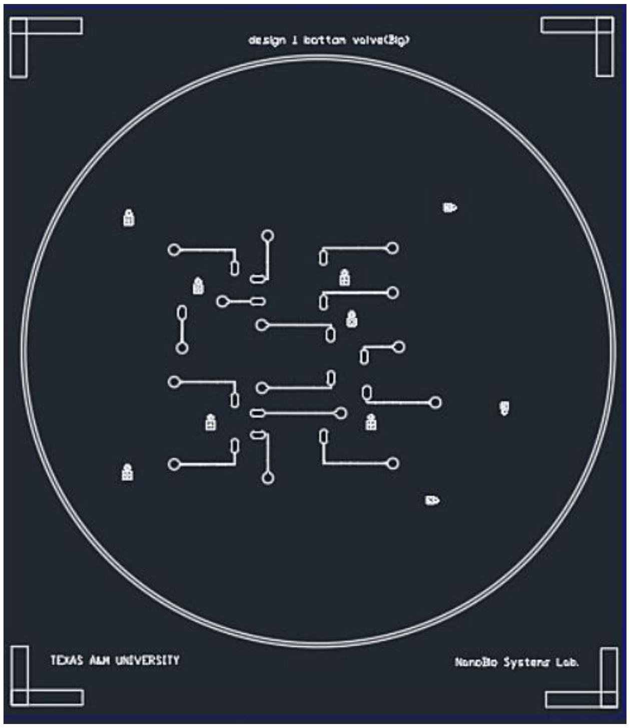

Fig. A.3 (Chapter 2) Valve layer design for SEER device, automatic controller chip.

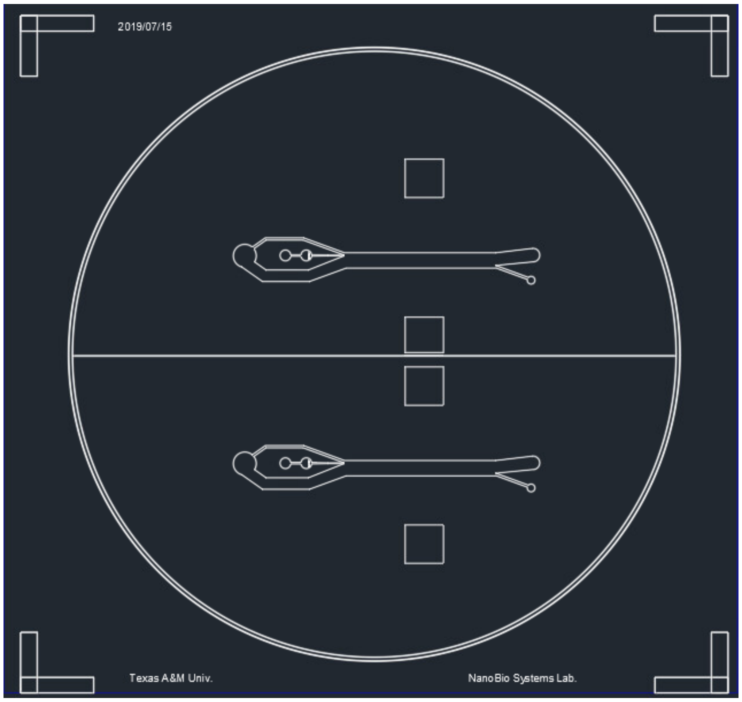

Fig. A.4 (Chapter 3) Fluidic design for lateral DEP adherence chip.

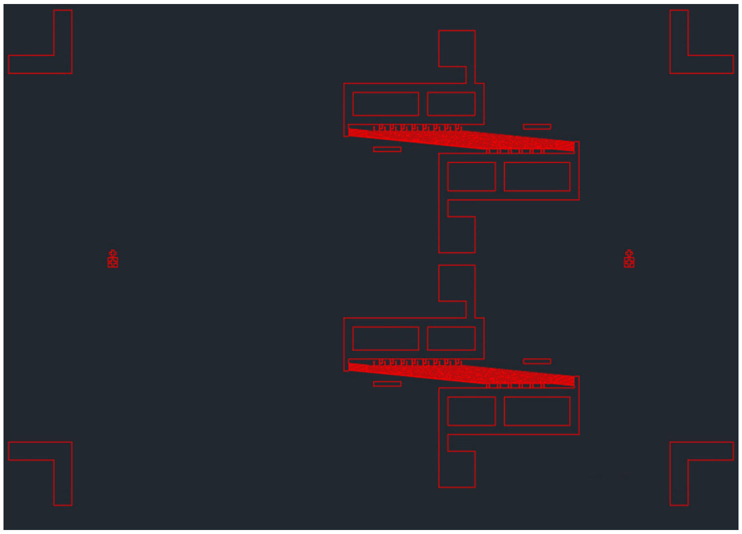

Fig. A.5 (Chapter 3) Positive metal pattern for lateral DEP adherence chip substrate.

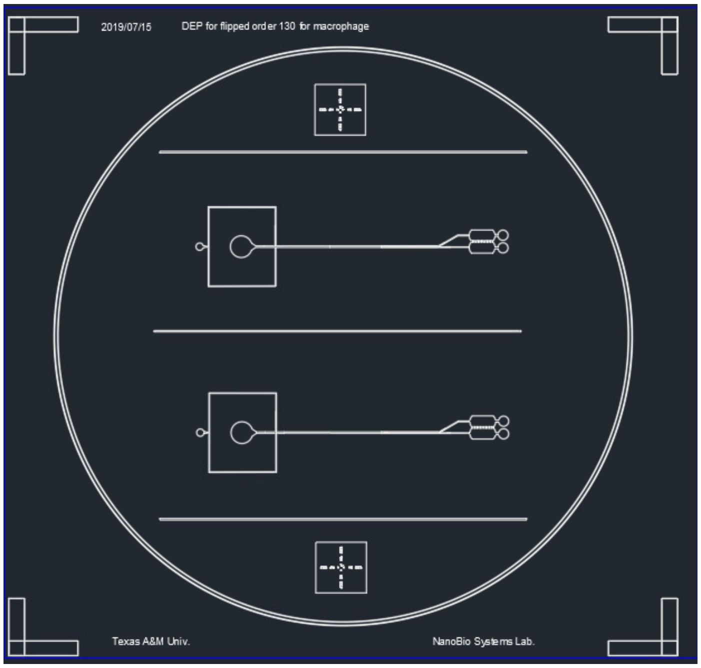

Fig. A.6 (Chapter 4) Fluidic channel design for in-droplet cell separation chip.

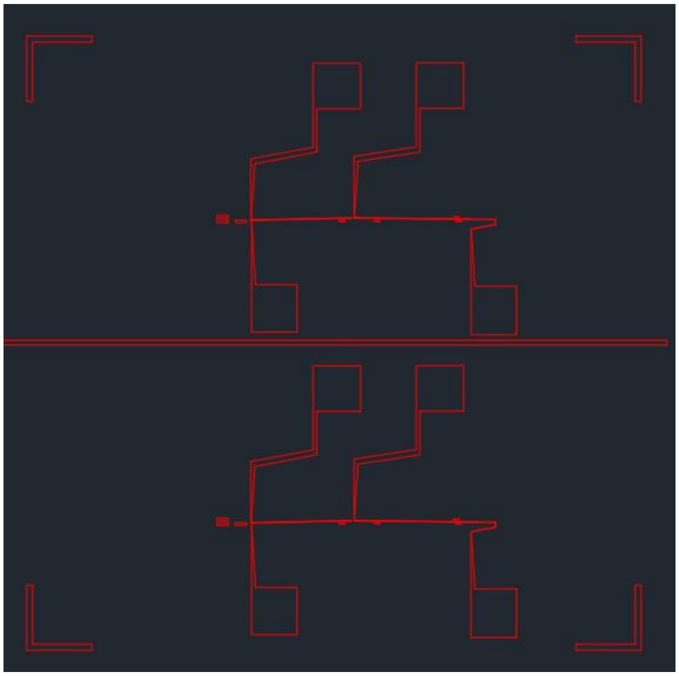

Fig. A.7 (Chapter 4) Positive metal pattern design for in-droplet cell separation chip substrate.

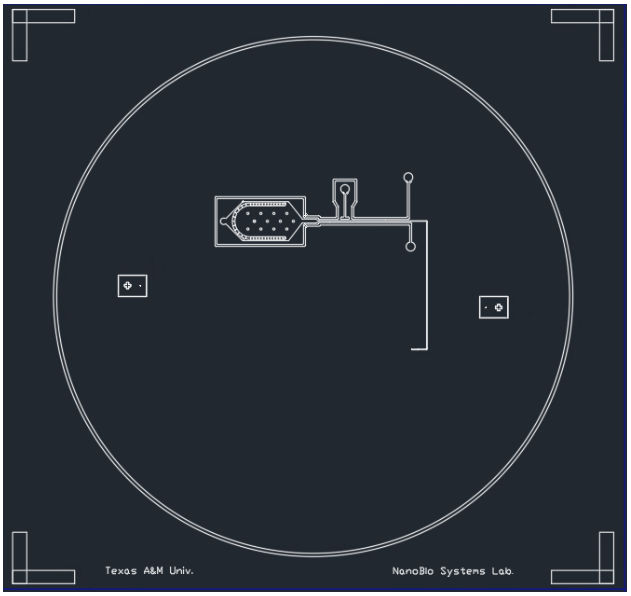

Fig. A.8 (Chapter 5) Fluidic channel design for in-droplet solution exchange chip (upper half).

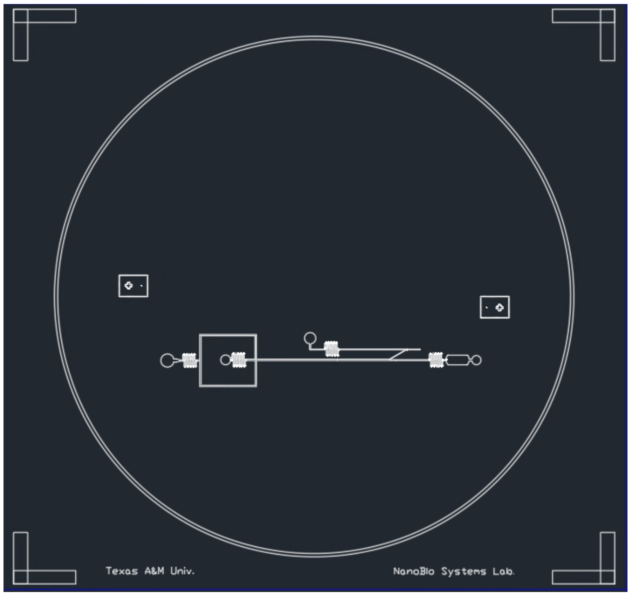

Fig. A.9 (Chapter 5) Fluidic channel design for in-droplet solution exchange chip (lower half).

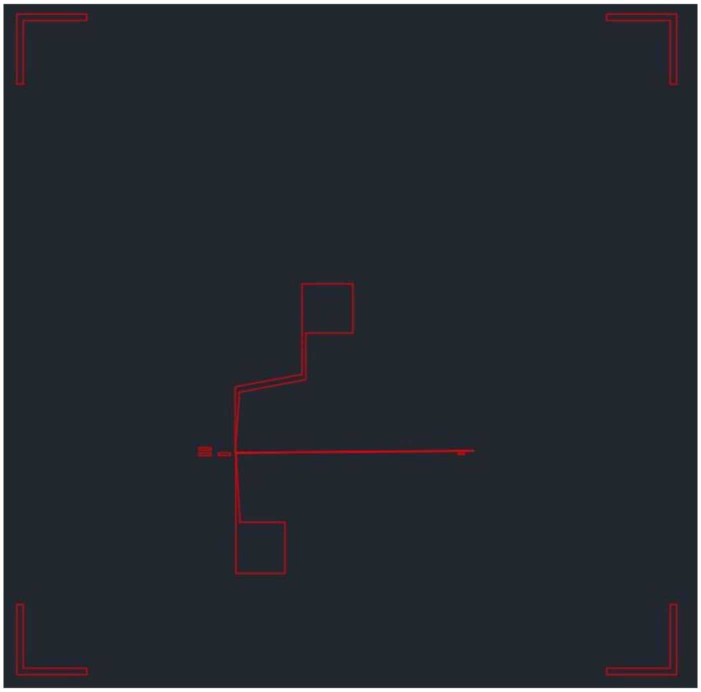

Fig. A.10 (Chapter 5) Positive metal pattern design for in-droplet solution exchange chip.

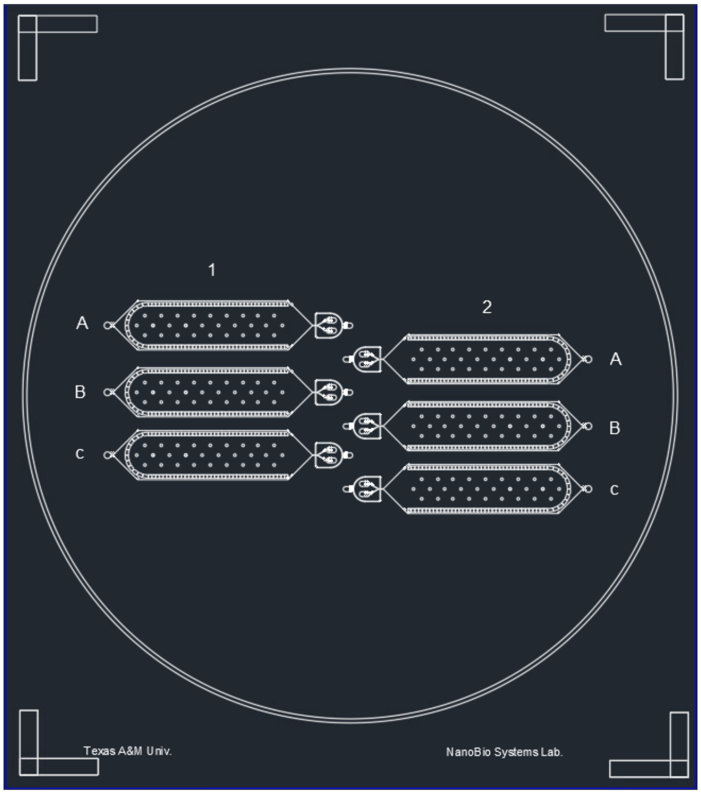

Fig. A.11 (Chapter 5) Fluidic channel design for droplet generation and collection.

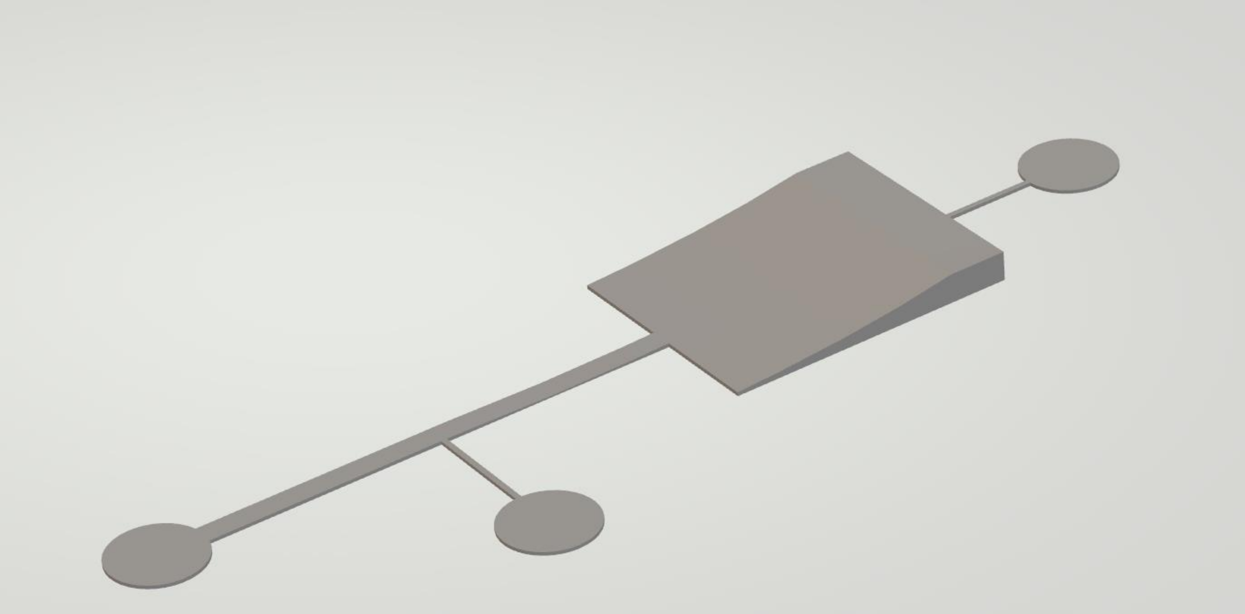

Fig. A.12 (Chapter 6) 2PP printing master mold design for bubble trapping device (first).

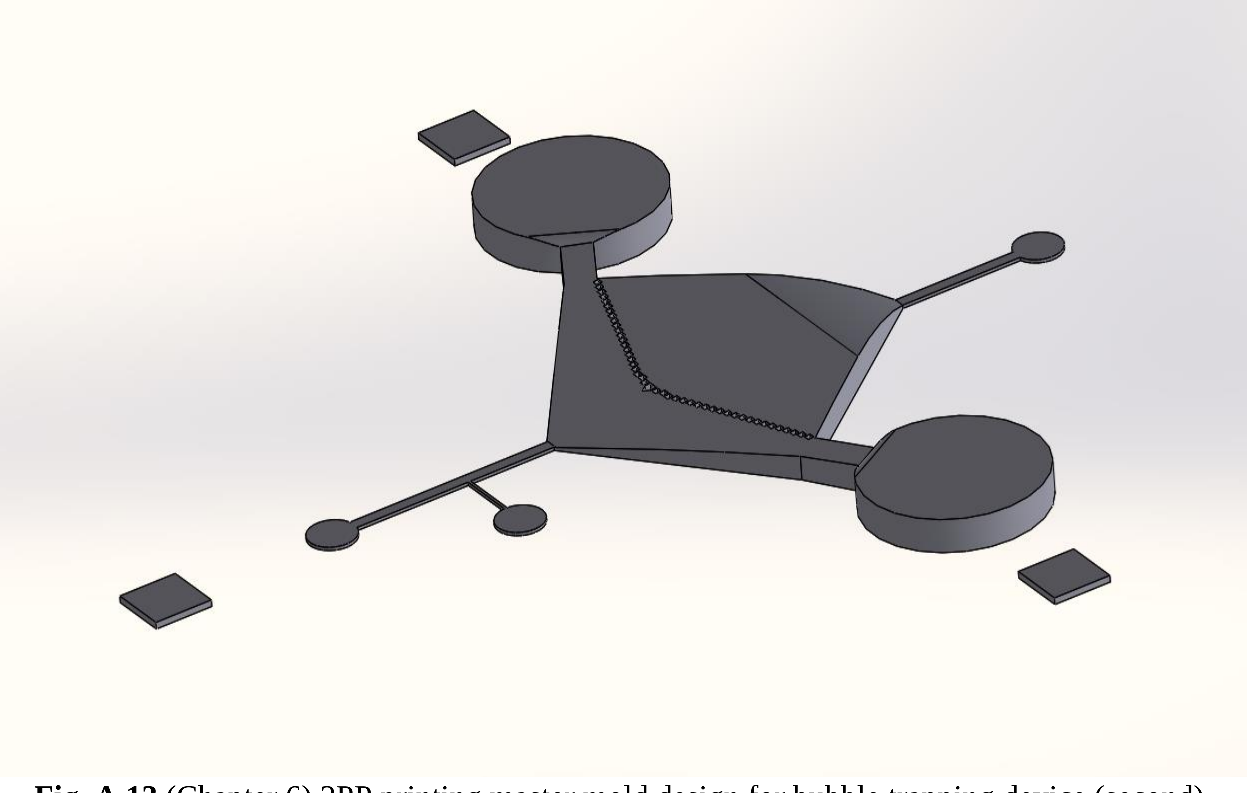

Fig. A.13 (Chapter 6) 2PP printing master mold design for bubble trapping device (second).

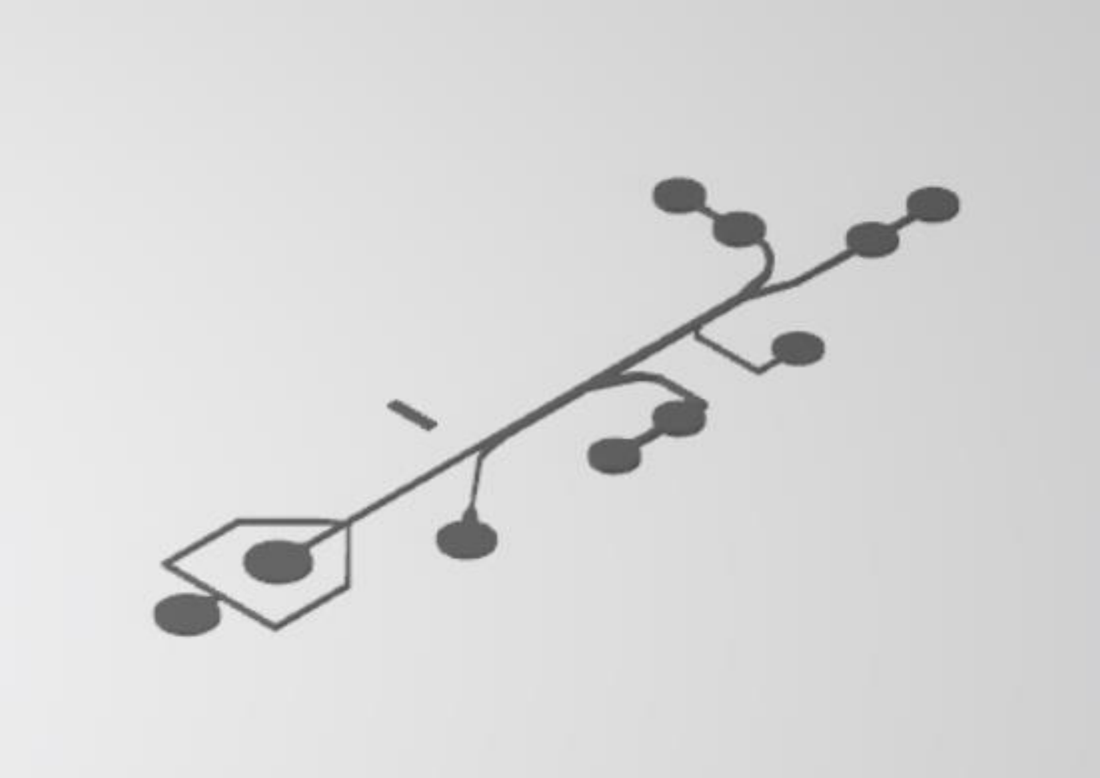

Fig. A.14 (Chapter 7) 2PP printing master mold design for droplet bandpass filter device.

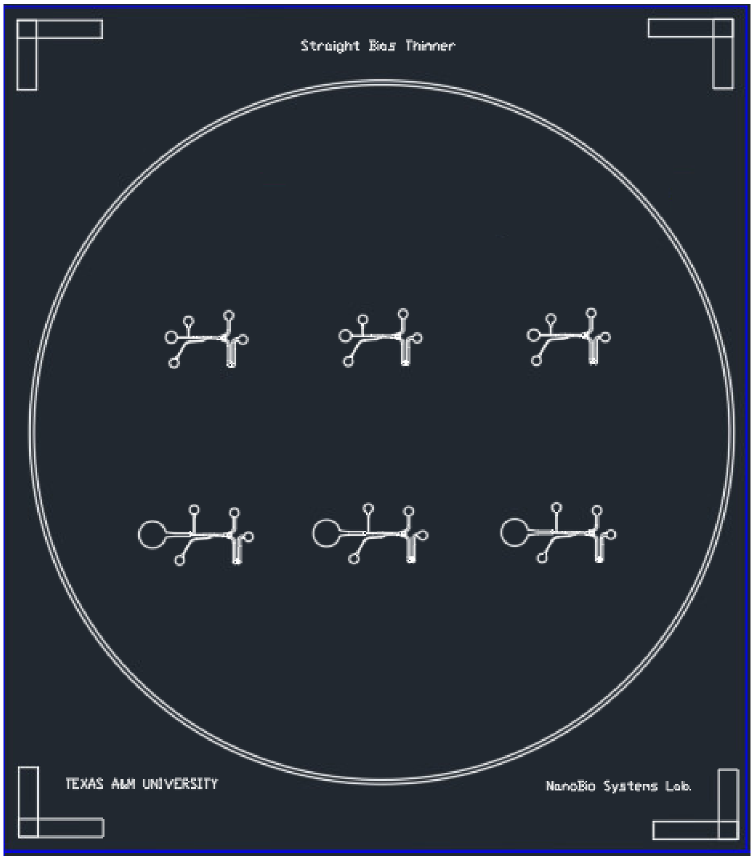

Fig. A.15 (Chapter 7) Fluidic channel design for droplet bandpass filter device.

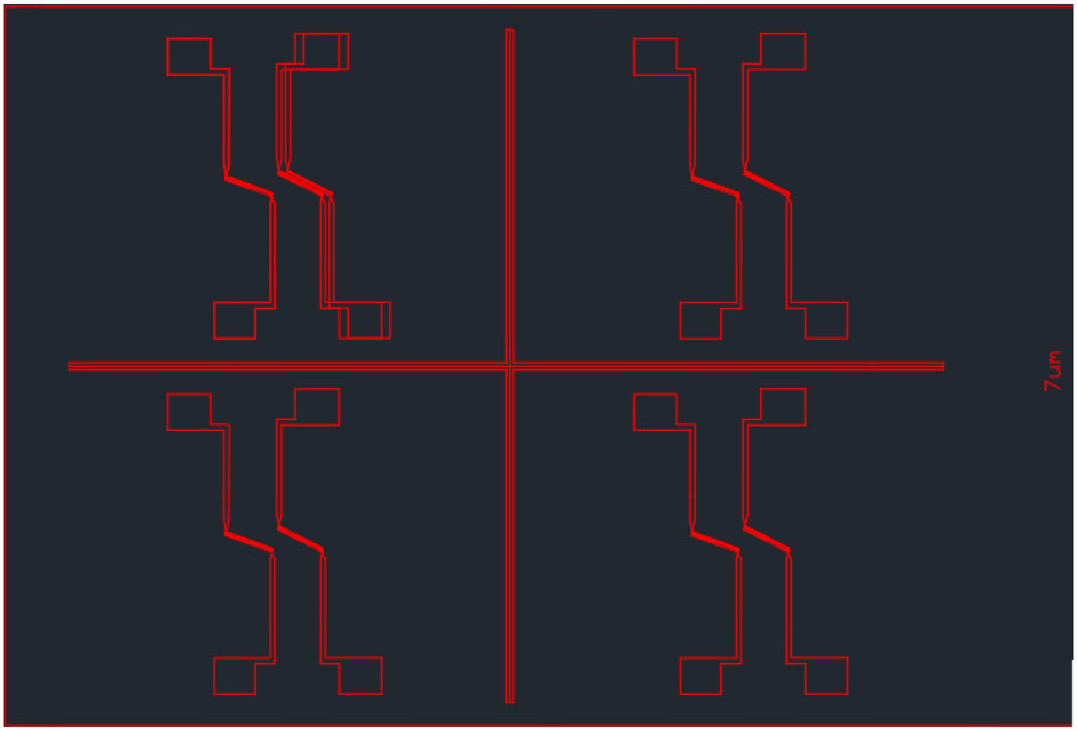

Fig. A.16 (Chapter 7) Positive metal pattern design for droplet bandpass filter device.

APPENDIX B

CALCULATION OF CLAUSIUS-MOSSOTTI FACTOR (C CODE)

```
/* Simulation for Real and Imaginary Parts of Clausius-Mossotti Factor, ReFcm and ImFcm. */

 #include <stdio.h>
 #include <math.h>
 #include <stdlib.h>


 /* -------- Physical parameter of blood cell -------- */

 #define r        0.8e-6              /* Radius of cell [m] */
 #define d        7.e-9               /* Thickness of membrane [m] */
 #define Ep       (108*8.854e-12)          /* Permitivity of plasma [F/m^2] */
 #define Sp       0.22                /* Conductivity of plasma [S/m] */
 #define Cmem   4.3e-2/3.33   /* Capacitance of memebrane [F/m^2] */ //2.81, 3.33
 #define Emem  (Cmem*d)    /* Permitivity of membrane [F/m] */
 #define Smem           10e-6               /* Conductivity of membrane [S/m] */
 #define Em     (80.*8.854e-12)          /* Permitivity of medium [F/m^2] */
 #define Sm     0.0103 /* Conductivity of medium [S/m] */
 #define M_PI 3.1415926 /*pi value*/
 /* ------------------------------------ */


 /* -------- Frequency Range  -------- */

 #define Fstart 1.e3                 /* Initial frequency [s^-1] */
 #define Ffin 1.e9                   /* Criterion of final frequency [s^-1]*/
 /* ------------------------------------------------------ */


 /* -------- Additional step value -------- */

 #define Fstep  1.1       /* Frequency Step */
 /* ---------------------------------- */


 int main()
 {

           FILE *out1;

           double f;                           /* frequency [S^-1] */
```

```
        double w;                       /* radian frequency [S^-1] */
        double a;                       /* ratio of r per r-d */

        double Epm;                     /* Permeability of the Clausius Mossotti of plasma and
membrane [F/m^2] */
        double Spm;                     /* Conductivity of the Clausius Mossotti of plasma and
membrane [S/m] */

        double Ei = 0.;                 /* Permeability of internal [F/m^2] */
        double Si;                      /* Conductivity of internal [S/m] */

        double reFcm;                   /* Real part of the Clausius-Mossotti factor of blood cell */
        double imFcm;                           /* Imaginary part of the Clausius-Mossotti factor of
blood cell */

        double  RFmin = -1.;            /* Minimum ReFcm */

      double    simfc = 0.;             /* Simulated crossover frequency [s^-1] */
      double    calfc = 0.;             /* calculated crossover frequency [s^-1] */

        double Tau = 0.;
        double Tpm = 0.;

        out1 = fopen("ReImFcm.dat","w");

        a = r/(r-d);


        for( f = Fstart ; f <= Ffin ; f = f*Fstep)
        {

                w = 2.*M_PI*f;


                Epm = (Ep-Emem)/(Ep+2.*Emem)+((Sp-Smem)/(Sp+2.*Smem)-(Ep-
Emem)/(Ep+2.*Emem))/(1.+w*w*Tpm*Tpm);

                Spm = (-(Ep-Emem)/(Ep+2.*Emem)+(Sp-
Smem)/(Sp+2.*Smem))*(w*w)*Tpm/(1.+w*w*Tpm*Tpm);



                Ei = (((a*a*a+2.*Epm)*(a*a*a-Epm)-2.*Spm*Spm/(w*w))*Emem -
3.*a*a*a*Spm*Smem/(w*w))/((a*a*a-Epm)*(a*a*a-Epm)+Spm*Spm/(w*w));

                Si = (((a*a*a+2.*Epm)*(a*a*a-Epm)-2.*Spm*Spm/(w*w))*Smem +
3.*a*a*a*Spm*Emem)/((a*a*a-Epm)*(a*a*a-Epm)+Spm*Spm/(w*w));
```

```
        Tau = (2.*Ei + 3.*Em)/(2.*Si + 3.*Sm);

                reFcm = (Ei-Em)/(2.*Ei+3.*Em)+((Si-Sm)/(2.*Si+3.*Sm)-(Ei-
Em)/(2.*Ei+3.*Em))/(1.+w*w*Tau*Tau);

                imFcm = (-(Ei-Em)/(2.*Ei+3.*Em)+(Si-
Sm)/(2.*Si+3.*Sm))*(w*Tau)/(1.+w*w*Tau*Tau);

                if( RFmin < reFcm && -RFmin > reFcm) {RFmin = reFcm; simfc = f;}

                fprintf(out1," %5.5e %5.5e %5.5e \n", f, reFcm, imFcm);
        }
        /* ------------------------------------------------------------ */
        /* --------      Calculation of the effective parameter of cell -------- */


        Tpm = (Ep + 2.*Emem)/(Sp + 2.*Smem);

        calfc = 1./(sqrt(2.)*M_PI)*Sm/Ei;

        /* ---------------------------------------------------- */


        /* ------------------      print     ------------------------ */

        /* printf(" Tau  =  %5.5e \n", Tau); */
        /* ------------------------------------------------------------ */


        /* ----------------       Calculation of ReFcm ---------------- */
        printf(" simfc = %5.5eMHz calfc = %5.5eMHz \n", simfc*1.e-6, calfc*1.e-6);

        fclose(out1);
 }
```

APPENDIX C

LOW CONDUCTIVE MEDIUM RECIPE (40 mL)

Normal low-conductive medium recipe (conductivity: 0.13 S/m @ 25 ˚C)

KH_2PO_4	1.63 mg	(0.3 mM)
K_2HPO_4	5.92 mg	(0.85 mM)
KCl	37.28 mg	(25 mM)
myo-Inositol (I5125, Sigma-Aldrich)	2.02 g	(280 mOsmol/kg)
DI Water	40 mL	

Ultra-low-conductive medium recipe (conductivity: 0.017 S/m @ 25 ˚C)

KH_2PO_4	1.63 mg	(0.3 mM)
K_2HPO_4	5.92 mg	(0.85 mM)
KCl	3.73 mg	(2.5 mM)
myo-Inositol (I5125, Sigma-Aldrich)	2.02 g	(280 mOsmol/kg)
DI Water	40 mL	